Development of 2D Nanomaterial Based Membranes for Nanofiltration Applications

Trinity College Dublin
Coláiste na Tríonóide, Baile Átha Cliath
The University of Dublin

A thesis submitted to the School of Chemistry,

Trinity College Dublin,

For the degree of Doctor of Philosophy

By

Natalia García Doménech

Under the supervision of Prof. Yurii K. Gun'ko

2022

Summary

The main aim of this work was to develop new membranes based on 2D nanomaterials, such as boron nitride (BN) and molybdenum disulphide (MoS_2) for potential nanofiltration applications. The exfoliation and membrane preparation processes for all the materials were optimised, with the goal to obtain high retention performance membranes. Composite membranes were also prepared to enhance the properties of the membranes, by introducing new materials into the membranes. These membranes have great potential to be use for nanofiltration applications, like wastewater treatment.

Chapter 1, Introduction, presents a literature review on the relevant topics of this thesis, as well as explaining the theoretical background behind this research. This chapter covers an introduction to Nanofiltration (NF), materials and different approaches used for making membranes, the mechanism of separation by these membranes, the different applications for NF and liquid-phase exfoliation, which are the main topics of our research. A broader discussion was also given on LDHs, magnetism, magnetic nanoparticles and carbon nanotubes, which are relevant for the composite membranes production.

Chapter 2 of this thesis presents all the information relevant to the experimental work carried out. This includes all the starting materials and experimental methods and protocols used in each chapter. All the characterisation techniques used were also described in detail in this chapter.

Chapter 3 focuses on the exfoliation of BN in different solvents, NMP, IPA and water, and its optimisation for each solvent. Once the exfoliation had been optimised, BN based membranes were fabricated using the produced nanosheets. The membranes were used for filtration of Evans Blue, a water soluble dye. The retention values of the membranes were recorded and it was found that the results obtained with the water exfoliated BN were superior to the other two solvents. The membranes made from the BN exfoliated in

water were also tested with two other water-soluble dyes, as a proof of concept to demonstrate the capacity of these membranes to retain different size molecules. The exfoliated 2D nanomaterials and membranes obtained from the BN exfoliated in the different solvents were fully characterised and compared, to try to elucidate the reason for the different results obtained with the three different solvents.

Chapter 4 describes the thermal oxidation of BN under air and the use of this nanomaterial for membrane preparation. The oxidised material, referred as BNOx, was fully characterised by various instrumental techniques and compared to regular BN. BNOx was exfoliated following the method already optimised for BN. Exfoliated BNOx was also fully characterised and any differences with BN and BNOx were noted. Membranes were prepared from the exfoliated BNOx nanosheets and their performance was tested using the three dyes used for the BN membranes. Furthermore, BNOx based membranes were tested for sugar separation using saccharides of different sizes. Moreover, the BNOx was functionalised using glucose as well as glutaraldehyde and other sugars, to try to improve the properties of the membranes as well as to introduce cross-linking between the layers of the nanosheets to improve their stability.

Chapter 5 details the addition of various nanomaterials to the BN/BNOx membranes to obtain composite membranes with improved properties. LDHs flakes were mixed with BNOx to clean the membranes, due to the photodegradation properties of the LDHs. The amount of both materials was optimised to maintain the high retention and the stability of the membrane. The two materials as well as the composite membranes were fully characterised by various techniques. In order to elucidate the best membranes, the retention for the different dyes was carried out. Once the composite membranes were optimised, studies on the photodegradation and quantification of the products were carried out to understand the mechanism and kinetics of the process. Fe_3O_4 nanoplates were used in order to introduce magnetic properties into the BN membranes. The magnetite nanoflakes and the composite membranes were fully characterised. The optimal amount of BN and Fe_3O_4 per membrane was studied and the membranes were tested for Evans Blue dye retention. The capacity of the membranes for magnetic separation was also tested. Finally, the effect of introducing a 1D nanomaterial as well

as carbon nanotubes (CNTs) into the BN based membranes was also studied. BN and CNTs were exfoliated in three different solvents and their performances for retaining Evans Blue were tested.

Chapter 6 is dedicated to the development of membranes using a 2D MoS_2 nanomaterial. The exfoliation of MoS_2 was optimised and membranes were produced from the exfoliated MoS_2 nanosheets. The solutions and membranes were characterised with several techniques. The retention performance of the membranes has been evaluated with the Evans Blue dye. MoS_2 was also functionalized with chiral ligands (cysteine and penicillamine), in order to introduced chirality in the membrane. The goal was to achieve enantiomeric separation, which was tested using racemic mixtures of L and D-cysteine. Finally, MoS_2 was also mixed with BNOs nanoflakes to produce composite membranes. This was achieved following two consecutive approaches: a layered approach and a simple mixture of the two solutions. These membranes were also tested for the retention of Evans Blue dye.

Finally, chapter 7 offers the conclusions of all the work carried out. It summarises the main achievements attained while studying these membranes. The future work for this project was also outlined.

Declaration

This thesis is submitted for the degree of Doctor of Philosophy to the University of Dublin, Trinity College and has not been submitted before for any degree or examination to this or any other university. Other than where acknowledged, all work described herein is original and carried out by the author alone. Permission is granted so that the Library may lend or copy this thesis upon request. This permission covers only single copied made for study purpose, subject to normal conditions of acknowledgement.

_____

Natalia García Doménech

Acknowledgements

First and foremost, I would like to thank my supervisor Prof. Yurii Gun'ko for giving me the opportunity to work in his research group and for guiding me during this past four years. His constant support and encouragement to follow and try any ideas I had and to pursue anything I wanted to in my professional career have shaped me as the researcher I am today. After these years in his group, I can say that I got extremely lucky while carrying out the PhD.

To Dr. Finn Purcell-Milton, thank you for all the help in the lab and when writing papers. Thank you for all the talks, discussions and experiments, I know that I can always turn to you. Thank you for all your help with TEM.

I would like to extend my gratitude to Dr. Sarah McCarthy for all her help, especially on the last year.

I would also like to thank the entire Gun'ko group, past and present. There couldn't be a better group to have spent these past years with. Thank you for all the coffees, talks and encouragement, after all of this time I'm lucky enough to consider you my friends.

To the Gun'ko gals, for making these years, especially the last two, so fun, coming to work was so much better because of you. For all the lunches, coffees and endless conversations. Thanks to Áine for all the proof reading, the TGAs, zeta potentials and all the discussions about our research, but also for all the fun we had outside from work. Munirah, thanks for proofreading this thesis and helping with the VSM, for all our walks and for always being there to listen and help. To Xue, thanks for all the memories and all these years of friendship.

To my students, Maeve, María, Kate and Amy, thanks for all the amazing work, it's been a pleasure supervising all of you.

To Adrián, Marc and Iñigo, the Spanish crew in Trinity. Thanks for being there, for all the coffee breaks, lunches, pints and talks. Thanks for always being willing to help when I was stuck and for making Dublin feel like home. Thanks to Adrián for the XRDs and

Ramans, for all the talks about our research and lives. And to Marc, thanks for the AFM and for always having a word of advice.

To Raquel, thanks for all the years of conversations, trips, movie days, brunches and days shopping. Thank you for being there and always ready to give me advice.

I would like to thank the ChemEd group, for all the fun and friendships made during these years, it was a pleasure working with all of you. John, Noelle and Niamh, thanks for all the support and encouragement as I transition to the Chemistry EPE world.

To all the staff in the School of Chemistry and especially to the technical staff (Peter, Patsy, Tom, Brendan, Manuel…), thank you for all the help these past years.

Nadia, thanks for all the help with the thesis and for always being there. Thank you for all the days out, the coffees, the lunches and for always listening to me (even when I'm rambling). To all the friends I made in the School, thank you for all the amazing memories.

To my parents, Ana and Jose, and my brother, Alberto, for always believing in me, for your constant support and love. Thank you for being my rock during this time. To my grandparents, Carmen, Pepe and Montsa, thank you for supporting me in all my decisions, even if they take me to a different country. Abuelo Pepe, your memory has accompany me during this time.

To Maria, Lu and Patri, my OT4, thanks for always being there. Even though I'm 1451 km away, I know that I can always count on you. For so many more concerts, dinners, secret santas and trips. For many more years together. Thank you for all the memories made and the ones will make. Thank you for believing in me and for showing me all the love and support these years. I love you. To all my friends back home, thank you for showing me that distance is just a number.

And, to everyone else who found their way into my life these past few years, thanks for being part of this journey.

Contents

List of figures

List of tables

Abbreviations

AFM- Atomic Force Microscopy

BET- Brunauer-Emmet-Teller

BN- Boron nitride

BuLi- n-buthyllithium

CD - Circular dichroism

FTIR- Fourier Transform Infrared

IPA- Isopropyl alcohol

MoS_2- Molybdenum disulfide

NF – Nanofiltration

NMP- N-methyl-2-pyrrolidode

PTFE- hydrophilic polytetrafluoroethylene

PVDF- hydrophilic polyvinylidene fluoride

PXRD- Powder X Ray diffraction

SEM – Scanning electron microscope

TEM- Transmission electron microscope

TGA- Thermogravimetric Analysis

VSM-Vibrating Sample Magnetometry

XRD – X-ray diffraction

Chapter 1: Introduction

1.1 Nanofiltration

1.1.1 Overview

Membrane based separation systems dominate for industrial process water treatment and many other applications due to their high efficiency, low energy usage, convenience for up- or down-scaling, and possibility of continuous flow operation. In particular, recently nanotechnology-based solutions (e.g. Nanofiltration) have emerged as potentially superior and cost-effective ways to remove sediments, charged particles, chemical effluents, bacteria and other pathogens in addition to removal of toxins like arsenic or impurities like oil [1–3]. There are four main membrane processes which are currently utilised in water purification: Microfiltration (MF), Ultrafiltration (UF), Reverse Osmosis (RO) and Nanofiltration (NF) [4–6].

NF refers to the utilisation of membranes with a pore size between 0.5 nm to 10 nm and operating pressures between 5 to 40 bar and is commonly used for the separation of solid dust, liquid droplets, sugars, proteins, dyes, multivalent ions, and microorganisms (such as viruses and bacteria). NF is considered "a process intermediate between reverse osmosis and ultrafiltration that rejects molecules which have a size in the order of one nanometre"[7], which is equivalent to molecular weight cut offs of 300-500 Da and acts as a type of pressure-driven filtration, with properties in between Reverse Osmosis (RO) and Ultrafiltration (UF) [8]. NF has a pore size bigger than those found in RO membranes, that in their ideal form can retain all components, but small enough that it retains many organic compounds such as sugars to pass through, unlike UF [9].

Important properties intrinsic to NF membranes include high permeation to monovalent ions, low permeation to divalent ions and higher flux than RO membranes. Due to these characteristics, NF membranes have been used in a wide range of applications, including water treatment, biotechnology and pharmaceuticals [10].

NF was first described in the 1970's and by the second half of 1980's, the initial applications for this type of filtration had been reported [7,11]. One of the main initial uses of NF was water treatment, producing drinking water and process water. The adoption of which was driven by elevated demand for high quality drinking water, therefore increasing the need for wastewater treatment. In addition, NF membranes offer

advantages over other membranes due to increased reliability and integrity, producing longer cycle times and hence lower costs[1].

In addition, over the last years, NF has been adopted by some industries, like the pharmaceutical and the food industry, since both can easily benefit from the use of NF. Specifically, the food industry tends to incorporate new technologies rapidly, but the regulation standard for high quality products present in the food industry still result in big challenges in the application of NF. Moreover, the increasing demand for products fitting strict dietary requirements requires further and more specialised separation approaches [1]. In overall, the applications of NF have increased steadily, nevertheless, a number of technical challenges remain, including: (i) membrane fouling, and regeneration, (ii) improved separation, (iii) further treatment of concentrates, (iv) chemical resistance of membranes and (v) insufficient rejection in water treatment. Moreover, large-scale use in wastewater treatment will require significant nanomembrane cost reductions, with NF offering a lower operating cost compared to RO (from 20% up to 40% lower), though it is still relatively expensive compared to other filtration methods, such as UF, with NF being approximately double the cost at present[4,5]. Thus, further development and improvement of NF technology is of immense importance and has spurred significant interest in the field, with publications showing a near 10 time increase in growth of papers mentioning the term nanofiltration over the past 24 years.

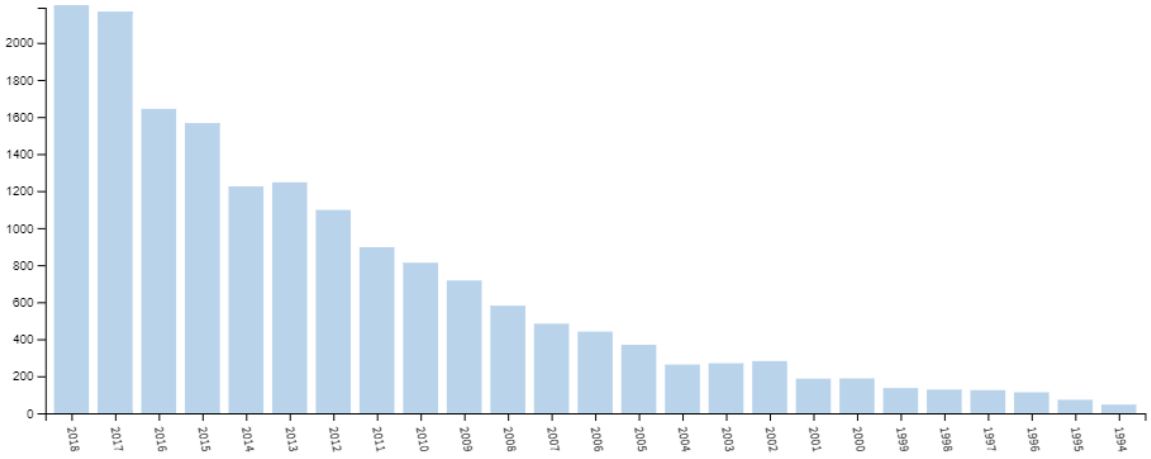

Figure 1.1: Number of papers on nanofiltration from 1994 to 2018. Image is taken from Web of Science.

1.1.2. Materials for NF membranes

The range of NF membranes can be most easily classified by dividing them according to their constituent materials. Typically, these are composed of either organic, inorganic or organic-inorganic hybrid membranes, each of which have specific advantages and disadvantages [12]. Organic membranes are usually produced using mainly polymeric materials, such as polysulfones, cellulose acetate or polyvinylidene fluoride [13–17]. Inorganic membranes are traditionally made from ceramics (TiO_2, SiO_2, ZrO_2, Al_2O_3, TiO_2-SiO_2, TiO_2-ZrO_2, Al_2O_3-SiC)[18–21], and more recently inorganic nanomaterials such as graphene[22–24], and carbon nanotubes [25,26]. While organic-inorganic hybrids are usually prepared by mixing a polymeric material with inorganic components (metal, metal oxide or a carbon based material) [27–30].

Nanomaterials are an outstanding starting material to fabricate a NF. The most common examples are nanoparticles (in most cases metal and metal oxide) and nanotubes, mostly carbon nanotubes [31]. Nanoparticles are usually mixed with a polymeric matrix, improving the properties of the membrane, like flux and rejection [32–35]. Carbon nanotubes (CNTs) show a particular water capability due to the hydrophobic and smooth inner walls. They have also been added to the mixed matrix membranes, which improves separation and antifouling properties [36–39]. This review aims to cover especially the emerging field of 2D material-based NF membranes, a class we judge as especially promising.

The most well-known 2D nanomaterial, graphene, has become established as an effective building-block for nanofiltration, especially for water treatment and the separation of small particles [40–42]. Graphene is the flat monolayer of carbon atoms ordered two-dimensionally in a honeycomb lattice [43]. And has a range of very interesting properties, including optical transmittance and excellent electrical conductivity [44,45] which makes it ideal for several different applications, including sensors [46–49] and transparent conductive films [50–53].Moreover, graphene presents a mixture of strong mechanical properties, being chemically inert and very large surface area [54–56]. Therefore, interestingly graphene allows the fabrication of membranes that possesses the advantage of the ceramic membranes (chemical inertness) and polymers, as it can be made into films using graphene/graphene oxide dispersions. Graphene membranes show excellent transport properties, such as high permeability and selectivity for liquids [23,55,57–59] and gases [60–63].

Graphene oxide (GO) is another 2D nanomaterial finding wide ranging application in NF with a variety of important publications showing the potential of it.[41,42,64–69] GO differs from graphene due to the presence of OH groups, produced through a partial oxidation process of the graphene sheets. This change introduces an assortment of reactive oxygen

functional groups, which makes GO a perfect candidate for a great variety of applications, including energy-related materials and biomedical applications, through chemical functionalization [70]. GO nanosheets are found to be quite attractive as membrane building blocks because they are straightforward to synthetize, mechanically robust and can be relatively easily upscaled for industry [56,71,72]. In addition, GO membranes have shown a range of favourable properties for nanofiltration applications, including thermal and chemical stability [56,73–77].

In the most recent years, new two -dimensional (2D) materials, similar to graphene, have found an important application as building blocks of membranes for NF. This 2D material family, which includes BN and transition metal dichalcogenides (TMD) like MoS_2, has gained attention recently as a result of the exceptional physical and chemical properties they possess [64,78–83].

BN can be considered as a structural counterpart of graphite, where the boron and nitrogen atoms intersperse, as carbon atoms would do in its analogue [84]. BN is a very useful and attractive 2D nanomaterial as it is colourless, transparent, electrically insulating (BN has a band gap of around 5-6 eV), chemically stable and mechanically strong. [84–87]. By contrast to graphene, BN nanosheets (BNNSs) are wide band gap semiconductors, and therefore do not absorb in the visible region of the electromagnetic spectrum thus, is frequently referred to as white graphene [88]. Currently, there are several procedures used to obtain BNNSs, including liquid-phase exfoliation [89], the reaction of boric acid and urea [90] or mechanical exfoliation [91]. Each method produces distinctively interesting properties, such as the obtainment of virtually extrinsic substance-free BNNSs solutions through liquid-phase exfoliation [89]. Nonetheless, the main disadvantage of this method is the poor stability of the solutions at normal conditions, with aggregates of BNNSs starting to form as soon as 12 hours after the exfoliation [92]. Functionalization of the nanosheets can lead to higher stability in the exfoliate material [92], as well as enable the use of this material in other novel practical applications via the functionality of the attached ligands, such as for enantiomeric separation. Membranes can be formed from exfoliated BNNSs [93], although it isn't as commonly used as other 2D nanomaterials, such as MoS_2 to date .

TMDs are normally presented as MX_2, where M is a central transition metal atom (group IV, V, VI, VII, IX or X) and X is a chalcogen atom (S, Se or Te)[94]. TMDs are formed by sandwiching metal atoms between two layers of the chalcogen atoms, forming hexagonal layers. The layers of metal and chalcogen are bound by covalent bonds, although

neighbouring sheets pile up trough Van der Waals interactions, forming 3D crystals [95–97] The weak Van der Waals connections that exist between the different layers allows the possibility of producing single or few-layer nanosheets by exfoliation of the bulk material. These 2D nanosheets present atypical physical and electronic properties, unlike those of the bulk material due to their dimensions [94]. Various methods have been proposed to obtain ultrathin 2D TMDs, including chemical intercalation and exfoliation [81,98], sonication-assisted liquid exfoliation [89,95], mechanical cleavage exfoliation [99,100] or chemical vapour deposition (CVD) , all of which have certain advantages and disadvantages.

A particularly interesting TMD for NF is molybdenum disulphide. This is a very well-studied TMD used in a range of applications including as a solid state lubricant and as a catalyst for a range of reactions including hydrodeoxygenation of phenols [101]. MoS_2, in its bulk form, has an energy gap of ~1.2 eV, and is an indirect band gap semiconductor [102]. The band gap increases with decreasing number of layers and is calculated to become 1.8 eV for a monolayer [103]. It is this property which has driven a wide range of applications in electronics and photonic applications. Another interesting property reported concerning MoS_2 membranes has been that as a filter it shows much higher water permeance than previously described graphene membranes, with similar thickness and reject ratio [41,42,104] due to the higher level of interaction between the MoS_2 sheets. In addition, it has been reported that the nanochannels present in the MoS_2 membranes do not deform under pressure of as much as 1.0 MPa, as has been shown by the linear relationship between pressure and water permeance [104]. Furthermore, this type of membrane demonstrates high chemical stability even under harsh conditions, and therefore can be employed repeatedly [104].

1.1.3. Methods of NF membrane Fabrication

There are several key methods to produce non-2D material-based membranes and are strongly dependent upon the materials used. Regarding all inorganic based NF membranes, these have been extensively reviewed [105,106] and are outside the scope of this project. Concerning organic or organic hybrid materials , four of the more commonly used procedures were reviewed and discussed in depth by Wang Zhuqing *et al* [12]. Here we will give a brief overview of these important methods; phase inversion, interfacial

polymerization, track-etching and electrospinning, all of which are presented in Figure 2 and in addition detail specific methods for 2D nanomaterial-based membranes.

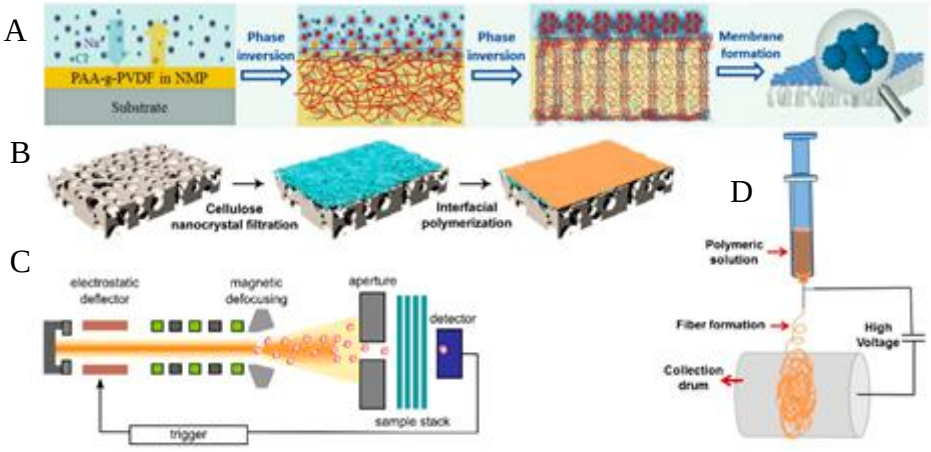

Figure 1.2 :Methods of membrane fabrication: A) phase inversion process; B) interfacial polymerization methodology, C) track-etching method and D) electrospinning process. Taken from reference [12].

Phase inversion is a technique to obtain membranes where there is a separation of the homogenous liquid polymer, transforming it into a solid state, in a controlled manner (figure 2a). This liquid to solid transformation can be achieved in different ways: (i) thermally induced phase separation (TIPS); (ii) controlled evaporation of solvent from three component systems; (iii) precipitation from the vapour phase and (iv) immersion precipitation (IP). [16]

Interfacial polymerization is based on a polycondensation reaction between two monomers dissolved in non-miscible solvents. Initially, one of the solutions covers the template and the second solution is laid on top so to enable the polymerization to take place (figure 1.2b). This method allows the quick formation of a layer on the interface of the polymer-template attached to the template as well as the easy control of the membrane structure by varying different parameter, like monomer concentration or reaction time [32,107]. Another way of obtaining porous membrane is by using track-etching. In this procedure, nanopores are created in an originally nonporous polymer thanks to a linear track damaged created by a high energy heavy ions beam (figure 1.2c). [108] Electrospinning is a technique where nanofibers or polymeric fibres are spun by electrostatic forces [109], which can be used to obtained polymeric membranes. This technique involves applying a high voltage between the solution and collector that

generates nanofibers. The nanofibers will form the nanofibrous mat in the collectors. [110,111] (figure 1.2d).

However, when concerning the use of 2D materials, a two-stage process is common in the production of these filters. Firstly, the 2D nanomaterial must be produced using an approach that yields appropriate quantity and quality of material needed for this form of application. Therefore, to date this has meant the use of a top down synthetic approach, in which a quantity of bulk non exfoliated material, is subjected to a technique which allows its conversion to a 2D nanomaterial, termed exfoliation. A range of approaches exists to produce this either in the solid state or in solution, including liquid or mechanical exfoliation and chemical vapor deposition. Of these approaches, liquid phase sonication assisted exfoliation and ball milling assisted exfoliation to date have been the most strongly favoured, due to both techniques' ability to produce large volumes and still a high level of exfoliation. Following this the non-exfoliated material is separated from the exfoliated via centrifugation in the solution phase, finally producing a solution of the desired 2D material.

Following this the most common means of preparing the membranes is by simple vacuum filtration [41,42,95,104]. Vacuum filtration occurs due to the difference between atmospheric pressure and a vacuum, using the pressure gradient as a driving force of the procedure (figure 1.3) [112]. This approach is low cost, scalable and therefore an excellent advantage of these emerging membranes.

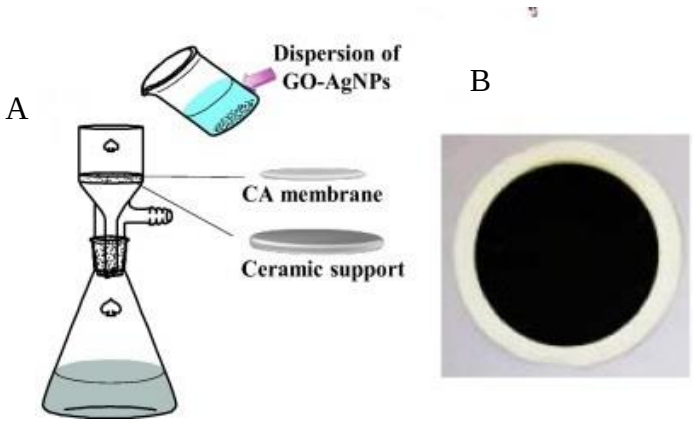

Figure 1.3. A) Vacuum filtration process to produce membrane. B) Photo of the membrane obtained. Taken from reference [113].

An excellent example of the technique in action include a MoS_2 membranes obtained by Sun, Luwei *et al* via the vacuum filtration of an exfoliated MoS_2 solution through a

polycarbonate membrane (47 mm of diameter and 20 nm of pore size)[104]. It was shown that different parameters can be easily controlled by this procedure, like membrane size (determined by the funnel size) and thickness of the membrane (directly dependent on the concentration of the exfoliated solution) [104]. Another important example has been performed by Ling Qui *et al*, obtaining membranes of chemically converted graphene (CCG), with corrugated sheets. They were also able to tune the corrugation and, therefore, the pore size of said membranes by performing hydrothermal treatment at different temperatures [42]. Another technique that has been used with 2D materials is the formation of aerogels [114–120]. Aerogels is a type of gels where the medium they incorporated is, basically, air [114]. The exchange of a liquid solvent for air, with no collapse of the structure, could end up in a novel porous materials that could be used for several applications, like catalysts support [121] or sensors for chemicals or biological materials [122,123]. Aerogels have also been used as adsorbents, showing great characteristics for adsorbing organic solvents, like toluene, cyclohexane or DMF [114,116,119,120,124] and oils, repelling water [114,116,117,124]. This could be used as a new way of producing nanofiltration membranes from 2D materials, increasing their strength and integrity.

Apart from the methods of fabrication, module geometry also plays an important role on the performance of the membrane, with this topic having been extensively reviewed [125–129]. Briefly, membrane module geometry is of great importance when considering the influence of mass transfer on the build up of rejected species, as it will increase the concentration polarization (CP), with high CP leading to a reduction of the performance of the membranes, due to higher trans-membrane osmotic pressure and lower salt rejection [125–129]. Additionally, an optimal module will also increase the energy efficiency of the membranes [128], an important parameter to consider in developing new technologies nowadays.

1.1.4. NF Separation mechanisms

NF is a very sophisticated process, controlled by the microhydrodynamic and interfacial processes that take place both on the surface and within the pores of the membrane. The rejection performed by NF membranes is due to a combination of different effects, including steric, dielectric, transport and the Donnan effect [10]. The steric mechanism, which is due to the size exclusion transit of neutral substances has been perfectly

described previously thanks to various experiments with ultrafiltration membranes [130] (figure 1.4).

The equilibria and membrane potential interaction that takes place between a charged solute and the interface of the membrane is explained by the Donnan effect [131] (figure 1.4). Due to the dissociation of ionizable groups both in the surface of the membrane and in the pore morphology, the membrane acquires a charge state [132,133]. Depending on the materials used when making the membrane, these potentially ionizable groups may be acidic, basic or a combination of both, with their dissociation from the surface of the membrane determined heavily by the pH of the containing solution and the amphoteric nature of the membrane itself. This also means that if the membrane is amphoteric, it will bear an isoelectric point at a specific pH [134].

Aside from the process previously described, the NF membrane can also have the ability of weakly interchanging ions, which can result in the adsorption of ions from the containing solution onto the surface membrane and consequently a minor variation in the membrane charge [135,136]. Electrostatic forces can therefore act according to the ion valence and the charge of the membrane, which can alter due to the formerly commented effect. The dielectric effect (figure 1.4) is less well understood, although some theories attempting to explain this phenomenon have been proposed [10]. One of the main hypothesis is called the "solvation energy barrier mechanism" [137] and comes from a combination of the spatial confinement and the nanoscale uniquely present in NF [138].

In addition, the movement of solutes through the pores of NF membranes is greatly influenced by the interaction of the confined space of the pores and the passage of the containing solution through them. Due to this, the free movement of the solutes is considered to be hindered and is described under the category of transport effects. This type of transport is formulated as a combination of the convective and diffuse component, acting both on the overall transport outcome. The comprehension of the physical structure and electrical properties of NF membranes has been delayed due to near atomic dimensions of the active layer of NF, which in turn has resulted in ambiguity and debate on the actual nature of the separation mechanism [10], with the dielectric exclusion principle being the most challenging [138].

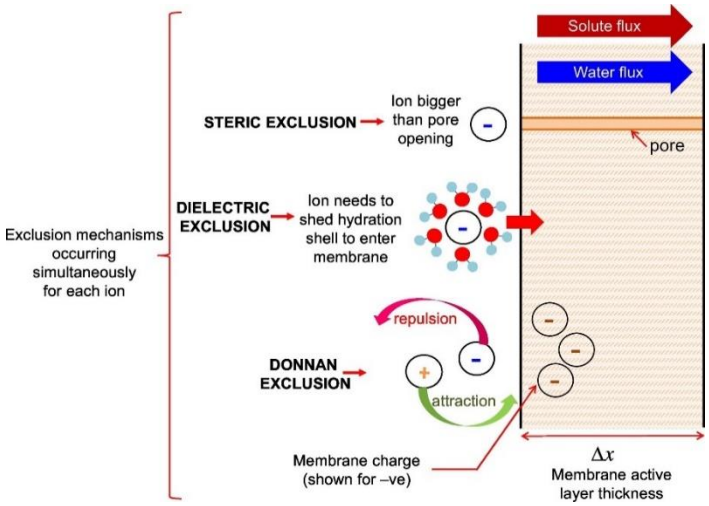

Figure 1.4: Schematic representation of solute exclusion mechanism in nanofiltration. Taken from reference [139].

The solution's passage through the NF membrane can also be explained through the solution diffusion model, which can be divided into three steps: absorption on the side of the feed, diffusion through the membrane and desorption on the side of the permeate [140]. The solution-diffusion model has gained more attention in the past decades, presenting as an alternative to the other models due to it needing less measurable parameters, like pore radius and membrane charge, which are difficult to determine for a nanofiltration membrane [141]. This model works by firstly assuming a continuous gradient of the chemical potential and that the rate of adsorption and desorption at the membrane interface are implicitly higher than the rate of diffusion through the membrane. Therefore, the overall transport rate of molecules is not influenced by the processes of absorption-desorption, and so the limiting process for the permeation rate is determined by the diffusion of the substances through the membrane, with molecules passing through the membrane in response to the concentration gradient and importantly with no pressure gradient inside the membrane [140,142]. For the case of 2D nanomaterials, the same mechanisms have been described as found in other membrane designs, but the relative importance of each is still a subject of hot debate within the field.

1.1.5. Characterization of Membranes

There are a range of different ways to characterize nanofiltration membranes and has been extensively reviewed in a number of publications [1,8,10,143], therefore we will present

a brief overview here. These approaches can be separated into two distinct categories, characterization of the filter and performance measurements of the filter, though some cross over does exist. In regard to filter characterisation, the most important factors are pore size, pore distribution, and the charge of the membrane. Pore size and pore distribution are crucial to understanding the steric separation that can be achieved with each membrane [10]. This is characterized most effectively using the approaches detailed below:

- Brunauer-Emmet-Teller (BET) method, a gas adsorption-desorption procedure, is used for obtaining the pore size directly [144,145]Neutral solute rejection can be used to determine directly the pore size of the membrane. It can also give the distribution when in combination with other methods [146–149].
- Atomic force microscopy (AFM) can be used to determine the pore size and distribution in a direct manner, as well as surface roughness, topography and force interactions between the membranes and solution [8,150–152].
- Transmission Electron Microscopy (TEM) in conjunction with reverse surface impregnation can be used to directly obtain pore size and distribution [153].

It is worth noting, to achieve the best results a combination these techniques should be utilised, due to length scales and various errors associated with each of these techniques.

The charged properties of the membrane is an inherently important characteristic to be studied in order to understand the exact process of filtration [10]. As it has been mentioned previously, these properties change depending on the pH, nature and concentration of the feed solution. To characterize these properties, different techniques can be applied, namely:

- Electro-osmosis measures the zeta (ζ) potential through pore, perpendicular to the surface of the membrane [154].
- The zeta (ζ) potential of the surface of the membrane can be obtained using streaming potential. This techniques gives a pseudo measurement of the Donnan potential [155–157].
- Streaming current, which is an alike measurement to the streaming potential [158–160].

- Charged solute rejection can be used to obtain indirectly the effective membrane charge density, with the requirement of other characterization methods *in situ*) [146,155,161,162].

In addition, aside from all the techniques aforementioned, other useful methods of characterization of NF membranes are SEM for surface, cross-section and fouling layers [32,36,150], contact angle for hydrophilicity/hydrophobicity[163–165] and some other spectroscopy methods such as Raman spectroscopy or positron annihilation spectroscopy for morphology and structure of the membranes [154–156].

Following on from this, the membrane's performance as a means to separate in a range of conditions must be tested, with the resulting properties defining the membranes ability, with the most common factors measured being water permeance, flux rate and rejection rate.

For water permeance (transport flux per unit transmembrane driving force) and flux rate (number of moles, volume or mass component passing through the membrane per unit of time)[143], dead-end membrane filtration systems are used to determine [22,40,166]. The dead-end filtration is a type of filtration where the flow of solution passes, under pressure, perpendicular to the surface of the membrane [167].

Another very important term is the rejection rate (R_x), which shows the capacity of the membrane to avoid the passage of certain molecules through its pores. The rejection rate of the membranes is calculated using the following equation:

$$\boldsymbol{R_x}\ (\%) = (\mathbf{1} - \frac{\boldsymbol{C_{P,X}}}{\boldsymbol{C_{F,X}}}) \cdot \mathbf{100}$$

Where:

- R_X is the retention rate
- $C_{F,X}$ is the concentration of the analyte in the feed
- $C_{P,X}$ is the concentration of the analyte in the permeate

The concentration used in this calculation can be calculated in different ways, depending on the nature of the solutes, using conductivity measurements and/or spectrophotometer [10,151,168–170].

When considering 2D nanomaterial filters, no alternative approaches have been developed exclusively to this area, with all of the techniques mentioned applicable to this emerging category of nano filters.

1.1.6. Fouling of membranes

Another important aspect to consider when designing a membrane is the issue of fouling, defined as the loss of filtration capacity due to the deposition of solute from the feed on the surface, pores or within the pores of the membranes [171]. This is especially a distinctively difficult problem when applied to NF due to the nanoscale interactions that take place [1] with fouling directly influencing the concentrate treatment ,membrane and stability [1]. In order to estimate fouling, it is very important to determine the flux of clean water and the flux reduction [143]. The negative consequences that fouling have on the membranes translate in the need for pretreatment, cleaning of the membranes, limited recoveries and losing feed water[1].

Foulants can be classified as organic and inorganic solutes, biological solids and colloids[1,172]. Organic solutes mostly produce fouling due to adsorption interactions with the membranes[1,173–175]. Component properties can influence the relation of fouling and adsorption[1,175]. Electrostatic and repulsion interactions played a crucial role for the degree of fouling caused by charged organic compounds[1]. Inorganic fouling is often due to the deposition of salts on the surface of the membrane (scaling)[1,143]. As NF are capable of retaining ions, their concentration increases in the surface as a result, causing solubility limit to be exceeded and, thus, causing the salts to precipitate on the membrane[1]. Although the point of saturation could, theoretically, be calculated, it's challenging to determine the critical point where supersaturation starts[1]. Colloidal fouling may occur both on the membrane surface (cake formation) or within the pores, depending on the size of the colloidal solution[1,176–179]. Colloidal fouling can be influenced from roughness of the membranes (valley clogging)[1,180,181], concentration (higher concentrations lead to increased fouling)[1,178,182–185] or size (large size may have a positive or negative effect when compared to small sizes)[1,182,186,187]. Biofouling is a problem that occurs in most membrane process, involving biologically active microorganisms, like bacteria[1,143]. The main issue with biofouling is the formation of a biofilm, which reduces or eliminates the flux of water through the membrane[1].

Solutions for fouling involve pretreatment methods or cleaning of the membranes[1]. The cleaning of the membranes is an area largely studied[1,188–190]. There are several methods used, including physical cleaning and chemical cleaning. Physical cleaning can be carried

out by flushing, scrubbing, vibrations or sonication[1,143,191,192]. Chemical cleaning can be accomplished by performing chemical reactions like hydrolysis, saponification, chelation or peptisation[1,193]. Another potential solution for fouling is the modification of the membranes, which would allow to obtain fouling-resistant membranes[1]. Colloidal fouling could, potentially, be reduced by using smoother membranes[1,177] or increasing the hydrophilicity of the membrane[1,188]. The use of antibacterial materials, like silver nanoparticles, could reduce the formation of the biofilm, eliminating the biofouling[1,194].

1.1.7. Applications of Nanofiltration

Nanofiltration has been used for a wide range of applications, including water treatment, desalination and in different industries such as the pharmaceutical, chemical and food industry.

1.1.7.1. Water treatment

Water scarcity is a very serious problem nowadays but with NF, new innovative solutions are possible to tackle this ever-increasing issue. Therefore, water treatment is one of the most important applications of NF membranes. Water treatment includes, filtration of ions and salts [195–200], water softening [201–205] , organic molecules, like dyes [42,57,64,206–208], nanoparticles [209], separation of oils [210–214] and bioorganisms such as viruses and bacterias [25,26,215–217].

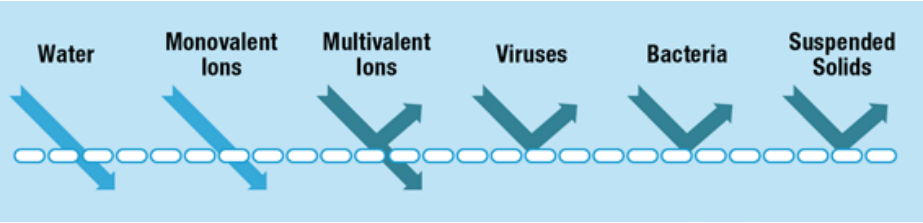

Figure 1.5: Schematic of materials separated by NF in water treatment. Taken from reference[218].

Research into NF is mostly focused on water treatment as the main goal from the governments is pollution control and prevention[219]. There are different subareas within the treatment of wastewaters where NF can be used. The majority of industrial and urban water treatment plants focused on the removal of organic materials, among others[219]. The

textile industry is also considered one of the most polluting industries, considered a great environmental problem due to, for example, the dyes used[220]. Membranes have been used for the removal of dyes from the textile industry wastewaters[221], like Congo Red[222].

Another area of interest related to the treatment of water is desalination[219]. The desalination industry mostly uses reverse osmosis (RO) techniques to filtrate the salt present in saline waters to obtain fresh, clean water ready for consumption, agriculture or industry. Nanofiltration can be used for the removal of divalent ions as well as small organic materials, so it has been utilized as a pretreatment for desalination processes[219,223]. NF membranes let some salt passed through, having a lower operating pressure than RO, which translates into economical savings from operating and reducing the fouling. Due to this, NF membranes have also been proposed as an effective technique for desalination of water, with most of the membranes showing between 97 and 99% rejection of salts [196,197,224].

NF, therefore, has a placed in water treatment, being on its own or in combination with more traditional processes, such as RO, microfiltration or ultrafiltration[219,225,226].

1.1.7.2. Organic Solvent Treatment

NF can also be applied to the separation of organic solvents. This technique is termed Organic solvent NF (OSN), also known as organophilic NF (ONF) or solvent resistant NF (SRNF), and is starting to be used to achieve membrane separation in a range of organic solvents [10]. Polymers with intrinsic microporosity (PIM), which have poor solubility in most solvents are expected to have high stability in different solvents and, in theory, make OSN possible, although more or less swelling is observed in other solvents [10,227]. OSN allows for the separation of low molecular weight (200-1000 g/mol) from organic solvents [228–230] using low energy consumption [228,231]. OSN processes are affected by finding the equilibrium between permeability and selectivity without losing one of them over gaining the other [232,233]. This is due to, on one hand, the low solvent permeance through the polymeric membrane as a result of the close-knit of the membrane [234] and, on the other hand, the difficulty of having a good control over the membrane selectivity [235].

1.1.7.3. Pharmaceutical industry

Currently, one of the main goals in the pharmaceutical industry is to obtain active pharmaceutical ingredients (APIs). During the synthesis process, different solvents are used, including organic solvents. These types of solvents are not inert and can be toxic or alter the stability of the API. Due to this, organic solvents are treated as waste. However, the use of OSN opens the possibility of recovering and recycling these solvents, making the process more economic and environmentally-friendly [166]. Researchers are also looking to develop systems that would allow the separation of APIs from common genotoxic impurities (GTIs) [10]. Another issue that arises from the synthesis of pharmaceuticals compounds is the possible appearance of by-products as impurities [236,237]. These impurities could, potentially be chemically reactive creating undesirable toxicities like genotoxicity or carcinogenity, impacting on the risk assessment [236,238].

1.1.7.4. Food Industry

Another industry that highly benefited from the use of NF is the food industry, where it has been used as a separation technique for vegetable oils [239–242], beverages [243–246], dairy industry [247–250] or sugar industry [251–254]. When it comes to food industry filtration, there are different specifications depending on the type of industry. In the dairy industry, there is the need for cleaning the wastewaters from dilute milk, which includes lipid, protein and lactose, and chemicals used for cleaning, like acids or detergents. Nanofiltration has been proposed as a very promising technique as it allows the recovery of protein and lactose as well as reusing water in the same operation [248,249,255,256]. In wine making there is the production of several components that are beneficial for humans, including polyphenols and resveratrol [243,257,258]. The main advantage of using nanofiltration to concentrate these valuable compounds of wine is that it can be carried out at room temperature so it protects the heat-sensitive products and volatile compounds [243]. One of the most energy-intensive procedures in food industry is sugar processing, as it involves solutions with high viscosity and high osmotic pressure, which makes the use of membranes difficult [252], though interestingly nanofiltration shows potential for use to processes sugars as these membranes showed higher retention for sucrose than for non-sugars [252,254].

NF has been used for separation of saccharides in fermentation and biotechnology[259,260]. NF can be utilized to separate monosaccharides from disaccharide as well as mono- and di-saccharides from high weight saccharides, like oligo- and polysaccharides based on their different sizes[259]. However, the separation of different monosaccharides from each other still present difficulties, due to their similar size and structure[259]. Another interesting type of saccharide is oligosaccharides, as they are considered beneficial for human health. Microfiltration and ultrafiltration have been used to separate and purified these oligosaccharides, but their product usually also contains low molecular weight sugars that do not add any beneficial properties to the oligosaccharide's ones[260]. NF could be used as a potential alternative for the scale method of purification and concentration of oligosaccharides, although this is still being research[260].

1.1.7.5. Enantiomeric Separation

The separation and purification of enantiomers is one of the most important yet most difficult areas in science [261]. Most organic and biomolecules are chiral, which translate to an increasing need for enantiopure solutions, as key intermediates in the pharmaceutical and chemical industry[262]. Traditionally, this has been achieved by using methods such as Gas Chromatography (GC) or High-Performance Liquid Chromatography (HPLC), which are effective at producing this separation but show serious issue due to high costs and long duration times (figure 1.6). Thus, there's a high demand for a new method, which will be enantioselective, cheap and have a wide range of applications[263]. The use of membranes for this type of separation is an attractive alternative to chromatography, as they can be used in continuous processes and their cost and energy usage is often reasonable[261]. The main way of achieving enantioselectivity is by performing enantioselective inclusion complexation (EIC), where a host molecule is used to complex specifically with one of the enantiomers and after which the two compounds are separated by distillation [264,265]. But this process has some limitations including the complexity and the high energy cost of carrying out separation by distillation. A possible improvement suggested in literture idea is the use of EIC followed by OSN [265,266]. The coupling of EIC-OSN will decrease the energy needed, as it could be performed at room temperature and would make the process simpler, as the hosts could be recycled and reused [264–266]. However, the ideal situation would be to use only a membrane process rather than complexation before the separation.

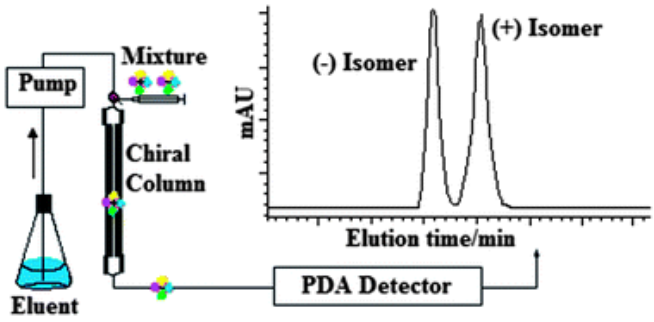

Figure 1.6: Schematic of chromatography based chiral separation. Taken from reference [267].

The use of membrane technology for this purpose has mostly been limited to liquid membranes [262], although solid membranes have also been adopted for this role, mainly using chiral polymers or chiral selectors (such as proteins) [268,269] (figure 1.7). An important product for chiral separation by NF, is amino acids. There are around 20 genetically encoded amino acids that are used as the building blocks for proteins, the basic constituents of all living organisms with most multicellular organisms using L-amino acids, whereas in bacteria, it is common to find D-amino acids[270]. Apart from playing such an important role in living organisms, amino acids can also be used as basic building blocks for organic chemistry synthesis[271]. In addition, other important products that could be enantiomerically separated by this NF is lactic acid.

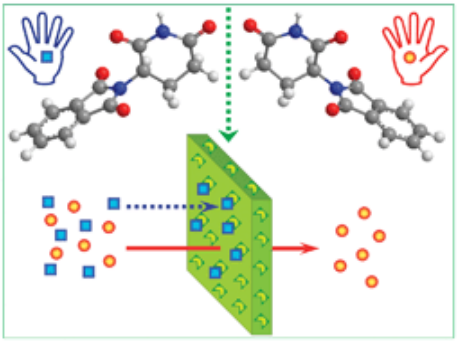

Figure 1.7: Schematic of chiral separation using membranes. Taken from reference [272].

Even though a membrane technique has not yet been established for enantiomeric separation, especially when it comes to solid membranes, some promising results have been obtained using chiral selectors [261,262,268,269,273]. These results seem to indicate that enantiomeric separation could be carried out with either solid or liquid membranes, with indications that solid membranes utilizing a chiral selector appear to give a minor

improvement over that of liquid ones. A particular inherent issue is that, these membranes depend on the addition of a chiral selector to the membranes to achieve chiral separation, but perhaps, these membranes could be made chiral by incorporating chiral ligands during the synthesis of the building blocks, as has been demonstrated with the production of a range of chiral nanomaterials [274–276].

1.2. Liquid phase exfoliation

Exfoliation can be used to produce 2D nanomaterials. Due to the exfoliation, the accessible surface area of a material significantly increases, which can entirely change the chemical and physical reactivity of catalytic or surface-active materials[89].

Liquid phase exfoliation could allow for the dispersion of large amounts of nanosheets in a given solvent. There are four main methods of liquid phase exfoliation, figure 1.8 shows the schematics of ion intercalation, ion exchange and sonication-assisted exfoliation[89].

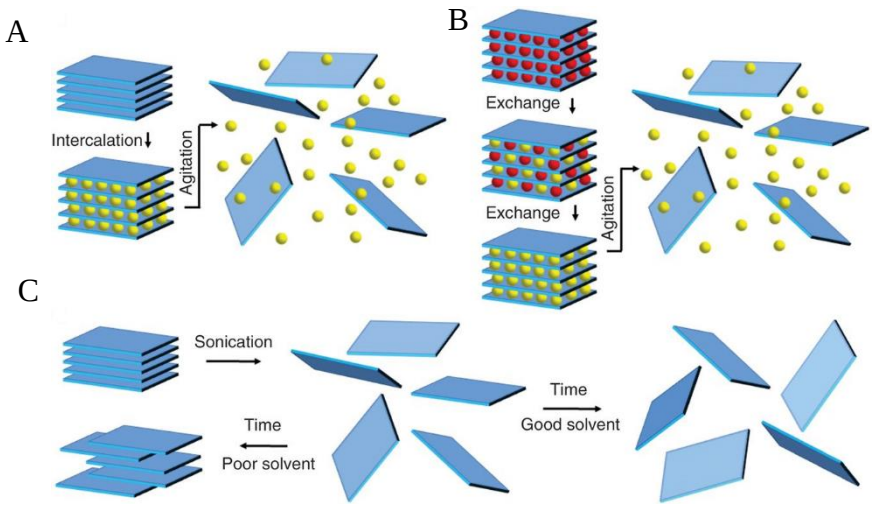

Figure 1.8: Schematic of different types if liquid exfoliation mechanisms, A) ion intercalation, B) ion exchange and C) sonication-assisted exfoliation. Taken from reference[89].

Ion intercalation between the nanosheest causes an increment of the layer spacing, which facilitates the exfoliation by weakening the interlayer forces and, thus, bringing down the energy barrier for exfoliation. Layered materials have the ability of strongly interacting

with guest molecules in between the layers, which is the principle upon which this method is based. Ion intercalation has been used for exfoliation of different types of layered materials, including TMDs[89,102,277]. More reduction of this interlayer binding can be achieved by introducing ions that will transfer charge to the layers, like n-butyllithium[89,102,277] and IBr[89,278]. Following the intercalation of ions, a treatment using ultrasonication[89,102,277] or thermal shock[89,278] in liquid phase will finish the exfoliation process. However, there are some disadvantages of using this type of exfoliation, mostly due with the sensitivity of the reaction to the ambient conditions[89,102,277,279].

Some layered materials, like LDHs, clays and certain metal oxides, have the ability of interchanging cations for the anions already contained in their structure, which is the basis for ion exchange exfoliation[89,280]. Usually, these new ions are bigger than the ones already present in the structure, which causes "swelling" into the structure[89,280]. This swelling, generally, aids in the exfoliation process by ultrasonication or shear mixing, giving a negative charge to the layers[89,281].

Recently, the use of ultrasonic waves for exfoliation have been gaining more attention. Here, the ultrasonication waves produces cavitation bubbles that have enough energy to break the forces in-between the layers, obtaining the exfoliated nanosheets[89]. Through modelling, it has been observed that when the surface energy of the solvent and layered material are similar, reaggreation will be decreased, as the main drive for this is the high energy difference between the exfoliated material and reaggreates, which is decreased here[89].

One of the most traditional method for liquid phase exfoliation is the oxidation and following dispersion in a suitable solvent of materials with a low reductive potential. The best example of this method is the formation of graphene oxide (GO) from graphene[70,89]. GO can then be reduced chemically in liquid phase, but it will reaggreate if a surfactant or stabiliser is not present. Moreover, structural defects will still be present, even if the reduction removes most of the oxides. These structural differences will make the properties of GO different from pristine graphene[89].

The main advantages of using liquid phase exfoliation for the production of 2D nanosheets are the scalability, versatility and sustainability[89]. Moreover, the production of nanosheets in solutions opens the possibility of using them in manners that could not

be accessed otherwise. Some of these examples are the easy mixing of different materials or the formation of thin free-standing films[89].

1.3 Layered Double Hydroxides (LDHs)

Layered double hydroxides (LDHs) are a class of ionic lamellar compounds, composed of positively charged layers and interlayers regions made with anions and solvation molecules[282]. The particular structure is formed by metal cation in the centres of edge sharing octahedral with hydroxide groups on their vertexes, connecting into infinite 2D nanosheets[282]. The most common type of LDHs follow the formular $[M^{2+}_{1-x}M^{3+}_{x}(OH)_2][A^{n-}]_{x/n}\cdot zH_2O$; where:

- M^{2+} represents divalent metal ions, like Mg^{2+}, Zn^{2+} or Ni^{2+}.
- M^{3+} represents trivalent metal ions, like Al^{3+}, Fe^{3+} or Mn^{3+}.
- An- represent the compensating anion (nonframework charge), like CO_3^{2-}, Cl^- or SO_4^{2-}.
- X is usually somewhere between 0.2 and 0.4.

LDHs can be synthesised as nanosheets following a top down or bottom up approach[282] (figure 1.9).

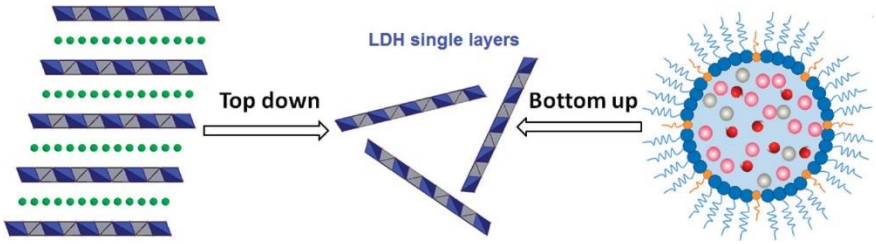

Figure 1.9: schematic of top down and bottom up for the synthesis if LDH nanosheets. Taken from reference[282].

The top down method is usually preferred, consisting of the delamination of the LDH. However, this method has been proven challenging as the charge density of these materials is significantly high[282–285]. This approach usually requires the modification of the structure, usually by ion exchange followed by sonication in an appropriate solvent[282].

Bottom up is usually carried out as a coprecipitation method. One way of synthesising the LDH is producing reverse micelles, which will act as nanoreactors where the LDH layers can be formed[282]. Another way of obtaining LDHs is a simple coprecipitation

method, where the $M(OH)_2$ (divalent metal ion) and $N(OH)_3$ (trivalent metal ion) precipitate together in a supersatureated solution[286]. As soluble forms of both types of metal ions are needed to compose the layers, soluble salts in a mixed metal solution is usually used. Furthermore, to precipitate the product, the counter ions are needed, along a strong base[286].

LDHs have been used for several applications, including catalysis[282,287,288], CO_2 absorption[282,289,290] or as electro and photoactive materials[282,291,292]. Like most layered materials, LDHs can also be made into thin films for applications like sensor technologies and optical devices[282,293,294].

1.4 Magnetism and magnetic nanoparticles

Magnetic nanoparticles (MNPs) have gained great interest in the past few years, due to their unique properties, like high surface to volume ratio and the difference between their magnetic parameters from the bulk material[295]. MNPs have a large range of applications including data storage[295] or as contrast agents for magnetic resonance imaging (MRI)[296]. Moreover, the use of magnetic nanoparticles allows the possibility of externally manipulating the nanoparticles using a magnetic field[296].

1.4.1 Magnetism

Magnetism can be defined by using intrinsic and extrinsic characteristics. Extrinsic properties are related to the crystal morphology and include the coercivity and remanence[297]. Intrinsic properties are defined based on the structure of the crystal and comprise saturation magnetization (M_s), Curie temperature (T_c) and anisotropy[297].

The main property that induces magnetism is the electro spin, as every electron is composed of an orbital and spin moment. When a certain high temperature is achieved, materials will be paramagnetic but below this temperature, these electron spins may adopted different arrangements. These different arrangements can be classified as diamagnetic, ferromagnetic, anti-ferromagnetic, ferromagnetic and paramagnetic (figure 1.10).

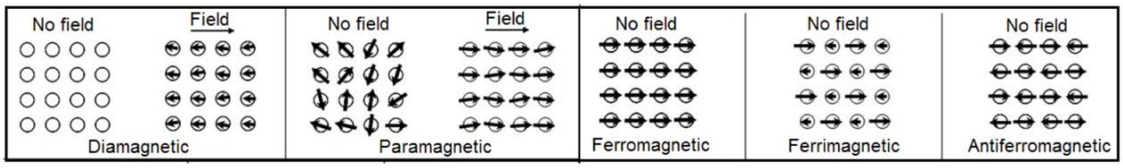

Figure 1.10: Magnetic dipoles and behaviour of materials when in the presence and absence of a magnetic field. Taken from reference[298].

Diamagnetic materials, under a magnetic field, will display a magnetic dipole in the opposite direction of the applied field, meaning it will be repelled by the magnetic field. In the absence of the magnetic field, however, the material doesn't present a magnetic dipole as it lacks on unpaired electrons. Paramagnetic materials, on the other hand, have magnetic dipoles even in the absence of a magnetic field, but they will only align when a magnetic field is applied. Ferromagnetic materials present net magnetic dipole moments, even in the absence of magnetic field. When a material is not exposed to a magnetic field, its true magnetic nature can be studied. Ferrimagnetic and anti-ferromagentic material have similar magnetic dipoles moments than the ones observed in ferromagnetic materials. Nonetheless, there are adjacent dipole moments in a different orientation that would cancel or reduce the magnetic behaviour, respectively[298].

Below certain sizes, MNPs have similar properties to paramagnetic materials, showing zero magnetic response in the absence of a magnetic field being applied. They also showed a fast increased in their magnetic response when an external magnetic field is applied, when compared to paramagnetic materials. This phenomenon occurs when the blocking temperature has been surpassed. Above this temperature, ferromagnetic and ferromagnetic will behave as superparamagnetic. Superparamagnetism is achieved as the energy barrier for moment reversal, which allows for quick flipping of the magnetic moments, is lower than the thermal fluctuations due to the blocking temperature being surpassed[298]. MNPs being superparamagnetic is quite important for certain applications, where the materials shouldn't showed magnetic response unless it's under the presence of an external magnetic field, like in the case of MRI or drug delivery[298]. This prevents the aggregation of the nanoparticles, as they are not attracted to each other. Furthermore, superparamagnetic nanoparticles, due to their strong response to an external magnetic field, display better control of the magnetic properties[298].

When using MNPs, the saturation magnetization is defined as the maximum magnetization possible and it occurs when all magnetic dipoles of a material are aligned with the external magnetic field. The typical magnetization curve is shown in figure 1.11.

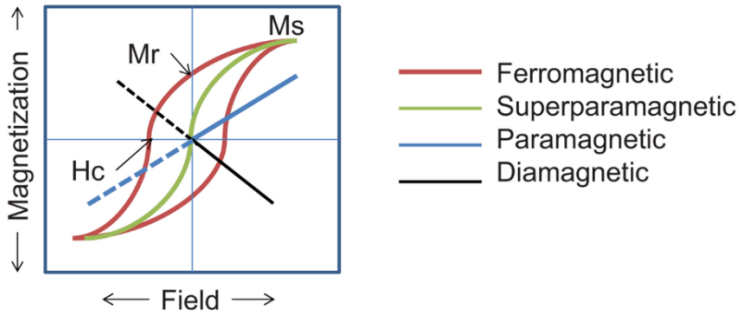

Figure 1.11: Magnetization curve showing the responses to applied magnetic field of ferromagnetic, superparamagnetic, paramagnetic and diamagnetic materials. Taken from reference[298].

The magnetization curve indicates the positions of the different parameters:

- Saturation magnetization (Ms): maximum induced magnetization.
- Remanent magnetization (Mr): induced magnetization that remains once the magnetic field has been removed.
- Coercivity (H): the intensity of an external coercive field that is needed to force the magnetization to be zero.

Different materials, as seen in figure 1.11, will response differently to an external magnetic field. Paramagnetic and diamagnetic have opposite behaviours under a magnetic field, where the magnetization of a paramagnetic material will increased with the force of the magnetic field; whereas the diamagnetic material will be repelled by that field. A hysteresis loop will be obtained when studying ferromagnetic materials. This loop will be significantly broad when working with multi-domain particles and, inversely, will narrow as the domain number decreases. Superparamagnetic materials, on the other hand, respond to a magnetic field quite strongly, but will not retain any magnetic memory once the magnetic field is removed. This is evident in the curve, which shows a similar sigmoidal shape to the ferromagnetic materials but has no hysteresis. Therefore, the magnetic behaviour of ferromagnetic and superparamagnetic materials is driven by their size, as the smaller the particle (thus, one particle, one domain), the nanoparticle will have a superparamagnetic behaviour.

1.4.2 Magnetite (Fe_3O_4)

Magnetite was first discover around 4000 years ago in Greece, where a shepherd found that the metal pins in his shoe were stuck to a rock[299]. This rock was known as lodestone and, later on, as magnetite[299].

Magnetite (Fe_3O_4) is a type of magnetic material, classified as a ferrite. A ferrite material is defined as an ionic compound made from positively charged iron and other metal ions as well as negatively charged oxygen ions. The structure these materials adapt is cubic close packed (ABCABC…). The octahedral sites alternate with the tetrahedral sites in the structure. These structures are called spinel, and the can be normal spinel or inversed spinel[300]. In a normal spinel structure, the tetrahedral sites are filled with the divalent atom; whereas in an inverse spinel these atoms occupy the octahedral sites (figure 1.12).

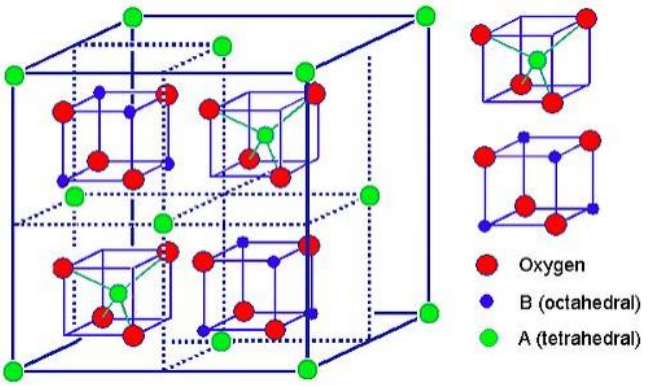

Figure 1.12: Schematic of an inverse spinel structure. In magnetite, Fe^{2+} ions occupy half the octahedral sites, whereas the Fe^{3+} fills the rest of the B sites and all A sites. Taken from reference[300]

Magnetite has an inverse spinel structure (figure 1.12). The Fe^{2+} ions will occupy half of the B sites, whereas Fe^{3+} fills the rest of the octahedral sites and all of the tetrahedral sites. The larger Fe^{2+} ions have preference to fill the octahedral spacious, as they are more spacious, this is why Fe_3O_4 presents an inverse spinel structure.

Magnetite nanostrucutres are of particular interest due their extraordinary properties, such as superparamagnetism, biocompatibility and non-toxicity for humans[301,302]. As a result of these, magnetite is widely used for several applications, like dyes for MRI[301,303,304], bio-sensing and diagnosis[301,305,306] or controlled drug delivery[301,303,305].

1.4.3 Fe_3O_4 nanoplates

Magnetite nanostructures have gained a lot of attention recently due to their unique properties, like optical, electronic, magnetic or catalytic, as well as their unique structure[307–309]. The exceptional properties of magnetite nanoparticles depend immensely on their shape, size and structure[307,309]. Therefore, studies into the control of size and shape that can be obtained are of interest and being actively looked into[307,310,311]. Different shapes of magnetite have already been achieved, including nanorods[307,312], nanoparticles[307,308] and nanowires[307,313]. 2D shape has been reported before using a substrate growth method and microwave radiation method[307,314,315]. Another way to obtain Fe_3O_4 in a 2D shape is using a soft template method, with the aid of P123 as structure-directing agent[307].

Nanoparticles are usually obtained by a co-precipitation method, but in order to obtain nanoplates, the copolymer P123 is used to act as a template for the synthesis (figure 1.13). P123 acts directing the growth of the particles, so that the crystal growth is restricted in specific directions to get the 2D shape.

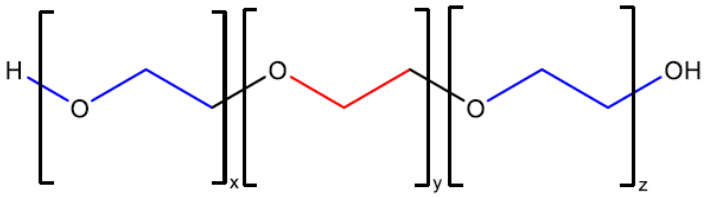

Figure 1.13: Copolymer P123 structure with hydrophobic part in red and hydrophilic parts in blue. Figure illustrated in ChemDraw.

P123 is composed of propylene glycol block (red in figure 1.13) in between two ethylene glycol blocks (blue in figure 1.13) at the end of the polymeric chain. The hydrophilic aspect of the molecule is due to ethylene glycol, whereas the propylene glycol gives the hydrophobic part of the molecule[316]. The way P123 works is by forming micelles on top of the Fe_3O_4 seeds in solution, due to the formation of an emulsion as a result of the dual hydrophilicity and hydrophobicity of the polymer. The P123 molecules will stacked side by side, blocking the access of more Fe_3O_4 to the surface and, effectively, preventing the crystal to grow in that direction (figure 1.14). The curved edges of the molecules makes the stacking of P123 more complicated, leaving gaps in between the chains. These gaps

let Fe_3O_4 access the surface of the particle, letting the crystal grow in that particular direction, which forms anisotropic structures like wires and, in this case, nanoplates[317].

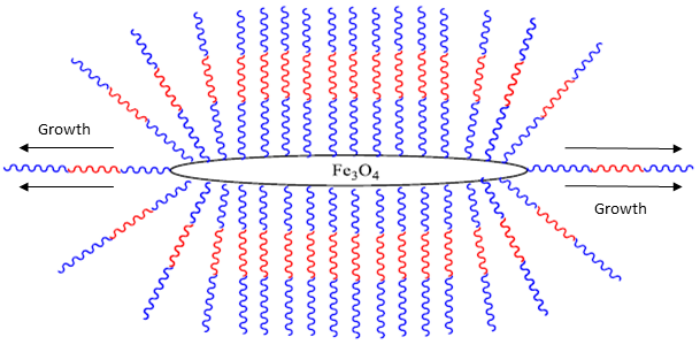

Figure 1.14: Schematic of the action of P123 in the growth of Fe_3O_4 nanoplates. Figure illustrated in ChemDraw.

1.5 Carbon Nanotubes (CNTs)

Carbon nanotubes (CNTs) were first described by Iijima in 1991[318]. CNTs have been extensively researched and aid in the development of different fields, like physics, material sciences and chemistry. CNTs, due to their nanotube shape, have very interesting properties. These properties are a direct result of the way the graphene sheet wraps around, forming the tube. CNTs are excellent candidates for several applications, e.g. hydrogen storage, due to their geometry and nanosize[319].

CNTs are defined as sheets of graphite rolled up forming a nanotube[319,320]. Due to their high length to diameter ration, CNTs are considered as 1D nanostructures. Unlike diamond, a 3D cubic crystal structure, where each carbon atom has four carbon neighbours forming a tetrahedral structure, graphene is a 2D structure, with the atoms of carbon arrange in a hexagonal shape, where each carbon only has three neighbours[320]. CNTs are dived into single walled carbon nanotubes (SWCNTs) and multi walled carbon nanotubes (MWCNTs). A SWCNT is a cylinder than is formed from a single graphene sheet wrapped into the nanotube structure. MWCNTs, on the other hand, are considered as a collection of concentric SWCNTs (figure 1.15). The properties of SWCNTs and MWCNTs are very different, as well as their lengths and diameters[319].

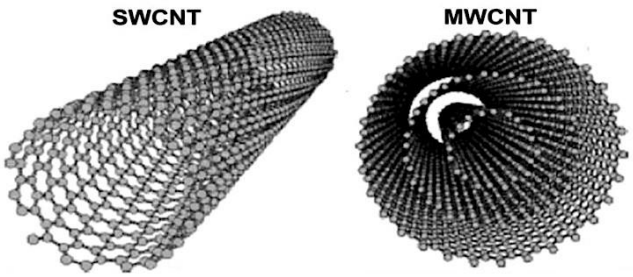

Figure 1.15: Schematic representation of a single walled CNT (SWCNT) and a multi walled CNT (MWCNT). Adapted from reference[321].

The properties associated to CNTs are dependent of the atomic arrangement found in their structure, i.e. the way the graphene sheet has rolled up, diameter and length of the nanotube and the nanostructure within the nanotube[320].

1.5.1 Structure of CNTs

The atomic structure of the CNTs is defined by the tube chirality or helicity. This helicity is defined by the chiral vector, C_h, and the chiral angle θ. The chiral vector is described by the following equation:

$$C_h = na_1 + ma_2$$

Where n and m, the integers, described the number of steps long the carbon bonds of the lattice and a1 and a2 are unit vectors (figure 1.16). it can also be observed the cutting of the graphene sheet by the dotted lines, where the rolling of the tube would occur so the tip of C_h touches its end[320].

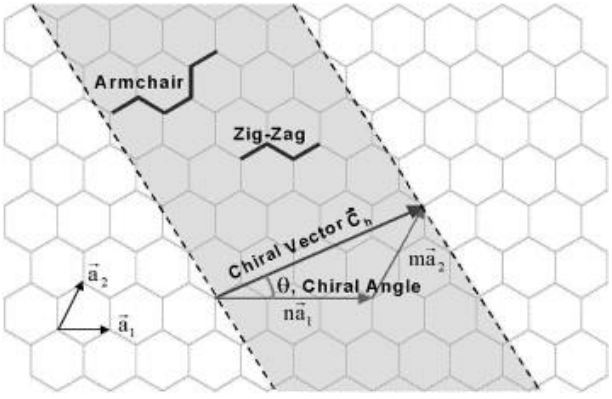

Figure 1.16: Diagram of the rolling of the graphene sheet to form the CNT. Taken from reference[320].

The other factor, the chiral vector, defines the amount of twisting that exist in the nanotube. There are two limiting cases, where the chiral vector can be either 0°, referred as zig-zag, and 30°, called armchair (figure 1.17). These names come from the geometry that the carbon bonds adopt around the diameter of the CNT[320]. In terms of the roll-up vector, a CNT with a zig-zag conformation will be (n,0) and an armchair one will be (n,n). This roll-up vector will define the diameter of the CNT as well, as the the inter-atomic spacing of the carbon atoms is known.

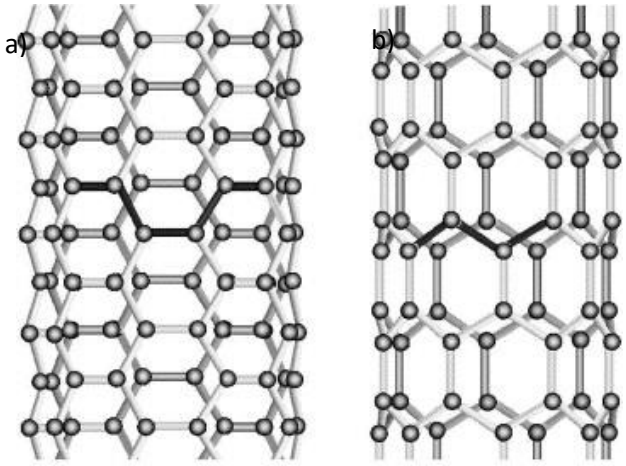

Figure 1.17: Schematic of a CNT with a) an armchair and b) zig-zag atomic structure. Adapted from reference[320].

1.5.2 Applications of CNTs

CNTs have been extensively researched in nanotechnology for several different applications. These applications appear in diverse fields, including medicine, material science, energy storage or electronics[322].

Carbon nanotubes have been used as fillers in different materials, forming composites. The goal of adding CNTs to another material or polymer, improving the properties of these materials. CNTs can enhance the thermal, electrical and mechanical properties of the materials they are being added too[322].

Another field where CNTs can be useful is in electronic devices and field-emission sources. In this case, a potential is applied in between the CNT and anode. Due to the curvature of the CNTs[322,323] or the existence of oxidised tips[322,324], the electrons can be

easily emitted from their tips. CNTs are also very good electron emitter, with advantages like long and stable field-emission or high current densities.

Due to their structure, hollow nanotubes, carbon nanotubes can potentially be used for efficient metal and gas storage. Different chemical compounds have already been successfully introduced in the CNT structure, including metals and oxides[322]. In terms of encapsulating gaseous substances, there is still some debate present, with some instances of successful encasing of H_2 and Ar in SWCNTs[322,325,326] and MWCNTs[322,327].

In the medical field, SWCNTS and MWCNTs have already shown the potential for drug delivery systems. CNTs can pass through the cellular membrane, delivering therapeutic drugs and vaccines, reaching the target deep into the cell. Moreover, they are non-toxic vehicles than can also increase the solubility of certain drugs, which results in better safety and efficiency[322].

1.6 Aims of this work

Nanofiltration using 2D nanomaterials has been gaining a lot of attention. These materials offer the option of high chemical inertness, as found in ceramics, combined with the ease of processability of polymers. Unique to 2D materials such as graphene and boron nitride is a very high breaking strength, and single layers have been shown to tolerate more than 20% elastic distortion, presenting exceptionally large flexibility[328]. In addition, these materials have a very large total surface area due to their intrinsic layered nature[329,330].

One of the first 2D materials used as a building block for nanofiltration membranes was graphene. Graphene has been proven very effective for water treatment and separation of small particles. When it comes to the dyes tested in this work, graphene oxide (GO) is usually used for the membranes showing good results. However, these membranes are usually made by intercalation with different materials (like lignin or TiO_2). Evans Blue has been tested with different GO membranes, with results varying from 83% when intercalating copper hydroxides nanostrands[331], 93% when using ligning[332] to 98% with GO and HNb_3O_8[333]. Other smaller dyes, like Methylene Blue and Methyl Orange, have also been used to test the performance of GO membranes. In the case of Methylene Blue, the retention of the membrane varied from low retentions of 66% when cross-linking

with 1,3,5-benzenetricarbonyl trichloride[334] and 89% with GO intercalated with Si_3N_4[335] and increasing to 99.3% when intercalating GO with TiO_2[336] and 99.66% when using GO and MoS_2 together[337]. Methyl Orange usually present more consistent retentions across the different membranes found in literature, with retentions in the area of 97% with GO intercalated with CNTs and GO intercalated with IPDI; and retentions of 99% for GO intercalated with SiO2[335] and with TiO_2[336].

Similar to graphene, boron nitride is also a potential great candidate for nanofiltration membranes. Most papers in literature focus on using BN as an adsorbent rather than a membrane, although membranes using BN have been prepared as well. Evans Blue and Methyl Orange are not usually used to evaluate the performance of BN membranes. However, functionalized BN with amino groups membranes have been reported to retain Evans Blue at >99% in methanol [338]. In the case of Methyl Orange, BN functionalized with a negative charge fibers have been tested for retention of this dye, but the retention obtain was lower than with other BN and materials, with only around 30-40%[339]. Methylene Blue, however, has been used as a test the retention performance of different BN compounds. Porous BN nanosheets exhibit a high retention of 99% for this dye over 180 minutes[340], whereas BN fibers are capable of retaining 99% of Methylene Blue in 20 min[341] and BN nanocarpets show a 99% retention for this organic dye[342]. Other BN compounds, like BN nanonets[343] and functionalized BN membranes[344] only shown a 98% retention for Methylene Blue. In the case of oxidized BN, an analogue to GO, membranes have yet to be synthesized.

Finally, TMDs, in particular MoS_2, have been used as building blocks more membranes. These membranes have been tested with some of the dyes already mentioned. In the case of Evans Blue, MoS_2 membranes have shown varying results, going from 89%[104], to 99% [345] and even achieving 100% retention in water and IPA[346]. Similar to the case with BN, MoS_2 shows lower retentions (60-70%) for Methyl Orange, when modified with polydopamine[67]. Methylene Blue has also been used for testing MoS_2 membranes, with retentions varying from 96% in water[346], 98%[346,347] in water and IPA to 99%[67,346,348]. However, these membranes were obtained by either chemically exfoliating the MoS_2 or modifying it with other molecules.

The literature dye retention performances are described for membranes obtained by chemically exfoliation or by modification/functionalization of the materials, therefore,

our approach is to obtain the membranes by mechanical exfoliation as well as using simple functionalization to obtain new membranes.

The main aim of this work is the development of a range of new membranes, which are based on 2D nanomaterials (BN and MoS_2), for separation and nanofiltration applications. Our goal is to use liquid phase exfoliation to obtain the 2D BN and MoS_2 nanosheets, which then will be used to produce the membranes using vacuum filtration. Furthermore, we plan to test different functionalisation approaches for the 2D nanomaterials as well as mixing of different materials to enhance the performance of the membranes.

The exfoliated materials and membranes are to be characterized by a range of techniques including SEM, XRD, UV-Vis, FTIR and CD spectroscopy, although not limited to these ones.

The main focus, initially, is to develop and optimise the production of membranes, which have highly reproducible parameters and performance. This will be achieved by testing different solvents for BN and $MoS_2$the exfoliation and the membrane formation and performance. Once the method is optimised, it will be used to produce a range of membranes and composite membranes using different materials, obtaining. The 2D nanomaterials will also be functionalised by different methods, including oxidising of BN and adding glucose, as well as binding chiral ligands to MoS_2, introducing chirality to the membrane. The membranes will be tested for several applications, including retention of dyes, sugars, chiral and magnetic separation.

Therefore, this project will include the following scientific and technical objectives:

1. To investigate the effect of different solvents on the exfoliation of BN and formation of the membranes.
2. To optimise the method to obtain highly reproducible membranes from BN with high retention values.
3. To test the performance of the membranes for retention of different water soluble dye molecules, with different sizes.
4. To oxidise BN by heating to introduce a functionalisation to this 2D nanomaterial.

5. To further functionalise the oxidise BN using glucose and other molecules to obtain extra separation functionalities.
6. To prepare BN-LDH composite membranes and investigate photodegradation of dyes in these membranes.
7. To prepare BN-Fe_3O_4 composite membranes for magnetic separation of magnetic nanoparticles and potential cleaning and recycling of the membranes using magnetic induction heating.
8. To prepare BN-CNTs composite membranes to attempt to control the pore size and retention parameters of the membranes.
9. To optimise the exfoliation of MoS_2 and formation of new membranes.
10. To functionalise MoS_2 with different chiral ligands to add chirality to the membrane.
11. To prepare BN-MoS_2 composite membranes for further nanofiltration applications.
12. To fully characterise the exfoliated solutions and membranes using SEM, TEM, XRD, FTIR, Raman, CD spectroscopy, UV-Vis, AFM, BET, mercury porosimetry, VSM, zeta potential and TGA.

We believe that this work will result in the development of a range of new functional membranes for water purification and nanofiltration applications.

Bibliography

1 B. Van der Bruggen, M. Manttari and M. Nystrom, *Sep. Purif. Technol.*, 2008, **63**, 251–263.

2 M. Paul and S. D. Jons, *Polymer (Guildf).*, 2016, **103**, 417–456.

3 M. Usmani, M.A.; Khan, I.; Bhat, A.H.; Pillai, R.S.; Ahmad, N.; Haafiz, M.K.M.; Oves, *Curr. Org. Synth.*, 2017, 206–226.

4 N. Shahkaramipour, N. T. Tran, S. Ramanan and H. Lin, *Membr.* , 2017, 7.

5 R. Zhang, Y. Liu, M. He, Y. Su, X. Zhao, M. Elimelech and Z. Jiang, *Chem. Soc. Rev.*, 2016, **45**, 5888–5924.

6 H. Lee, Y. Jin and S. Hong, *Desalination*, 2016, **399**, 185–197.

7 P. Eriksson, *Environ. Prog.*, 1988, **7**, 58–62.

8 N. Hilal, H. Al-Zoubi, N. A. Darwish, A. W. Mohammad and M. Abu Arabi, *Desalination*, 2004, **170**, 281–308.

9 M. Cheryan and M. Cheryan, 1998.

10 A. W. Mohammad, Y. H. Teow, W. L. Ang, Y. T. Chung, D. L. Oatley-Radcliffe and N. Hilal, *Desalination*, 2015, **356**, 226–254.

11 B. M. Watson and C. D. Hornburg, *Desalination*, 1989, **72**, 11–22.

12 Z. Wang, A. Wu, L. Colombi Ciacchi and G. Wei, *Nanomaterials*, 2018, **8**, 65.

13 E. Saljoughi and S. M. Mousavi, *Sep. Purif. Technol.*, 2012, **90**, 22–30.

14 A. L. Ahmad, A. A. Abdulkarim, B. S. Ooi and S. Ismail, *Chem. Eng. J.*, 2013, **223**, 246–267.

15 T. Shibutani, T. Kitaura, Y. Ohmukai, T. Maruyama, S. Nakatsuka, T. Watabe and H. Matsuyama, *J. Memb. Sci.*, 2011, **376**, 102–109.

16 F. Liu, N. A. Hashim, Y. Liu, M. R. M. Abed and K. Li, *J. Memb. Sci.*, 2011, **375**, 1–27.

17 E. Yuliwati, A. F. Ismail, T. Matsuura, M. A. Kassim and M. S. Abdullah, *Desalination*, 2011, **283**, 214–220.

18 I. Mohmood, C. B. Lopes, I. Lopes, I. Ahmad, A. C. Duarte and E. Pereira, *Environ. Sci. Pollut. Res.*, 2013, **20**, 1239–1260.

19 X. P. Cao, D. Li, W. H. Jing, W. H. Xing and Y. Q. Fan, *J. Mater. Chem.*, 2012, **22**, 15309–15315.

20 K. A. DeFriend, M. R. Wiesner and A. R. Barron, *J. Memb. Sci.*, 2003, **224**, 11–28.

21 M. Facciotti, V. Boffa, G. Magnacca, L. B. Jørgensen, P. K. Kristensen, A. Farsi, K. König, M. L. Christensen and Y. Yue, *Ceram. Int.*, 2014, **40**, 3277–3285.

22 Y. Han, Z. Xu and C. Gao, *Adv. Funct. Mater.*, 2013, **23**, 3693–3700.

23 D. Cohen-Tanugi and J. C. Grossman, *Nano Lett.*, 2012, **12**, 3602–3608.

24 P. Zhang, H. Wang, X. Zhang, W. Xu, Y. Li, Q. Li, G. Wei and Z. Su, *Biomater. Sci.*, 2015, **3**, 852–860.

25 M. S. Rahaman, C. D. Vecitis and M. Elimelech, *Environ. Sci. Technol.*, 2012, **46**, 1556–1564.

26 A. S. Brady-Estévez, M. H. Schnoor, S. Kang and M. Elimelech, *Langmuir*, 2010, **26**, 19153–19158.

27 M.-L. Luo, J.-Q. Zhao, W. Tang and C.-S. Pu, *Appl. Surf. Sci.*, 2005, **249**, 76–84.

28 J. Yin and B. Deng, *J. Memb. Sci.*, 2015, **479**, 256–275.

29 P. Wang, J. Ma, F. Shi, Y. Ma, Z. Wang and X. Zhao, *Ind. Eng. Chem. Res.*, 2013, **52**, 10355–10363.

30 P. S. Goh, B. C. Ng, W. J. Lau and A. F. Ismail, *Sep. Purif. Rev.*, 2015, **44**, 216–249.

31 Y. Ji, W. Qian, Y. Yu, Q. An, L. Liu, Y. Zhou and C. Gao, *Chinese J. Chem. Eng.*, 2017, **25**, 1639–1652.

32 B.-H. Jeong, E. M. V Hoek, Y. Yan, A. Subramani, X. Huang, G. Hurwitz, A. K. Ghosh and A. Jawor, *J. Memb. Sci.*, 2007, **294**, 1–7.

33 M. L. Lind, B.-H. Jeong, A. Subramani, X. Huang and E. M. V Hoek, *J. Mater. Res.*, 2009, **24**, 1624–1631.

34 M. L. Lind, A. K. Ghosh, A. Jawor, X. Huang, W. Hou, Y. Yang and E. M. V Hoek, *Langmuir*, 2009, **25**, 10139–10145.

35 H. Huang, X. Qu, H. Dong, L. Zhang and H. Chen, *RSC Adv.*, 2013, **3**, 8203–8207.

36 H. Wu, B. Tang and P. Wu, *J. Phys. Chem. C*, 2010, **114**, 16395–16400.

37 A. Tiraferri, C. D. Vecitis and M. Elimelech, *ACS Appl. Mater. Interfaces*, 2011, **3**, 2869–2877.

38 H. D. Lee, H. W. Kim, Y. H. Cho and H. B. Park, *Small*, 2014, **10**, 2653–2660.

39 F.-Y. Zhao, Y.-L. Ji, X.-D. Weng, Y.-F. Mi, C.-C. Ye, Q.-F. An and C.-J. Gao, *ACS Appl. Mater. Interfaces*, 2016, **8**, 6693–6700.

40 M. Hu and B. Mi, *Environ. Sci. Technol.*, 2013, **47**, 3715–3723.

41 H. Huang, Y. Mao, Y. Ying, Y. Liu, L. Sun and X. Peng, *Chem. Commun.*, 2013, **49**, 5963–5965.

42 L. Qiu, X. Zhang, W. Yang, Y. Wang, G. P. Simon and D. Li, *Chem. Commun.*, 2011, **47**, 5810–5812.

43 A. K. Geim and K. S. Novoselov, *Nat. Mater.*, 2007, **6**, 183.

44 W. Cai, Y. Zhu, X. Li, R. D. Piner and R. S. Ruoff, *Appl. Phys. Lett.*, 2009, **95**, 123115.

45 X. Li, Y. Zhu, W. Cai, M. Borysiak, B. Han, D. Chen, R. D. Piner, L. Colombo and R. S. Ruoff, *Nano Lett.*, 2009, **9**, 4359–4363.

46 J. T. Robinson, F. K. Perkins, E. S. Snow, Z. Wei and P. E. Sheehan, *Nano Lett.*, 2008, **8**, 3137–3140.

47 Y. Ohno, K. Maehashi, Y. Yamashiro and K. Matsumoto, *Nano Lett.*, 2009, **9**, 3318–3322.

48 N. Mohanty and V. Berry, *Nano Lett.*, 2008, **8**, 4469–4476.

49 O. Leenaerts, B. Partoens and F. M. Peeters, *Phys. Rev. B*, 2008, **77**, 125416.

50 X. Wang, L. Zhi and K. Müllen, *Nano Lett.*, 2008, **8**, 323–327.

51 Y. Zhu, W. Cai, R. D. Piner, A. Velamakanni and R. S. Ruoff, *Appl. Phys. Lett.*, 2009, **95**, 103104.

52 P. Blake, P. D. Brimicombe, R. R. Nair, T. J. Booth, D. Jiang, F. Schedin, L. A. Ponomarenko, S. V Morozov, H. F. Gleeson, E. W. Hill, A. K. Geim and K. S. Novoselov, *Nano Lett.*, 2008, **8**, 1704–1708.

53 J. Wu, M. Agrawal, H. A. Becerril, Z. Bao, Z. Liu, Y. Chen and P. Peumans, *ACS Nano*, 2010, **4**, 43–48.

54 A. Akbari, P. Sheath, S. T. Martin, D. B. Shinde, M. Shaibani, P. C. Banerjee, R. Tkacz, D. Bhattacharyya and M. Majumder, *Nat. Commun.*, 2016, **7**, 10891.

55 J. E. Kim, T. H. Han, S. H. Lee, J. Y. Kim, C. W. Ahn, J. M. Yun and S. O. Kim, *Angew. Chemie Int. Ed.*, 2011, **50**, 3043–3047.

56 R. K. Joshi, P. Carbone, F. C. Wang, V. G. Kravets, Y. Su, I. V Grigorieva, H. A. Wu, A. K. Geim and R. R. Nair, *Science (80-.).*, 2014, **343**, 752 LP – 754.

57 K. Huang, G. Liu, Y. Lou, Z. Dong, J. Shen and W. Jin, *Angew. Chemie*, 2014, **126**, 7049–7052.

58 K. Celebi, J. Buchheim, R. M. Wyss, A. Droudian, P. Gasser, I. Shorubalko, J.-I. Kye, C. Lee and H. G. Park, *Science (80-.).*, 2014, **344**, 289 LP – 292.

59 S. P. Surwade, S. N. Smirnov, I. V Vlassiouk, R. R. Unocic, G. M. Veith, S. Dai and S. M. Mahurin, *Nat. Nanotechnol.*, 2015, **10**, 459.

60 H. W. Kim, H. W. Yoon, S.-M. Yoon, B. M. Yoo, B. K. Ahn, Y. H. Cho, H. J. Shin, H. Yang, U. Paik, S. Kwon, J.-Y. Choi and H. B. Park, *Science (80-.).*, 2013, **342**, 91 LP – 95.

61 S. P. Koenig, L. Wang, J. Pellegrino and J. S. Bunch, *Nat. Nanotechnol.*, 2012, **7**, 728.

62 D. Jiang, V. R. Cooper and S. Dai, *Nano Lett.*, 2009, **9**, 4019–4024.

63 S. Saliba, C. Mingotaud, M. L. Kahn and J.-D. Marty, *Nanoscale*, 2013, **5**, 6641–6661.

64 L. Sun, H. Huang and X. Peng, *Chem. Commun.*, 2013, **49**, 10718–10720.

65 Y. Liu, H. Wu, L. Min, S. Song, L. Yang, Y. Ren, Y. Wu, R. Zhao, H. Wang and

Z. Jiang, *J. Memb. Sci.*, 2019, 117663.

66 P. M. G. van Deursen, Z. Tang, A. Winter, M. J. Mohn, U. Kaiser, A. A. Turchanin and G. F. Schneider, *Nanoscale*, 2019, **11**, 20785–20791.

67 J. Gao, M. Zhang, J. Wang, G. Liu, H. Liu and Y. Jiang, *ACS Omega*, 2019, **4**, 4012–4022.

68 T. Liu, X. Liu, N. Graham, W. Yu and K. Sun, *J. Memb. Sci.*, 2020, **593**, 117431.

69 J. Zhang, Z. Li, K. Zhan, R. Sun, Z. Sheng, M. Wang, S. Wang and X. Hou, *Electrophoresis*, 2019, **40**, 2029–2040.

70 D. R. Dreyer, S. Park, C. W. Bielawski and R. S. Ruoff, *Chem. Soc. Rev.*, 2010, **39**, 228–240.

71 D. A. Dikin, S. Stankovich, E. J. Zimney, R. D. Piner, G. H. B. Dommett, G. Evmenenko, S. T. Nguyen and R. S. Ruoff, *Nature*, 2007, **448**, 457.

72 G. Eda and M. Chhowalla, *Adv. Mater.*, 2010, **22**, 2392–2415.

73 Y. Han, Y. Jiang and C. Gao, *ACS Appl. Mater. Interfaces*, 2015, **7**, 8147–8155.

74 Y. Yuan, X. Gao, Y. Wei, X. Wang, J. Wang, Y. Zhang and C. Gao, *Desalination*, 2017, **405**, 29–39.

75 R. Han and P. Wu, *J. Mater. Chem. A*, 2019, **7**, 6475–6481.

76 L. Chen, J.-H. Moon, X. Ma, L. Zhang, Q. Chen, L. Chen, R. Peng, P. Si, J. Feng, Y. Li, J. Lou and L. Ci, *Carbon N. Y.*, 2018, **130**, 487–494.

77 X.-L. Xu, F.-W. Lin, Y. Du, X. Zhang, J. Wu and Z.-K. Xu, *ACS Appl. Mater. Interfaces*, 2016, **8**, 12588–12593.

78 D. J. Late, B. Liu, H. S. S. R. Matte, C. N. R. Rao and V. P. Dravid, *Adv. Funct. Mater.*, 2012, **22**, 1894–1905.

79 W. Hirunpinyopas, E. Prestat, S. D. Worrall, S. J. Haigh, R. A. W. Dryfe and M. A. Bissett, *ACS Nano*, 2017, **11**, 11082–11090.

80 A. Castellanos-Gomez, M. Poot, G. A. Steele, H. S. J. Van Der Zant, N. Agra??t and G. Rubio-Bollinger, *Adv. Mater.*, 2012, **24**, 772–775.

81 R. J. Smith, P. J. King, M. Lotya, C. Wirtz, U. Khan, S. De, A. O'Neill, G. S. Duesberg, J. C. Grunlan, G. Moriarty, J. Chen, J. Wang, A. I. Minett, V. Nicolosi and J. N. Coleman, *Adv. Mater.*, 2011, **23**, 3944–3948.

82 Z. Li, Y. Zhang, C. Chan, C. Zhi, X. Cheng and J. Fan, *ACS Nano*, 2018, **12**, 2764–2772.

83 T. Sainsbury, A. Satti, P. May, A. O'Neill, V. Nicolosi, Y. K. Gun'Ko and J. N. Coleman, *Chem. - A Eur. J.*, 2012, **18**, 10808–10812.

84 D. Golberg, Y. Bando, Y. Huang, T. Terao, M. Mitome, C. Tang and C. Zhi, *ACS Nano*, 2010, **4**, 2979–2993.

85 M. Corso, W. Auwärter, M. Muntwiler, A. Tamai, T. Greber and J. Osterwalder,

Science (80-.)., 2004, **303**, 217–220.

86 L. Ci, L. Song, C. Jin, D. Jariwala, D. Wu, Y. Li, A. Srivastava, Z. F. Wang, K. Storr, L. Balicas, F. Liu and P. M. Ajayan, *Nat. Mater.*, 2010, **9**, 430.

87 Y. Lin, T. V Williams and J. W. Connell, *J. Phys. Chem. Lett.*, 2010, **1**, 277–283.

88 A. Pakdel, X. Wang, Y. Bando and D. Golberg, *Acta Mater.*, 2013, **61**, 1266–1273.

89 V. Nicolosi, M. Chhowalla, M. G. Kanatzidis, M. S. Strano and J. N. Coleman, *Science (80-.).*

90 A. Nag, K. Raidongia, K. P. S. S. Hembram, R. Datta, U. V Waghmare and C. N. R. Rao, *ACS Nano*, 2010, **4**, 1539–1544.

91 D. PaciÍ, J. C. Meyer, Ç. Girit and A. Zettl, *Appl. Phys. Lett.*, 2008, **92**, 1–4.

92 P. Ma and J. T. Spencer, *J. Mater. Sci.*, 2015, **50**, 313–323.

93 J. C. Meyer, A. Chuvilin, G. Algara-Siller, J. Biskupek and U. Kaiser, *Nano Lett.*, 2009, **9**, 2683–2689.

94 X. Zhang, Z. Lai, Q. Ma and H. Zhang, *Chem. Soc. Rev.*, 2018, **47**, 3301–3338.

95 J. N. Coleman, M. Lotya, A. O'Neill, S. D. Bergin, P. J. King, U. Khan, K. Young, A. Gaucher, S. De, R. J. Smith, I. V. Shvets, S. K. Arora, G. Stanton, H. Y. Kim, K. Lee, G. T. Kim, G. S. Duesberg, T. Hallam, J. J. Boland, J. J. Wang, J. F. Donegan, J. C. Grunlan, G. Moriarty, A. Shmeliov, R. J. Nicholls, J. M. Perkins, E. M. Grieveson, K. Theuwissen, D. W. McComb, P. D. Nellist and V. Nicolosi, *Science (80-.).*, 2011, **331**, 568–571.

96 E. A. Marseglia, *Int. Rev. Phys. Chem.*, 1983, **3**, 177–216.

97 J. A. Wilson and A. D. Yoffe, *Adv. Phys.*, 1969, **18**, 193–335.

98 X. Geng, W. Sun, W. Wu, B. Chen, A. Al-Hilo, M. Benamara, H. Zhu, F. Watanabe, J. Cui and T. Chen, *Nat. Commun.*, 2016, **7**, 10672.

99 H. Li, J. Wu, Z. Yin and H. Zhang, *Acc. Chem. Res.*, 2014, **47**, 1067–1075.

100 H. Li, G. Lu, Y. Wang, Z. Yin, C. Cong, Q. He, L. Wang, F. Ding, T. Yu and H. Zhang, *Small*, 2013, **9**, 1974–1981.

101 Y. Q. Yang, C. T. Tye and K. J. Smith, *Catal. Commun.*, 2008, **9**, 1364–1368.

102 G. Eda, H. Yamaguchi, D. Voiry, T. Fujita, M. Chen and M. Chhowalla, *Nano Lett.*, 2011, **11**, 5111–5116.

103 T. Li and G. Galli, *J. Phys. Chem. C*, 2007, **111**, 16192–16196.

104 L. Sun, H. Huang and X. Peng, *Chem. Commun.*, 2013, **49**, 10718.

105 D. Mancinelli and C. Hallé, *Nano-Filtration and Ultra-Filtration Ceramic Membranes for Food Processing: A Mini Review*, 2015, vol. 05.

106 P. S. Goh and A. F. Ismail, *Desalination*, 2018, **434**, 60–80.

107 B. Khorshidi, T. Thundat, B. A. Fleck and M. Sadrzadeh, *Sci. Rep.*, 2016, **6**, 22069.

108 M. E. Toimil-Molares, *Beilstein J. Nanotechnol.*, 2012, **3**, 860–883.

109 Z. Su, J. Ding and G. Wei, *RSC Adv.*, 2014, **4**, 52598–52610.

110 H. R. Pant, H. J. Kim, M. K. Joshi, B. Pant, C. H. Park, J. I. Kim, K. S. Hui and C. S. Kim, *J. Hazard. Mater.*, 2014, **264**, 25–33.

111 F. E. Ahmed, B. S. Lalia and R. Hashaikeh, *Desalination*, 2015, **356**, 15–30.

112 United States Patente, 5,948,246, 1999, 16.

113 X.-F. Sun, J. Qin, P.-F. Xia, B.-B. Guo, C.-M. Yang, C. Song and S.-G. Wang, *Chem. Eng. J.*, 2015, **281**, 53–59.

114 H.-W. Liang, Q.-F. Guan, L.-F. Chen, Z. Zhu, W.-J. Zhang and S.-H. Yu, *Angew. Chemie Int. Ed.*, 2012, **51**, 5101–5105.

115 M. Wang, T. Zhang, D. Mao, Y. Yao, X. Zeng, L. Ren, Q. Cai, S. Mateti, L. H. Li, X. Zeng, G. Du, R. Sun, Y. Chen, J.-B. Xu and C.-P. Wong, *ACS Nano*, , DOI:10.1021/acsnano.9b03225.

116 S. Nardecchia, D. Carriazo, M. L. Ferrer, M. C. Gutiérrez and F. del Monte, *Chem. Soc. Rev.*, 2013, **42**, 794–830.

117 Y. Song, B. Li, S. Yang, G. Ding, C. Zhang and X. Xie, *Sci. Rep.*, 2015, **5**, 10337.

118 J. Yang, E. Zhang, X. Li, Y. Zhang, J. Qu and Z.-Z. Yu, *Carbon N. Y.*, 2016, **98**, 50–57.

119 J. Lin, X. Yuan, G. Li, Y. Huang, W. Wang, X. He, C. Yu, Y. Fang, Z. Liu and C. Tang, *ACS Appl. Mater. Interfaces*, 2017, **9**, 44732–44739.

120 H. Sun, Z. Xu and C. Gao, *Adv. Mater.*, 2013, **25**, 2554–2560.

121 C. Moreno-Castilla and F. J. Maldonado-Hódar, *Carbon N. Y.*, 2005, **43**, 455–465.

122 A. Richter, G. Paschew, S. Klatt, J. Lienig, K.-F. Arndt and P. H.-J. Adler, *Sensors* , 2008, 8.

123 J. Zou, J. Liu, A. S. Karakoti, A. Kumar, D. Joung, Q. Li, S. I. Khondaker, S. Seal and L. Zhai, *ACS Nano*, 2010, **4**, 7293–7302.

124 Y. Xue, P. Dai, M. Zhou, X. Wang, A. Pakdel, C. Zhang, Q. Weng, T. Takei, X. Fu, Z. I. Popov, P. B. Sorokin, C. Tang, K. Shimamura, Y. Bando and D. Golberg, *ACS Nano*, 2017, **11**, 558–568.

125 E. M. V Hoek, A. S. Kim and M. Elimelech, *Environ. Eng. Sci.*, 2002, **19**, 357–372.

126 K. K. Sirkar, P. T. Dang and G. H. Rao, *Ind. Eng. Chem. Process Des. Dev.*, 1982, **21**, 517–527.

127 K. K. Sirkar and G. H. Rao, *Ind. Eng. Chem. Process Des. Dev.*, 1981, **20**, 116–

127.

128 F. Evangelista, *Ind. Eng. Chem. Process Des. Dev.*, 1985, **24**, 211–223.

129 D. E. Wiley, C. J. D. Fell and A. G. Fane, *Desalination*, 1985, **52**, 249–265.

130 W. M. Deen, *AIChE J.*, 1987, **33**, 1409–1425.

131 F. G. Donnan, *J. Memb. Sci.*, 1995, **100**, 45–55.

132 G. Hagmeyer and R. Gimbel, *Desalination*, 1998, **117**, 247–256.

133 M. Ernst, A. Bismarck, J. Springer and M. Jekel, *J. Memb. Sci.*, 2000, **165**, 251–259.

134 A. E. Childress and M. Elimelech, *J. Memb. Sci.*, 1996, **119**, 253–268.

135 J. Schaep and C. Vandecasteele, *J. Memb. Sci.*, 2001, **188**, 129–136.

136 M. D. Afonso, G. Hagmeyer and R. Gimbel, *Sep. Purif. Technol.*, 2001, **22**–**23**, 529–541.

137 W. R. Bowen and J. S. Welfoot, *Chem. Eng. Sci.*, 2002, **57**, 1121–1137.

138 D. L. Oatley, L. Llenas, R. Pérez, P. M. Williams, X. Martínez-Lladó and M. Rovira, *Adv. Colloid Interface Sci.*, 2012, **173**, 1–11.

139 Y. Roy, D. M. Warsinger and J. H. Lienhard, *Desalination*, 2017, **420**, 241–257.

140 D. Fierro, A. Boschetti-de-Fierro and V. Abetz, *J. Memb. Sci.*, 2012, **413**–**414**, 91–101.

141 J. Qian, R. Yan, X. Liu, C. Li and X. Zhang, *Green Energy Environ.*, , DOI:https://doi.org/10.1016/j.gee.2018.10.001.

142 P. Silva, S. Han and A. G. Livingston, *J. Memb. Sci.*, 2005, **262**, 49–59.

143 A. I. Schäfer, N. Andritsos, J. Anastasios, E. M. V Hoek and R. Schneider, *Chapter 8 Fouling in Nanofiltration*, 2004.

144 Y. Fang, L. Bian, Q. Bi, Q. Li and X. Wang, *J. Memb. Sci.*, 2014, **454**, 390–397.

145 H. Qian, J. Zheng and S. Zhang, *Polymer (Guildf).*, 2013, **54**, 557–564.

146 S. Lee, G. Park, G. Amy, S.-K. Hong, S.-H. Moon, D.-H. Lee and J. Cho, *J. Memb. Sci.*, 2002, **201**, 191–201.

147 Y. Kiso, K. Muroshige, T. Oguchi, M. Hirose, T. Ohara and T. Shintani, *J. Memb. Sci.*, 2011, **369**, 290–298.

148 N. García-Martín, V. Silva, F. J. Carmona, L. Palacio, A. Hernández and P. Prádanos, *Desalination*, 2014, **344**, 1–11.

149 D. L. Oatley, L. Llenas, N. H. M. Aljohani, P. M. Williams, X. Martínez-Lladó, M. Rovira and J. de Pablo, *Desalination*, 2013, **315**, 100–106.

150 J. Stawikowska and A. G. Livingston, *J. Memb. Sci.*, 2013, **425**–**426**, 58–70.

151 N. Misdan, W. J. Lau, A. F. Ismail, T. Matsuura and D. Rana, *Desalination*, 2014, **344**, 198–205.

152 A. L. Carvalho, F. Maugeri, V. Silva, A. Hernández, L. Palacio and P. Pradanos, *J. Mater. Sci.*, 2011, **46**, 3356–3369.

153 J. Stawikowska and A. G. Livingston, *J. Memb. Sci.*, 2012, **413**–**414**, 1–16.

154 M. R. Teixeira, M. J. Rosa and M. Nyström, *J. Memb. Sci.*, 2005, **265**, 160–166.

155 S. Cheng, D. L. Oatley, P. M. Williams and C. J. Wright, *Adv. Colloid Interface Sci.*, 2011, **164**, 12–20.

156 S. Déon, P. Fievet and C. Osman Doubad, *J. Memb. Sci.*, 2012, **423**–**424**, 413–421.

157 G. Rice, A. R. Barber, A. J. O'Connor, A. Pihlajamaki, M. Nystrom, G. W. Stevens and S. E. Kentish, *J. Food Eng.*, 2011, **107**, 164–172.

158 T. Luxbacher, *Desalination*, 2006, **199**, 376–377.

159 H. Xie, T. Saito and M. A. Hickner, *Langmuir*, 2011, **27**, 4721–4727.

160 S. Lee, E. Lee, M. Elimelech and S. Hong, *J. Memb. Sci.*, 2011, **366**, 17–24.

161 V. S. Kumar, K. S. Hariharan, K. S. Mayya and S. Han, *Desalination*, 2013, **322**, 21–28.

162 N. S. Kotrappanavar, A. A. Hussain, M. E. E. Abashar, I. S. Al-Mutaz, T. M. Aminabhavi and M. N. Nadagouda, *Desalination*, 2011, **280**, 174–182.

163 G. Hurwitz, G. R. Guillen and E. M. V Hoek, *J. Memb. Sci.*, 2010, **349**, 349–357.

164 V. T. Do, C. Y. Tang, M. Reinhard and J. O. Leckie, *Water Res.*, 2012, **46**, 5217–5223.

165 Y. Baek, J. Kang, P. Theato and J. Yoon, *Desalination*, 2012, **303**, 23–28.

166 S. Darvishmanesh, L. Firoozpour, J. Vanneste, P. Luis, J. Degrève and B. Van Der Bruggen, *Green Chem.*, 2011, **13**, 3476–3483.

167 X. Li and J. Li, eds. E. Drioli and L. Giorno, Springer Berlin Heidelberg, Berlin, Heidelberg, 2015, pp. 1–3.

168 G. Székely, J. Bandarra, W. Heggie, B. Sellergren and F. C. Ferreira, *Sep. Purif. Technol.*, 2012, **86**, 79–87.

169 M. B. Martínez, B. Van der Bruggen, Z. R. Negrin and P. Luis Alconero, *J. Ind. Eng. Chem.*, 2012, **18**, 1635–1641.

170 D. J. Johnson, S. A. Al Malek, B. A. M. Al-Rashdi and N. Hilal, *J. Memb. Sci.*, 2012, **389**, 486–498.

171 T. Koros, W.J, Ma, Y.H and Shimidzu, *Pure Appl. Chem.*, 1996, 68, 1479.

172 B. Van Der Bruggen, C. Vandecasteele, T. Van Gestel, W. Doyen and R. Leysen, *Environ. Prog.*, 2003, **22**, 46–56.

173 L. Braeken, K. Boussu, B. Van Der Bruggen and C. Vandecasteele, *ChemPhysChem*, 2005, **6**, 1606–1612.

174 D. Violleau, H. Essis-Tome, H. Habarou, J. P. Croué and M. Pontié, *Desalination*, 2005, **173**, 223–238.

175 B. Van Der Bruggen, L. Braeken and C. Vandecasteele, *Sep. Purif. Technol.*, 2002, **29**, 23–31.

176 V. V. Tarabara, I. Koyuncu and M. R. Wiesner, *J. Memb. Sci.*, 2004, **241**, 65–78.

177 M. Elimelech, X. Zhu, A. E. Childress and S. Hong, *J. Memb. Sci.*, 1997, **127**, 101–109.

178 X. Zhu and M. Elimelech, *Environ. Sci. Technol.*, 1997, **31**, 3654–3662.

179 J. Warczok, M. Ferrando, F. López and C. Güell, *J. Food Eng.*, 2004, **63**, 63–70.

180 E. M. Vrijenhoek, S. Hong and M. Elimelech, *J. Memb. Sci.*, 2001, **188**, 115–128.

181 E. M. V. Hoek, S. Bhattacharjee and M. Elimelech, *Langmuir*, 2003, **19**, 4836–4847.

182 M. Zhang and L. Song, *Environ. Sci. Technol.*, 2000, **34**, 3767–3773.

183 L. Song, K. L. Chen, S. L. Ong and W. J. Ng, *J. Colloid Interface Sci.*, 2004, **271**, 426–433.

184 M. S. Chun, H. Il Cho and I. K. Song, *Desalination*, 2002, **148**, 363–368.

185 G. Singh and L. Song, *J. Colloid Interface Sci.*, 2005, **284**, 630–638.

186 B. Van der Bruggen, J. H. Kim, F. A. DiGiano, J. Geens and C. Vandecasteele, *Sep. Purif. Technol.*, 2004, **36**, 203–213.

187 A. R. Costa and M. N. De Pinho, *J. Memb. Sci.*, 2005, **255**, 49–56.

188 A. Al-Amoudi and R. W. Lovitt, *J. Memb. Sci.*, 2007, **303**, 4–28.

189 W. S. Ang, S. Lee and M. Elimelech, *J. Memb. Sci.*, 2006, **272**, 198–210.

190 R. Liikanen, J. Yli-Kuivila and R. Laukkanen, *J. Memb. Sci.*, 2002, **195**, 265–276.

191 E. R. Cornelissen, J. S. Vrouwenvelder, S. G. J. Heijman, X. D. Viallefont, D. van der Kooij and L. P. Wessels, *Desalination*, 2007, **204**, 145–147.

192 J. Q. J. C. Verberk and J. C. van Dijk, *J. Memb. Sci.*, 2006, **284**, 339–351.

193 G. Trägårdh, *Desalination*, 1989, **71**, 325–335.

194 S. Y. Lee, H. J. Kim, R. Patel, S. J. Im, J. H. Kim and B. R. Min, *Polym. Adv. Technol.*, 2007, **18**, 562–568.

195 M. Henmi, K. Nakatsuji, T. Ichikawa, H. Tomioka, T. Sakamoto, M. Yoshio and T. Kato, *Adv. Mater.*, 2012, **24**, 2238–2241.

196 L. D. Tijing, Y. C. Woo, W.-G. Shim, T. He, J.-S. Choi, S.-H. Kim and H. K. Shon, *J. Memb. Sci.*, 2016, **502**, 158–170.

197 J. Yin, E.-S. Kim, J. Yang and B. Deng, *J. Memb. Sci.*, 2012, **423**–**424**, 238–246.

198 J. Yin, G. Zhu and B. Deng, *Desalination*, 2016, **379**, 93–101.

199 S. Sarkar and A. K. SenGupta, *J. Memb. Sci.*, 2008, **324**, 76–84.

200 C. Jiang, L. Tian, Y. Hou and Q. J. Niu, *J. Memb. Sci.*, 2019, **586**, 192–201.

201 S. Lee and C.-H. Lee, *Water Res.*, 2000, **34**, 3854–3866.

202 W. Fang, L. Shi and R. Wang, *J. Memb. Sci.*, 2013, **430**, 129–139.

203 A. Rahimpour, M. Jahanshahi, N. Mortazavian, S. S. Madaeni and Y. Mansourpanah, *Appl. Surf. Sci.*, 2010, **256**, 1657–1663.

204 M. Homayoonfal, A. Akbari and M. R. Mehrnia, *Desalination*, 2010, **263**, 217–225.

205 C. Liu, L. Shi and R. Wang, *J. Memb. Sci.*, 2015, **486**, 169–176.

206 B. Van der Bruggen, J. Schaep, D. Wilms and C. Vandecasteele, *J. Memb. Sci.*, 1999, **156**, 29–41.

207 M. Thanuttamavong, K. Yamamoto, J. Ik Oh, K. Ho Choo and S. June Choi, *Desalination*, 2002, **145**, 257–264.

208 Y. Zhang, C. Causserand, P. Aimar and J. P. Cravedi, *Water Res.*, 2006, **40**, 3793–3799.

209 H. Li, X. Gui, L. Zhang, S. Wang, C. Ji, J. Wei, K. Wang, H. Zhu, D. Wu and A. Cao, *Chem. Commun.*, 2010, **46**, 7966–7968.

210 C. Lee and S. Baik, *Carbon N. Y.*, 2010, **48**, 2192–2197.

211 W. Zhang, Y. Zhu, X. Liu, D. Wang, J. Li, L. Jiang and J. Jin, *Angew. Chemie Int. Ed.*, 2013, **53**, 856–860.

212 H.-H. Tseng, J.-C. Wu, Y.-C. Lin and G.-L. Zhuang, *J. Memb. Sci.*, 2018, **559**, 148–158.

213 N. J. Kaleekkal, R. Radhakrishnan, V. Sunil, G. Kamalanathan, A. Sengupta and R. Wickramasinghe, *Sep. Purif. Technol.*, 2018, **205**, 32–47.

214 S. K. Hong, S. Bae, H. Jeon, M. Kim, S. J. Cho and G. Lim, *Nanoscale*, 2018, **10**, 3037–3045.

215 A. Sato, R. Wang, H. Ma, B. S. Hsiao and B. Chu, *J. Electron Microsc. (Tokyo).*, 2011, **60**, 201–209.

216 S. Y. Yang, J. Park, J. Yoon, M. Ree, S. K. Jang and J. K. Kim, *Adv. Funct. Mater.*, 2008, **18**, 1371–1377.

217 X. Zhang, T. Zhang, J. Ng and D. D. Sun, *Adv. Funct. Mater.*, 2009, **19**, 3731–3736.

218 NANOFILTRATION Archives - Oltremare S.p.A., http://www.oltremaremembrane.com/en/category/nanofiltration/, (accessed 10 December 2021).

219 D. L. Oatley-Radcliffe, M. Walters, T. J. Ainscough, P. M. Williams, A. W. Mohammad and N. Hilal, *J. Water Process Eng.*, 2017, **19**, 164–171.

220 S. A. Avlonitis, I. Poulios, D. Sotiriou, M. Pappas and K. Moutesidis, *Desalination*, 2008, **221**, 259–267.

221 W. J. Lau and A. F. Ismail, *Desalination*, 2009, **245**, 321–348.

222 N. H. H. Hairom, A. W. Mohammad and A. A. H. Kadhum, *J. Water Process Eng.*, 2014, **4**, 99–106.

223 C. Kaya, G. Sert, N. Kabay, M. Arda, M. Yüksel and Ö. Egemen, *Desalination*, 2015, **369**, 10–17.

224 C. Feng, K. C. Khulbe, T. Matsuura, R. Gopal, S. Kaur, S. Ramakrishna and M. Khayet, *J. Memb. Sci.*, 2008, **311**, 1–6.

225 I. Michael-Kordatou, C. Michael, X. Duan, X. He, D. D. Dionysiou, M. A. Mills and D. Fatta-Kassinos, *Water Res.*, 2015, **77**, 213–248.

226 M. Pontié, J. S. Derauw, S. Plantier, L. Edouard and L. Bailly, *New pub Balaban*, 2013, **51**, 485–494.

227 D. Fritsch, P. Merten, K. Heinrich, M. Lazar and M. Priske, *J. Memb. Sci.*, 2012, **401**–**402**, 222–231.

228 P. Marchetti, M. F. Jimenez Solomon, G. Szekely and A. G. Livingston, *Chem. Rev.*, 2014, **114**, 10735–10806.

229 X. Q. Cheng, Y. L. Zhang, Z. X. Wang, Z. H. Guo, Y. P. Bai and L. Shao, *Adv. Polym. Technol.*, , DOI:10.1002/adv.21455.

230 P. Vandezande, L. E. M. Gevers and I. F. J. Vankelecom, *Chem. Soc. Rev.*, 2008, **37**, 365–405.

231 C. Castel and E. Favre, *J. Memb. Sci.*, 2018, **548**, 345–357.

232 T. J. Park, J. Reznick, B. L. Peterson, G. Blass, D. Omerbašić, N. C. Bennett, P. H. J. L. Kuich, C. Zasada, B. M. Browe, W. Hamann, D. T. Applegate, M. H. Radke, T. Kosten, H. Lutermann, V. Gavaghan, O. Eigenbrod, V. Bégay, V. G. Amoroso, V. Govind, R. D. Minshall, E. S. J. Smith, J. Larson, M. Gotthardt, S. Kempa and G. R. Lewin, *Science (80-.).*, 2017, **356**, 307 LP – 311.

233 M. S. Denny Jr., J. C. Moreton, L. Benz and S. M. Cohen, *Nat. Rev. Mater.*, 2016, **1**, 16078.

234 D. L. Gin and R. D. Noble, *Science (80-.).*, 2011, **332**, 674 LP – 676.

235 P. Marchetti, L. Peeva and A. Livingston, *Annu. Rev. Chem. Biomol. Eng.*, 2017, **8**, 473–497.

236 G. Székely, J. Bandarra, W. Heggie, B. Sellergren and F. C. Ferreira, *J. Memb. Sci.*, 2011, **381**, 21–33.

237 D. I. Robinson, *Org. Process Res. Dev.*, 2010, **14**, 946–959.

238 Fda, *FDA Guid.*, 2008, 1–31.

239 M. V Tres, H. C. Ferraz, R. M. Dallago, M. Di Luccio and J. V. Oliveira, *J. Memb. Sci.*, 2010, **362**, 495–500.

240 L. R. Firman, N. A. Ochoa, J. Marchese and C. L. Pagliero, *J. Memb. Sci.*, 2013, **431**, 187–196.

241 H. J. Zwijnenberg, A. M. Krosse, K. Ebert, K. V Peinemann and F. P. Cuperus, *J. Am. Oil Chem. Soc.*, 1999, **76**, 83–87.

242 I. Sereewatthanawut, I. I. R. Baptista, A. T. Boam, A. Hodgson and A. G. Livingston, *J. Food Eng.*, 2011, **102**, 16–24.

243 S. Banvolgyi, I. Kiss, E. Bekassy-Molnar and G. Vatai, *Desalination*, 2006, **198**, 8–15.

244 A. Massot, M. Mietton-Peuchot, C. Peuchot and V. Milisic, *Desalination*, 2008, **231**, 283–289.

245 N. García-Martín, S. Perez-Magariño, M. Ortega-Heras, C. González-Huerta, M. Mihnea, M. L. González-Sanjosé, L. Palacio, P. Prádanos and A. Hernández, *Sep. Purif. Technol.*, 2010, **76**, 158–170.

246 L. F. Sotoft, K. V Christensen, R. Andrésen and B. Norddahl, *Chem. Eng. Process. Process Intensif.*, 2012, **54**, 12–21.

247 H. C. van der Horst, J. M. K. Timmer, T. Robbertsen and J. Leenders, *J. Memb. Sci.*, 1995, **104**, 205–218.

248 J. Luo, L. Ding, B. Qi, M. Y. Jaffrin and Y. Wan, *Bioresour. Technol.*, 2011, **102**, 7437–7442.

249 M. Vourch, B. Balannec, B. Chaufer and G. Dorange, *Desalination*, 2005, **172**, 245–256.

250 H. S. Alkhatim, M. I. Alcaina, E. Soriano, M. I. Iborra, J. Lora and J. Arnal, *Desalination*, 1998, **119**, 177–183.

251 United States Patente, US 6,464,881 B2, 2002, 6.

252 A. Hinkova, Z. Bubník, P. Kadlec and J. Pridal, *Sep. Purif. Technol.*, 2002, **26**, 101–110.

253 S. Cartier, M. A. Theoleyre and M. Decloux, *Desalination*, 1997, **113**, 7–17.

254 J. Gyura, Z. Šereš, G. Vatai and E. B. Molnár, *Desalination*, 2002, **148**, 49–56.

255 J. Luo, L. Ding, Y. Wan, P. Paullier and M. Y. Jaffrin, *Chem. Eng. J.*, 2010, **163**, 307–316.

256 B. Sarkar, P. P. Chakrabarti, A. Vijaykumar and V. Kale, *Desalination*, 2006, **195**, 141–152.

257 M. Dell'Agli, A. Buscialà and E. Bosisio, *Cardiovasc. Res.*, 2004, **63**, 593–602.

258 R. M. Niles, M. McFarland, M. B. Weimer, A. Redkar, Y.-M. Fu and G. G. Meadows, *Cancer Lett.*, 2003, **190**, 157–163.

259 X. Li, S. Tan, J. Luo and M. Pinelo, *Front. Chem. Sci. Eng. 2021 154*, 2021, **15**, 837–853.

260 A. K. Goulas, P. G. Kapasakalidis, H. R. Sinclair, R. A. Rastall and A. S.

Grandison, *J. Memb. Sci.*, 2002, **209**, 321–335.

261 M. BRYJAK, J. KOZLOWSKI, P. WIECZOREK and P. KAFARSKI, *J. Memb. Sci.*, 1993, **85**, 221–228.

262 P. Hadik, L.-P. Szabó, E. Nagy and Z. Farkas, *J. Memb. Sci.*, 2005, **251**, 223–232.

263 C. Han and H. Li, *Small*, 2008, **4**, 1344–1350.

264 I. Sereewatthanawut, A. T. Boam and A. G. Livingston, *Macromol. Symp.*, 2008, **264**, 184–188.

265 N. F. Ghazali, F. C. Ferreira, A. J. P. White and A. G. Livingston, *Tetrahedron: Asymmetry*, 2006, **17**, 1846–1852.

266 N. F. Ghazali, F. C. Ferreira, A. J. P. White and A. G. Livingston, *Desalination*, 2006, 398–400.

267 T. Ramesh, P. Nageswara Rao and K. Suresh, *Anal. Methods*, 2014, **6**, 223–228.

268 J. H. Kim, J. H. Kim, J. Jegal and K.-H. Lee, *J. Memb. Sci.*, 2003, **213**, 273–283.

269 M. Nakamura, S. Kiyohara, K. Saito, K. Sugita and T. Sugo, *J. Chromatogr. A*, 1998, **822**, 53–58.

270 R. Bhushan and H. Brückner, *Amino Acids*, 2004, **27**, 231–247.

271 M. Reetz, *Angew. Chemie Int. Ed. …*, 1991, **30**, 1531–1546.

272 R. Xie, L.-Y. Chu and J.-G. Deng, *Chem. Soc. Rev.*, 2008, **37**, 1243–1263.

273 P. Hadik, L.-P. Szabó and E. Nagy, *Desalination*, 2002, **148**, 193–198.

274 F. Purcell-Milton, R. McKenna, L. J. Brennan, C. P. Cullen, L. Guillemeney, N. V Tepliakov, A. S. Baimuratov, I. D. Rukhlenko, T. S. Perova, G. S. Duesberg, A. V Baranov, A. V Fedorov and Y. K. Gun'ko, *ACS Nano*, 2018, **12**, 954–964.

275 R. Serrano-García, F. Purcell-Milton, S. McCarthy and Y. K. Gun'ko, *ChemistrySelect*, 2018, **3**, 4726–4729.

276 O. Cleary, F. Purcell-Milton, A. Vandekerckhove and Y. K. Gun'ko, *Adv. Opt. Mater.*, 2017, **5**, 1601000.

277 P. Joensen, R. F. Frindt and S. R. Morrison, *Mater. Res. Bull.*, 1986, **21**, 457–461.

278 C. J. Shih, A. Vijayaraghavan, R. Krishnan, R. Sharma, J. H. Han, M. H. Ham, Z. Jin, S. Lin, G. L. C. Paulus, N. F. Reuel, Q. H. Wang, D. Blankschtein and M. S. Strano, *Nat. Nanotechnol. 2011 67*, 2011, **6**, 439–445.

279 G. Eda, T. Fujita, H. Yamaguchi, D. Voiry, M. Chen and M. Chhowalla, *ACS Nano*, 2012, **6**, 7311–7317.

280 R. Ma and T. Sasaki, *Adv. Mater.*, 2010, **22**, 5082–5104.

281 G. E. Gadd, M. Blackford, S. Moricca, N. Webb, P. J. Evans, A. M. Smith, G. Jacobsen, S. Leung, A. Day and Q. Hua, *Science (80-.).*, 1997, **277**, 933–936.

282 Q. Wang and D. Ohare, *Chem. Rev.*, 2012, **112**, 4124–4155.

283 M. Meyn, K. Beneke and G. Lagaly, *Inorg. Chem.*, 1990, **29**, 5201–5207.

284 K. A. Carrado, J. E. Forman, R. E. Botto and R. E. Winans, *Chem. Mater.*, 1993, **5**, 472–478.

285 O. Okay, W. O.- Macromolecules and undefined 2007, *ACS Publ.*, 2007, **40**, 3378–3387.

286 F. L. Theiss, G. A. Ayoko and R. L. Frost, *Appl. Surf. Sci.*, 2016, **383**, 200–213.

287 A. McKenzie, C. Fishel, R. D.-J. of Catalysis and undefined 1992, *Elsevier*.

288 B. Sels, D. De Vos, M. Buntinx, F. Plerard, A. Kirsch-De Mesmaeker and P. Jacobs, *Nature*, 1999, **400**, 855–857.

289 A. Goeppert, M. Czaun, R. B. May, G. K. S. Prakash, G. A. Olah and S. R. Narayanan, *J. Am. Chem. Soc.*, 2011, **133**, 20164–20167.

290 Q. Wang, Z. Wu, H. H. Tay, L. Chen, Y. Liu, J. Chang, Z. Zhong, J. Luo and A. Borgna, in *Catalysis Today*, 2011, vol. 164, pp. 198–203.

291 V. Rives, M. U.-C. chemistry reviews and undefined 1999, *Elsevier*.

292 A. Sugimoto, S. Ishida and K. Hanawa, *J. Electrochem. Soc.*, 1999, **146**, 1251–1255.

293 U. Guth, S. Brosda, J. S.-A. clay science and undefined 1996, *Elsevier*, 1996, **11**, 229–236.

294 J. Lee, S. Rhee, D. J.-C. of materials and undefined 2006, *ACS Publ.*, 2006, **18**, 4740–4746.

295 M. Sadeghi-Goughari, S. Jeon, H.-J. Kwon -, J. Carlos Camacho-Fernández, G. Karendash González-Quijano, C. Séverac, al -, S.-J. Tu, S.-Y. Wu, F.-S. Wang, C.-J. Chiang, C.-H. Chang -, K. Wu, D. Su, J. Liu, R. Saha and J.-P. Wang, *Nanotechnology*, 2019, **30**, 502003.

296 S. Mornet, S. Vasseur, F. Grasset, P. Veverka, G. Goglio, A. Demourgues, J. Portier, E. Pollert and E. Duguet, *Prog. Solid State Chem.*, 2006, **34**, 237–247.

297 S. P. Gubin, *Magnetic Nanoparticles*, 2009.

298 A. G. Kolhatkar, A. C. Jamison, D. Litvinov, R. C. Willson and T. R. Lee, *Int. J. Mol. Sci. 2013, Vol. 14, Pages 15977-16009*, 2013, **14**, 15977–16009.

299 Who Discovered the Very First Magnet? | Dowling Magnets, https://www.dowlingmagnets.com/blog/2016/who-discovered-the-very-first-magnet/, (accessed 15 December 2021).

300 8.7: Spinel, Perovskite, and Rutile Structures - Chemistry LibreTexts, https://chem.libretexts.org/Bookshelves/Inorganic_Chemistry/Book%3A_Introduction_to_Inorganic_Chemistry/08%3A_Ionic_and_Covalent_Solids_-_Structures/8.07%3A_Spinel_Perovskite_and_Rutile_Structures, (accessed 15 December 2021).

301 A. G. Niculescu, C. Chircov and A. M. Grumezescu, *Methods*, ,

DOI:10.1016/J.YMETH.2021.04.018.

302 A. Sirivat and N. Paradee, *Mater. Des.*, 2019, **181**, 107942.

303 T. Gu, Y. Zhang, S. A. Khan and T. A. Hatton, *Colloid Interface Sci. Commun.*, 2019, **28**, 1–4.

304 J. Ma, S. M. Y. Lee, C. Yi and C. W. Li, *Lab Chip*, 2017, **17**, 209–226.

305 C. X. Zhao, L. He, S. Z. Qiao and A. P. J. Middelberg, *Chem. Eng. Sci.*, 2011, **66**, 1463–1479.

306 D. Ficai, V. Grumezescu, O. M. Fufă, R. C. Popescu, A. M. Holban, A. Ficai, A. M. Grumezescu, L. Mogoanta, G. D. Mogosanu and E. Andronescu, *Nanomater. 2018, Vol. 8, Page 633*, 2018, **8**, 633.

307 D. H. Sun, D. X. Sun and Y. Hao, *Mater. Sci. Forum*, 2011, **663**–**665**, 1125–1128.

308 B. L. Cushing, V. L. Kolesnichenko and C. J. O'Connor, *Chem. Rev.*, 2004, **104**, 3893–3946.

309 Y. Jun, J.-H. Lee and J. Cheon, *Angew. Chemie Int. Ed.*, 2008, **47**, 5122–5135.

310 P. Lu, J. L. Zhang, Y. L. Liu, D. H. Sun, G. X. Liu, G. Y. Hong and J. Z. Ni, *Talanta*, 2010, **82**, 450–457.

311 A. Shavel and L. M. Liz-Marzán, *Phys. Chem. Chem. Phys.*, 2009, **11**, 3762–3766.

312 J. Wan, X. Chen, Z. Wang, X. Yang and Y. Qian, *J. Cryst. Growth*, 2005, **276**, 571–576.

313 Y. Zhang, Z. Huang, F. Tang and J. Ren, *Solid State Commun.*, 2006, **138**, 132–135.

314 K. C. Chin, G. L. Chong, C. K. Poh, L. Van Hui, C. H. Sow, J. Lin and A. T. S. Wee, *J. Phys. Chem. C*, 2007, **111**, 9136–9141.

315 H. Zhou, R. Yi, J. Li, Y. Su and X. Liu, *Solid State Sci.*, 2010, **12**, 99–104.

316 Z. He and P. Alexandridis, *Polym. 2018, Vol. 10, Page 32*, 2017, **10**, 32.

317 Z. Huang, Y. Zhang and F. Tang, *Chem. Commun.*, 2005, 342–344.

318 S. Iijima, *Nat. 1991 3546348*, 1991, **354**, 56–58.

319 T. Belin and F. Epron, *Mater. Sci. Eng. B*, 2005, **119**, 105–118.

320 E. T. Thostenson, Z. Ren and T. W. Chou, *Compos. Sci. Technol.*, 2001, **61**, 1899–1912.

321 L. F. Dumée, K. Sears, J. Schütz, N. Finn, C. Huynh, S. Hawkins, M. Duke and S. Gray, *J. Memb. Sci.*, 2010, **351**, 36–43.

322 K. Saeed Ibrahim and A. Info, *Carbon Lett.*, 2013, **14**, 131–144.

323 A. De Vita, J. C. Charlier, X. Blase and R. Car, *Appl. Phys. A 1999 683*, 1999, **68**, 283–286.

324 A. G. Rinzler, J. H. Hafner, P. Nikolaev, L. Lou, S. G. Kim, D. Tománek, P. Nordlander, D. T. Colbert and R. E. Smalley, *Science (80-.).*, 1995, **269**, 1550–1553.

325 S.-J. Park and S.-Y. Lee, *Carbon Lett.*, 2009, **10**, 19–22.

326 C. Liu, Y. Y. Fan, M. Liu, H. T. Cong, H. M. Cheng and M. S. Dresselhaus, *Science (80-.).*, 1999, **286**, 1127–1129.

327 G. E. Gadd, M. Blackford, S. Moricca, N. Webb, P. J. Evans, A. M. Smith, G. Jacobsen, S. Leung, A. Day and Q. Hua, *Science (80-.).*, 1997, **277**, 933–936.

328 A. Gupta, T. Sakthivel and S. Seal, *Prog. Mater. Sci.*, 2015, **73**, 44–126.

329 A. Jayakumar, A. Surendranath and M. PV, *Int. J. Pharm.*, 2018, **551**, 309–321.

330 C. Kim, J.-C. Park, S. Y. Choi, Y. Kim, S.-Y. Seo, T.-E. Park, S.-H. Kwon, B. Cho and J.-H. Ahn, *Small*, 2018, **14**, 1704116.

331 H. Huang, Z. Song, N. Wei, L. Shi, Y. Mao, Y. Ying, L. Sun, Z. Xu and X. Peng, *Nat. Commun. 2013 41*, 2013, **4**, 1–9.

332 J. Ding, H. Zhao, B. Xu and H. Yu, *ACS Sustain. Chem. Eng.*, 2020, **8**, 8986–8993.

333 K. Nakagawa, M. Kunimatsu, K. Yasui, T. Yoshioka, T. Shintani, T. Yasui, E. Kamio, W. S. Hung, K. R. Lee, S. C. Edman Tsang and H. Matsuyama, *ACS Appl. Nano Mater.*, 2021, **4**, 3455–3466.

334 M. Hu and B. Mi, *Environ. Sci. Technol.*, 2013, **47**, 3715–3723.

335 L. Chen, N. Li, Z. Wen, L. Zhang, Q. Chen, L. Chen, P. Si, J. Feng, Y. Li, J. Lou and L. Ci, *Chem. Eng. J.*, 2018, **347**, 12–18.

336 Y. Liu, Z. Yu, Y. Peng, L. Shao, X. Li and H. Zeng, *Chem. Phys. Lett.*, 2020, **749**, 137424.

337 J. Ma, X. Tang, Y. He, Y. Fan, J. Chen and HaoYu, *Desalination*, 2020, **480**, 114328.

338 C. Chen, J. Wang, D. Liu, C. Yang, Y. Liu, R. S. Ruoff and W. Lei, *Nat. Commun.*, 2018, **9**, 1902.

339 J. Li, Y. Huang, Z. Liu, J. Zhang, X. Liu, H. Luo, Y. Ma, X. Xu, Y. Lu, J. Lin, J. Zou and C. Tang, *J. Mater. Chem. A*, 2015, **3**, 8185–8193.

340 W. Lei, D. Portehault, D. Liu, S. Qin and Y. Chen, *Nat. Commun. 2013 41*, 2013, **4**, 1–7.

341 L. Xue, B. Lu, Z.-S. Wu, C. Ge, P. Wang, R. Zhang and X.-D. Zhang, *Chem. Eng. J.*, 2014, **243**, 494–499.

342 X. Zhang, G. Lian, S. Zhang, D. Cui and Q. Wang, *CrystEngComm*, 2012, **14**, 4670–4676.

343 G. Lian, X. Zhang, H. Si, J. Wang, D. Cui and Q. Wang, *ACS Appl. Mater. Interfaces*, 2013, **5**, 12773–12778.

344 A. Hafeez, Z. A. Karim, A. F. Ismail, A. Samavati, K. A. M. Said and S. Selambakkannu, *J. Memb. Sci.*, 2020, **612**, 118473.

345 Y. Su, D. Liu, G. Yang, Q. Han, Y. Qian, Y. Liu, L. Wang, J. M. Razal and W. Lei, *ACS Appl. Mater. Interfaces*, 2020, **12**, 45453–45459.

346 J. Ran, P. Zhang, C. Chu, P. Cui, X. Ai, T. Pan, Y. Wu and T. Xu, *J. Memb. Sci.*, 2020, **602**, 117963.

347 J. Zhou, Z. Qin, Y. Lu, X. Li, Q. An, S. Ji, N. Wang and H. Guo, *J. Taiwan Inst. Chem. Eng.*, 2018, **84**, 196–202.

348 M. Zhang, J. Gao, G. Liu, M. Zhang, H. Liu, L. Zhou, Y. Liu, X. Zheng and Y. Jiang, *Langmuir*, 2021, **37**, 417–427.

Chapter 2. Experimental

2.1 Starting Materials

Hexagonal boron nitride (h-BN) powder was purchased from Merck (particle size = 6-30 μm). N-methyl-2-pyrrolidone (NMP), n-buthyllithium (1.6 M in hexane), (99%, HPLC) Evans Blue (≥75%), Methylene Blue (≥82%) MoS_2, sodium cholate, D and L-penicillamine, L-cysteine, (S)-(+)-citronellyl bromide, iron (III) chloride hexahydrate ($FeCl_3 \cdot 6 H_2O$, %), iron (II) chloride tetrahydrate ($FeCl_2 \cdot 4 H_2O$), P123 (2K), ethylene glycol (99+%), hexamethylenetetramine (HMTA, ≥99%), D-(+)-glucose, D-(+)-sucrose, dextran (from *Leuconostoc spp*), starch from wheat and carbon nanotubes (MW) were obtained from Sigma-Aldrich. Methyl Orange (≥95%) was bought from VWR international Ltd. Isopropyl alcohol (99.5%), sodium hydroxide (NaOH, general purpose grade) and potassium hydroxide (KOH, general purpose grade) were obtained from Fischer. Millipore Water was obtained using a Milli-Q system, with resin filters; this filtration was carried out in Trinity College laboratories. HyPure water was purchased from HyClone Laboratories. HPLC 2-propanol, ethanol, methanol and acetone were purchased from the Trinity College Solvent stores. All solvents were analytically pure and used without further purification. Omnipore membrane filter (hydrophilic polytetrafluoroethylene, PTFE, with 20 nm pore size and 47 mm diameter) and Durapore membrane filter (hydrophilic polyvinylidene fluoride, PVDF, with 22 and 45 nm pore size and 47 mm diameter) were purchased from Merck Millipore Limited. The sonic bath used was Ultrawave model U100H from Ultrawave Ltd.

2.2 Experimental procedures for chapter 3

2.2.1 BN Exfoliation

Bulk BN (0.3 g) was dispersed in 100 mL of the chosen solvent: N-methyl-2-pyrrolidone (NMP), isopropyl alcohol (IPA) or Millipore water to prepare a 3 mg/mL or 3% v/v solution. These solutions were then continuously sonicated for 48 hours for NMP and IPA and 24 hours for Millipore water (using an Ultrawave model U100H), with the

temperature in the bath rising from room temperature to 50°C. After exfoliation, any precipitated material was discarded, as the exfoliated BN stays in solution. The solution was then immediately used for further studies and membrane formation. Exfoliation schematic is shown in figure 2.1.

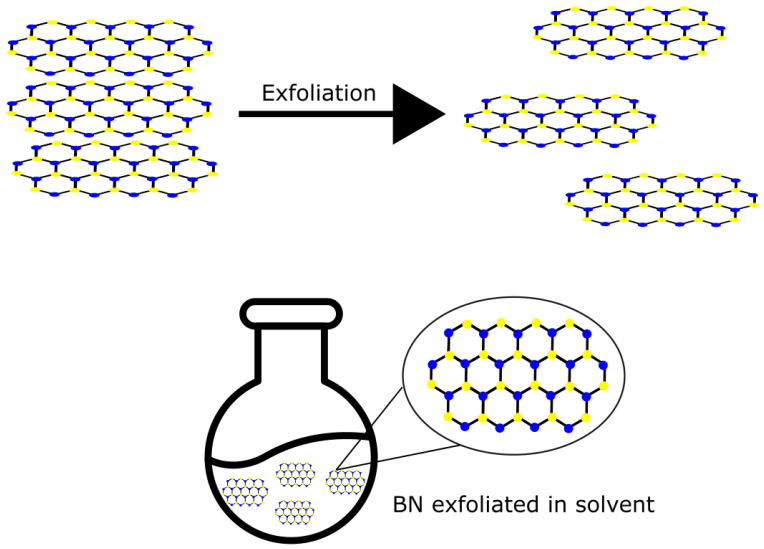

Figure 2.1: Schematic of BN exfoliation in a giving solvent

2.2.2 Preparation of membranes

BN membranes were produced by vacuum filtration of exfoliated BN solution through a PTFE or PVDF filter (45 nm pore size). 50 mL of the exfoliated BN solution (150 mg of BN) was passed through the PTFE/PVDF template under vacuum filtration (Figure 2.2). Once all the solution had passed through, the pump was left on for a further 10-15 minutes to obtain a dried membrane. When using NMP, the membranes were washed three times with acetone (3x30 mL) to remove residual NMP.

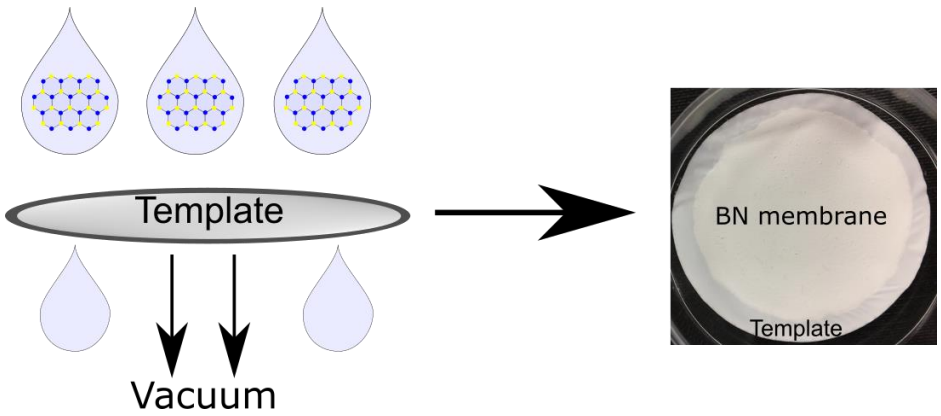

Figure 2.2: Schematic of BN membrane formation using vacuum filtration.

2.2.3 Retention tests

Three water soluble dyes were selected for testing the membranes retention: Evans Blue, Methyl Orange and Methylene Blue. The concentrations were chosen based on the maximum of absorbance, which was between 1 and 1.5 a.u, as seen in table 2.1 and matches with concentration used in literature[1].

Table 2.1: Concentration and absorbance on the maximum of absorbance of the dyes.

Dye	Concentration (μM)	Max. Abs (nm)	Absorbance (a.u)
Evans Blue	15	600	1
Methylene Blue	27	663	1.5
Methyl Orange	50	445	1.2

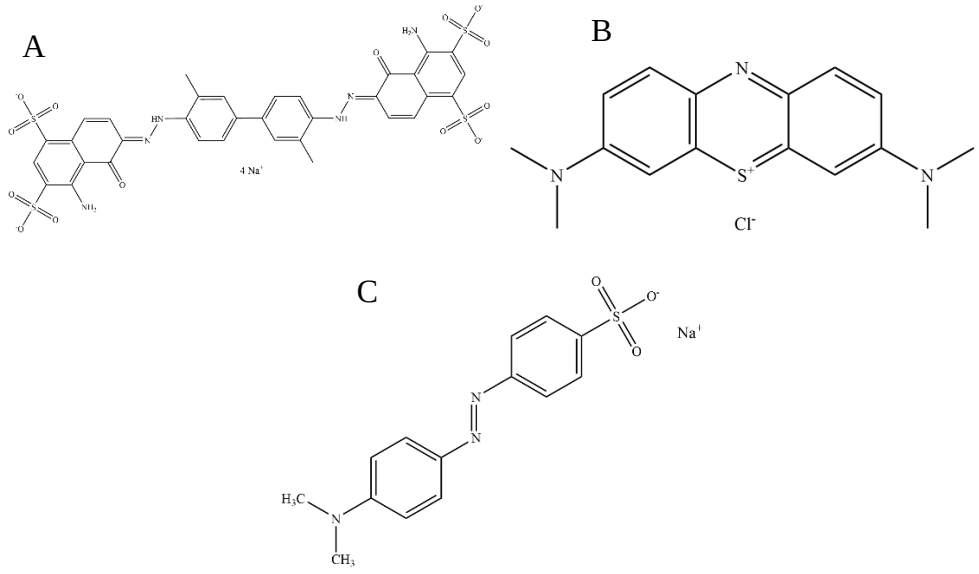

Figure 2.3: Structures of A) Evans Blue, B) Methylene Blue and C) Methyl Orange. Figure illustrated in ChemDraw.

20 mL of the dye solution were passed through the membrane and a UV-Vis spectrum of the permeate was recorded. Once the permeate was obtained, further concentration of it was required, to collect an adequate UV-vis spectrum, for this, a vacuum evaporation

(rotavapor) was carried out until only solid matter was present. Later, 3 mL of Millipore water were added, and this solution was placed on the cuvette; this concentrated solution was measured with an UV-vis spectrometer.

In order to calculate the retention, the following formula was used as found in literature[2,3]:

$$R_x(\%) = \left(1 - \frac{C_{P,X}}{C_{F,X}}\right) \cdot 100$$

Where:

R_X is the retention in percentage.

$C_{F,X}$ is the concentration of the analyte in the feed

$C_{P,X}$ is the concentration of the analyte in the permeate.

However, since concentration is proportionally correlated to the absorbance at a particular wavelength, the retention was calculated using the maximum absorbance. Therefore, the corrected formula was:

$$R_x(\%) = \left(1 - \frac{A_{P,\lambda max}}{A_{F,\lambda max}}\right) \cdot 100$$

Where:

R_X is the retention in percentage.

$A_{F,\lambda max}$ is the absorbance at 600 nm of the analyte in the feed

$A_{P,\lambda max}$ is the absorbance at 600 nm of the analyte in the permeate

The statistics of the retention were calculated using Origin software 2018.

2.3 Experimental procedures for chapter 4

2.3.1 Preparation and exfoliation of BNOx

Bulk BN was oxidised by heating it in an oven in the lab. The temperature of the oven was increased 5°C per minute and the temperature was kept at a 1000°C for 30 min, producing the oxidised BN denoted BNOx.

Once the BNOx was obtained, 3 mg/mL of the powder was dispersed in 100 mL of Millipore water and sonicated continuously for 24 h (using an Ultrawave model U100H) with the temperature in the bath rising from room temperature to 50 °C.

2.3.2 Preparation of membranes

BNOx membranes were produced by vacuum filtration of exfoliated BNOx solution through a PTFE or PVDF (45 nm pore size) template. 50 mL of the exfoliated BNOx solution (150 mg of BNOx) was passed through the PTFE/PVDF template under vacuum filtration. Once all the solution had passed through, the pump was left on for a further 10-15 minutes to produce a dried membrane.

2.3.3 Retention test

Retention of the membranes was done as described in section 2.2.3.

2.3.4 Testing BNOx membranes with sugars

The BNOx membranes were tested using di- and polysaccharides, sucrose, dextran and starch (table 2.2). The solutions were prepared by dissolving the sugars in 100 mL of Millipore water.

Table 2.2: Concentrations of sugars used for the testing

Sugar	Concentration (mg/mL)	Concentration (M)
Sucrose	342.3	1
Sucrose	171.15	0.5
Sucrose	85.58	0.25
Sucrose	17.12	0.05
Dextran	10	0.02
Starch	10	-

20 mL of each solution was passed through the membranes. The permeate was then evaporated and the remaining solid were weight. The amount retained by the membrane was calculated by subtracting the expected weight in each solution and the weight recorded after evaporation.

2.3.5 Functionalisation of BNOx with glucose

BNOx (300 mg) was mixed with glucose (150 mg) and dispersed in 100 mL of Millipore water. The solution was then sonicated for 24 hours continuously to obtain the exfoliated functionalised BNOx. 50 mL of the solution was used to make each membrane.

2.3.6 Functionalisation of BNOx with glutaraldehyde and glucose

Two concentrations of glucose were tested, 5% w/v (5 mg) and 10% w/v (10 mg), table 2.3. After the exfoliation of BNOx, 5% w/v and 10% w/v of a glucose were added followed by the addition of glutaraldehyde (50% v/v, 225 µL). The solutions were then stirred for 48 hours. 50 mL of the solution was used to make each membrane.

Table 2.3: BNOx functionalised with glucose and glutaraldehyde.

Sample	BNOx (mg)	Glucose (mg)	Gluteraldehyde (µL)
5% w/v glucose	300	5	225
5% w/v glucose	300	5	225
10% w/v glucose	300	10	225
10% w/v glucose	300	10	225

2.3.7 Testing functionalised BNOx membranes

A racemic solution of L- and D-penicillamine was prepared by mixing equal amounts of each enantiomer (table 2.4). The solution was tested using circular dichroism (CD) to make sure the racemic mixture was achieved (signal would be zero). The solution was diluted 1/10 to have an UV-Vis absorption of 1 a.u.

Table 2.4: Volume of both enantiomers mixed to obtain the racemic mixture. CD spectroscopy was used to find that 0.75 mL extra of L-Pen were needed to obtain the racemic mixture.

Enantiomer	Volume (mL)
L-Pen	25.75
D-Pen	25

20 mL were passed through the membranes, with aliquots being collected every 5 minutes. The solutions were studied using UV-Vis and CD spectroscopy.

2.4 Experimental procedures for chapter 5

2.4.1 Exfoliation of BNOx with LDH

LDH has a positive surface charge and BNOx presents a negative charge. Thus, the two were mixed together as the electrostatic interaction between them will hold them together in the membrane. The LDHs were synthesized by Áine Coogan in the group.

Different percentages in weight of LDH and BNOx (table 2.5) were dispersed in 100 mL Millipore water. The final concentration of the solutions was always 3 mg/mL. These solutions were then continuously sonicated for 24 hours using an Ultrawave model U100H, except for sample B, where the BNOx was sonicated and then stirred with LDH.

Table 2. 5: Percentages weight of LDH and BN-Ox for each solution.

Sample	wt% BNOx	wt% LDH
A	50	50
B	80	20
C	80	20
D	30	70
E	40	60

2.4.2 BNOx-LDH composite membranes

After the exfoliation, the membranes were produced by vacuum filtration of exfoliated BNOx-LDH solution through a PVDF (45 nm pore size) template. 50 mL of each solution (150 mg from the combination of BNOx and LDH described in table 2.5) was passed through the PVDF template under vacuum filtration. Once all the solution had passed through, the pump was left on for a further 10-15 minutes to produce a dried membrane.

2.4.3 Photodegradation studies

Membranes made with 20% LDH and 80% BNOx were tested for retention of two dyes; Methylene Blue and Methyl Orange. Some of the membranes were kept in the dark by covering them with aluminium foil; while the others were exposed to UV light or the light in the lab. Photos were taken at different times, for a period of up to 14 days.

2.4.4 Kinetics studies

A BNOx-LDH (80:20) membrane was synthesised and resuspended in Millipore water after drying. A higher concentrated Methyl Orange (60 mL, 500 μM) was added. The solution was stirred in darkness (wrapped in tin foil) for 3 hours, to allow the adsorption of the dye to the BNOx-LDH to happen. After this time, the foil was removed, and the solution was exposed to light. Aliquots were taken every 30 min, centrifuged and UV-Vis was carried out of each aliquot, to determine the concentration of the dye at each stage.

2.4.5 Synthesis of magnetic nanoplates

400 mL of HyPure water were degassed in a 1L round bottom flask at room temperature and then flushed with argon. Once the solution was under argon, 30 mL of ethylene glycol, 30 mL of hexamethylenetetraamine (HMTA) 50% w/w in water and 20 mL of P123K (2k Mw) were added to the flask and the solution was stirred and the temperature raised to 100° C. While the solution it's getting to the target temperature, 7 g of $FeCl_3 \cdot 6 H_2O$ were dissolved in 30 mL of HyPure water. In a different sample tube, 3 g of $FeCl_2 \cdot 4 H_2O$ were weighed. Once the solution was at 100° C, the iron (II) was added to the

solution of iron (III), mixed together and rapidly injected in the solution. The solution was then left stirring for 2 hours at 100° C.

Once the reaction took place, the product was washed alternating a solution of KOH (4 g) in HyPure water (250 mL) and MeOH. This was repeated until no more foaming was observed and the solution was clear once the product was precipitated using a magnet. Finally, the nanoplates were dried on the air on top on an oven.

2.4.6 Exfoliation of BN with magnetic nanoplates

Different percentages in weight of Fe_3O_4 nanoplates and BN (table 2.6) were dispersed in 100 mL Millipore water. The final concentration of the solutions was always 3 mg/mL. These solutions were then continuously sonicated for 24 hours using an Ultrawave model U100H.

Table 2.6: Percentages weight of Fe_3O_4 and BN for each solution.

Sample	wt% BN	wt% Fe_3O_4
F	95	5
G	90	10
H	85	15
I	80	20
J	50	50
K	40	60

As there were concerns about the stability of the membranes, it was decided to prepare new membranes, keeping the amount of BN the same as a normal membrane (150 mg/membrane) and changing the amounts of Fe_3O_4 added to each membrane (table 2.7). Each sample was dispersed in 100 mL of Millilipore water and continuously sonicated for 24 hours using an Ultrawave model U100H.

Table 2.7: Amounts and ratio of BN:Fe_3O_4 per solution of 100 mL.

Sample	BN	Fe_3O_4	Ratio BN:Fe_3O_4
L	300	150	1:0.5
M	300	200	1:0.6
N	300	250	1:0.8

All solutions were immediately used for the preparation of the membranes or put back under sonication until they were used.

2.4.7 Preparation of composite membranes

After the exfoliation, the membranes were produced by vacuum filtration of exfoliated BN-Fe_3O_4 or solution through a PTFE or PVDF (0.22 μm pore size) template. 50 mL of each solution (150 mg from the combination of BN and Fe_3O_4 as described in tables 2.6 and 2.7) was passed through the PTFE/PVDF template under vacuum filtration. Once all the solution had passed through, the pump was left on for a further 10-15 minutes to obtain a dried membrane.

2.4.8 Magnetic separation

A solution of magnetite nanoparticles has been synthesised by Áine Coogan. 20 mL of the magnetite nanoparticles solution were passed through a BN and BN-Fe_3O_4 (1:0.6) membranes to test the retention of the magnetic material. The permeate was put against a magnet to test the presence or absence of magnetic nanoparticles.

2.4.9 BN exfoliated with CNTs

Different percentages in weight of the CNTs and BN were dispersed in the different solvents, IPA, NMP and water (table 2.8). The final concentration of the solutions was always 3 mg/mL. These solutions were then continuously sonicated for 24 hours using an Ultrawave model U100H.

Table 2.8: Percentages weight of CNTs and BN and solvent for each solution.

Sample	% wt BN	% wt CNTs	Solvent
O	95	5	IPA
P	90	10	IPA
Q	85	15	IPA
R	80	20	IPA
S	95	5	NMP
T	90	10	NMP
U	85	15	NMP
V	80	20	NMP
W	50	50	NMP
X	25	75	NMP
Y	80	20	Water
Z	50	50	Water
AA	25	75	Water

All solutions were immediately used for the preparation of the membranes or put back under sonication until they were used.

2.4.10 Preparation of BN-CNTs composite membranes

After the exfoliation, 50 mL of each solution (150 mg from the combination of BN and CNTs as described in table 2.8) was passed through a PVDF template (0.45 µm pore size) under vacuum. Once all the solution had passed through, the pump was left on to help drying the membrane.

2.4.11 Retention test

Retention of the membranes was done as described in 2.2.3.

2.5 Experimental procedures for chapter 6

2.5.1 Mechanical ultrasound assisted exfoliation of MoS_2

MoS_2 (3 g, 12.5 mmol) was added to 150 ml of HPLC 2-propanol and sonicated in a sonic bath for 15 minutes in a conical flask. This mixture was centrifuged at 9000 rpm for 10 minutes. The supernatant was then discarded, and the precipitate was dispersed in 100 ml of Millipore water, placed into a round-bottom flask with a ground glass fitting. 2 mg/ml of sodium cholate, a surfactant, were added to greatly increase yield and stability of MoS_2 produced in solution. Firstly, this was degassed using a condenser under vacuum, for 15 minutes, and then put under an Argon atmosphere. The solution was then sonicated for 5.5-6 hours in a sonic bath (schematic shown in figure 2.3) and then centrifuged for 10 minutes at 4,000 rpm. The remaining supernatant was the MoS_2 dispersion used for further work, which was degassed and placed under an argon atmosphere again for storage.

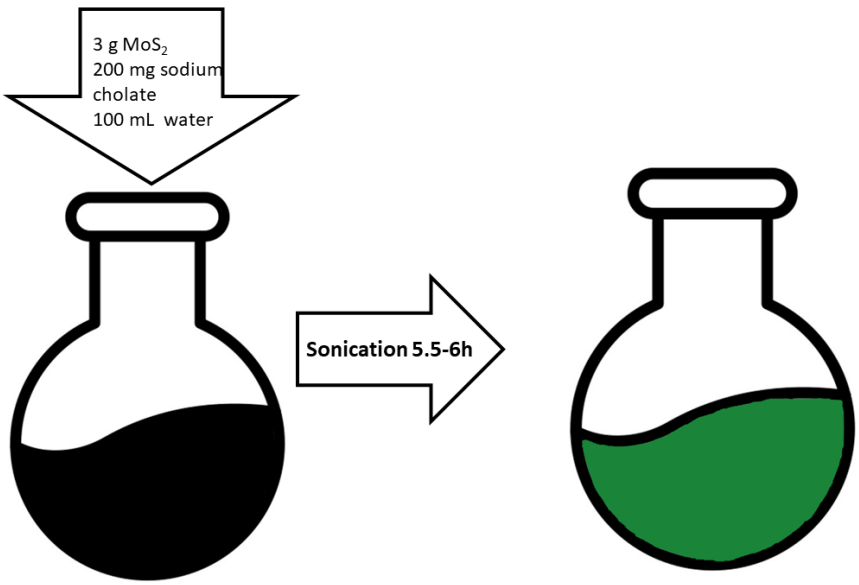

Figure 2.3: Exfoliation of MoS_2, showing the change of colour produced by the exfoliation.

2.5.2 Functionalisation with D/L-Cysteine and D/L-Penicillamine

After mechanical exfoliation of MoS_2, 0.15 M of ligand (D- or L- cysteine or D- or L-penicillamine) was added to 15 or 30 mL of the exfoliated material. Following the addition of the ligands, the samples were sonicated for 90 min under Argon in a sonic bath. Then, the samples were centrifuged at 4000 rpm for 10 minutes, keeping the

supernatant which contains the ligand functionalised MoS_2. The final suspensions of MoS_2 were kept under inert atmosphere at temperatures between 2-5°C to ensure their stability.

2.5.3 Preparation of MoS_2 membranes

After the exfoliation, the membranes were produced by vacuum filtration of exfoliated MoS_2 solution through a porous polycarbonate membrane (20 nm of pore size, 47 mm diameter). 50 mL of each solution (0.45 mg/mL of MoS_2) was passed through the template under vacuum filtration. Once all the solution had passed through, the pump was left on for a further 10-15 minutes to obtain a dried membrane.

2.5.4 Retention tests

Retention of the membranes was done as described in 2.2.3.

2.5.5 Chiral filtration

A racemic solution of L- and D-cysteine was prepared by mixing equal amounts of each enantiomer (20.5 mL of L-Cys plus 20 mL of D-Cys). The solution was tested using circular dichroism (CD) spectroscopy to make sure the racemic mixture was achieved (signal would be zero). Using CD It was observed that 0.5 mL extra of L-Cys were needed to obtain the racemic mixture. The solution was diluted 1/10 to have an UV-Vis absorption of 1 a.u.

20 mL of the racemic solution was passed through the L-Cys functionalized MoS_2 membrane using vacuum filtration. The CD of the permeate was recorded in order to test the separation efficacy.

2.5.6 MoS_2-BNOx composite membranes

Two procedures were followed when producing these composites membranes.

The first one was carried out by depositing different amounts of exfoliated BNOx (as previously described) on a PVDF template (0.45 µm pore size), as seen in table 2.9. After

this layer was settle, 50 mL of exfoliated MoS_2 in the presence of sodium cholate (as previously described) were deposited on top and allowed to form the membrane.

Table 2.9: different amounts of exfoliated BNOx used to produce the composite membranes

Membrane	BNOx (mL)	MoS_2 (mL)
BB	20	50
CC	10	50
DD	5	50

The second method was carried out by mixing 50 mL of exfoliated BNOx (as previously described) with 50 mL of exfoliated MoS_2 in the presence of sodium cholate (as previously described) and sonicated for 10 min. Once they were mixed, 50 mL of the solution was passed through a PVDF template (0.45 μm pore size) to form the membrane.

These membranes were tested using the methods described above.

2.6 Experimental procedures for preliminary MoS_2 work

2.6.1 Chemical exfoliation of MoS_2

Bulk powder MoS_2 (0.3 g) was mixed with 3 mL of 1.6 M n-butyllithium under an argon atmosphere and then heated under reflux for 48 hours. Then, the mixture was filtered out under Argon and washed with hexane, to eliminate any excess of n-butyllithium. Any unreacted n-butyllithium was quenched with isopropanol. The powder of the intercalated MoS_2 was then further exfoliated in 300 mL of Millipore water, obtaining a concentration of 1 mg/mL, under sonication for 1 hour.[5] The sample was then left for 24 hours to eliminate any non-stable exfoliated material, which would appear as a precipitate.

2.6.2 Functionalisation with (S)-(+)-citronellyl bromide

(S)-(+)-citronellyl bromide (200 mg) was added to 20 mL of the chemically exfoliated MoS_2 (20 mg) in Millipore water (tenfold excess of the ligand). The solution was kept stirring for 5 days at room temperature. Following this, the sample was washed multiple times with 2-propanol (3 x 50 mL), ethanol (3 x 50 mL) and water (3 x 50 mL). The final product was kept in Millipore water.[5]

2.7 Instrumentation

2.7.1 UV-Visible Absorbance Spectroscopy

This technique uses light in the UV-Visible spectral range (200-800 nm) and passes it through a sample, measuring the absorbance of said sample. Typically, a white light is used as the light source, which is passed then through a monochromator, such as a prism, splitting the light source into the different wavelengths.

The absorbance of any sample is defined by the Beer-Lambert law:

$$A = \varepsilon C l$$

Where:

- A: is the absorbance of the sample.

- ε: is the molar extinction coefficient.

- C: is the concentration of the sample.

- l: is the path length that the light passes through.

The molar extinction coefficient is specific of each chemical species or substance as it describes how strongly it absorbs light at a distinct wavelength. This coefficient depends on the composition and structure, being an intrinsic property of each substance. Therefore, the concentration of a sample is directly proportional to its concentration.

All UV-Vis spectra were recorded using a Cary 60 spectrophotometer and a quartz cuvette with a path length of 1 cm was used for all measurements.

2.7.2 Powder X-Ray Diffraction

X-Ray Diffraction (XRD) is a non-destructive and fast technique used to analyse samples and identify a sample's crystalline structure. XRD works best for the materials that are, at least, partially crystalline (i.e., that they have a periodic structural order). XRD relies on the fact that electron scatter light and this scattering depends on how many electrons are surrounding it. Due to this, a periodic array of atoms will diffract the x-rays in such a way that a pattern can be constructed, providing information about the internal structure of the compound on length scales from 0.1 to 100 nm.

When Bragg's law is satisfied, a constructive interference would be produced from the interaction of the incident rays and the sample, forming a diffracted ray (figure 2.4). When studying XRD patterns, Miller indices are adopted to define the planes of atoms using (hkl) coordinates. The d_{hkl} vector expands from the origin to the hkl planes and is used with Bragg's law to estimate diffraction peaks. Bragg's law is shown below:

$$n\lambda = 2d_{hkl}sin\theta$$

Where:

- **n**: is a positive integer (1,2,3…)
- **λ**: is the wavelength of x-ray beam
- **θ**:is the angle which causes constructive interference from x-rays will produce diffraction peaks.
- **d_{hkl}**: is the distance between atomic layers in a crystal

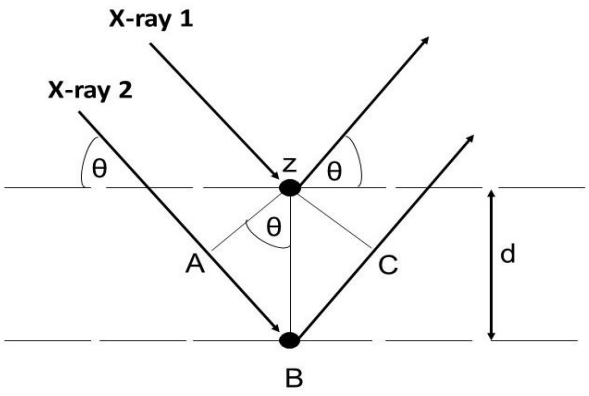

Figure 2.4: Schematic of Bragg's Law.

Powder XRD was used for this work. This is a specific case where the Bragg-Bretano geometry (figure 2.5) is used to calculate the diffraction pattern. In powder XRD, the sample rotates in order to obtain a reliable pattern by observing a higher number of crystallites.

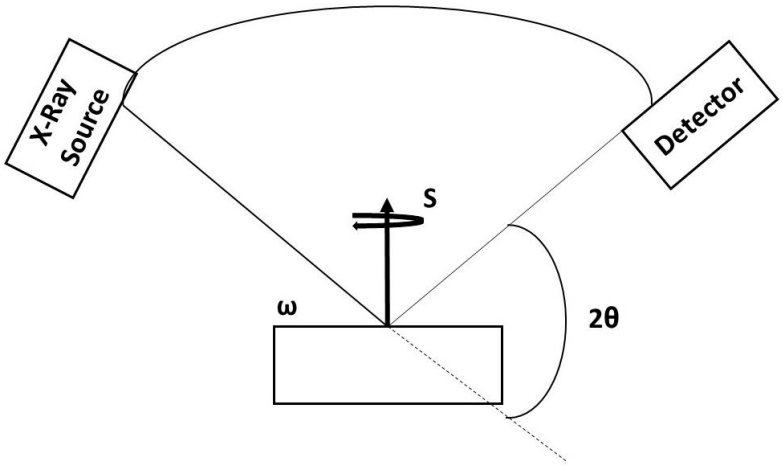

Figure 2.5: Schematic of Bragg-Bretano geometry for powder XRD, where ω is the incident angle, 2θ is the diffraction angle and S is the plane rotation angle.

X-ray powder diffraction was carried out on a zero background Si sample holder using a Bruker: D2 Phaser 2nd Gen. benchtop diffractometer using Cu Kα radiation (λ = 1.5418 Angstrom) across:

- For BN/BNOx: 2θ between 10 and 80°, no fluorescence correction and 0.01 increment per second.
- For LDH/BNOx-LDH: 2θ between 5 and 80°, no fluorescence correction and 0.01 increment per second.
- For Fe_3O_4/BN-Fe_3O_4: 2θ between 15 and 80°, no fluorescence correction and 0.01 increment per second.
- For MoS_2: 2θ between 20 and 80°, fluorescence correction and 0.01 increment per second.

XRD analysis was carried out by Adrián Sanz Arona.

2.7.3 Scanning Electron Microscopy

Scanning electron microscopy (SEM) is a type of microscopy where a focused beam of electron is used to scan the sample, obtaining information about its topography and atomic structure. Backscattered and secondary electrons are produced due to the interaction between the bean and the sample. These electrons can be used to form an image of the surface of the material. A schematic of an SEM microscope is shown in figure 2.6.

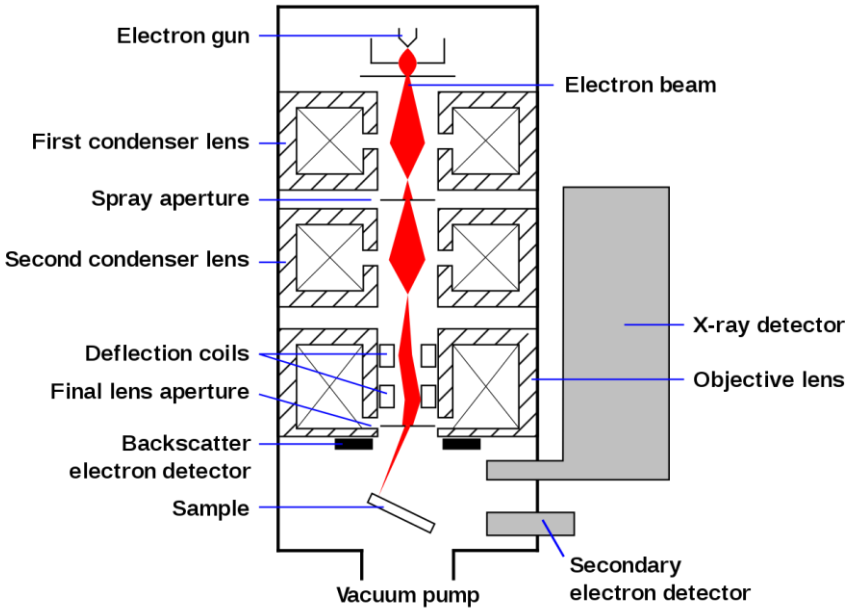

Figure 2.6: Schematic of an SEM microscope adapted from reference[6] [Online, accessed December 2021].)

Resolution of modern SEM is in the region of 2 nm. Imaging must be carried out in a vacuum. Electrons are emitted at the top of the column by the electron gun or electron source. The electron sources can be divided in:

- Thermionic: either W or LaB_6. The electron gun works on the basis that if a metal is heated to a high enough temperature, electrons can get sufficient energy to overcome the natural barrier that prevents them from leaking out.
- Schottky or field emission: requires a pristine surface (free of contaminants and oxides), and operates in UHV. The strength of an electric field is considerably increased at sharp points. A field emission gun (FEG) is usually a single crystalline tungsten tip, usually in a [310] or [111] orientation. You need two anodes. One provides the extraction voltage of several keV. The second anode then accelerate the electron to the required voltage.

Electrons are emitted from the electron source/cathode when their thermal energy surpasses the work function of the gun. The electrons are then accelerated by an anode and a series of electromagnetic lenses (around ~ 20 kV). These electromagnetic lenses are made of coils of wire within metal pole pieces; therefore, as a current passes through the coil of wire a magnetic field is created and can be used to control the path of the electron beam. They pass through a condenser and objective lenses, and then through a set of scan coils and an aperture. A scan is simultaneously generated on a computer monitor. Electrons are emitted by the specimen and detected, amplified and then this signal is used to conduct an image.

All SEM images were obtained using a Zeiss Ultra Plus Scanning Electron Microscope.

2.7.4 Transmission electron microscopy

Transmission electron microscopy (TEM) is another type of electron microscopy, similar to SEM in that it also uses an electron beam to visualize materials that cannot be seen with a traditional light microscope due to resolution limits. However, differently than SEM, TEM operates under a much higher accelerating voltage (around 60-300 kV versus the 1-5 kV for SEM). Another main difference with SEM is that the electrons are transmitted through the samples instead of scanning the scanning the surface of the

material. This higher accelerating voltage translate in much higher resolution images, allowing the possibility of obtaining crystallographic information. A schematic diagram of TEM is shown in figure 2.7.

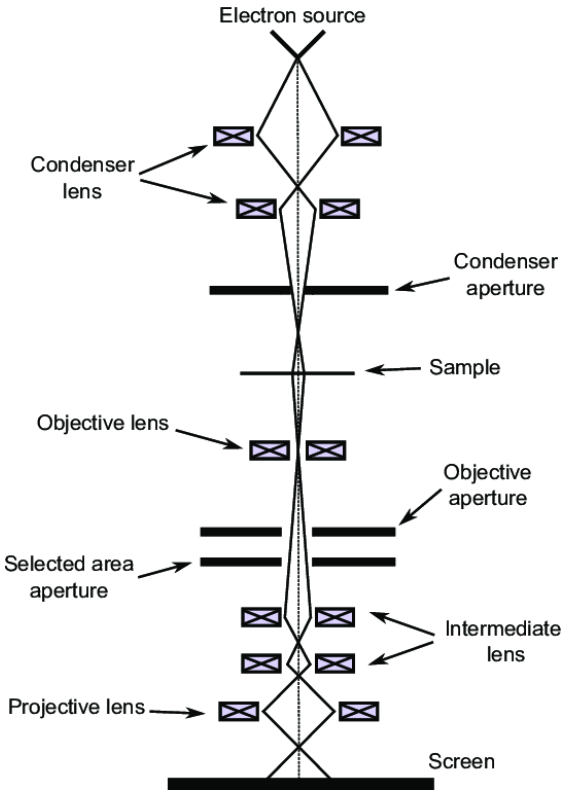

Figure 2.7: Schematic diagram of a Transmission electron microscope, adapted from reference[7].

A TEM instrument has three main components: electron source, condenser system and imaging system. As an electron sources, TEM can use a thermionic electron source (like tungsten or lanthanum hexaboride) or a field emission gun (cold field emission or Schottky-type), very similar to SEM. The electrons are then accelerated from the source towards an anode, where the beam will pass through to the sample. The condenser system, as explained in the SEM (section 2.7.3), is then used to focus and converge the beam into the sample. The last component is the imaging system, where the electron beam is focused on the sample. The beam is then transmitted into a second series of condenser lenses that will focus the electrons into a phosphorescent or fluorescent screen, which will create the image of the material.

Features of SEM and TEM can be combined in Scanning Transmission Electron Microscopy (STEM). STEM, as contrary as TEM, focuses the electron beam onto a small spot of the sample and it is scanned in a raster. There are different detectors for STEM, like Bright Field (BF) and High Angle Annular Dark Field (HAADF). BF works by collecting the transmitted electrons, which causes the holes in the sample to appear bright. HAADF, however, collects inelastic scattered electrons, excluding the transmitted electrons, hence the holes in the sample looking dark.

Transmission electron microscopy images were taken using a FEI Titan-Transmission Electron Microscope. High resolution transmission electron microscopy (HRTEM) and scanning transmission electron microscopy (STEM) high-angle annular dark-field imaging (HAADF) were carried out using a FEI Titan operating at a beam voltage of 300 kV. TEM and STEM images were taken Dr. Finn Purcell-Milton. TEM of Fe_3O_4 nanoplates was carried out by Dr. Sarah McCarthy.

2.7.5 Fourier Transform-Infrared Spectroscopy

Infrared spectroscopy is based on the interaction of materials with electromagnetic radiation with wavelengths between 1-1000 μm. Fourier Transform-Infrared Spectroscopy (FTIR) spectroscopy is a non-destructive analytical technique used to identify mostly organic, but inorganic as well, materials. FTIR shows the absorption of infrared radiation by the material as a function of the wavelength of the light that was absorbed. The bands in the spectra can be employed to determine functional groups in the material and, therefore, the chemical structure of the compound. This technique measures the absorption of the infrared radiation by the material as a function of the wavelength absorbed. These interactions between the material and the radiation causes the excitation of the vibrational or rotational states of the molecules, which can be detected by the absorbance or transmittance of the infrared radiation.

FTIR spectroscopy is based on the principle than certain frequencies of light are differently absorbed by different functional groups in compounds, causing a change in the dipole moment of the molecule. When a molecule is IR inactive, this change in the dipole moment doesn't occur. The absorbance or transmittance of the infrared radiation by the sample can be detected due to the interaction of the sample with the radiation,

which causes the excitation of the vibrational or rotational states of the molecules. The absorbed wavelengths are, therefore, characteristic of the molecular structure.

FTIR spectrometer employs an interferometer rather than a monochromator, to regulate the wavelengths of a broad-band IR light source. The interferometer works by splitting the beam into two, which pass through to mirrors, one of them through a stationary and the other through a movable mirror. This split causes a time delay, allowing the measurement of temporal coherence between the two signals. The detector then analyses the intensity of the transmitted light as a function of the wavelength.

FTIR was performed by a Perkin Elmer Spectrum 100 with Perkin Elmer Universal ATR Sampling Accessory. It consists of 4 recording iterations collected, summed and averaged. The full spectra wavelength range was from 4000 cm^{-1} to 350 cm^{-1} in steps of 2 cm^{-1}.

2.7.6 Raman spectroscopy

Electromagnetic radiation, when interacts with molecules can produce three different types of events: absorption, scattering or emission. Raman spectroscopy is used to measure the vibrational energy modes of a sample through scattered light, specifically the inelastic scattering of light.

There are two types of scattering: elastic and inelastic. Elastic scattering or Rayleigh scattering happens when the energies of the incident and emitted photons are equal. Inelastic scattering occurs when they are different (figure 2.8), which involves the transfer of energy between the molecule and the incident photon.

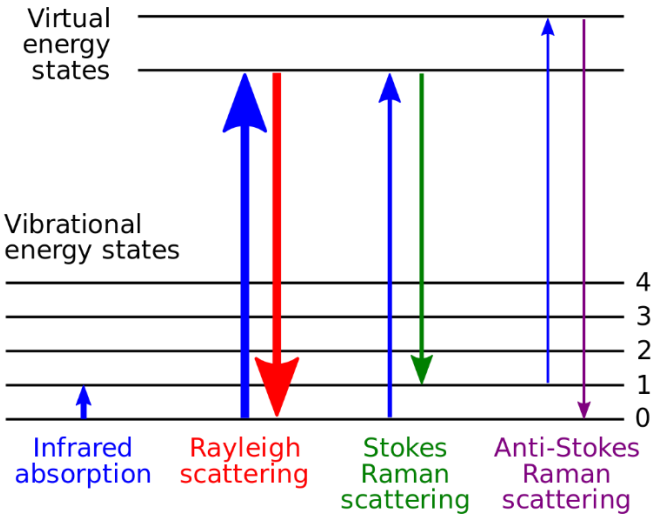

Figure 2.8: Energy level diagram showing the elastic and inelastic scattering involved in Raman process.

Inelastic scattering can be divided into Stokes, which shows decreased of energy; and anti-Stokes, which shows increased energy. The energy due to the Rayleigh scattering appeared as strong intensity lines in the Raman spectrum, around 103-104 greater than the Stokes and anti-Stokes bands. Therefore, a notch filter is used to block the elastic scattering. Moreover, the Stokes shift has higher intensity than the anti-Stokes, so it's usually viewed as more important in Raman spectroscopy. The difference in the frequency between the scattered and exciting radiation is characteristic of each molecule, which allows the use of this technique to characterize molecules. A change in the polarisation of a molecule makes a transition Raman active. Polarisability is referred as the ease which with electrons can be distorted from their original position. This polarizability decreases as the electron density is increased, which increases bond length and decreases bond strength.

Raman and FTIR spectroscopy can be used in combination, as complimentary techniques to give combined information and help explain the vibrational sates of a molecule. These two techniques are mutually exclusive, meaning that if a transition is strongly Raman-active it will have a weak IR signal and vice-versa.

Raman was obtained using a Renishaw in via Raman Microscope with 785 nm laser. It is equipped with three lenses and an automated xyz stage. Using laser at 100% power with an exposure of 60 from 1600 to 1100 cm^{-1}. Raman was carried out by Adrián Sanz Arjona.

2.7.7 Circular Dichroism Spectroscopy

Circular dichroism (CD) is a spectroscopy technique that measures the difference in absorption of right-handed circularly polarised light (R-CPL) and left-handed circularly polarised light (L-CPL). This difference occurs when a molecule contains one or more chiral light-absorption groups or chromophores.

CD spectroscopy is carried out in the visible and ultra-violet region of the electromagnetic spectrum. If the sample contains chiral chromophores, one of the circularly polarised light (CPL) will be absorbed to a greater extent than the other, causing the CD signal over the corresponding wavelength to be different than zero. CD signal can be positive or negative, depending in which CPL is absorbed preferentially. If more L-CPL is absorbed, the signal will be positive and contrary, if the R-CPL is preferentially absorbed, the signal will be negative. CD varies in function of the wavelength, so a CD spectrum may exhibit both positive and negative peaks.

Circular Dichroism spectra were recorded using a Jasco J-815 CD spectrometer, operating under a N_2 flow of 5-8 L/min. The samples were carried out:

- Exfoliated 2D materials from 700 to 200 nm.
- Ligands from 400 to 200 nm.

2.7.8 Thermogravimetric Analysis

Thermogravimetric analysis (TGA) is a technique that studies the thermal stability of a sample as well as the faction of volatile components in a sample. This is achieved by heating a sample at a constant rate while measuring constantly the weight of the sample, which allows to see the loss or gain of weight as the temperature increases. This technique can be used to see absorption (weight gain) or desorption (weight loss) of different species, addition of ligands, phase transitions, loss of solvents, and other chemical events.

The instrument has a sample pan, made of a highly heat resistant material, usually ceramic. This sample pan is held by a precision balance, which monitors and records the weight of the sample throughout the heating process. The sample pan is then place in a furnace, which will heat at a constant rate and plot the change in the sample mass as function of the measured temperature (figure 2.9).

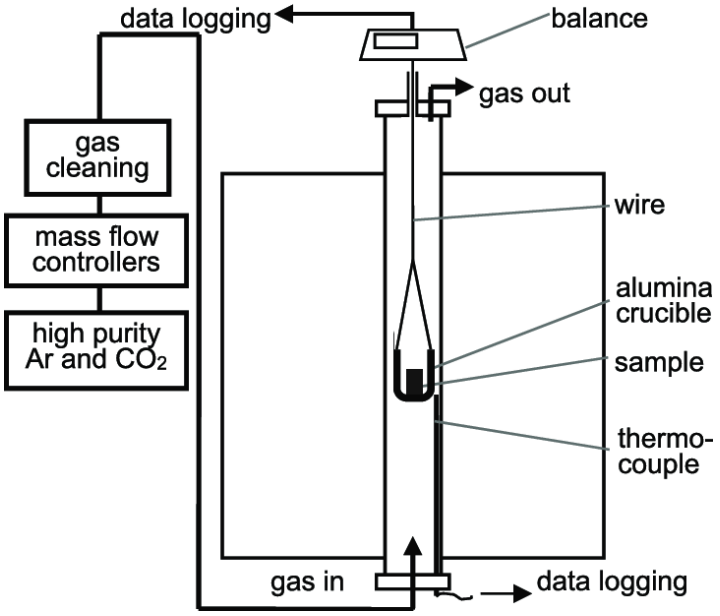

Figure 2.9: Diagram of a TGA instrument adapted from reference [8].

TGA was carried out using a ceramic sample pan on a Pyris 1 TGA Thermogravimetric Analyzer. Heating from 30°C to 900°C at a rate of 10°C/min for the BNOx with sugars.

TGA was performed by Áine Coogan.

2.7.9 Vibrating Sample Magnetometer

Vibrating sample magnetometer (VSM) is one method that can be used to determine the magnetic properties of bulk and nanomaterials. VSM gives information on the magnetic moment of the sample and inform of whether the material is ferromagnetic, ferromagnetic or superparamagnetic. This is done based on the hysteresis loop obtained

from the VSM. When a material is exposed to an external magnetic field, a magnetic moment is induced in the sample. This will cause mechanical vibrations, which will then produce a magnetic flux. The magnetic flux results in a voltage in the sensing coils, which is proportional to the magnetic moment of the sample. The magnetism of the sample will then be plotted in the form of a characteristic hysteresis loop. The parameters of the hysteresis loop allow a material to be characterised based on its saturation magnetisation (Ms), remanence (Mr) and coercivity (Hc). Superparamagnetic materials have a coercivity of 0 Am^2/Kg. A schematic diagram of a VSM is shown in figure 2.10.

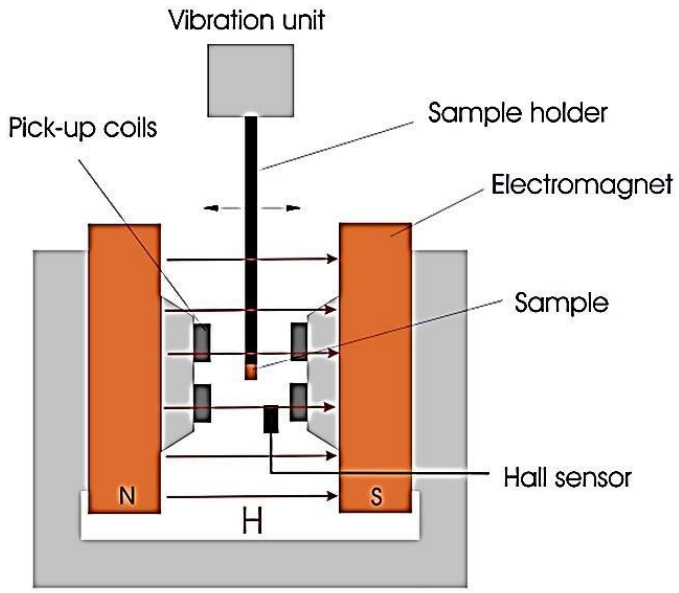

Figure 2.10: Schematic of the internal layout of a VSM, adapted from reference[9]

VSM measurements were carried out on 'The Magic Roundabout' VSM apparatus, courtesy of Prof. Michael J. Coey. The measurements were carried out at room temperature with an applied field up to 1 T. The VSM was calibrated using a nickel sample of known mass with a magnetic moment of 55.4 Am^2/Kg at 1 T at room temperature. The sample was dried, weighed precisely and placed in paper in a PVC holder in order to carry out the measurements.

VSM measurements were carried out by Munirah Ghariani.

2.7.10 Zeta potential measurements

Surface charge of nanoparticles in a solution can be determined using zeta-potential measurements, which is a useful tool to determine their stability. Nanoparticles have a surface charge that then attracts a thin layer of counter-ions, this is called the Stern layer. This layer is an immobile layer at the surface of the nanoparticles that moves with it through the solution. The zeta-potential is the electric potential at the interface of this double layer. Zeta-potential is a useful method to determine the stability of a colloidal solution. If a solution has a zeta-potential between -25 and +25 mV it will agglomerate over time due to interparticle interactions.

The experimental set-up of zeta-potential measurements are carried out in a dynamic light scattering (DLS) spectrophotometry (shown in figure 2.11). In order to obtain the measurements, an electric field is applied to the sample in the zeta-potential cell, as well as also being illuminated with laser light. Particles move due to the applied electric field and this motion is measured through the amount of light that they scatter. The frequency of the scattered light is a function of the velocity of the particle due to the Doppler Effect. A reference beam is mixed with the scattered beam to obtain the frecuency from the scattered light. To determine the particle velocity, the magnitude of the frequency shift is measured.

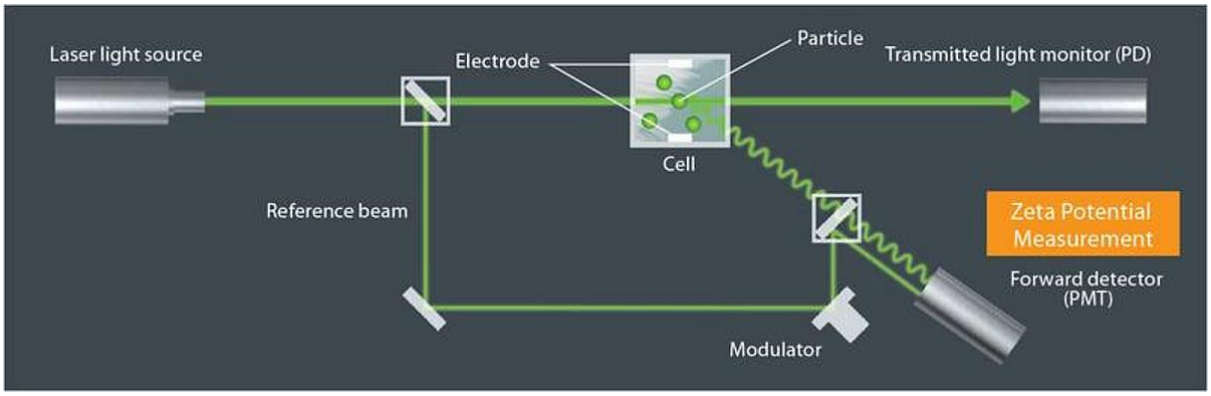

Figure 2.11: Schematic of the experimental set-up for zeta-potential measurements, adapted from reference[10].

Zeta Potential was carried out by Áine Coogan.

2.7.11 Brunauer-Emmett-Teller measurements

Brunauer-Emmett-Teller (BET) is used to measure the physical adsorption of gas molecules on solid surfaces, providing information on the specific surfaced are of materials[11]. BET is applied to systems with multilayer adsorption, usually using a probe gas (adsorbate) that doesn't react with the material being tested (adsorptive), allowing the quantification of the surface area. Nitrogen gas is usually used as the adsorbate for probing the sample, as it doesn't typically react with the materials.[12]

BET model describes the physisorption of the adsorbate as a function of the relative pressure (P/P_0). It uses the measured data to obtain the quantity of an adsorbed gas to a monolayer of the sample, fitting the model to the data obtained. The area per molecule allows the possibility to find the total area of the material sampled.[12]

As BET uses relative pressure of the material studied, the gas used as adsorbate has to be condensable at the adsorption temperature, meaning it has to be a vapour. In order to carry out the measurement, a determined amount of the sample has to be place in the sample cell, followed by an outgassing and other treatments to remove impurities and moisture.[12] Afterwards, the pressure of the adsorbate is increased as the amount adsorbed to the adsorptive is measure. In order to obtain the best precision in the data, this last step is carried out at different discrete pressures. P_0 value (saturation vapour pressure) is often measured at the same time or calculated from the known temperature.[12]

BET surface area analysis was performed using a Nova 2400e Surface Area Analyser (Quantachrome, UK). Membranes were cut to size using a blade. Prior to analysis, samples were de-gassed for 6 hrs. at 200 °C under vacuum. The BJH method was used to calculate the pore size diameter and pore volume, from the desorption branch of the isotherms. The BJH values presented here include pores in the range 1-30 nm. BET measurements were carried out by Dr. Aran Rafferty.

2.7.12 Mercury Intrusion Porosimetry measurements

Mercury intrusion porosimetry is a technique used to obtain information on the porosity, pore size distribution, pore volume, and others, allowing the characterization of a wide variety of materials. The instrument, a porosimeter, uses pressure to force mercury to intrude into the spaces in a porous substrate. The pressure required to fill the pores is inversely proportional to the size of those. The bigger pores are filled at lower pressures,

whereas the smaller pores required more pressure for the mercury to intrude in them. This technique can be used to characterize both the intra- (inside the particles) and inter-particle (between the particles) pores (figure 2.12).

The volume of mercury that intrudes in the sample is monitored by change in the capacitance in the metal clad capillary in the analytical cell, known as the penetrometer. The sample is placed in a part of the penetrometer cell, which has different volumes to adjust to the amount of sample.

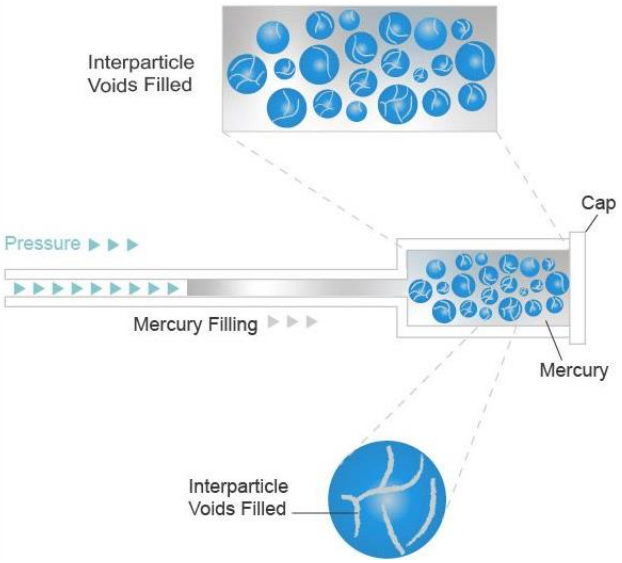

Figure 2.12: Schematic of the intrusion of mercury in a porous sample. Adapted from reference[13]

Mercury porosimetry was performed using an Autoscan-33 Porosimeter (Quantachrome, UK) with a default contact angle of 140°. Mercury porosimetry measurements were carried out by Dr. Aran Rafferty.

2.7.13 Atomic Force Microscope

Atomic force microscope (AFM) allows topographical imaging of nanostructures. A probe consisting of a cantilever with a sharp tip at the end is oscillated at its resonance frequency and a controlled amplitude. In non-contact mode (NCM) the AFM tip is placed at a close proximity to the surface, and it scans the surface in X-Y axis, via a piezo controlled mechanism (figure 2.13). As the AFM probe moves over surface features the amplitude and phase of cantilever oscillations vary due to attractive interaction (NCM)

between surface and tip end. The amplitude and phase changes are tracked by reflecting a laser beam on the flat top of the cantilever and detecting the deflection with a photodiode detector. The amplitude changes are used to run a feedback loop over the Z-axis (Z-piezo controller). In non-contact mode the feedback loop ensures the tip is kept at a constant distance from the surface (defined as setpoint) regardless of the surface features. A three-dimensional topographic image can be generated by monitoring the X-Y-Z displacement during the scan.

Atomic force microscopy (AFM) characterization was performed on a Park Systems NX10. The AFM images were obtained using PPP-NCHR probe (42 N/m and 330kHz, Nanosensors) in non-contact mode.

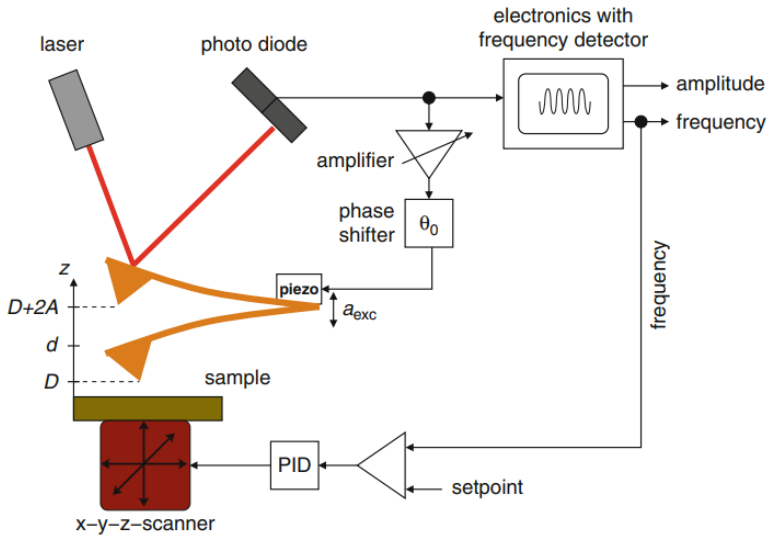

Figure 2.13: Schematic of an AFM, non-contact mode. Adapted from reference[14].

AFM measurements were carried out on a Park NX10 (Park Systems, South Korea). The AFM images were obtained in a non-contact mode (NCM) with a PPP-NCHR cantilever type (force constant = 42 N/m, resonance frequency = 330 kHz, Nanosensors). Single BN flakes were deposited by dropcasting of 0.03 mg/ml of exfoliated BN solution on gold coated glass slides purchased from Evaporated Metal Films (TS-TA-134). BN-NMP samples were dried in a vacuum oven at 200°C for 2 hours prior to AFM measurement. AFM studies were carried out by Marc Brunet Cabré.

Bibliography

1 L. Sun, H. Huang and X. Peng, *Chem. Commun.*, 2013, **49**, 10718.

2 M. Amirilargani, E. Saljoughi and T. Mohammadi, *J. Appl. Polym. Sci.*, 2010, **115**, 504–513.

3 E. Saljoughi and S. M. Mousavi, *Sep. Purif. Technol.*, 2012, **90**, 22–30.

4 G. Wiederschain, *Glycoscience. Chemistry and chemical biology*, 2009, vol. 74.

5 D. Voiry, A. Goswami, R. Kappera, C. de C. C. e Silva, D. Kaplan, T. Fujita, M. Chen, T. Asefa and M. Chhowalla, *Nat. Chem.*, 2014, **7**, 45.

6 Scanning Electron Microscopy - Nanoscience Instruments, https://www.nanoscience.com/techniques/scanning-electron-microscopy/, (accessed 8 December 2021).

7 N. Marturi, 2013.

8 R. J. Longbottom, B. J. Monaghan, A. A. Chowdhury, M. H. Reid, G. Zhang, M. R. Mahoney and K. Hockings, *ISIJ Int.*, 2016, **56**, 1553–1558.

9 M. Rafique, P. Thesis and I.- Pakistan, *Study of the Magnetoelectric Properties of Multiferroic Thin Films and Composites for Device Applications*, 2014.

10 Z. Potential, 2020, 4–7.

11 S. Brunauer, P. H. Emmett and E. Teller, *J. Am.Chem.Soc.*, 1938, **60**, 309–319.

12 BET Surface Area analysis - measurement and method, https://mercer-instruments.com/en/applications/BET-surface-area-analysis.html, (accessed 8 December 2021).

13 Mercury Intrusion Porosimetry - Particle Technology Labs, https://www.particletechlabs.com/analytical-testing/gas-adsorption-and-porosimetry/mercury-intrusion-porosimetry, (accessed 8 December 2021).

14 A. Aliano, G. Cicero, H. Nili, N. G. Green, P. García-Sánchez, A. Ramos, A. Lenshof, T. Laurell, A. Qi, P. Chan, L. Yeo, J. Friend, M. Evander, T. Laurell,

A. Lenshof, T. Laurell, J. Chen, J. C. Lacroix, P. Martin, H. Randriamahazaka, W. J. P. Barnes, B. W. Hoogenboom, K. Fukuzawa, H. Hölscher, H. Hölscher, A. Bottos, E. Astanina, L. Primo, F. Bussolino, X. Gao, V.-N. Phan, N.-T. Nguyen, C. Yang, P. Abgrall, F. G. Barth, P. Gurman, Y. Rosen, O. Auciello, C. J. Kähler, C. Cierpka, M. Rossi, B. Bhushan, M. L. B. Palacio and C. L. Dezelah, *Encycl. Nanotechnol.*, 2012, 93–99.

Chapter 3: BN based membranes

3.1 Introduction

3.1.1 Boron nitride

Boron Nitride (BN) is a 2D material that has gained a lot of attention in recent years, composed of alternating, equal number of boron (B) and nitrogen (N) atoms. It is not found in nature, so it's synthetically produced from boric acid (H_3BO_3) or boron trioxide (B_2O_3)[1]. Some BN polymorphs are isostructural to carbon and it can be found in various crystalline forms, hexagonal, rhombohedral, cubic and wurtzite (figure 3.1)[1]. Hexagonal boron nitride (h-BN) is a white and slippery BN polymorph with a layered structure and is often regarded as a white counterpart of graphite, with the boron and nitrogen atoms appearing where the carbon atoms do in its analogue[2] . However, the B-N bonds present in the BN layers are stronger than the graphene C-C bonds. This draws more attention to BN, as it has high hardness (15-24 kg mm^{-2}), chemical stability, mechanical strength, high thermal stability (~1100°C), high thermal conductivity and electrical insulation due to its band gap of around 5-6 eV[1–7].

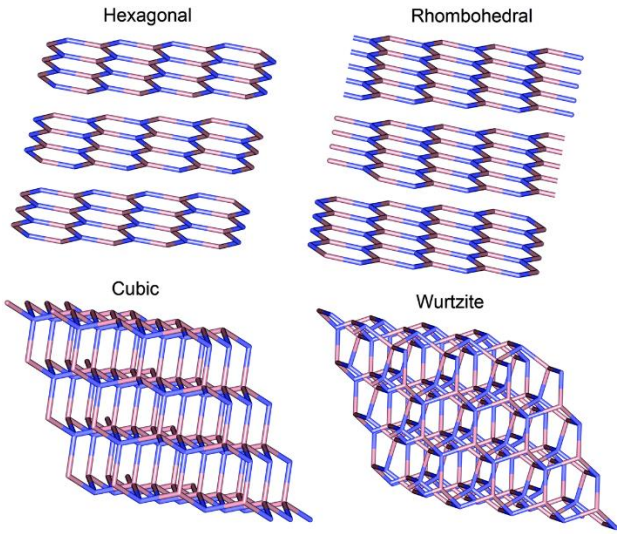

Figure 3.1: Boron nitride crystal polymorphs (adapted from reference[1]).

BN also presents a very attractive 2D nanomaterial for NF, as it is cheap and environmentally friendly[2,5–7]. In addition, it has been reported to show a distinctly unique property of having high thermal conductivity, while being an electrical insulator, an

emergent property due to the nanostructure of the material, which offers unique design capability[2,8–10].

3.1.2 BN membranes and exfoliation

BN-based membranes have previously been reported for several applications, including organic molecule filtration and pharmaceutical applications[10–17]. BN can form several different nanostructures, including nanosheets, nanoribbons and nanotubes (figure 3.2). h-BN layers are held together by weak Wan-der-Waals forces (with ~0.33 nm interlayer space)[18]. BN nanosheets (BNNs) can consist of few to mono-layered sheets.

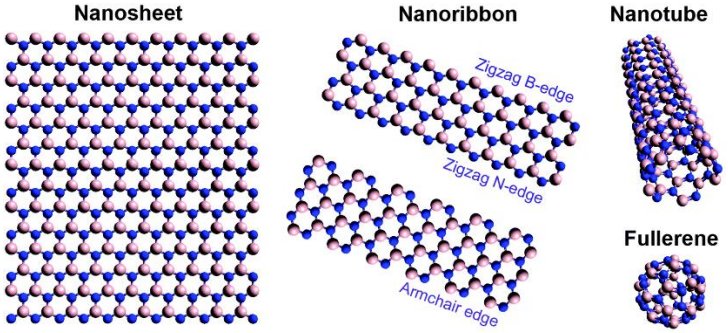

Figure 3.2: BN nanostructures structural models. The edge of nanosheets or nanoribbons can be formed as armchair (BN pair edged) or zigzag (B- or N- edged). Image taken from reference[1].

BN nanosheets have some interesting advantages over already established materials used for organic separation and purification, due their large surface area, porous structure, high chemical, thermal and mechanical stability [14,19], making BN nanostructures good adsorbents of various substances, ranging from organic pollutants to gases[12,20,21]. Recent examples of highly effective BN-based membranesreported in the literature include BN materials used for water treatment to remove[14,22,23] organic (ranging from oils, solvents and dyes) [12,19,20,24–27] and inorganic pollutants (like heavy metals)[26–32] as well as pharmaceutical components from water[13,33]. BN-based membranes can broadly be categorised into 2 types: composite membranes formed from a mixture of polymer and BN, and membranes made from pure BN. Naturally, the major advantage of pure BN filters is the stability across a large temperature, chemical, and pH range, although membranes which incorporate polymers benefit from ease of use and more wide-ranging mechanical properties.

There are several ways to produce the exfoliated 2D BN materials, with most of them based upon a top down approach, including micromechanical cleavage, chemical exfoliation, mechanical exfoliation (most commonly ball milling) and sonication-assisted liquid-phase exfoliation[34]. Each approach has its advantages and disadvantages, with the most successful to date for membrane preparation being either based on ball milling or liquid phase exfoliation. In the case of liquid exfoliation, it has been shown that exfoliation in bulk can be performed in common solvents (NMP, IPA and DMF), yielding mono- and low-number layers. The method is insensitive to ambient conditions and shows good potential for scale up[35]. In addition, BN is known to be dispersed in water due to sonication-assisted hydrolysis[36]. Solvent exfoliation is one of the preferred methods for 2D nanosheet production as it is a simple procedure and does not always use a third-phase dispersant, like a surfactant. [37] During liquid exfoliation under ultrasound, an appropriate solvent is capable to provide sufficient external energy to reduce the interlayer energy, which keeps the nanosheets tightly bound together, that results in expanding the stacking distance between the different layers. [38] Afterwards, also depending on the ability of the solvent to stabilise the layers, the bulk material can be exfoliated. Nevertheless, the reverse process (re-aggregation of the nanosheets) could occur due to their interlayer binding energy. Therefore, when it comes to liquid-phase exfoliation, it is very important to choose the correct solvent that will promote the exfoliation and suspension of the nanosheets in the solvent. [39] Selection of solvents, however, frequently is carried out based on trial-and-error methods and experience. [39] Coleman *et al* have proposed that in order to obtain a stable dispersion of the exfoliated material, the solvent of choice has to match the surface energy of the nanosheet and, thus, minimise the enthalpy of mixing. [40]

The preferential choice for BN has been a polar solvent for sonication assisted-exfoliation such as dimethylformamide, (DMF), [41,42] dimethyl sulfoxide (DMSO), [43] N-methyl-2-pyrrolidone (NMP),[35,44,45] isopropanol (IPA)[35,46] and even water. [47] However, the best results for exfoliation of BN have so far been achieved in NMP. [35] In addition, the sonication-assisted exfoliation of BN is well suited to the production of BN based membrane fabrication by vacuum filtration, which is an effective and easy method for membrane fabrication. [16,33,48,49]

In this study, for the first time, we compare three commonly used solvents for sonication-assisted liquid phase exfoliation of BN, using NMP, IPA and water, and demonstrate the key role this plays in the resulting performance aspects of vacuum filtration-produced

BN membranes. We demonstrate a low cost, green and scalable process, using water as the solvent of choice to produce a new BN-based membrane, and fully characterised it, demonstrating impressive retention across a number of dyes. We demonstrate that, the level of exfoliation achieved during sonication is crucial to producing an effective membrane. This study also specifically attributes the use of water as an solvent for exfoliation to achieve the most appropriate exfoliation of BN for the preparation of utmost effective membranes.

3.1.3 Aims of this chapter

The main aim of this part of the project is to develop BN membranes for nanofiltration applications. Our initial goal is to optimise the exfoliation process, in order to find the most efficient but also the least toxic and greenest solvent for exfoliation. Then, once the exfoliation is optimised, our objective is to develop the preparation of new BN-based membranes for removal of selected dyes from water. The membranes are then to be tested and optimised, in order to achieve the best membrane performance.

3.2 Results and discussion

3.2.1 Exfoliation of BN in NMP, IPA and water

The exfoliation of BN was carried out in three different solvents (water, IPA and NMP) with samples denoted as BN-water, BN-IPA and BN-NMP, respectively. NMP and IPA were chosen as they are the solvents of choice for exfoliating BN. However, NMP is a toxic solvent with a high boiling point, which makes it difficult to eliminate from the membranes. For this reason, it was decided to try water as well, as a "green" and non-toxic alternative. BN suspensions were produced with a concentration of 3 mg/ml which compares favourably with results reported in the literature using similar approaches[35,50–52], with the three solutions appearing very similar after exfoliation, with no distinct visible differences. UV-Vis spectra of the exfoliated BN solutions are presented in figure 3.3 showing a decreased absorption at longer wavelengths while an increased absorption at shorter wavelengths. This can be related to the contribution of scatter and absorbance as the samples degree of exfoliation increases. These results fit with reported spectra given in the literature[53]. All three samples clearly demonstrate the Tyndall effect, as shown in figure 3.3, using diluted solutions of 0.03 mg/mL.

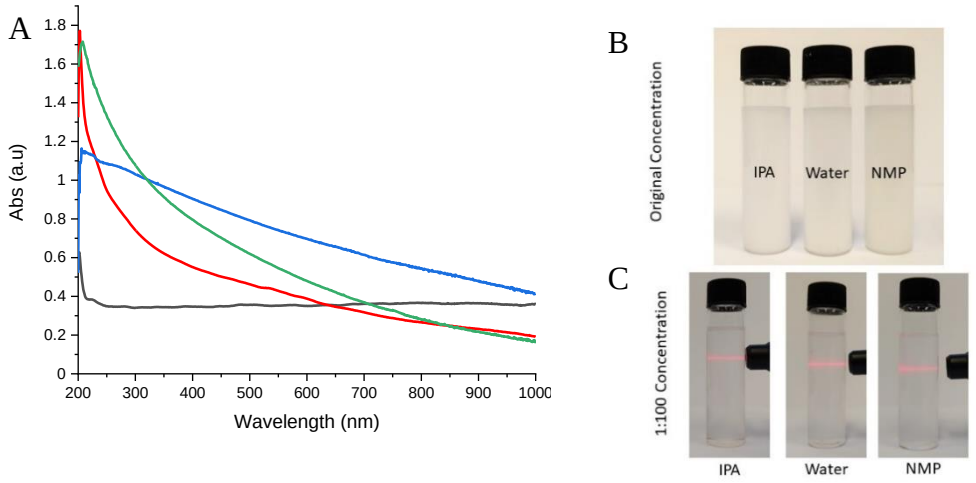

Figure 3.3. A) UV-Vis spectra of bulk BN (dark grey) and exfoliated BN in NMP (red), IPA (blue) and water (green), B) photograph of original solutions of BN exfoliated in the three solvents (3 mg/mL) and C) Tyndall effect on BN-exfoliated in IPA, NMP and Water (0.03 mg/mL).

SEM images were taken of the bulk BN as well as the BN exfoliated in the three solvents. The sizes of the nanosheets produced through exfoliation in the different solvents were found to be very similar. The bulk BN has shown a lower degree of exfoliation, with the nanosheets stacked on top of each other with barely any single to few nanosheetspresent.

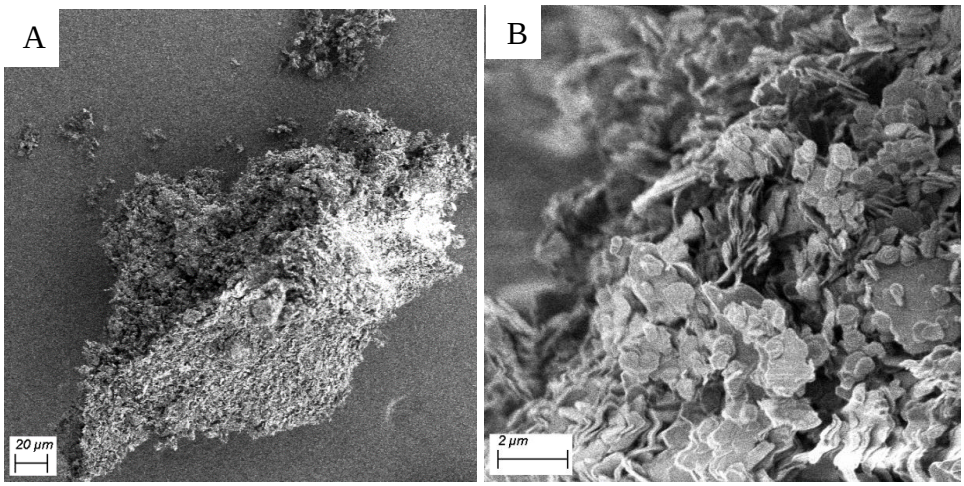

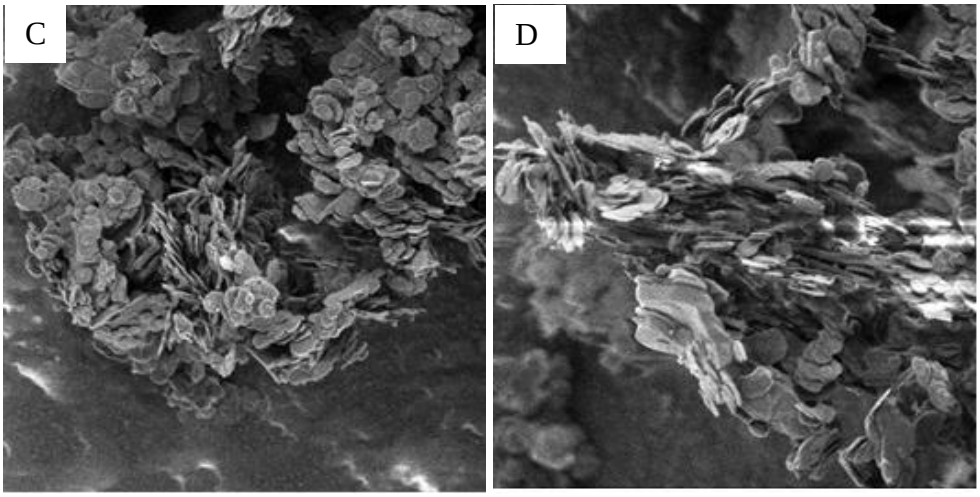

Figure 3.4: SEM images of bulk BN. Voltage 1.50 kV. Images taken with SE2.

The nanoflakes obtained are similar in appearance, with each exfoliated to a similar degree, especially when compared to SEM of non- exfoliated BN (figure 3.4). The nanosheets obtained following exfoliation in NMP had a flake-size distribution of 0.548 ± 0.279 μm, while IPA had mean size of 0.536 ± 0.178 μm and the water sample had a mean size of 0.581 ± 0.314 μm (figures 3.5 D, 3.6 D and 3.7 D). This indicates that the three solvents produce similar size nanosheets with no visual differences between the samples under SEM.

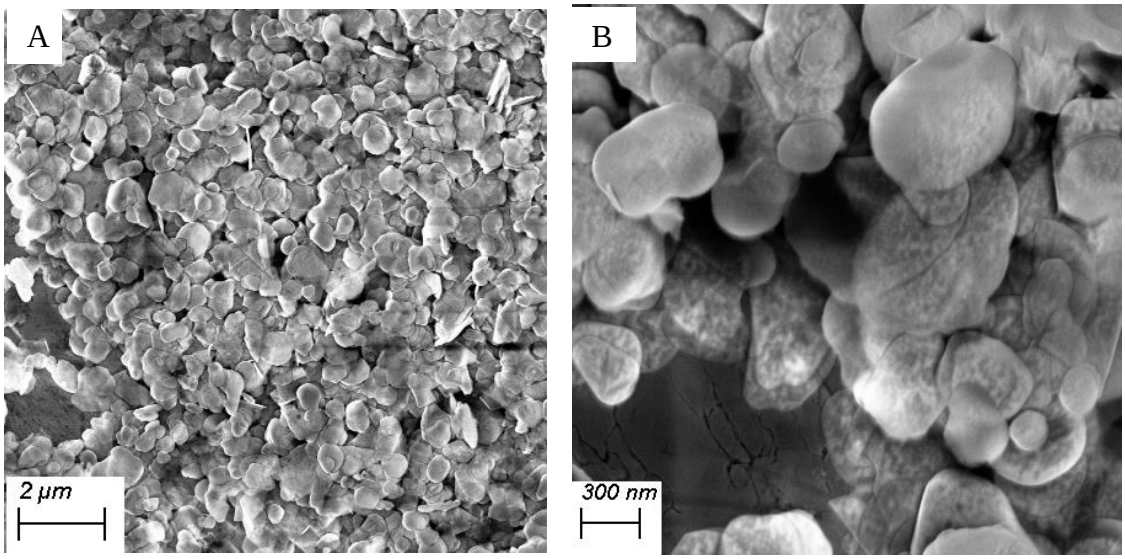

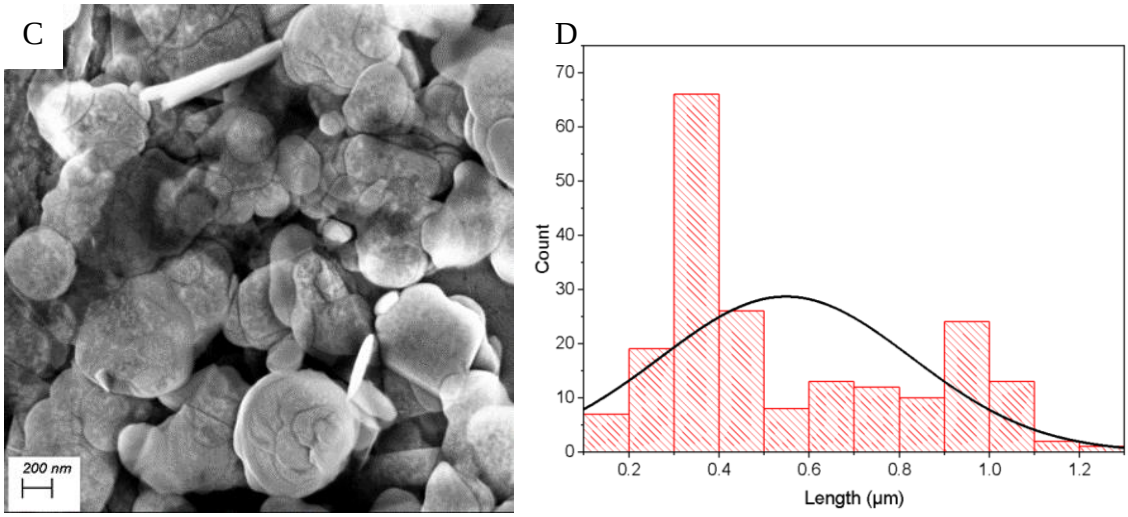

Figure 3.5: SEM of BN exfoliated in NMP (A, B and C) and size distribution of the nanosheets D). Voltage 5.00 kV, images taken using SE2.

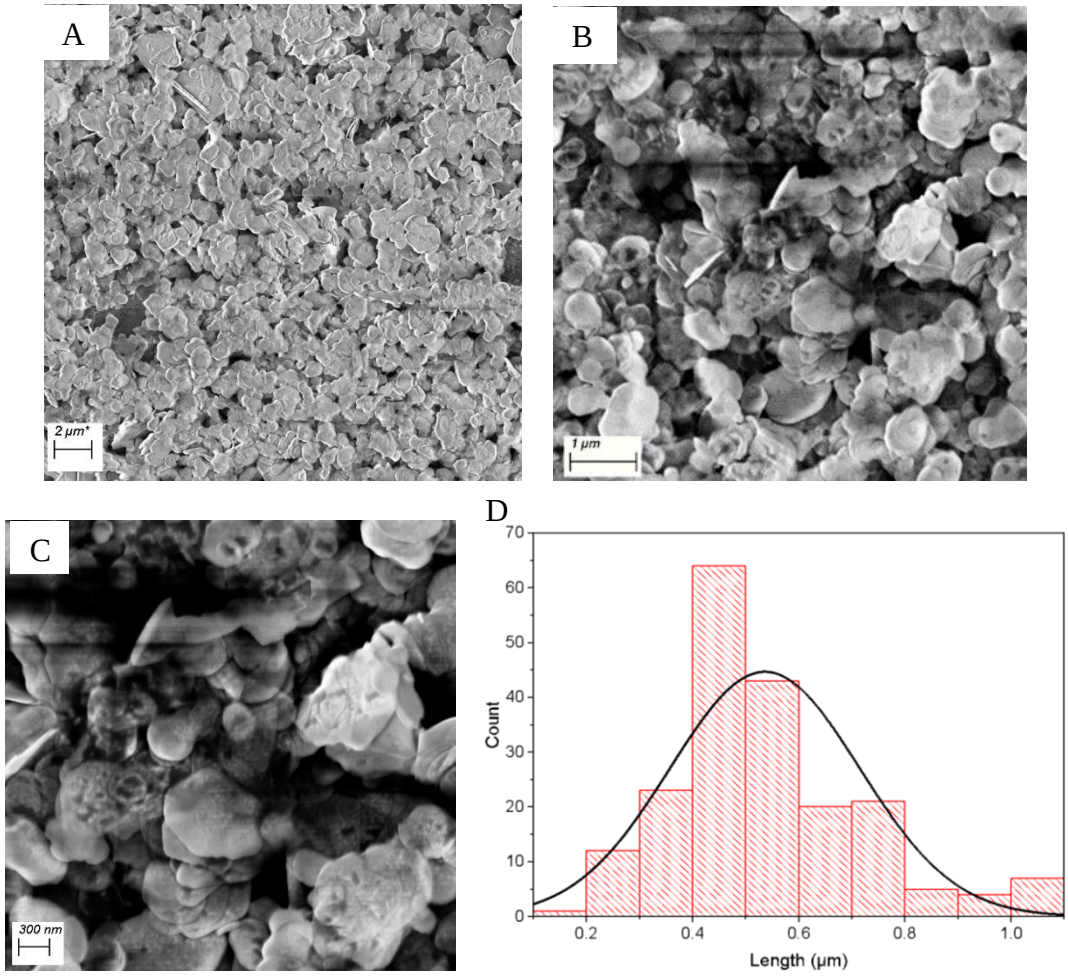

Figure 3.6: SEM of BN exfoliated in IPA (A, B and C) and size distribution of the nanosheets D). Voltage 5.00 kV, images taken using SE2.

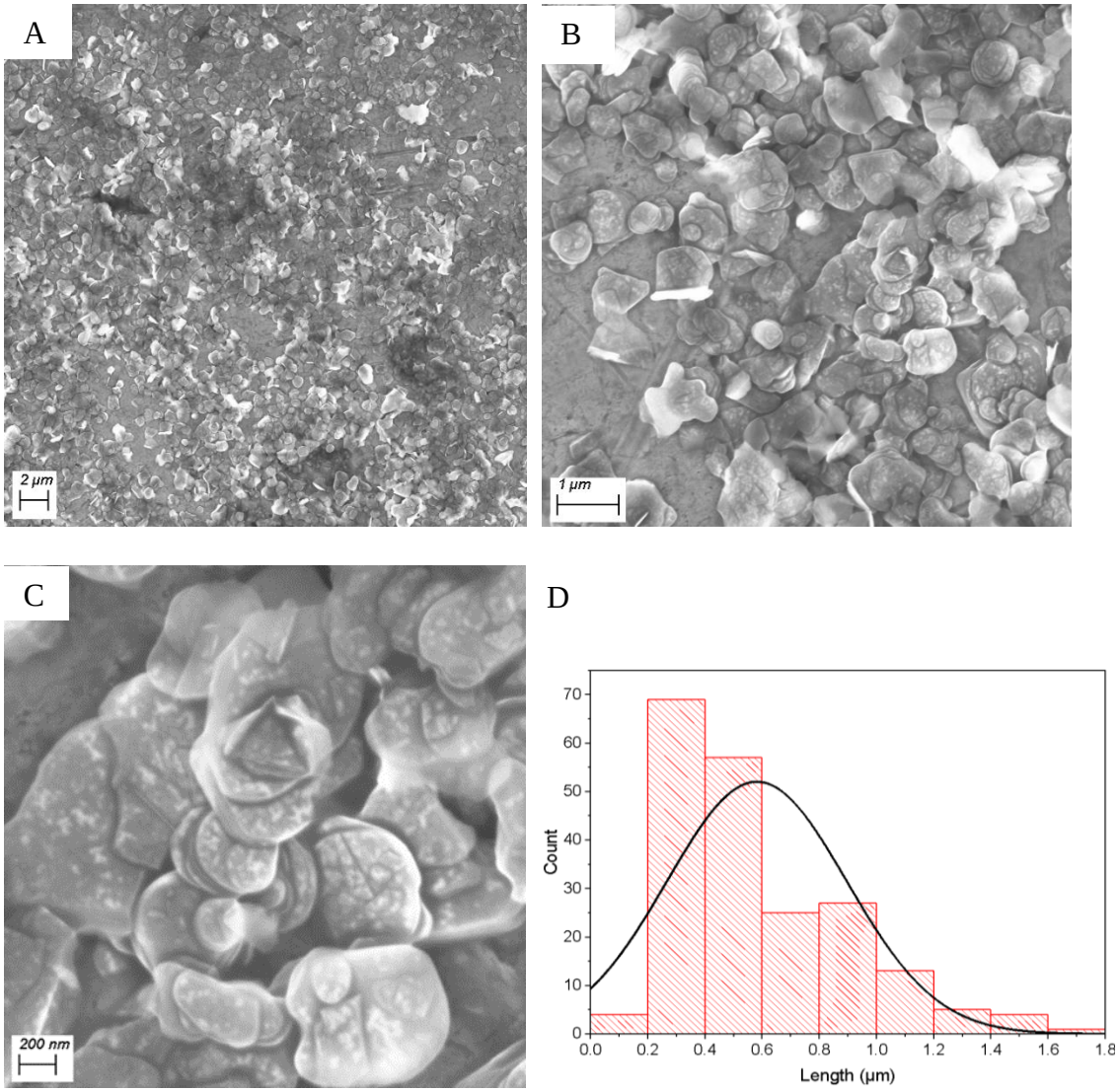

Figure 3.7: SEM of BN exfoliated in water (A, B and C) and size distribution of the nanosheets D). Voltage 5.00 kV, images taken using SE2.

TEM and STEM images of the three samples of 2D-BN have also been taken (figure 3.8 and figure 3.9). These images effectively confirm that exfoliation has taken place in each solvent case, with each sample showing minimal contrast, and strong BN flakes' transparency in TEM images, indicative of a thin exfoliated material. In addition, HRTEM analysis of the end of sheets confirmed that each flake comprised just a few monolayer sheets of BN. STEM confirmed this information and allowed the clear round edge structure of the sheets to be clearly seen. NMP and water demonstrated similar levels of exfoliation, while the IPA showed the lowest prevalence of exfoliated BN

sheets. This was observed through the difference in contrast between few layers to more layers stackedon top of each other.

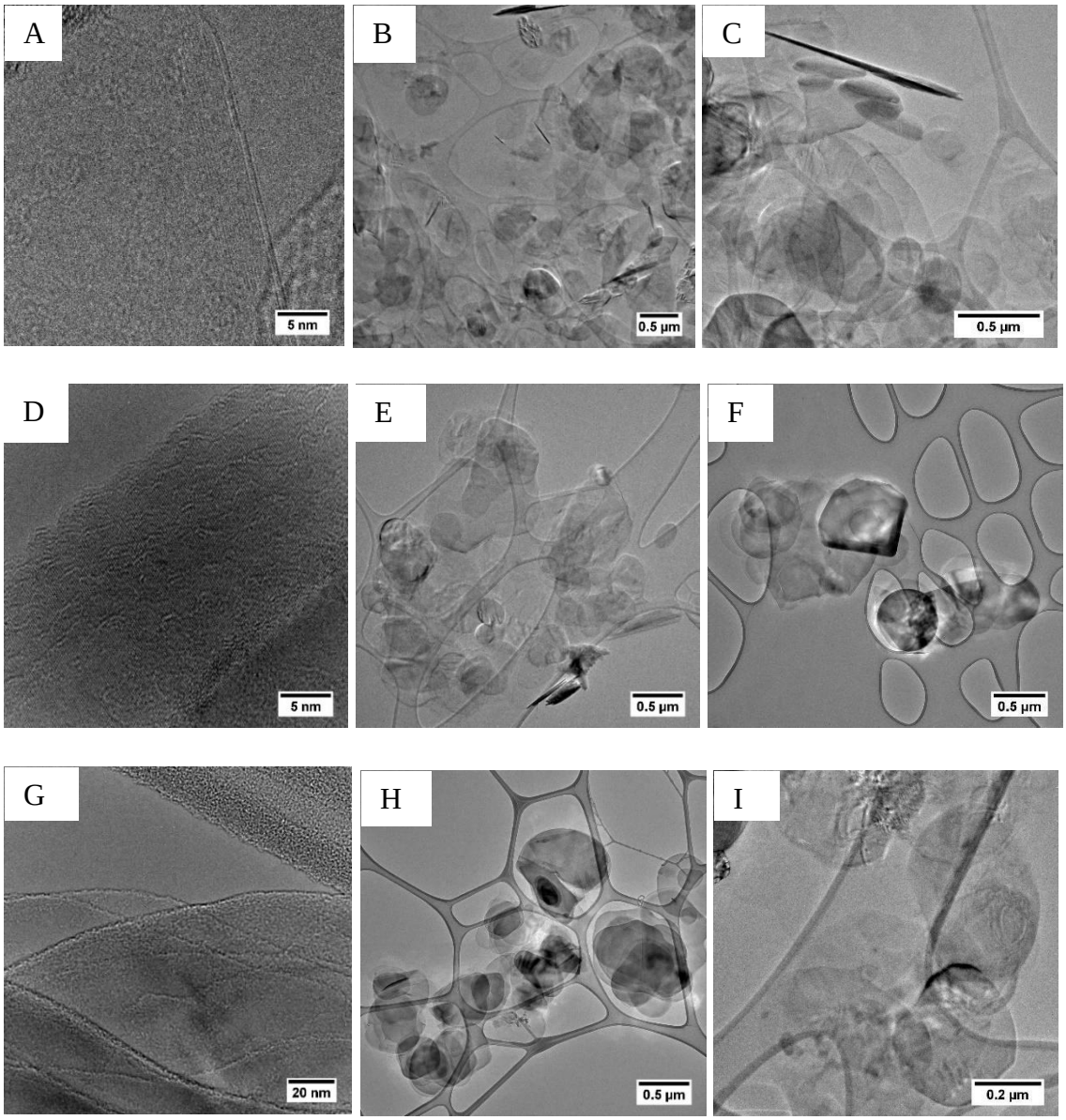

Figure 3.8: TEM images of 2D-BN produced in NMP (A-C), IPA (D-F) and water (G-I).

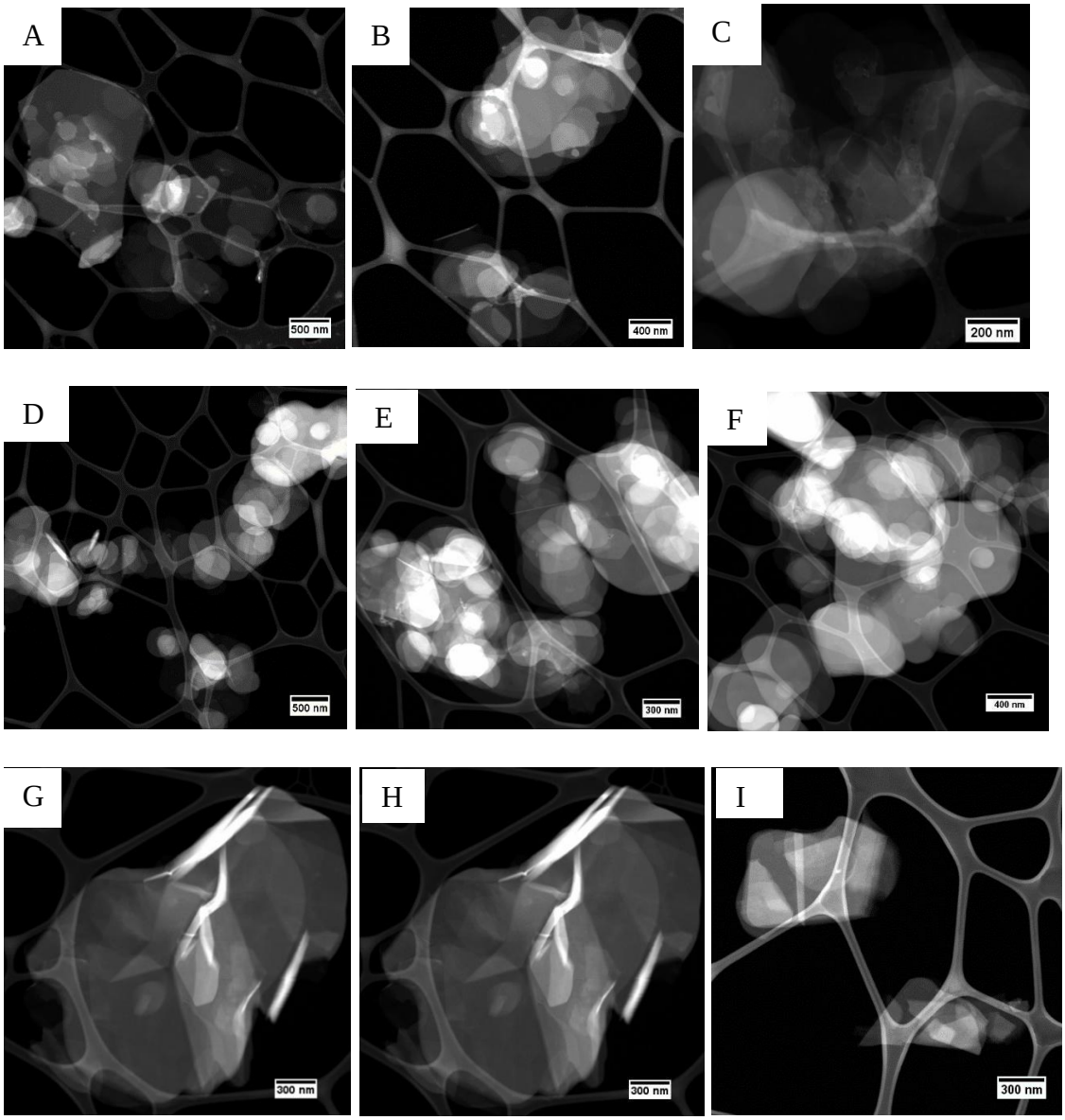

Figure 3.9: STEM images of 2D-BN produced in NMP (A-C), IPA(D-F) and water (G-I).

3.2.2. Membrane preparation

Following bulk BN exfoliation, the samples of 2D-BN, BN-Water, BN-NMP and BN-IPA were used to fabricate the corresponding membranes, named as BN-Water-Mem, BN-NMP-Mem and BN-IPA-Mem, respectively. The membranes have been prepared using vacuum filtration, as described in the methods section, and schematically presented in figure 3.10.

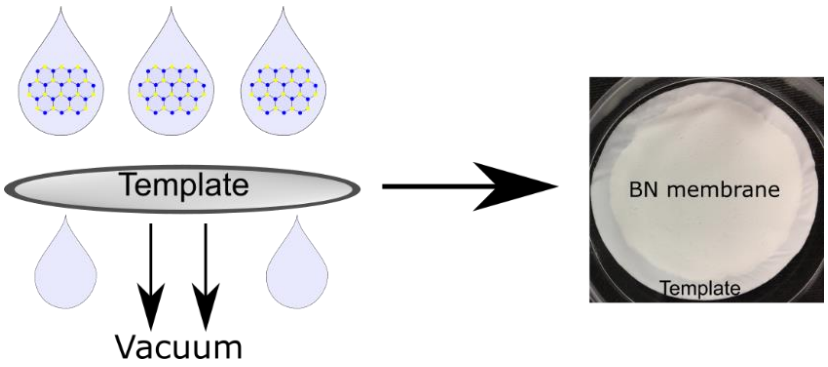

Figure 3.10: Schematic representation of BN membrane formation using vacuum filtration.

SEM images of each resulting membrane were taken and shown in figure 3.11-3.13. The top view of the three membranes (figure 3.11-3.13 A and B) made from BN exfoliated in 3 different solvents had very small differences between them. However, in the cross-section images of each membrane quite distinct variances could be observed. Firstly, BN-IPA-Mem had a slightly increased mean thickness of 174.40 ± 1.60 µm (table 3.1) than that found in the cases of BN-NMP-Mem and BN-Water-Mem, which showed similar thickness values of 148.90 ± 2.79 µm and 142.20 ± 3.55 µm, respectively. Another observation was of differing packing when comparing the cross-sections of the BN-NMP-Mem, BN-IPA-Mem and BN-Water-Mem (figure 3.11-3.13 C and D). BN-NMP-Mem and BN-IPA-Mem showed a more disorderly organization of the nanosheets, whereas BN-Water-Mem displayed more stacked, ordered and strongly-aligned horizontal sheets of BN, with evidence of a wave-like perturbation in the stacking. This unique morphology can be ascribed to the better exfoliation achieved using water.

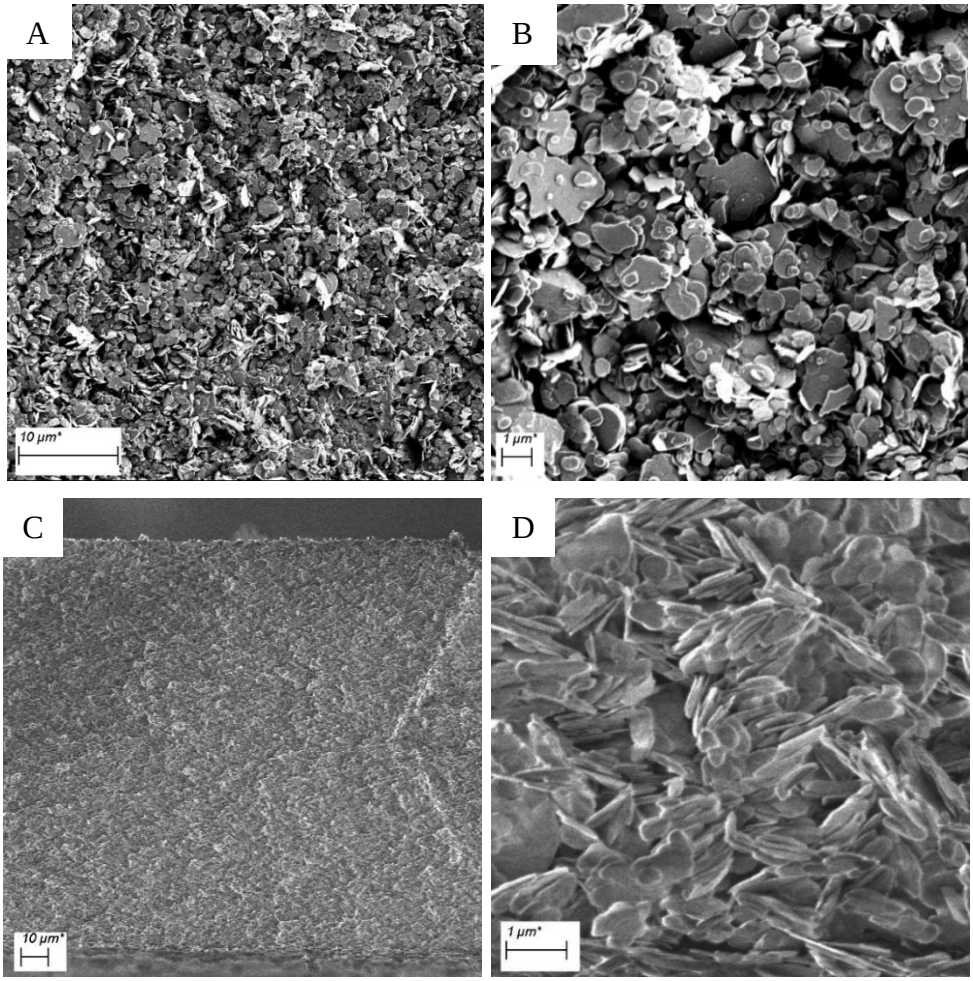

Figure 3.11: SEM of BN membrane made with exfoliated NMP (BN-NMP-Mem) top-view taken with SE2 (A and B) and cross-section taken with In-Lens (C and D). Voltage 5.00 kV.

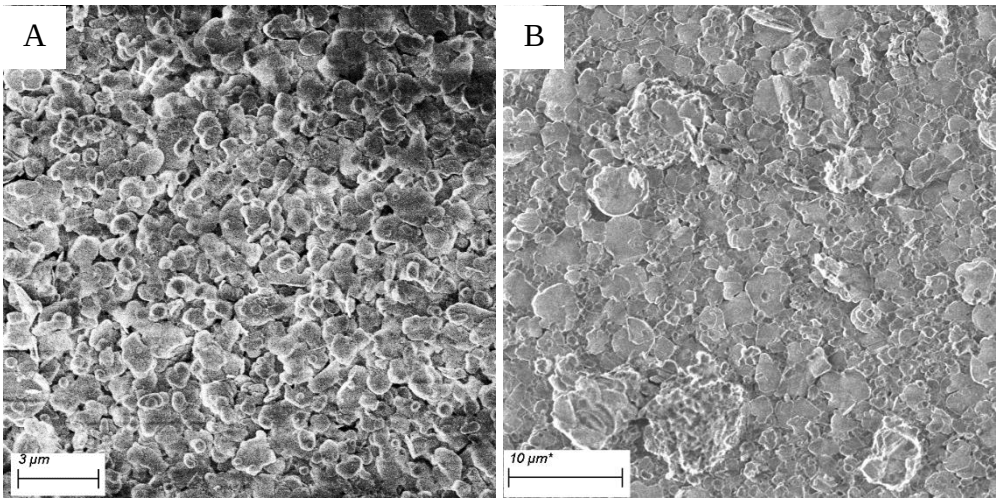

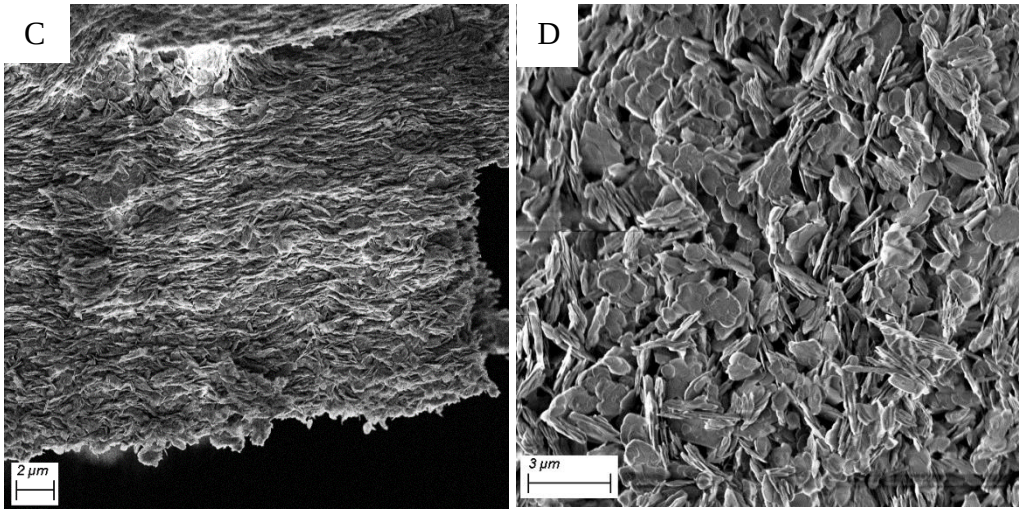

Figure 3.12: SEM of BN membrane made with exfoliated IPA (BN-IPA-Mem) top-view (A taken with SE2 and B taken with In-Lens) and cross-section taken with In-Lens (C and D). Voltage 5.00 kV.

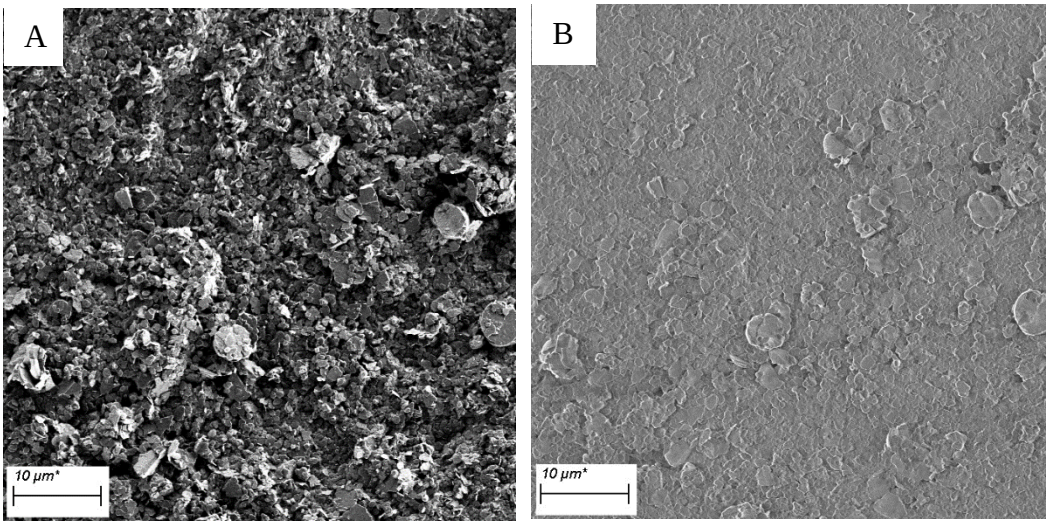

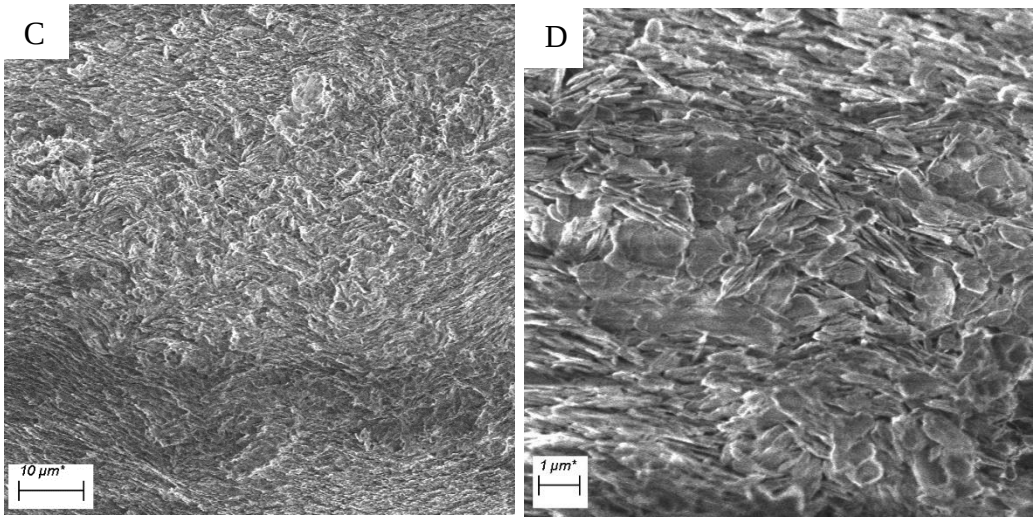

Figure 3.13: SEM of BN membrane made with exfoliated water (BN-water-Mem) top-view (A taken with SE2 and B taken with In-Lens) and cross-section taken with In-Lens (C and D). Voltage 5.00 kV.

3.2.3 Membrane testing

Three types of membranes, BN-NMP, BN-IPA, and BN-Water were produced. The thickness of the membranes and comparative dye-retention data is shown in table 3.1. The membranes were tested firstly for retention of a standard dye, Evans Blue[54], at a concentration of 15 µM and volume 20 ml, using UV-Vis spectroscopy for dye presence monitoring (figure 3.15). The BN-NMP and BN-IPA membranes showed similar retention values of 73±4% for NMP (figure 3.15 A) and 55± 12% for IPA (figure 3.15 B). By contrast, BN-water membrane showed far higher retention, with a mean value of 98± 1% (fgure 3.15 C). A close-up of the retention of the BN-water membranes is presented in figure 3.15 D, showing the low absorbance recorded. This result was highly reproducible, with very low standard deviation across the samples (table 3.2), relative to the NMP and IPA membranes. The results obtained in water compare favourably with best literature results, such as those reported for MoS_2 based membranes (89%)[54] and results obtained for membranes produced from BN, which were prepared and functionalized by ball milling with urea.[48] However, our membranes have the advantage that no functionalization is required and our retention values compare very favourably with similar dyes reported in literature such as Basic Yellow[12,19,23], Rhodamine B[55–59],

Congo Red[12,19,60] and Malachite Green[32], that showed high retentions between 90 and 99% .

Table 3.1: Retention and thickness of the membranes made from BN exfoliated, BN-NMP-Mem, BN-IPA-Mem and BN-Water-Mem

Sample	Retention (%)	Thickness (µm)
BN-NMP	73	149
BN-IPA	60	174
BN-Water	98	142

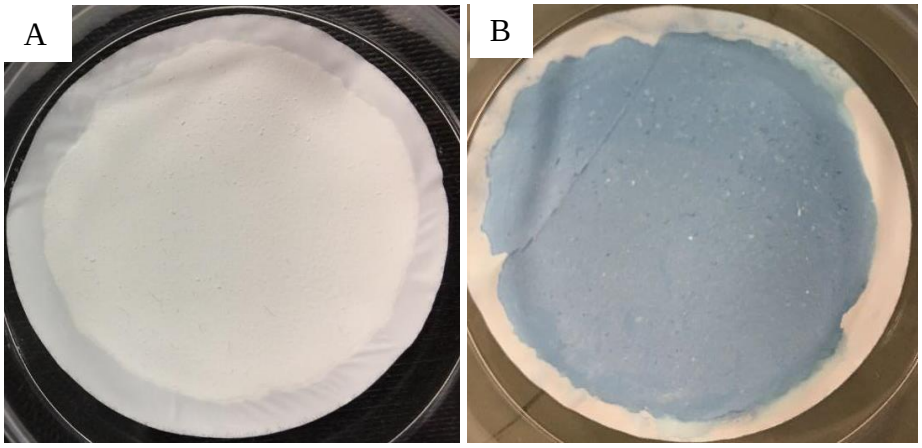

Figure 3.14: Picture of BN membrane A) before and B) after filtration with Evans Blue

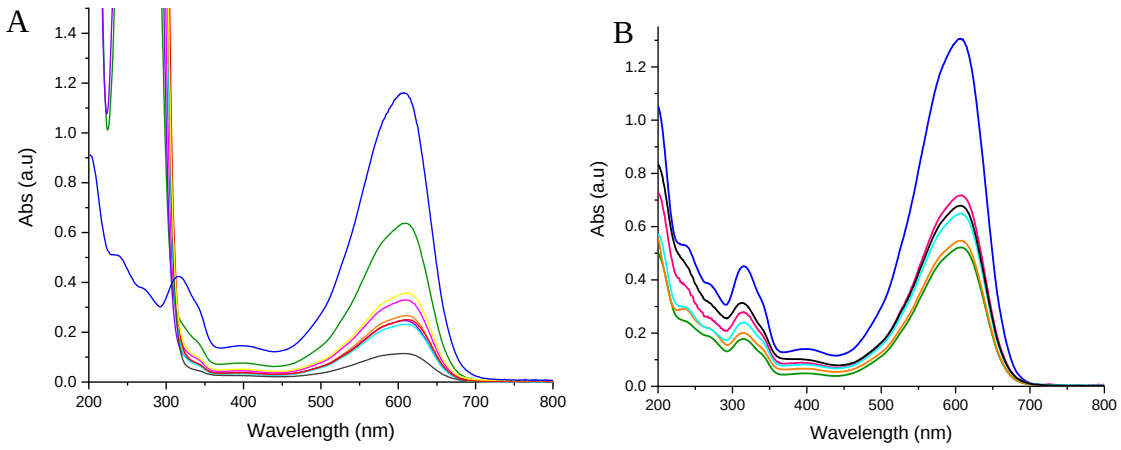

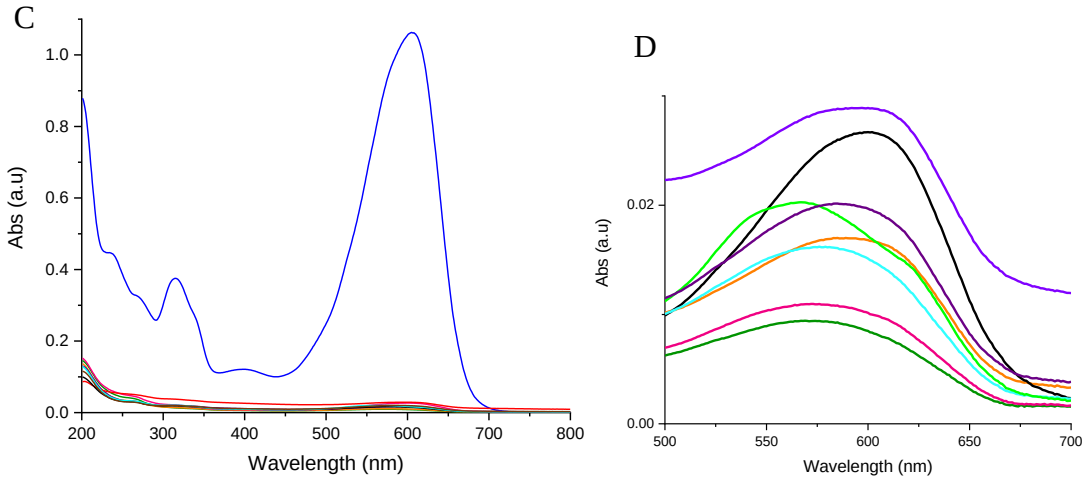

Figure 3.15: UV-Vis spectra of the retention of 20 mL of Evans Blue (15 µM) through BN membranes made from exfoliation in A) NMP, B) IPA, C) Millipore water and D) close up of the maximum absorbance peaks of the BN membranes from exfoliation in Millipore water.

Table 3.2: Statistics from the retention of the membranes obtained with the different solvents, NMP, IPA and Millipore water. The values were calculated using Origin 2018.

Solvent used	N total	Mean	Standard Deviation	Minimum	Median	Maximum
NMP	14	73	4	67	72	80
IPA	13	55	12	41	51	84
Millipore water	30	98	1	97	99	99

Due to the variations in retention values for membranes made from BN exfoliated in water, it was decided to further modify these membranes and investigate them in more details.

Wefirst added L-Phe molecule to further stabilize the BN flakes exfoliated in water. L-Phe was chosen because it has a benzene ring, which could interact with the BN structure. The solutions looked very similar to the pure BN exfoliated in water. The retention of the membranes was also tested with Evans Blue and the UV-Vis is shown in figure 3.16.

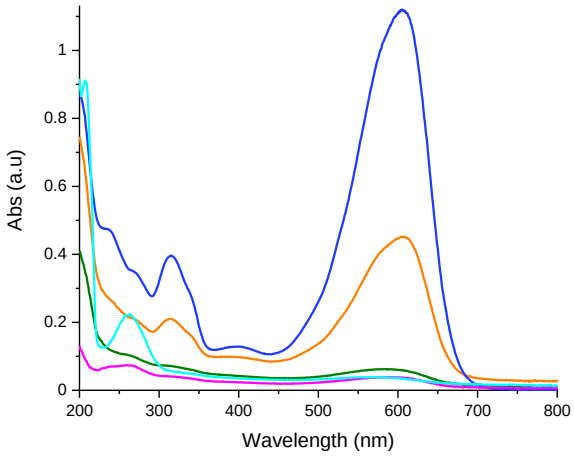

Figure 3.16: UV-Vis spectra of the retention of 20 mL of Evans Blue (15 µM) through membranes made from BN exfoliation in water with L-Phe.

Table 3.3: Retention of membranes made from BN exfoliated in water in the presence of L-Phe.

Membranes	% Retention
EB 15uM	0
BN+L-Phe	94
BN+L-Phe	60
BN+L-Phe	96
BN+L-Phe	97

The retention values obtained for these membranes were slightly lower than those observed for membranes made from the BN exfoliated in water (94-97% and up to 98%), with one of the membranes showing low retention at 59.7%. However, these retentions are still higher than those found for the membranes produced by exfoliating BN in NMP and IPA. This indicates that the addition of L-Phe doesn't improve the performance of the membranes made with BN exfoliated in water, reducing the retention by 2-4 %. Nevertheless, the membranes are still better at retaining the dye than the membranes formed from BN exfoliated in NMP and IPA.Therefore, the addition of L-Phe is not needed to improve the performance of the membranes.

Since there doesn't seem to be a clear link between the level of exfoliation of the nanosheets and the retention of dye, it was decided to study whether the BN exfoliation is needed or if even lower levels of exfoliation are sufficient to obtain the membranes

high retentions. For example NMP has similar levels of exfoliation to water, but the retention that was achieved by corresponding membranes was significantly lower (72% in the case of NMP vs 98% obtain by the BN-Water-Mem). Due to this, it was decided to test membranes obtained by dispersing bulk BN in water without any exfoliation, as well as BN sonicated for shorter periods of time, 3 and 4 hours respectively. Some top-view SEM images of the membranes produced without BN sonication and from BN samples with 3 hours sonication are presented in figure 3.17-3.18. Cross-section SEM images of the membranes made from BN after 3 hours of sonication are shown in figure 3.18 C and D.

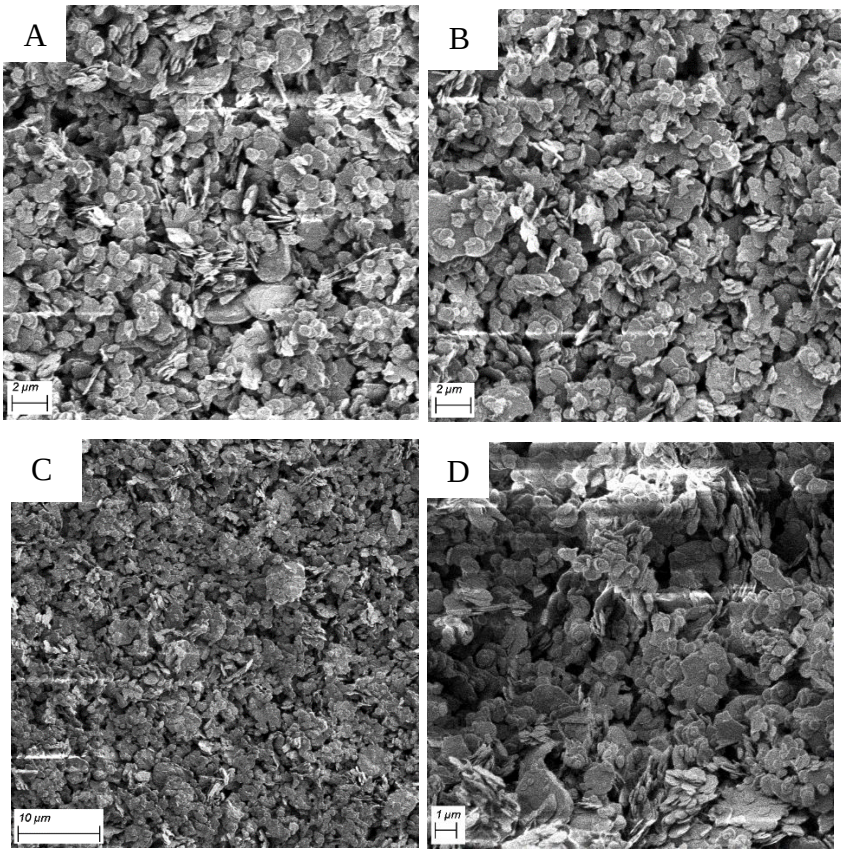

Figure 3.17: Top-View of BN membrane made without any sonication. Voltage 1.50 kV. Images taken with SE2.

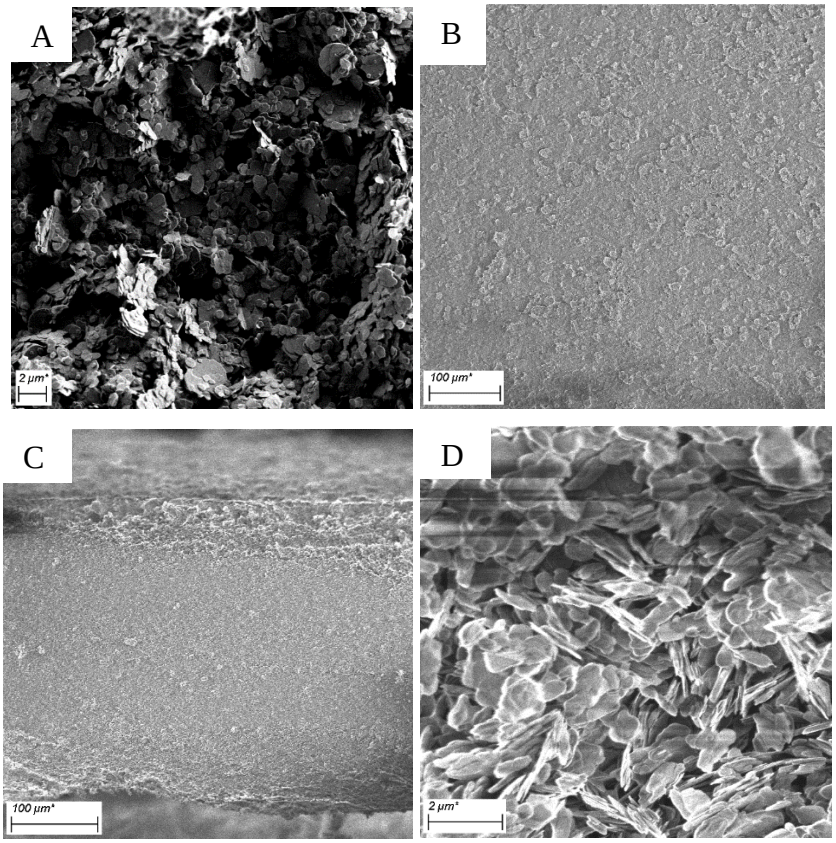

Figure 3.18: SEM images of top-view (A and B) and cros section (C and D) of membranes made from BN sonicated in water for 3 hours. Voltage 1.50 kV. Images taken using SE2 A) and In-Lens (B-D).

The top-view of the membanes made with BN dispersed in water with no sonication and BN sonicated in water for 3 hours looked very similar to those obtained with BN exfoliated in the other tested solvents. The membranes didn't look any different from the other membranes from the top. The cross-section of the mambrane made from BN sonicated for 3 hours looks very similar to the IPA membrane, with the nanosheets very disorganized throughout the membrane. This varies from the cross-section obtained from the water exfoliated BN membrane, where the nanosheets present an orderly formation. Moreover, the thickness of the membrane was calculated to be 269.70±30 µm, which was around 120 µm thicker than the BN-Water-Mem and BN-NMP-Mem and around 90 µm thicker than BN-IPA-Mem. This seems to indicate that lower levels of exfoliation forms thicker membranes. This also coincides with the previous membranes, where the BN-IPA-Mem showed to have the thicker profile and lower levels of exfoliation; whereas

the BN-Water-Mem and BN-NMP-Mem showed lower thickness as well as greater levels of exfoliation.

The membranes were then tested for Evans Blue retention, to compare with the previous results. UV-Vis spectra of permeates and stock solution are shown in figure 3.19.

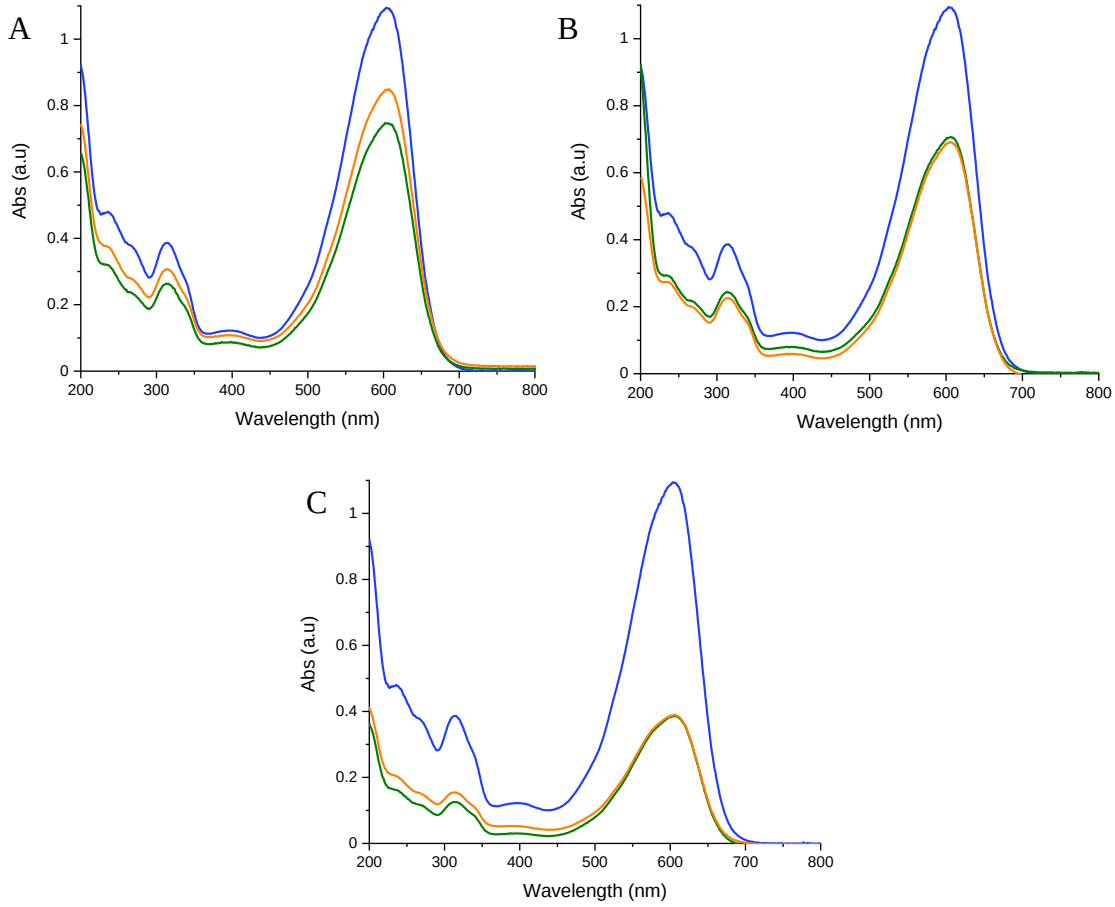

Figure 3.19: UV-Vis spectra of the retention of 20 mL of Evans Blue (15 µM) through BN membranes made from BN dispersed in water without any sonication A) and from BN sonicated for 3 hours B) and 4 hours C) in water respectively.

Table 3.4: Retentions of membranes made with dispersing BN in water and BN sonicated in water for 3 and 4 hours.

Membranes	% Retention
EB 15uM	0
Non-Sonication	32
Non-Sonication	22
3 hours	35
3 hours	37
4 hours	65
4 hours	64

Studying the testing results of these new membranes, a few trends could be observed. The first that could be noted is that the membranes made with BN dispersed in water with no sonication showed very low retention, around 22-32%, whereas the other two made from sonicated BN had higher retentions. However, the membranes, made with BN sonicated for 3 hours had only a slightly higher retentions. These retentions from the dispersed BN and BN sonicated for 3 hours are much lower than those obtained with the IPA, which was the lowest up until this point. The membrane made with BN sonicated for 4 hours, a higher retention was achieved (64-65%). This retention was in between the ones recorded for IPA (55%) and NMP (73%), indicating that the amount of time the BN is sonicated in water will increased the retention, with even a noticeable difference with one hour more of sonication. As the best results were still obtained with 24 hours exfoliation, it was decided to keep this time of sonication.

Therefore, due to the performance of the water-exfoliated BN-based membranes, a further investigation was carried out to determine the performance using two smaller dye molecules with different functionality, often utilised in retention studies: Methyl Orange and Methylene Blue. This is also necessary to test if the nanofiltration is effective for a wider range of possible molecules. The retention of these dyes (figure 3.20 A and C) showed values close to those obtained with Evans Blue. Methyl Orange showed a retention from 97-99±1%, with the retention obtained with the Methylene Blue being 99-100 ± 0.1%. As with the results of Evans Blue, the samples showed excellent reproducibility (table 3.5). The results obtained for Methylene Blue are higher or similar[32] than reported values in literature for BN (95% retention), as well as functionalized BN (98% retention) [61]. Methyl Orange is more often tested with other compounds[62,63], but it has been tested using functionalized BN with a negative charge, producing lower retentions than the values reported here[24].

From these results, we propose that BN retains the dyes via physisorption, with π-π interactions taking place between the BN rings and the benzene rings present in the dye structures[29,64]. This is supported by the results indicating all three dyes show strong retention by the membranes. In addition, no relationship is observed between the size of the dyes and the level of retention of the membranes.

Overall, these results present a strong case for applying water-exfoliated BN-based membranes in nanofiltration applications.

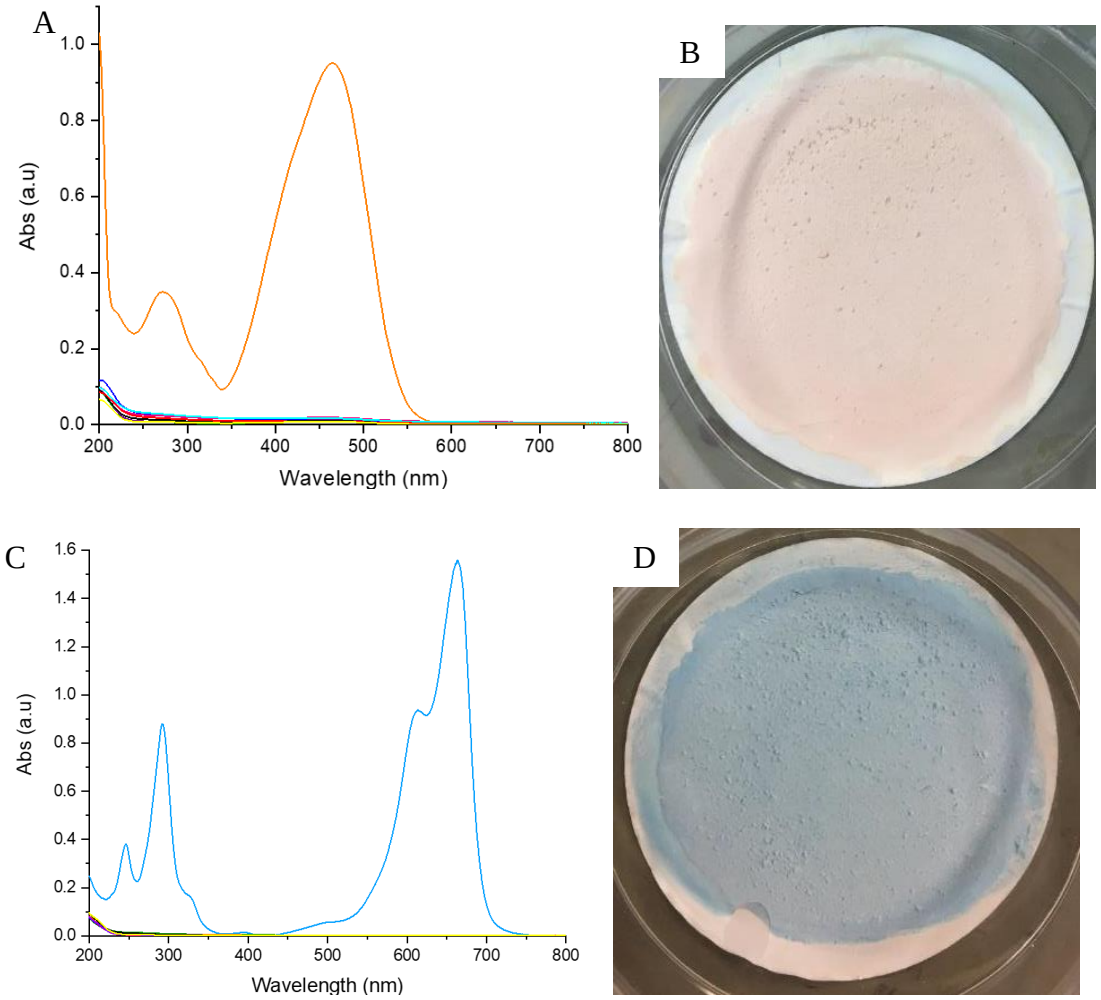

Figure 3.20: UV-Vis spectra monitoring the retention of 20 mL of A) Methyl Orange (50 µm) and C) Methylene Blue (27 µm) through BN membranes exfoliated in Millipore water. Images B) and D) show the membranes after retention test with Methyl Orange and Methylene Blue respectively.

Table 3.5: Statistics from the retention of the membranes obtained with Millipore water and tested with two dyes, Methyl Orange and Methylene Blue. The values were calculated using Origin 2018.

Dye tested	N total	Mean	Standard Deviation	Minimum	Median	Maximum
Methyl Orange	16	99	1	97	99	100
Methylene Blue	23	100	0.1	99	100	100

3.2.4 Comparison of solvents

Due to the differences observed between the three solvents, NMP and IPA (the solvents of choice for BN exfoliation) and water (the greener and non-toxic alternative), it was decided to carry out a more intensive comparison of the solvents performance. For this, Powder XRD, FT-IR, Raman, AFM, BET and mercury porosimetry were carried out and compared between the three samples.

Powder XRD (PXRD) results are presented figure 3.21 A and B showing the patterns typical for the boron nitride starting material *(P -3 m 1, trigonal, a=2.5100 Å c=6.6900 Å*), designated as "bulk" and the samples obtained from BN-NMP, BN-IPA and BN-water. All four samples match perfectly with the BN model pattern, showing the (002), (010), (011), (012), (004) and (-120) peaks with decreasing intensity from left to right. In addition, no impurities can be observed.

BN-NMP and BN-IPA samples show a lower crystallinity. Although peaks do become visually broader, they are not as remarkable as for the water-exfoliated sample. It has been suggested that this improved exfoliation in water is due to the sonication-assisted hydrolysis of the solvent, helping the separation and dispersion of the BN nanosheets.[47] That dispersion between films is observed by comparing different peak intensities. Taking Miller indices (001) such as the most intense (002) and comparing it with (hk0) peaks, such as (010) or (011), it can be seen that the relative intensity ($I_{(00l)}/I_{(hk0)}$) gets larger in BN samples after exfoliation. The related intensity of the (002) and (010) peaks gives a ratio (Ratio=$I_{(002)}/I_{(010)}$) of 1.26 for the bulk and 68.05 for the water exfoliated sample and might be due to the random orientated stacking of films after drying. This has been previously reported by Bhimanapati and colleagues[65]. Due to exfoliation and

later treatment, the layers stack on top of each other with a shifted angle along the c-axis, while there is a reduction of the intensity on the a- and b-axis lowering the intensity due to random orientation, the c-axis keeps the same. This effect of shifting along the vertical axis therefore might generate the improved filtration capabilities of the material.

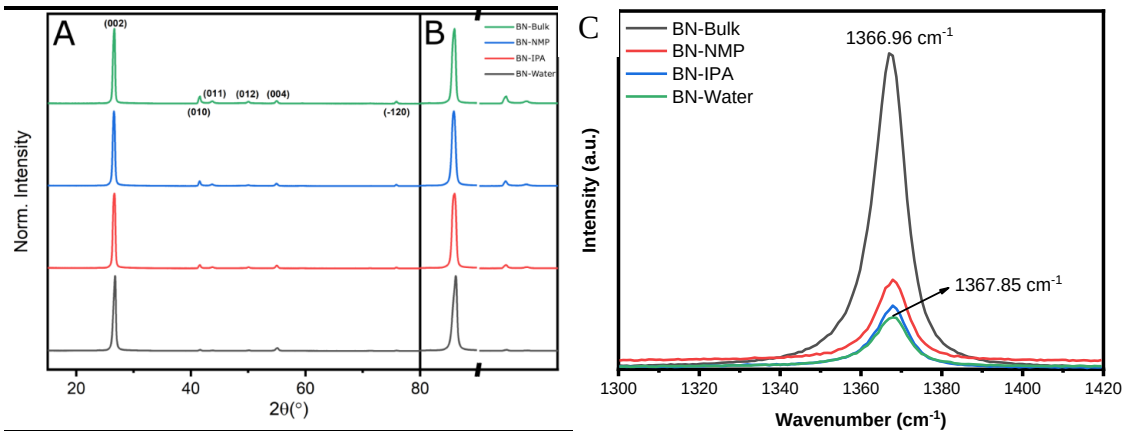

Figure 3.21: A) Normalized PXRD patterns of bulk-BN and exfoliated BN-NMP, BN-IPA and BN-Water. Miller indices are shown for the bulk material. B) Comparison of (002), (010) and (011). C) Raman spectra of h-BN in bulk form (black) and exfoliated BN-NMP (red), BN-IPA (blue) and BN-Water (green).

Raman spectra are shown in figure 3.21 C for the initial h-BN of the bulk material and the NMP, IPA and water exfoliated samples. The peaks shown correspond to the Raman E_{2g} peak, with a bibliographic value of 1366 cm^{-1} [66]. This shows a characteristic decrease in intensity from the pristine material to the water-exfoliated one of 77% (table 3.6). This is due to the reduction of layer-thickness in the structure and is corroborated by the peak shift ($\Delta\nu = 0.89$ cm^{-1}), with the red-shift of the peak reported to be due to the exfoliation of the multi-layered material. It can be explained by the slight shortening of the B-N bond as a result of the absence of interlayer interactions due to exfoliation.[52] In addition, there is a substantial increase of the FWHM of 0.68 cm^{-1}. This is attributed to a decrease of the overlapping of various peaks that form the characteristic peak due to a more heterogeneous orientation of the sheets that comprise the material. This Raman data reaches the same conclusion; that BN-Water shows a reduction in the homogeneous stacking of layers due to a more efficient exfoliation of BN, giving a reduction in thickness of the material.

Table 3.6: Main features of bulk and exfoliated BN in Raman.

Sample	Peak Shift (cm^{-1})	Intensity (a.u.)	FWHM (cm^{-1})
BN-Bulk	1366.96	32077.4	9.37
BN-NMP	1367.85	12502.7	9.48
BN-IPA	1367.85	8884.2	9.36
BN-Water	1367.85	7248.1	10.05

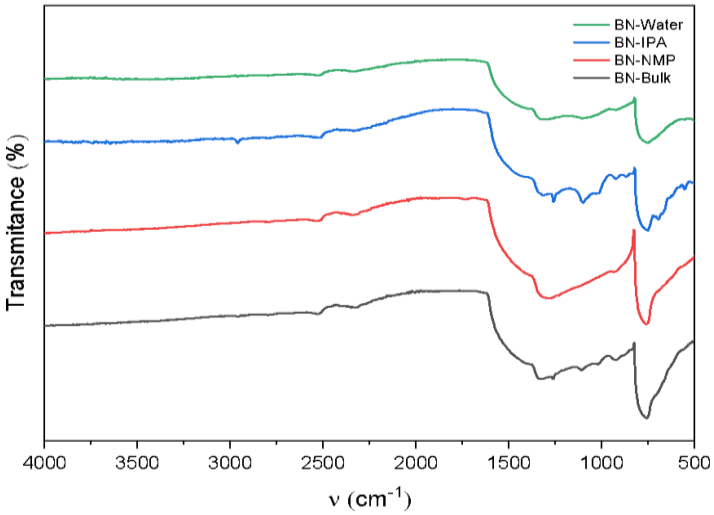

Figure 3.22: FTIR spectra of exfoliated BN, BN-NMP (blue), BN- IPA (red), BN-Water (black) and BN-Bulk

FTIR spectra (figure 3.22) show a broad band around 1370–1390 cm^{-1}, corresponding to B-N stretching and slightly narrower band around 800-820 cm^{-1} as a result of B–N bending[67], characteristic of BN. No major differences were observed between the samples exfoliated in the three solvents.

AFM images of single flakes of BN exfoliated in water, IPA and NMP are displayed in figure 3.23. The BN flake size ranges from 100's of nm up to µm, for water and NMP exfoliation. Only µm-size flakes were measured for exfoliation from IPA, as shown in figure 3.23 E-F. The flake size distribution corresponds to that measured from TEM data, presented in figures 3.8-3.9. The morphology of the flakes is different in water, IPA and NMP. As observed in AFM images shown in figure 3.23, water and NMP exfoliation produces flakes with characteristic steps and terraces. The line profiles, also displayed in figure 3.23, show that step height between terraces is 8-9 nm. This observation suggests that each BN flake exists within an oriented stack of BN layers. The flakes resulting from

exfoliation with IPA media dot no present such distinctive steps and terraces, as shown in figure 3.23 E and F. AFM images of single BN flakes reveal that while flake size is not significantly affected by a specific sonication media, the exfoliation with water or NMP could favour an oriented stacking of BN flakes. 3D AFM images of the nanosheets were also taken and are shown in figure 3.24.

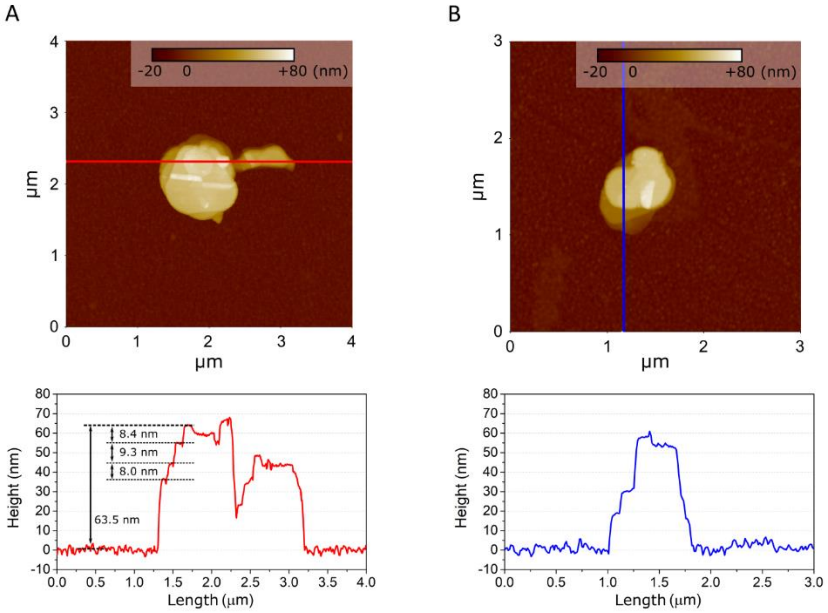

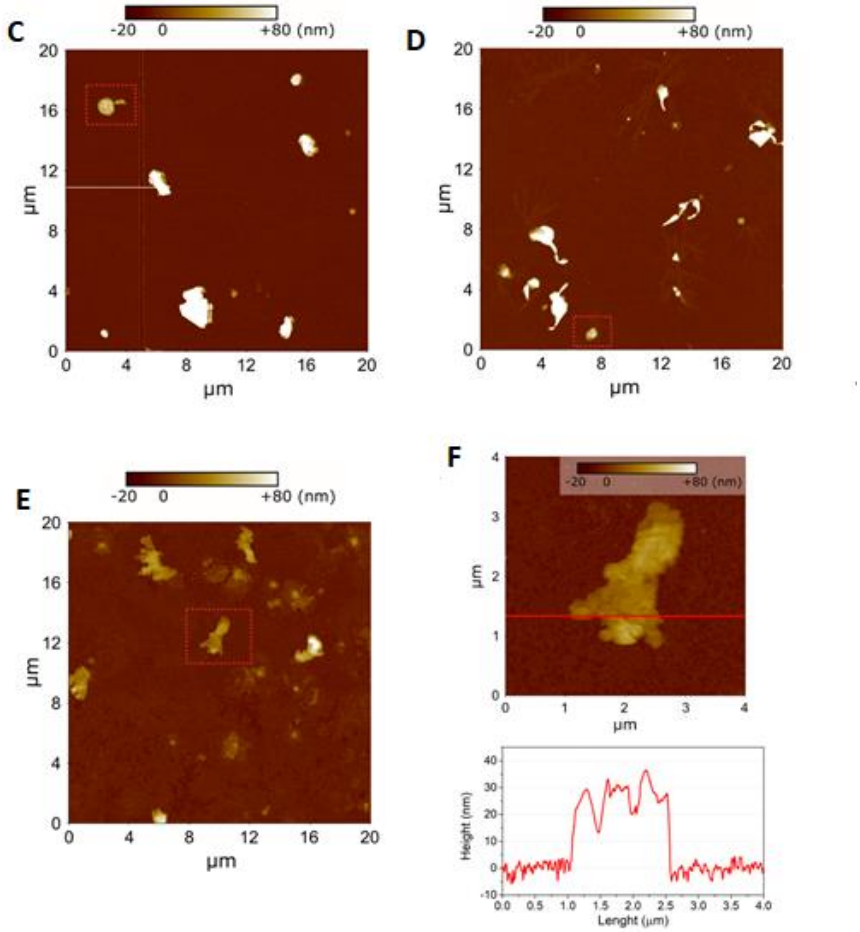

Figure 3.23: AFM images of single BN flakes obtained from A) water exfoliation, with corresponding line profile B) BN flakes from NMP exfoliation, with corresponding line profile. AFM images of dropcasted BN samples. C) BN-H_2O D) BN-NMP and E) BN-IPA, with red square indicating magnified area for higher resolution AFM, as displayed in images A), B) and F). Image F) AFM image of single flake of BN prepared using IPA and corresponding height profile.

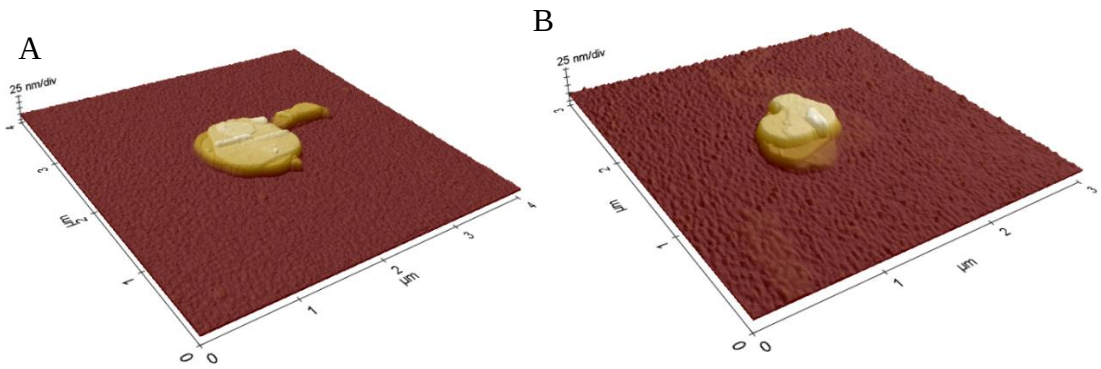

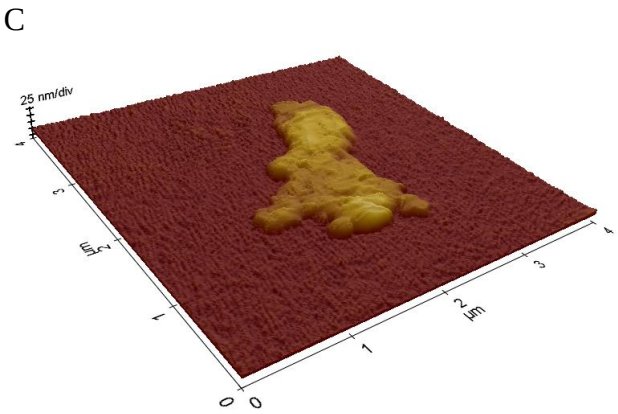

Figure 3.24: 3D AFM images of single BN flakes obtained from A) water exfoliation, B) NMP and C) IPA exfoliation (images taken using 3x magnification on Z axis).

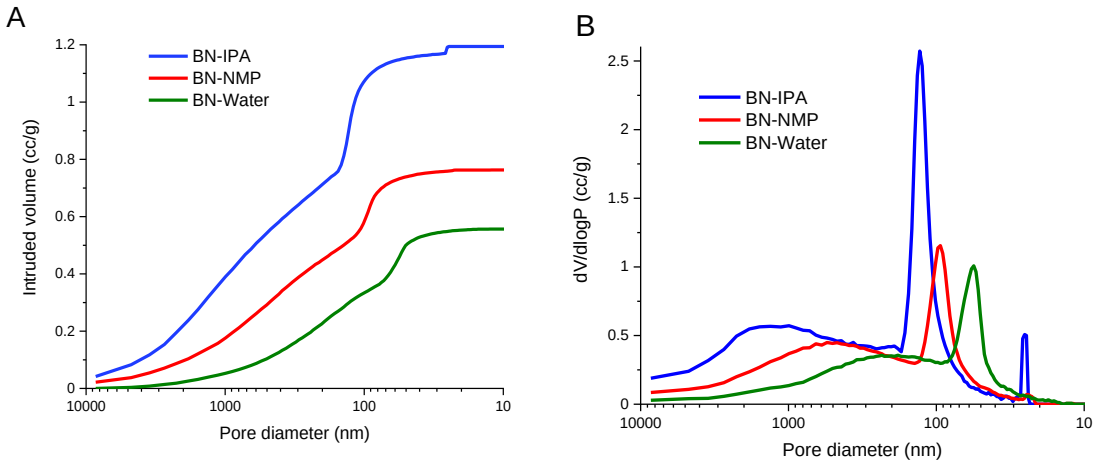

Figure. 3.25. Comparison of mercury intrusion characteristics of the BN membrane samples A) and B) comparison of mercury pore size distributions of the BN membrane samples.

Mercury porosimetry was carried out to investigate the porosity of the BN samples, in the approximate range 10 nm to 10 µm. Figure 3.25 A) shows the intrusion of mercury into the membrane samples as a function of pressure, with pressure being analogous to pore diameter. As pressure is increased, the largest pores fill first, followed by increasingly smaller ones. For the BN-IPA sample, a very gradual filling is observed initially, for pores <3 µm. A subsequent change in the slope of the curve corresponds to more rapid pore-filling. This continues until a sharp intrusion of mercury occurs (the

slope rises sharply) as pores of approx. 130 nm diameter are filled. The curve then begins to plateau, before a further minor uptake of mercury occurs, corresponding to 25 nm pores, after which the curve plateaus out as all pores are fully filled.

The curves obtained for the BN-NMP and BN-Water samples are of a similar shape to BN-IPA, but the intrusion profiles are shifted to the right, corresponding to smaller pore sizes. In terms of pore volume, the trend mimics that of the pore size, in so far as the BN-IPA sample has the largest pore volume (1.19 cm^3/g), compared to BN-NMP (0.76 cm^3/g), and BN-Water (0.56 cm^3/g). It is interesting to note that the pore volume of the BN-IPA sample is approximately double that of BN-Water – this implies that although the overall membrane morphologies have similarities (as evidenced by the similarity in *shape* of the intrusion curves) BN-water and, to a lesser extent, BN-NMP, comprise more compact morphologies, and have higher bulk densities, relative to BN-IPA.

It is useful also to consider the pore size distributions of the membranes, plotted as pore diameter vs. the change in intruded volume with respect to the log of change in pressure (dV/dlogP) as shown in figure 3.25B. When plotted this way, the pore size distributions can be evaluated in terms of sharpness, with sharp peaks corresponding to tight pore size distributions, and vice versa.
For BN-IPA, a broad peak is observed initially, indicative of pores in the approximate range 0.4 – 4 μm. Broad peaks are also observed for the BN-NMP and BN-Water samples; these peaks are shifted to the right, relative to BN-IPA, corresponding to smaller pore sizes. A clear trend exists, therefore, in terms of micrometer- and sub-micrometer sized pores being present and shifting to smaller sizes in the order: IPA $\rightarrow$ NMP $\rightarrow$ Water.

A second and more significant characteristic of figure 3.25 B, is the presence of sharp peaks in the sub-200 nm range. For BN-IPA, a major peak occurs at 130 nm. The sharpness of this peak is indicative of a high concentration of pores, all of which are of a similar size. Less prominent peaks are observed for BN-NMP and BN-Water, respectively, and it is noted that these peaks shift to smaller pore sizes. Also, worth noting is the presence of a minor, secondary peak for the BN-IPA sample, corresponding to pores of 25.3 nm diameter.

It is clear from the shape of the pore size distribution curves that the membranes studied here are derived from the same parent material, but it is also clear that each membrane has unique porous characteristics, depending on which solvent is used to conduct the membrane preparation.

BET analysis was carried out to further investigate the porous characteristics, specifically the surface area, pore diameter, and pore volume. The measured data is summarised in Table 3.7.

Table 3.7: Summary of BET surface area analysis data

Sample	Surface area (m^2/g)	BJH desorption pore diameter (nm)	BJH desorption pore volume (cm^3/g)
BN-IPA	20.1	28.8	0.055
BN-NMP	12.9	3.6	0.021
BN-Water	26.7	3.5	0.089

Taking the surface area data, we observe values of 20.1, 12.9, and 26.7 m^2/g, for BN-IPA, BN-NMP, and BN-Water, respectively. The largest surface area, for BN-Water can be attributed to the fact that this sample has a high concentration of 'small pores' (less than 80 nm in diameter), relative to the other two samples, as observed in figure 3.25 B above. BN-IPA has the largest pore size (130 nm) and, thus, might reasonably be expected to have the lowest surface area, but in fact it has a value intermediate between that of BN-Water and BN-IPA. This can be attributed to the secondary porosity peak observed at 25.3 nm, on the basis that this subset of mesopores generates sufficient surface area to elevate the surface area value of BN-IPA above that of BN-NMP. In the literature, there is an established relationship between surface area and pore size; as pore size decreases, surface area increases, and generally speaking, as pore volume increases, surface area increases[68]. It must be remembered that the BET surface area value applies to the sample as a whole, and includes all surfaces and macro-porosity, whereas the BJH pore diameter and pore volume values presented here are restricted to, and are representative of pores <30 nm only.

In terms of pore diameter, there is a clear distinction between the BN-IPA (28.8 nm), BN-NMP (3.6 nm) and BN-Water (3.5 nm) samples; the diameter of BN-IPA is of an order of magnitude greater. This is significant in the context of the porosimetry data,

where the BN-IPA sample was the only sample to yield a peak sub-30 nm, i.e. a peak falling within the BET measurement range. Clearly, the BN-IPA sample has a subset of mesopores, which are absent for the BN-NMP and BN-Water samples. It is further noted that the BJH mean pore diameter value of 28.8 nm determined for the BN-IPA sample is in good agreement with the value of 25.3 nm measured using mercury porosimety.

The BN-NMP sample has the lowest pore volume. At 0.021 cm^3/g, the pore volume is just under one third that of BN-IPA and less than a quarter that of BN-Water. This very low pore volume may be a contributing factor to BN-NMP's low surface area value, relative to BN-IPA and BN-Water. Clearly, however, the porous characteristics of these membrane samples are overwhelmingly dominated by macroporosity, as evidenced from both mercury porosimetry data and microscopic imaging.

Excellent agreement has been established between the membrane's physical porous properties and the corresponding morphologies, as imaged using electron microscopy. The SEM images (figures 3.5-3.7) demonstrate a clear hierarchy in terms of the packing factor, in the order IPA $\rightarrow$ NMP $\rightarrow$ Water, where BN-IPA could be described as 'loosely-packed,' and BN-Water as 'tightly-packed.' This morphological difference is most evident from images shown in figure 3.11-3.13, where BN-IPA displays obvious porosity (black regions in the image); whereas BN-Water could be perceived as non-porous (it appears grey, with low contrast across the image). Porosity can clearly be observed in the BN-IPA sample, with openings between the flakes on the order of 0.5 – 2 μm. A noticeable difference in feature size is also apparent, particularly between the BN-IPA and BN-Water samples, with BN-Water one exhibiting a much finer texture and more compact arrangement of the BN flakes.

The 'loosely-packed' BN-IPA morphology is depicted by mercury porosimetry in the form of a broad peak in the approximate range 0.4 – 4 μm as well as a high pore volume (1.19 cm^3/g). The physical porous characteristics of BN-NMP and BN-Water are also consistent with the imaged morphologies observed in figure 3.5-3.7. The sample with the least obvious porosity when viewed under SEM is BN-Water. However, the true porous nature of this sample was successfully captured by a combination of mercury porosimetry and BET analysis. The high surface area (26.7 m^2/g) is attributed to the network of 50

nm pores, coupled with a reasonably high pore volume (0.56 cm^3/g). These properties are characteristic of a low bulk density, nanoporous material having a predominantly open, interconnected porous network.

3.2.5 Discussion of Trends

The outstanding performance of the membranes made from water-exfoliated BN can be explained by a number of factors. Firstly, as seen in Raman, TEM and STEM, water exfoliates BN very efficiently, producing a high amount of monolayered BN nanosheets. This is due to the partial hydroxylation of the BN caused by sonication in water. This sonication-assisted hydrolysis of the solvent, has been suggested to help the separation and dispersion of the BN nanosheets, which would effectively, improve the level of exfoliation of the sample [47]. Secondly, the packing of the water-exfoliated BN nanosheets in the produced membranes is distinct when compared to the cases of NMP or IPA as solvents, which we postulate is playing a key role in the performance of the membrane. This distinct packing is also confirmed by XRD, where it can be seen as a difference in the intensity of the peak[65]. This packing must affect the formation of the pores or channels where the water and dye are passing through the membrane, resulting in this better performance uplift. This is supported by data obtained from mercury porosimetry, in which the BN-water membranes present smaller pores than BN-NMP, whereas BN-IPA presents two subsets of pores, one being the biggest of the three cases. This small size of the pores therefore could be the reason why BN-water is more efficient in retaining the tested dye molecules. Moreover, data obtained from BET shows a higher surface area and high pore volume for the BN-water sample, which results in a more dense and compact membrane. This combination provides better retention performance of the membrane, showing the characteristics of a nanoporous material with a predominantly open and interconnected porous network.

Therefore, overall the performance of the BN-Water-Mem samples is linked to both the excellent exfoliation level obtained by exfoliating BN in water, the high surface area and small pore size, as well as the packing of the nanosheets from the solvent, a combination that yields the best retention performance. Denser and more orderly packing of membranes have been reported to increase their performance[69,70], which agrees with what we found in this study.

3.3 Conclusions

BN was successfully exfoliated in three solvents: NMP, IPA and water. Out of the three, NMP and water showed the best results of BN exfoliation. Nevertheless, the BN suspensions in all three solvents were used to produce membranes, with some differences observed between them. The membranes from water-exfoliated BN showed a different packing pattern than the other two, but had a similar thickness to the membranes made from the NMP-exfoliated BN.

The membranes produced from the BN suspensions in three solvents were tested for the retention of Evans Blue dye. The retention of the membranes made from water-exfoliated BN was superior, with values of 98-99%. The membranes made NMP-exfoliated BN showed the next best values, with the lowest retention being obtained with the IPA-exfoliated BN membranes. These differences are due to a combination of the level of exfoliation, differences in surface area, pore size and specific packing of the nanosheets in the membrane.

The exfoliation of BN in water was further studied. L-Phe ligand was added to the exfoliated mixture to try to see its effects on the stability of the solution, but not major differences were observed in the performance of the membranes. The effect of the time of exfoliation was also tested, which showed that longer sonication times improved the retention of the membranes, with 24 hours sonication time yielding the best results.

Another two, smaller dyes, Methyl Orange and Methylene Blue were also tested with the membranes made from water-exfoliated BN. The results obtained were outstanding, with high retention (98-100%) observed for both dyes as well. This indicates that BN exfoliated in water is an excellent building block for membranes for water treatment, as it can remove big molecules and smaller dye molecules very efficiently.

Bibliography

1 A. Pakdel, Y. Bando and D. Golberg, *Chem. Soc. Rev.*, 2014, **43**, 934–959.

2 D. Golberg, Y. Bando, Y. Huang, T. Terao, M. Mitome, C. Tang and C. Zhi, *ACS Nano*, 2010, **4**, 2979–2993.

3 X. Wan, T. Wan, C. Cao, C. Tang, Y. Xue, Y. Yan, Z. Li, Z. Ye and X. Peng, *Chem. Eng. J.*, 2021, **423**, 130309.

4 X. Gao, Y. Yao and X. Meng, *Mater. Sci. Semicond. Process.*, 2020, **120**, 105256.

5 M. Corso, W. Auwärter, M. Muntwiler, A. Tamai, T. Greber and J. Osterwalder, *Science (80-.).*, 2004, **303**, 217–220.

6 L. Ci, L. Song, C. Jin, D. Jariwala, D. Wu, Y. Li, A. Srivastava, Z. F. Wang, K. Storr, L. Balicas, F. Liu and P. M. Ajayan, *Nat. Mater.*, 2010, **9**, 430.

7 Y. Lin, T. V Williams and J. W. Connell, *J. Phys. Chem. Lett.*, 2010, **1**, 277–283.

8 W. Luo, Y. Wang, E. Hitz, Y. Lin, B. Yang and L. Hu, *Adv. Funct. Mater.*, 2017, **27**, 1701450.

9 S. Qin, D. Liu, G. Wang, D. Portehault, C. J. Garvey, Y. Gogotsi, W. Lei and Y. Chen, *J. Am. Chem. Soc.*, 2017, **139**, 6314–6320.

10 C. Chen, J. Wang, D. Liu, C. Yang, Y. Liu, R. S. Ruoff and W. Lei, *Nat. Commun.*, , DOI:10.1038/s41467-018-04294-6.

11 S. Abdikheibari, W. Lei, L. F. Dumée, N. Milne and K. Baskaran, *J. Mater. Chem. A*, 2018, **6**, 12066–12081.

12 W. Lei, D. Portehault, D. Liu, S. Qin and Y. Chen, *Nat. Commun.*, 2013, **4**, 1777.

13 D. Liu, W. Lei, S. Qin, K. D. Klika and Y. Chen, *Phys. Chem. Chem. Phys.*, 2016, **18**, 84–88.

14 D. Liu, L. He, W. Lei, K. D. Klika, L. Kong and Y. Chen, *Adv. Mater. Interfaces*, 2015, **2**, 1500228.

15 M. Weber, B. Koonkaew, S. Balme, I. Utke, F. Picaud, I. Iatsunskyi, E. Coy, P. Miele and M. Bechelany, *ACS Appl. Mater. Interfaces*, 2017, **9**, 16669–16678.

16 W. Lei, V. N. Mochalin, D. Liu, S. Qin, Y. Gogotsi and Y. Chen, *Nat. Commun.*, 2015, **6**, 8849.

17 Q. Weng, B. Wang, X. Wang, N. Hanagata, X. Li, D. Liu, X. Wang, X. Jiang, Y. Bando and D. Golberg, *ACS Nano*, 2014, **8**, 6123–6130.

18 Z. Rafiei-Sarmazdeh, S. H. Jafari, S. J. Ahmadi and S. M. Zahedi-Dizaji, *J. Mater. Sci.*, 2016, **51**, 3162–3169.

19 D. Liu, W. Lei, S. Qin and Y. Chen, *Sci. Rep.*, 2014, **4**, 4453.

20 X. Zhang, G. Lian, S. Zhang, D. Cui and Q. Wang, *CrystEngComm*, 2012, **14**, 4670–4676.

21 D. Portehault, C. Giordano, C. Gervais, I. Senkovska, S. Kaskel, C. Sanchez and M. Antonietti, *Adv. Funct. Mater.*, 2010, **20**, 1827–1833.

22 J. Li, H. Jia, J. Lin, H. Luo, Z. Liu, X. Xu, Y. Huang, P. Jin, J. Zhang, S. Abbas and C. Tang, *RSC Adv.*, 2015, **5**, 71537–71543.

23 G. Lian, X. Zhang, S. Zhang, D. Liu, D. Cui and Q. Wang, *Energy Environ. Sci.*, 2012, **5**, 7072–7080.

24 J. Li, Y. Huang, Z. Liu, J. Zhang, X. Liu, H. Luo, Y. Ma, X. Xu, Y. Lu, J. Lin, J. Zou and C. Tang, *J. Mater. Chem. A*, 2015, **3**, 8185–8193.

25 L. Xue, B. Lu, Z.-S. Wu, C. Ge, P. Wang, R. Zhang and X.-D. Zhang, *Chem. Eng. J.*, 2014, **243**, 494–499.

26 G. Lian, X. Zhang, H. Si, J. Wang, D. Cui and Q. Wang, *ACS Appl. Mater. Interfaces*, 2013, **5**, 12773–12778.

27 J. Li, X. Xiao, X. Xu, J. Lin, Y. Huang, Y. Xue, P. Jin, J. Zou and C. Tang, *Sci. Rep.*, 2013, **3**, 1–7.

28 J. Li, J. Lin, X. Xu, X. Zhang, Y. Xue, J. Mi, Z. Mo, Y. Fan, L. Hu, X. Yang, J. Zhang, F. Meng, S. Yuan and C. Tang, *Nanotechnology*, 2013, **24**, 155603.

29 Y. Xue, P. Dai, X. Jiang, X. Wang, C. Zhang, D. Tang, Q. Weng, X. Wang, A.

Pakdel, C. Tang, Y. Bando and D. Golberg, *J. Mater. Chem. A*, 2016, **4**, 1469–1478.

30 R. Chen, C. Zhi, H. Yang, Y. Bando, Z. Zhang, N. Sugiur and D. Golberg, *J. Colloid Interface Sci.*, 2011, **359**, 261–268.

31 J. Li, P. Jin and C. Tang, *RSC Adv.*, 2014, **4**, 14815–14821.

32 F. Liu, J. Yu, X. Ji and M. Qian, *ACS Appl. Mater. Interfaces*, 2015, **7**, 1824–1832.

33 G. Yang, D. Zhang, C. Wang, H. Liu, L. Qu and H. Li, *Nanomaterials*, , DOI:10.3390/nano9030386.

34 H. Tao, Y. Zhang, Y. Gao, Z. Sun, C. Yan and J. Texter, *Phys. Chem. Chem. Phys.*, 2017, **19**, 921–960.

35 J. N. Coleman, M. Lotya, A. O'Neill, S. D. Bergin, P. J. King, U. Khan, K. Young, A. Gaucher, S. De, R. J. Smith, I. V. Shvets, S. K. Arora, G. Stanton, H. Y. Kim, K. Lee, G. T. Kim, G. S. Duesberg, T. Hallam, J. J. Boland, J. J. Wang, J. F. Donegan, J. C. Grunlan, G. Moriarty, A. Shmeliov, R. J. Nicholls, J. M. Perkins, E. M. Grieveson, K. Theuwissen, D. W. McComb, P. D. Nellist and V. Nicolosi, *Science (80-.).*, 2011, **331**, 568–571.

36 R. J. Smith, P. J. King, M. Lotya, C. Wirtz, U. Khan, S. De, A. O'Neill, G. S. Duesberg, J. C. Grunlan, G. Moriarty, J. Chen, J. Wang, A. I. Minett, V. Nicolosi and J. N. Coleman, *Adv. Mater.*, 2011, **23**, 3944–3948.

37 G. Cunningham, M. Lotya, C. S. Cucinotta, S. Sanvito, S. D. Bergin, R. Menzel, M. S. P. Shaffer and J. N. Coleman, *ACS Nano*, 2012, **6**, 3468–3480.

38 T. K. Mukhopadhyay and A. Datta, *J. Phys. Chem. C*, 2017, **121**, 811–822.

39 T. K. Mukhopadhyay and A. Datta, *J. Phys. Chem. C*, 2017, **121**, 811–822.

40 J. N. Coleman, *Adv. Funct. Mater.*, 2009, **19**, 3680–3695.

41 C. Zhi, Y. Bando, C. Tang, H. Kuwahara and D. Golberg, *Adv. Mater.*, 2009, **21**, 2889–2893.

42 G. Lian, X. Zhang, M. Tan, S. Zhang, D. Cui and Q. Wang, *J. Mater. Chem.*, 2011, **21**, 9201–9207.

43 G. Lian, X. Zhang, M. Tan, S. Zhang, D. Cui and Q. Wang, *J. Mater. Chem.*, 2011, **21**, 9201–9207.

44 X. Chen, J. F. Dobson and C. L. Raston, *Chem. Commun.*, 2012, **48**, 3703–3705.

45 C. Zhi, Y. Bando, C. Tang, H. Kuwahara and D. Golberg, *Adv. Mater.*, 2009, **21**, 2889–2893.

46 J. Taha-Tijerina, T. N. Narayanan, G. Gao, M. Rohde, D. A. Tsentalovich, M. Pasquali and P. M. Ajayan, *ACS Nano*, 2012, **6**, 1214–1220.

47 Y. Lin, T. V Williams, T.-B. Xu, W. Cao, H. E. Elsayed-Ali and J. W. Connell, *J. Phys. Chem. C*, 2011, **115**, 2679–2685.

48 C. Chen, J. Wang, D. Liu, C. Yang, Y. Liu, R. S. Ruoff and W. Lei, *Nat. Commun.*, 2018, **9**, 1902.

49 M. Fan, J. D. Jimenez, S. N. Shirodkar, J. Wu, S. Chen, L. Song, M. M. Royko, J. Zhang, H. Guo, J. Cui, K. Zuo, W. Wang, C. Zhang, F. Yuan, R. Vajtai, J. Qian, J. Yang, B. I. Yakobson, J. M. Tour, J. Lauterbach, D. Sun and P. M. Ajayan, *ACS Catal.*, 2019, **9**, 10077–10086.

50 D. Gonzalez Ortiz, C. Pochat-Bohatier, J. Cambedouzou, M. Bechelany and P. Miele, *Nanomaterials*, 2018, **8**, 1–12.

51 P. Ma and J. T. Spencer, *J. Mater. Sci.*, 2015, **50**, 313–323.

52 T. Sainsbury, A. Satti, P. May, Z. Wang, I. McGovern, Y. K. Gun'ko and J. Coleman, *J. Am. Chem. Soc.*, 2012, **134**, 18758–18771.

53 A. S. Nazarov, V. N. Demin, E. D. Grayfer, A. I. Bulavchenko, A. T. Arymbaeva, H.-J. Shin, J.-Y. Choi and V. E. Fedorov, *Chem. – An Asian J.*, 2012, **7**, 554–560.

54 L. Sun, H. Huang and X. Peng, *Chem. Commun.*, 2013, **49**, 10718–10720.

55 Q. Li, T. Yang, Q. Yang, F. Wang, K.-C. Chou and X. Hou, *Ceram. Int.*, 2016, **42**, 8754–8762.

56 Y. Chao, M. Liu, J. Pang, P. Wu, Y. Jin, X. Li, J. Luo, J. Xiong, H. Li and W. Zhu, *Ceram. Int.*, 2019, **45**, 18838–18843.

57 X. Wang, Y. Yang, G. Jiang, Z. Yuan and S. Yuan, *Diam. Relat. Mater.*, 2018, **81**, 89–95.

58 K. Maiti, T. D. Thanh, K. Sharma, D. Hui, N. H. Kim and J. H. Lee, *Compos. Part B Eng.*, 2017, **123**, 45–54.

59 J. Lin, L. Xu, Y. Huang, J. Li, W. Wang, C. Feng, Z. Liu, X. Xu, J. Zou and C. Tang, *RSC Adv.*, 2016, **6**, 1253–1259.

60 Z. Liu, Y. Fang, H. Jia, C. Wang, Q. Song, L. Li, J. Lin, Y. Huang, C. Yu and C. Tang, *Sci. Rep.*, 2018, **8**, 1104.

61 A. Hafeez, Z. A. Karim, A. F. Ismail, A. Samavati, K. A. M. Said and S. Selambakkannu, *J. Memb. Sci.*, 2020, **612**, 118473.

62 Y. Jiang, B. Liu, J. Xu, K. Pan, H. Hou, J. Hu and J. Yang, *Carbohydr. Polym.*, 2018, **182**, 106–114.

63 K. El Hassani, B. H. Beakou, D. Kalnina, E. Oukani and A. Anouar, *Appl. Clay Sci.*, 2017, **140**, 124–131.

64 T. Chen, M. Li and J. Liu, *Cryst. Growth Des.*, 2018, **18**, 2765–2783.

65 G. R. Bhimanapati, D. Kozuch and J. A. Robinson, *Nanoscale*, 2014, **6**, 11671–11675.

66 E. S. Tarleton, J. P. Robinson, C. R. Millington, A. Nijmeijer and M. L. Taylor, *J. Memb. Sci.*, 2006, **278**, 318–327.

67 D. S. Muratov, D. V Kuznetsov, I. A. Il'inykh, I. N. Burmistrov and I. N. Mazov, *Compos. Sci. Technol.*, 2015, **111**, 40–43.

68 R. C. Aran Raffertya, Trevor Woodsb, Alex Conwayc, Yurii Gun'koa, James Kennedyd, Martin Schwentenweine, *Ceram. Mod. Technol.*, 2019, **1**, 145–151.

69 C.-H. Tsou, Q.-F. An, S.-C. Lo, M. De Guzman, W.-S. Hung, C.-C. Hu, K.-R. Lee and J.-Y. Lai, *J. Memb. Sci.*, 2015, **477**, 93–100.

70 Z. Wu, L. Gao, J. Wang, F. Zhao, L. Fan, D. Hua, S. Japip, J. Xiao, X. Zhang, S.-F. Zhou and G. Zhan, *J. Memb. Sci.*, 2020, **601**, 117948.

Chapter 4. Oxidised BN (BNOx) based membranes

4.1 Introduction

4.1.1 Oxidation of BN

BN is very stable, both chemically and thermally, which can pose a problem with its further functionalisation, as harsh chemical reactions might be needed. Due to the similar characteristics of BN and graphene, the oxidation (GO) of BN as an analogue to graphene oxide has been tried. The main problem is the resistance of BN to oxidation due to its high thermal resistance[1], which means that the chemistry used with GO doesn't work for BN. However, the introduction of oxygen in the BN structure is still under investigation [2,3].

One of the option to change the properties of h-BN, is to do an elemental doping. Some theoretical studies have estimated that oxygen might be able to alter the properties of h-BN when acting as a dopant[3]. Oxygen, once inserted into the BN lattice, could possibly decrease h-BN bandgap, making the material more conductive[3–6], regulate molecular interactions[3,7,8] and cause some strong spontaneous magnetization[3–5]. Some recent experimental works have supported these theoretical simulations[3,9–11]. There are several reports on the effects that introducing oxygen has on the h-BN structure. The signature peak of h-BN in Raman has been stated to broaden due to the oxidation of the material[3,12], indicating a possible change in the crystal domain size, amorphization or disordering[3,12]. The improvement of the production of BNNs has been reported, due to the oxidation of h-BN[3,13]. However, how the oxygen doping affects the exfoliation of h-BN is still unclear. Furthermore, the addition of oxygen atoms could cause a distortion to the structure of the h-BN sample[3,11].

When it comes down to experimental work, BNNS functionalized with hydroxyl groups (OH-BNNs) can be obtained using several different methods. Some of these methods include heating bulk h-BN in air[1,2], treating BN in powder with a hot solution of H_2SO_4/$KMnO_4$[2,14] or functionalization by oxygen radicals, followed by hydrolytic defunctionalisation[2,15]. The surface energy of the BNNs, as well as their solubility in various solvents, could be changed as a result of the introduction of these OH groups[2]. Hydroxyl groups, as they are very common in nature, can interact with different types of

organic and inorganic materials. Thus, BNNs intrinsic properties can be taken advantage of for the better by inserting OH groups to the structure[2].

One of the most effective and straightforward ways of introducing oxygen and OH groups into h-BN is via heating under air[3]. Treating h-BN with high temperatures (800-1000 °C) in air environment is capable of introducing oxygen to the structure of the 2D material. This introduction of oxygen displaces preferentially the nitrogen atoms, forming covalent bonds with the boron atoms[3].

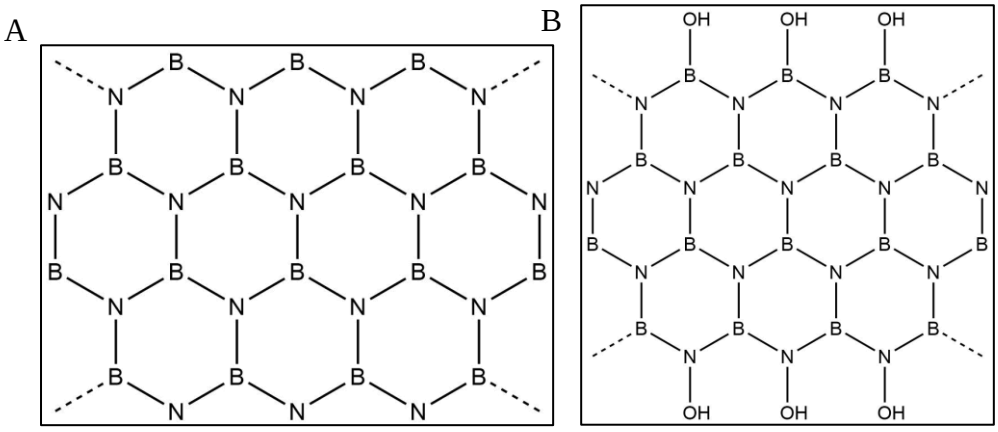

Figure 4.1: Comparison of a) BN and b) oxidised BN structure.

As a result of these hydroxyl groups due to the oxidation of BN, the BNOx is more reactive than its parent material, which could allow further functionalisation of the material.

4.1.2 Functionalisation with carbohydrates

Boric acid, $B(OH)_3$is capable of reacting with molecules containing hydroxyl-groups, like carbohydrates through esterification[16]. Partial esterification produces monoesters, which are rapidly hydrolysed to the original compounds in aqueous solutions[16]. These types of esters can be used as protective groups or chiral auxiliary agents in specific asymmetric synthesis[17]. Boronic acid can also form cyclic esters with carbohydrates through complexation[18]. Boronic acid forms five or six membered cyclic esters by covalently bonding with 1,2- or 1,3-diols, but in non-aqueous or basic solutions[19]. The selectivity of monoboronic acids and saccharides has already been studied[19].

Previously BNNS have been simultaneously functionalized and exfoliated using sugars[20], by assisted mechanochemical exfoliation. Sucrose crystals are bio-renewable, cheap, noncorrosive, and easy to recycle. The reaction between the sucrose and the BN happens as a result of the grafting of the sugar powder with the thin h-BN when they come in close contact[20]. Another way to functionalise BNOx is through the use of glutaraldehyde. Glutaraldehyde is used as a linker between the hydroxyl groups of BN and the sugars, like glucose[21].

The addition of sugars could change the intrinsic properties of the material, like increasing the hydrophilicity[21] or it's used for separation compounds through the action of the sugars. Furthermore, the functionalization of BN with carbohydrates could allow the possibility of cross-linking of the BN nanosheets forming the membrane, increasing the strength of the membrane produced.

4.1.3 Aims of this chapter

The main aim of this project was to produce new membranes by functionalisation of BN. For doing, the first thing was to introduce hydroxyl groups to the structure by oxidising the bulk BN. Once this was achieved, the membranes needed to be tested to make sure that the oxidation was not affecting the performance. The introduction of the OH groups could be used to further functionalise the membranes by incorporating sugars. The sugars could be used for achieving enantiomeric separation, as there is an increased demand for enantiomeric pure solutions. Furthermore, the use of sugars as functionalising agents could allow the possibility of separating sugars, in particular, mono- from di- and polysaccharides.

4.2 Results and discussion

4.2.1 BN oxidation and exfoliation

BN was oxidised by heat treatment at 1000 °C for 30 min under air in a tubular furnace, which allowed the formation of OH groups on the BN nanosheets, most likely in the edges of the BNNs as it has been previously reported by Andriani *et al*[3]. The BNOx product was initially characterised by XRD (figure 4.2).

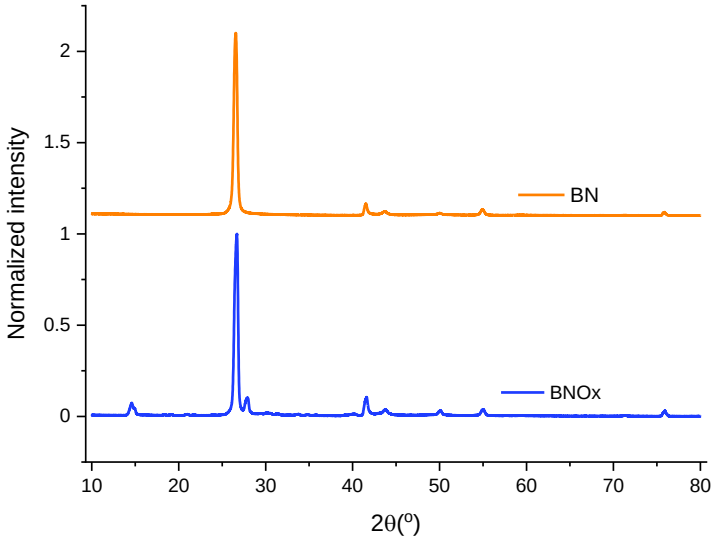

Figure 4.2: XRD patterns of BNOx (blue) and BN (orange).

The XRD pattern showed the characteristic peaks corresponding to BN, showing high crystallinity. In addition, we can observe a peak at 27.7° (010) corresponding to $B(OH)_3$[3,22], which seems to be indicating the presence of oxidation taking place. Furthermore, FTIR was also carried out for the BNOx and compared to the one for normal BN (figure 4.3).

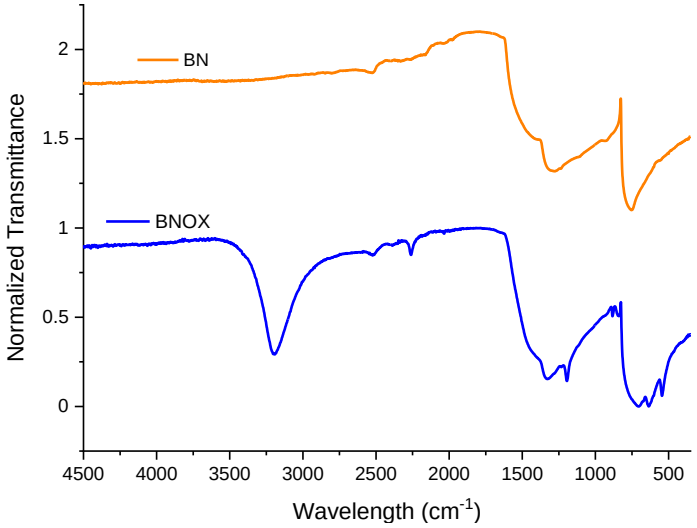

Fig. 4.3: FTIR spectra of BN (orange) and BNOx (blue).

FTIR spectra of both BN and BNOx show the peaks corresponding to B-N bending, around 769 cm^{-1} and B-N stretching at 1344 cm^{-1}, characteristic of BN[3]. In BNOx, there's

a second peak, due to the splitting of the 1344 cm^{-1} peak, at around 1190 cm^{-1}, that can be attributed to the B-O bonds[23]. In addition, there's a peak emerging at round 3200 cm^{-1} area corresponding to the B-OH stretching vibrations[3]. There is a peak at 883 cm^{-1} due to B-O stretching vibrations and at 636 cm^{-1} attributed to B-O bending vibrations[3]. These peaks are proof of the successful oxidizing of BN via heating.

TGA curve of bulk h-BN was also recorded (from 25°C to 900°C) to simulate the process happening in the furnace (figure 4.4). The TGA was only recorded to 900°C due to the limit of the machine, as the high temperature had to be hold for 30 min, which could have broken the thermocouple of the TGA.

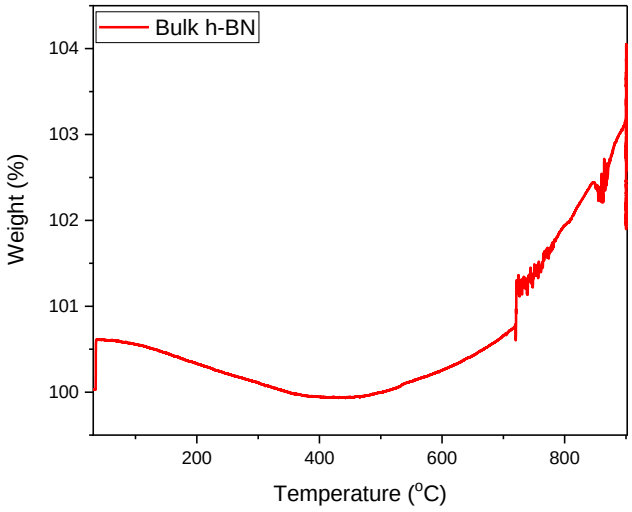

Figure 4.4: TGA curve of bulk h-BN to monitor the oxidation.

The TGA shows an increased in the weight of the sample of around 2-3%. This increment in weight starts happening around 700°C and continues to increase with the rise of temperature, until it stabilises with the holding of the temperature at 900°C. This increase of the weight would correspond to the addition of the OH groups to the edges of the sheets, most likely[3]. As it has been reported in literature, the increase in temperature results in a higher number of OH groups[3], which corresponds to the increment in weight that is observed in the TGA curve.

After the heat treatment of the BN in order to produce BNOx, it was observed that in some occasions, the product can be produced in two forms. Part of the BNOx would appear as a powder, similar to BN, while the rest will form "rocks" that were hard and

difficult to break (figure 4.5). The powder appeared at the top of the sample, whereas the rocks were found toward the bottom and sides of the vessel, mixed in with the powder.

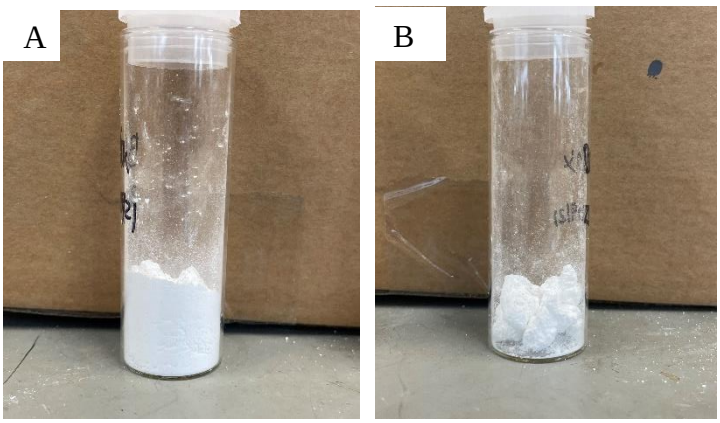

Figure 4.5: BNOx out of the furnace as a) powder and b) “rocks”.

These different morphologhies could be due to a difference in the product obtained, so an analysis of both samples has been performed. The “rocks” were hammered in order to obtain a powder to analyze. PXRD was carried out and patterns have been compared (figure 4.6).

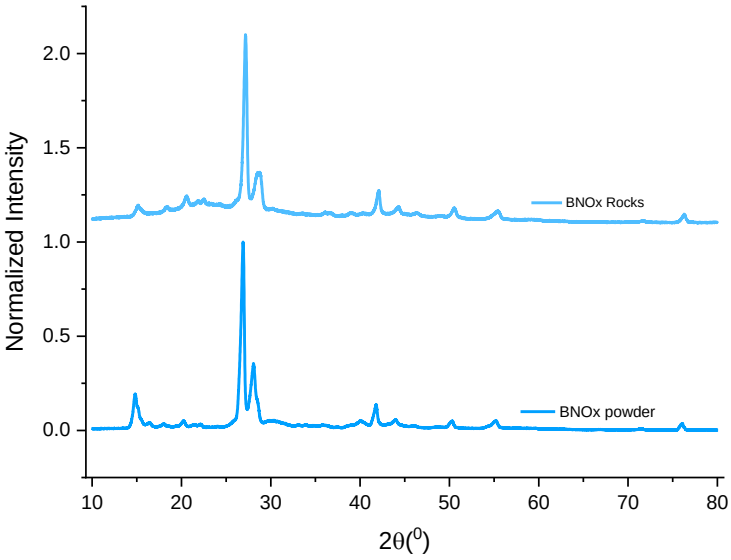

Figure 4.6: PXRD patterns of BNOx powder and BNOx rocks.

The XRD pattern of the two samples doesn’t show any major differences between the two compounds, which indicates that the two have the same crystalline structure. The

peaks appearing correspond to the BN and H_3BO_3, which corresponds to the samples of BNOx where only powder is present. FTIR of the two samples was also recorded and compared (figure 4.7)

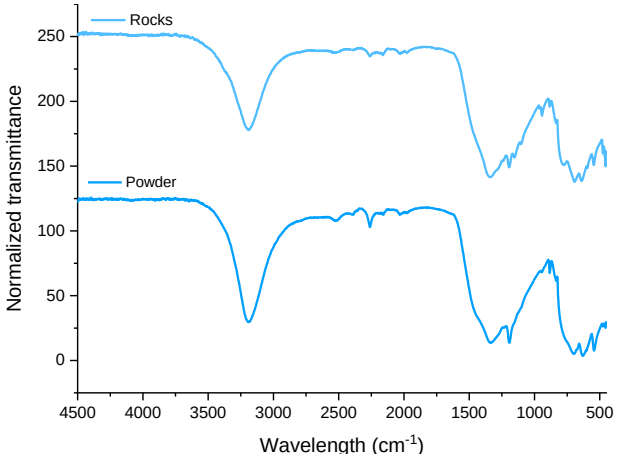

Figure 4.7: FTIR of BNOx powder and BNOx rocks.

FTIR of the two samples (powder and rocks) did not reveal any major changes between the two. Overall, the peaks that could be identified due to the presence of BN and partially oxidised BN were present (as described in figure 4.2). There were more peaks appearing in the case of the rocks in the areas of H_3BO_3, B-N and NH_2 and NH bonds, which could indicate differences in the vibration of the bonds. This could be associated to the different morphology, while the compound remains the same form, partially oxidised BN. This has been reported previously by Andriani et al[3], where they noted the sample heated at 1000 °C was the hardest and had to be ground for following handling. This would be very similar to the formation of the rocks in this case, where the rocks are formed most likely due to agglomeration of the powder in the furnace as a result of different heating (sides and bottom vs top of the sample). Hydrogen bonds can be formed in layered materials with hydroxyl groups, like graphene oxide[24] or clays[25]. High temperature treatment, as it has been done here, results in samples rich in hydroxyl groups, which could form hydrogen bonds. These strong hydrogen bonding may facilitate the clustering of BNOx, forming these rocks[3].

BNOx was then sonicated for 24 hours in Millipore water to obtain the exfoliated material, as this solvent was the one that gave the best performance membranes after the exfoliation. It was noted that when using the BNOx as rocks, even though they are quite

hard and difficult to break, this sample was completely dispersed in water after exfoliation. Therefore, the powder and rocks were both used. UV-Vis of the BNOx solution was taken and compared with bulk BN and exfoliated BN (figure 4.8).

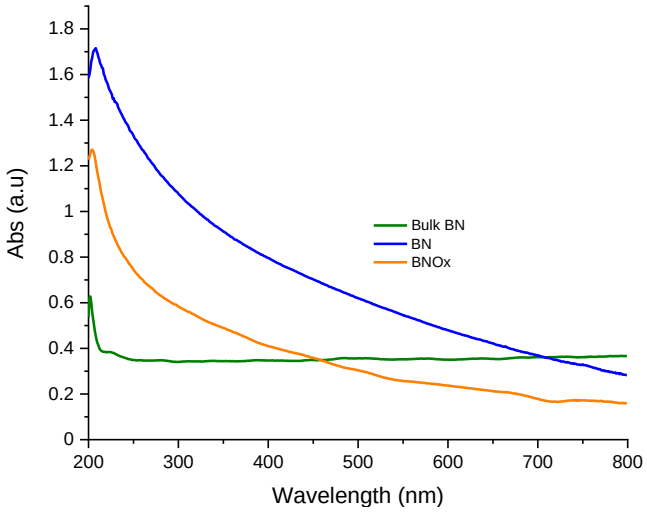

Figure 4.8: UV-Vis spectra of bulk BN (green), exfoliated BN (blue) and exfoliated BNOx (orange).

UV-Vis spectra of BNOx didn't show differences with that of the exfoliated BN, displaying the same shape. The difference in the absorbance is likely due to a different concentration. Both samples are easily differentiated from bulk BN disperse in water.

XRD and FTIR of the exfoliated BNOx were also carried out to check whether the exfoliation has an effect on the oxidation/hydroxylation of the BN.

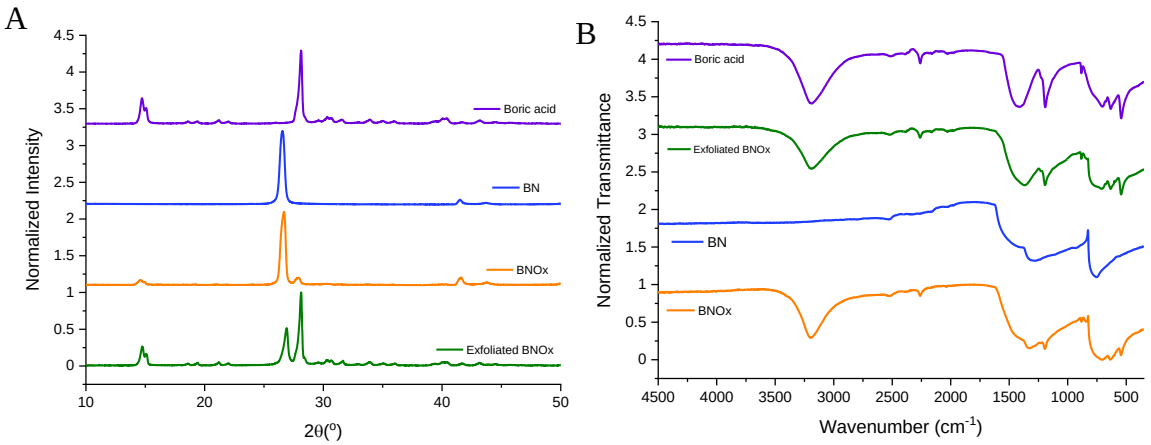

Figure 4.9: A) XRD patterns and B) FTIR spectra of BN, BNOX and exfoliated BNOx

The XRD pattern of the exfoliated BNOx samples shows the peaks corresponding to the oxidation/hydroxylation more prominent than in the case of BNOx. The peaks for $B(OH)_3$ are more intense than the BN peaks, which indicates that there's a higher proportion of the oxidation after the exfoliation in water. The stronger peaks in the exfoliated BNOx can be matched to boric acid (purple in the graph). One possible explanation for this is that the introduction of OH in the structure through the heating process results in the formation of more OH groups at the surface of the BN during the exfoliation, due to sonication-assisted hydrolysis[25]. The use of steam at the same time as heating has been previously reported[2], but the amount of hydroxylation was smaller than the one observed by heating h-BN at 1000 °C following by 24 hours of sonication in water. The FTIR also shows some differences between the exfoliated BNOx and bulk BNOx, with the peaks at 1344, 1190, 883 and 636 cm^{-1} becoming sharper and more define in the exfoliated sample, which further proves the higher level of hydroxylation of the BN thanks to the combination of heat and sonication in water. The peak at 540 cm^{-1} is clearer in the exfoliated BNOx than the not exfoliated BNOx. The FTIR of the exfoliated BNOx is very similar to the FTIR obtained when measuring boric acid, which further proves that degree of oxidation of the sample increases under sonication in water.

SEM images of the BNOx were taken after exfoliation to study the nanosheets. These are shown in figure 4.10.

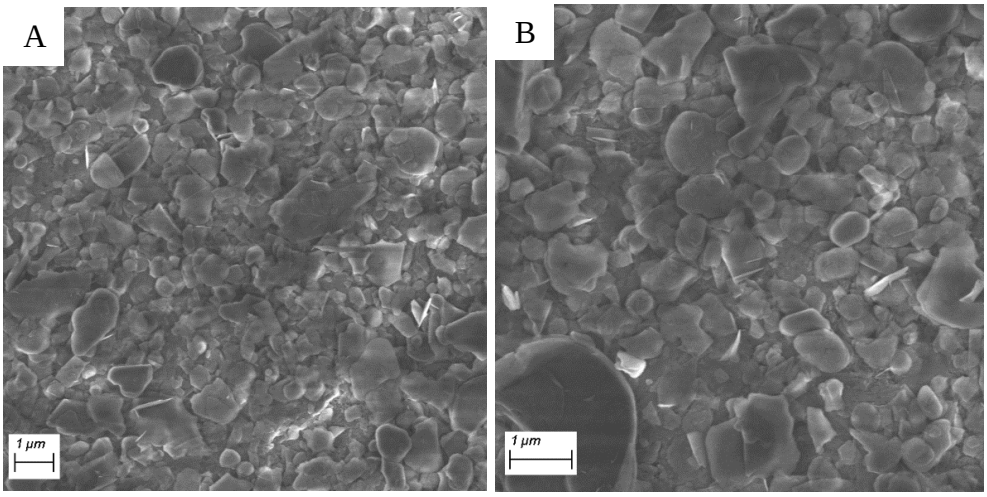

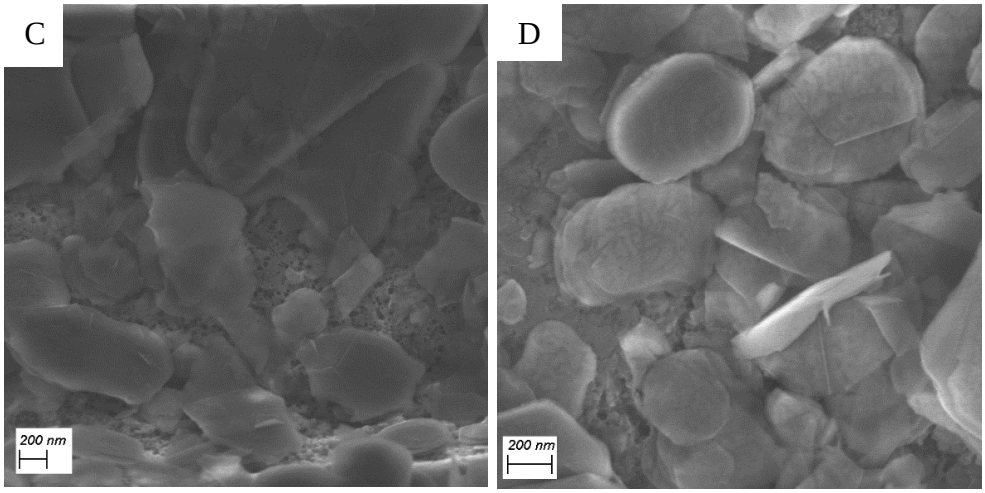

Figure. 4.10: SEM images of BNOx nanosheets after exfoliation. A) and B) showing a general view and C) and D) showing a closer view of the nanosheets using InLens and HET 3.0 kV.

SEM images of the nanosheets of the BNOx show no major differences with regular exfoliated BN, indicating that the oxidation doesn't change the shape of the nanosheets, which would make the BNOx a good candidate for membranes, as it would allow to functionalise the membranes while keeping the performance of the membranes. However, the size of the nanosheets was calculated to be 0.76±0.3 µm (figure 4.11), which is around 0.2 µm bigger than those nanosheets obtain when exfoliating regular BN.

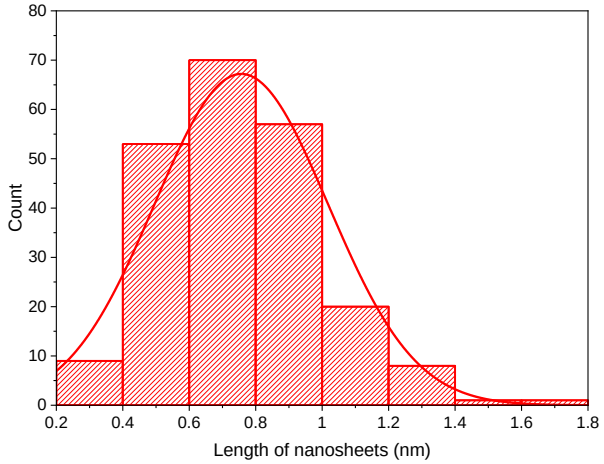

Figure 4.11: size distribution of BNOx nanosheets after exfoliation.

Raman of the bulk and exfolaited BNOx was also carried out and compared to the one from bulk BN (figure 4.12).

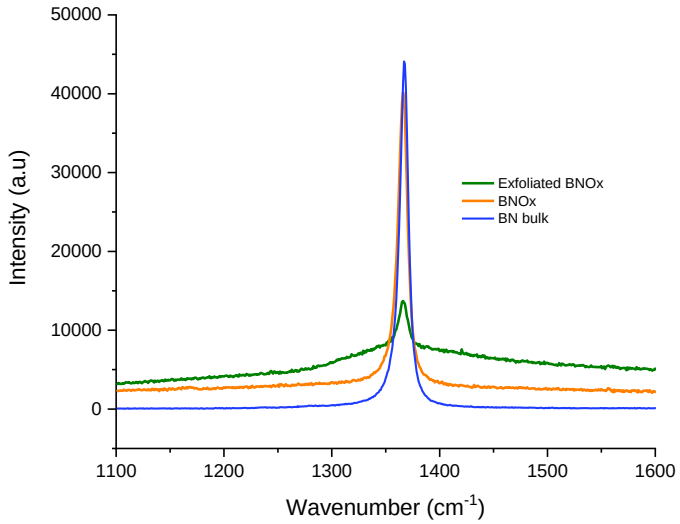

Figure 4.12: Raman spectra of Bulk BN (blue), BNOx (orange) and exfoliated BNOx (green).

The Raman spectra shows the peak corresponding to E_{2g} peak, with a bibliographic value of 1366 cm^{-1} [26]. Two main features can be observed in the spectra. The first one is that, as in the case of exfoliated BN vs bulk BN, the exfoliated BNOx shows a decrease in the intensity of the peak of 65% when compared to the bulk BNOx peak. This is due to the reduction of layer thickness in the structure. In contrast with the exfoliated BN, no shift of the peak was observed (table 4.1). There is a clear broadening of the peak when BNOx is exfoliated and, to a less degree, with bulk BNOx too. This has been previously reported in literature by Li *et al*, where the broadening of the peak is attributed to the oxidation of the material[27]. Furthermore, this broadening, larger in the case of the exfoliated BNOx, is also due to the exfoliation process

.

Table 4.1: Main features of bulk BN and BNOx and exfoliated BNOx in Raman spectra.

Sample	Peak shifht (cm^{-1})	Intensity (a.u)	FWHM (cm^{-1})
Bulk BN	1367	32077	9.32
Bulk BNOx	1367	40160	11.72
Exfoliated BNOx	1367	13710	15.3

AFM images of the exfoliated BNOx was also carried out and it is shown in figure 4.13.

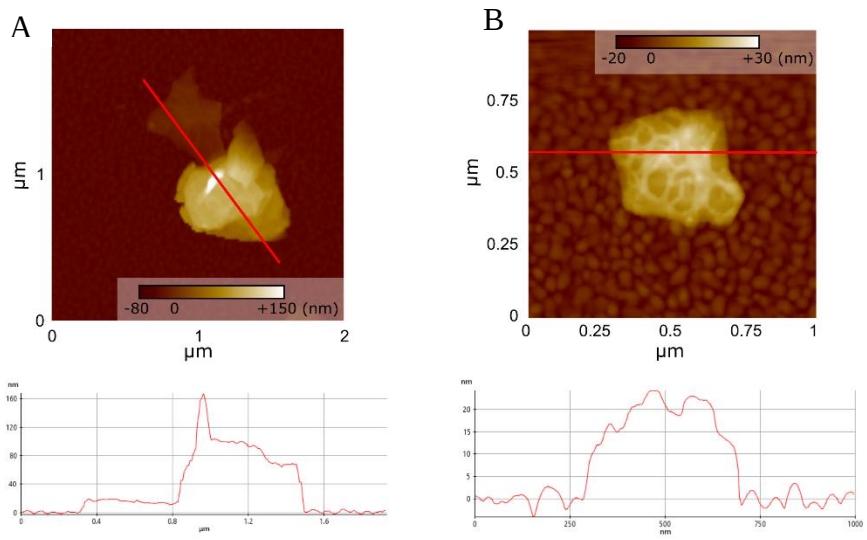

Figure 4.13: AFM images of BNOx A) nanosheets and profile and B) single BNOx nanoflake with its profile.

AFM image of the flakes, figure 4.13 A), shows that they are thicker than the BN nanoflakes, being more than 100 nm of height. Most of the flakes present in the sample were over 100 nm in height, which difficulties the AFM analyses. However, there were some thinner nanoflakes present in the sample, which were chosen for the analysis, as the one shown in figure 4.13 A). These thinner nanosheets show a different morphology than the ones observed in the regular BN nanosheets, that had less "peaks" and were more uniform. Furthermore, in figure 4.13, which shows a single BNOx nanosheet, it is easy to see that the nanosheet is not smooth, showing some roughness on the surface of the nanoflake. This is probably due to the effect of the oxide layer present in the nanoflake.

4.2.2 Preparation and investigation of BNOx based membranes

Exfoliated BNOx was used to fabricate membranes, using vacuum filtration as described previously in other chapters. The exfoliated solution looked very similar to the BN exfoliated one, with no major differences observed. The production of the membranes

was also very similar to the BN membranes, with the process being identical for both samples.

These membranes were characterised using SEM, BET and mercury Porosimetry and their performance was tested using several dyes.

Visual inspection of the membranes showed no differences with those obtained using regular BN (figure. 4.14).

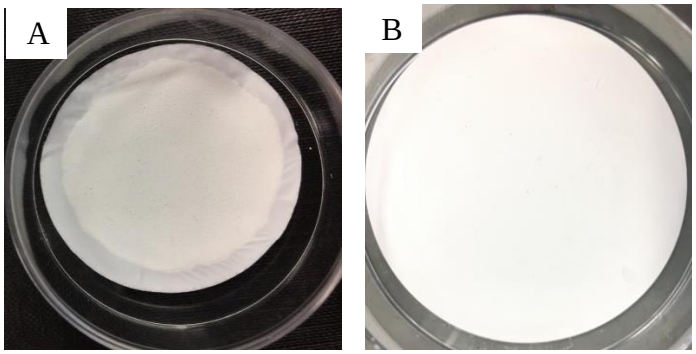

Figure 4.14: Photos of (a) BN and (b) BNOx membranes.

SEM images of the resulting membranes including both from top-view and from cross-section are shown in figures. 4.15 and 4.16.

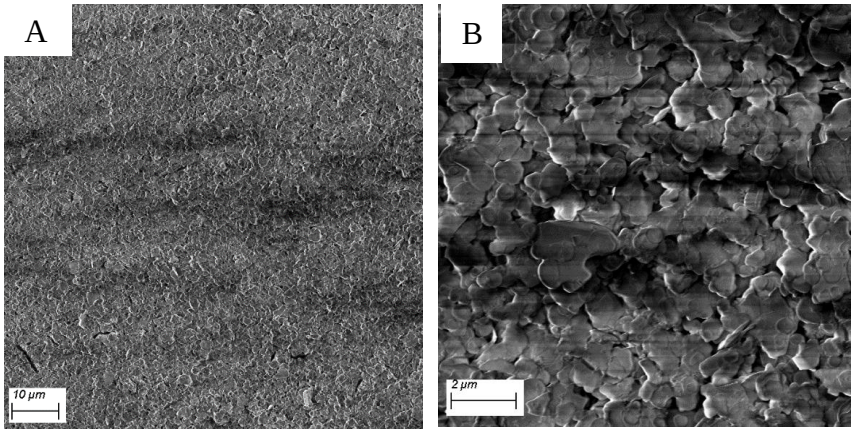

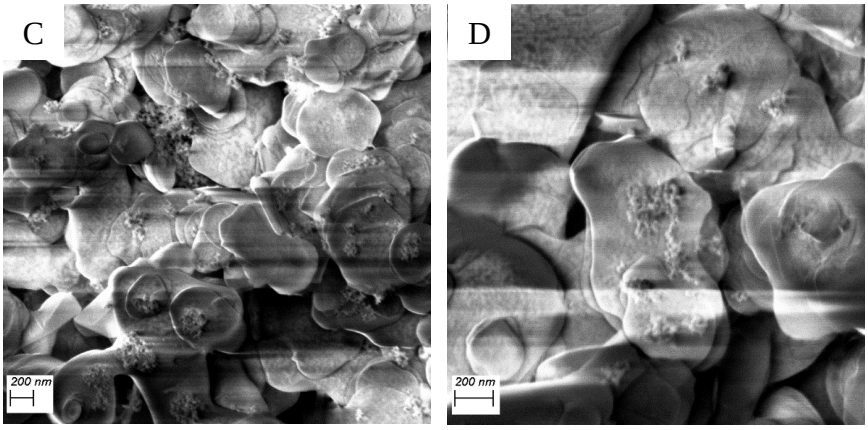

Figure 4.15: SEM A) and B) top view and C) and D) closer view of the top-view of BNOx using InLens and EHT: 2.50 kV.

Top-view SEM images of the membranes showed no major differences from the regular BN membranes, with the nanosheets clearly visible. The membranes looked very similar to the BN ones, indicating that the oxidation of the BN doesn't affect the formation of the membranes, which should make the membranes have similar if not equal performances that those obtained from original BN.

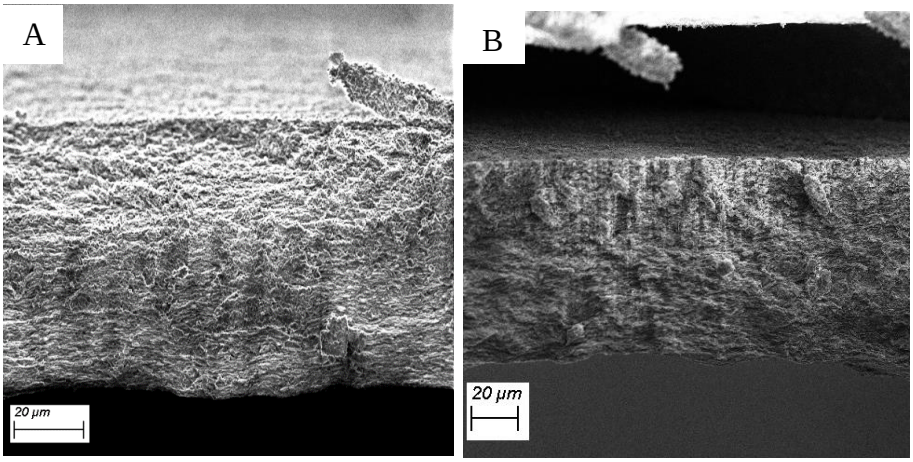

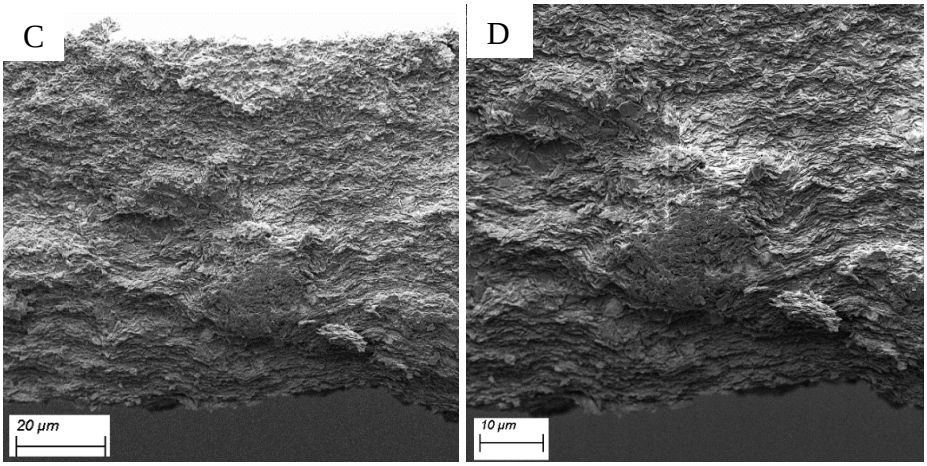

Figure 4.16: SEM cross-section of the BNOx membranes using InLens and EHT: 2.50 kV.

The cross-section profiles of the membranes showed the nanosheets tightly packed across the membranes. The thickness of the membrane was measured as 81 ± 4 µm, which is significantly thinner than the values obtained for the BN membranes (140-170 µm). This more compact membrane could have an effect on the performance and characteristics of the membranes.

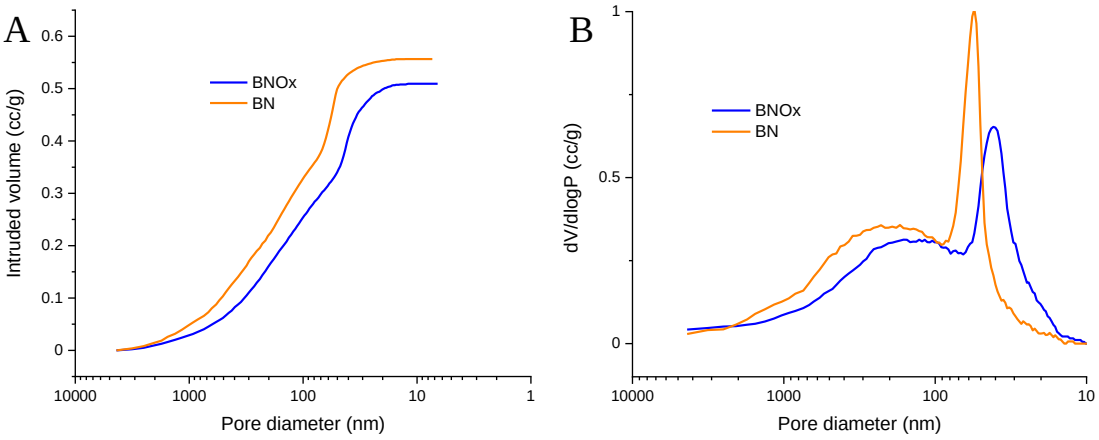

Figure 4.17: A) Comparison of mercury intrusion characteristics of the BN and BNOx membrane samples and B) comparison of mercury pore size distribution of the BN and BNOx samples.

Mercury porosimetry was carried out to investigate porosity, in the approximate range of 10 nm to 10 µm. Figure 4.17 A shows the intrusion of mercury into the membrane samples as a function of pressure, with pressure being analogous to pore diameter. As

pressure is increased, the largest pores fill first, followed by increasingly smaller ones. For the BN sample, a very gradual filling is observed initially, for pores <3 μm. A subsequent change in the slope of the curve corresponds to more rapid pore-filling. This continues until a sharp intrusion of mercury occurs (the slope rises sharply) as pores of approx. 80 nm diameter are filled. The curve then plateaus. In comparison, the curve for BNOx is of a similar shape to BN, but the intrusion profile is shifted to the right, corresponding to smaller pore sizes. In terms of pore volume, the results obtained show similar values, with BN having 0.56 cm^3/g and BNOx 0.51 cm^3/g. Although the values are very similar, the trend mimics that of the pore size, as the BNOx shows a smaller pore volume than BN. This indicates that the membranes have both morphological similarities (as evidenced by the similarity in *shape* of the intrusion curves), as well as high bulk densities as seen by the pore volumes values.

It is also useful to consider the pore size distributions of the membranes, plotted as pore diameter vs the change in intruded volume with respect to the log of change in pressure (dV/dlogP) as shown in figure 4.17 B. When plotted this way, the pore size distributions can be evaluated in terms of sharpness, with sharp peaks corresponding to tight pore size distributions, and vice versa. Both BN and BNOx have a broad peak initially, but the BNOx peak is shifted to the right, which indicates smaller pore sizes. A second peak can be observed for the two samples, BN and BNOx. The sharp peaks correspond to the sub-100 nm range, with a peak at 54 nm for BN and 44 nm for the BNOx. The sharpness of the peak is due to a high concentration of pores with similar sizes. The peak is less prominent in the case of BNOx, but still sharper than the broad peak at bigger pore sizes. This indicates that the porous properties of both the BN and BNOx are similar, but BNOx has smaller pores.

It is clear from the shape of the pore size distribution curves that the membranes studied here are derived from the same parent material, but the partial oxidation changes the porous characteristics of the membrane.
BET analysis was carried out to further investigate the porous characteristics, specifically the surface area, pore diameter, and pore volume. The measured data is summarised in Table 4.2.

Table 4.2: Summary of BET surface area analysis data.

Sample	Surface area (m^2/g)	BJH desorption pore diameter (nm)	BJH desorption pore volume (cm^3/g)
BN	26.7	3.5	0.089
BNOx	27.3	22.6	0.141

In terms of pore diameter, there is a clear distinction between the BNOx (22.6 nm) and BN (3.5 nm) samples; the diameter of BNOx is of an order of magnitude greater. This is significant in the context of the porosimetry data, as the BNOx has the pore sizes closer to the BET measurement range.

Taking the surface area data, values of 26.7 and 27.3 m^2/g are observed, for BN and BNOx, respectively, i.e. both samples have identical surface areas when the decimal place is removed. In the literature, there is an established relationship between surface area and pore size; as pore size decreases, surface area increases, and generally speaking, as pore volume increases, surface area increases[28]. This relationship is illustrated here, whereby BNOx has a smaller pore size and pore volume (3.5 nm and 0.089 cm^3/g), relative to BN (22.6 nm and 0.141 cm^3/g). The two competing properties cancel each other out, resulting in identical surface area values.

The high surface areas (26.7 and 27.3 m^2/g) is attributed to the network of 50 and 40 nm pores, coupled with a reasonably high pore volume (0.56 and 0.51 cm^3/g). These properties are characteristic of a nanoporous material having a predominantly open, interconnected porous network.

4.2.3 Retention studies of BNOx membranes

The BNOx based membranes were then tested using the same dyes used to test the BN membranes. Initially, BNOx membranes were tested for retention of Evans Blue dye.

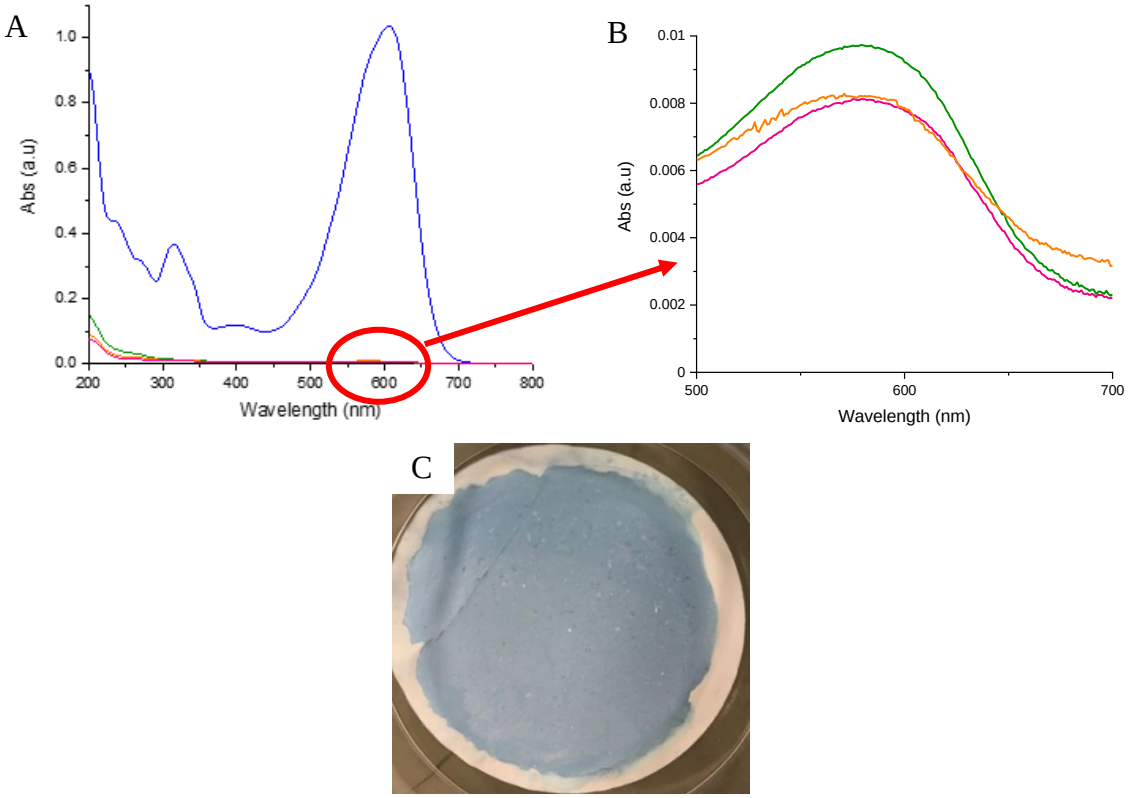

Figure. 4.18: A) UV-Vis spectra of the retention of 20 mL of Evans Blue (15 µM) through BNOx membranes and B) closed up of the absorbances of the absorbances of the permeates and C) BNOx membrane after Evans Blue filtration.

The retention of the BNOx membranes was 99% ± 1 (data is shown in table 4.3), which is very similar to those observed for original BN. This further proves that the oxidation of the BN doesn't affect the formation or performance of the membranes.

Table 4.3: Summary of data for the retention of Evans Blue of the membranes obtained with BNOx. The values where calculated using Origin 2018.

	N total	Mean	Standard Deviation	Minimum	Median	Maximum
Evans Blue	18	99	1	97	99	100

Therefore, due to the outstanding performance of the water exfoliated BNOx based membranes, a more detailed investigation was carried out on the samples to determine the performance of it using two smaller dyes with different functionalities, which are often utilised in retention studies, Methyl Orange and Methylene Blue. This was also necessary to test the universality of these membranes in nanofiltration for a wide range of possible molecules. The tests were performed in the same manner as the Evans Blue

ones. The retention of these dyes showed values close to those obtained for Evans Blue (figure. 4.19 A and B). Methyl Orange and Methylene Blue showed a retention from 99-100% higher than those obtained when testing Evans Blue. In all cases, these retentions indicated that these membranes would be capable of retaining bigger dyes, like Evans Blue, as well as smaller dyes, like Methylene Blue.

Table 4.4: Statistics from the retention of Methyl Orange and the Methylene Blue of the membranes obtained with BNOx. The values where calculated using Origin 2018.

	N total	Mean	Standard Deviation	Minimum	Median	Maximum
Methyl Orange	10	99	0.3	99	100	100
Methylene Blue	10	100	0.2	99	100	100

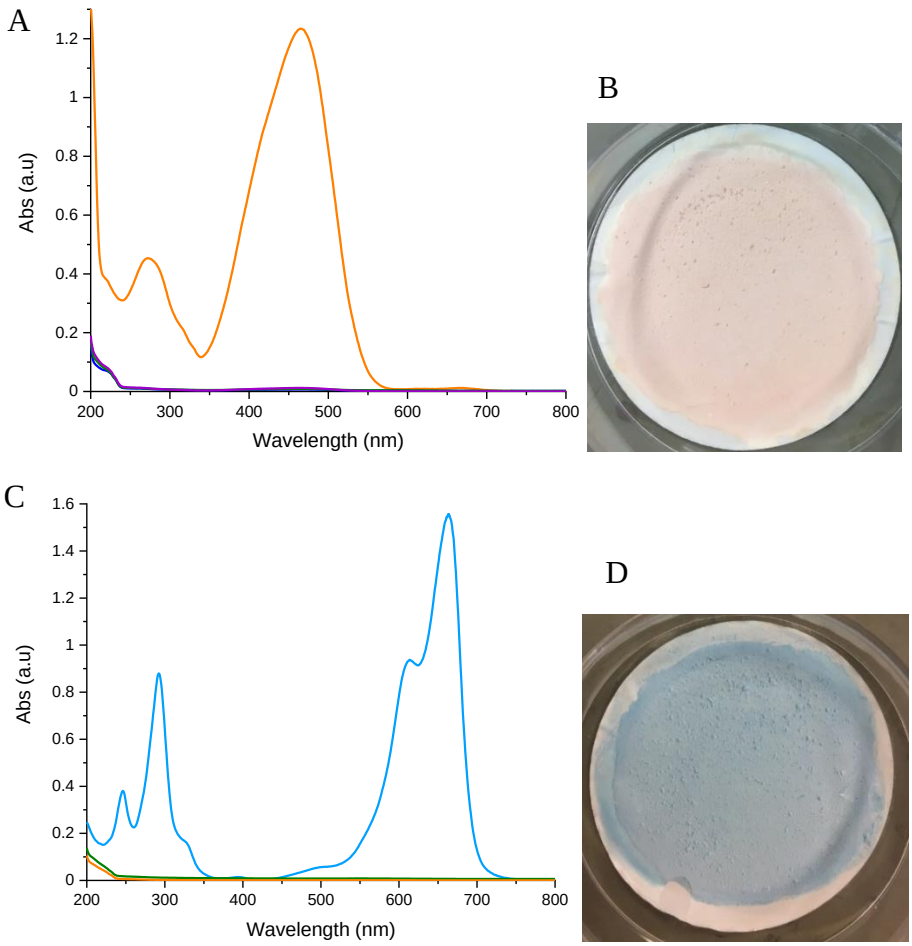

Figure 4.19: UV-Vis spectra showing the retention of 20 mL of A) Methyl Orange (50 µM), B) Methylene Blue (27 µM) through BNOx membranes, C) BNOx membrane after Methyl Orange filtration and D) BNOx membrane after Methylene Blue filtration.

These performances are showing that the oxidation of the BN doesn't affect the formation of the membranes, keeping the outstanding perfomance observed for the BN membranes. In fact, the membranes formed with the oxidised BN showed better mean retentions than those obtained with regular BN. This indicates that the oxidation already offers an advantage in comparison with regular BN, improving the retention of the membrane. Moreover, this oxidation BN could be used to functionalise BN and, therefore, the membranes, opening the posibility to use them for retention of other interesting molecules, such as sugars.

4.2.4 Testing of BNOx membranes for saccharides filtration

The excellent results obtained for dyes retention using BNOx membranes, encouraged us to extent the focus of the research and try to apply these membranes for filtration of other compounds. One interesting group of molecules is saccharides. Mono-, di- and poly- saccharides separation is one of the problems in food industry and sugar production. The separation of disaccharides from polysaccharides constitutes one of the basis of sugar purification[29]. Therefore, it is of great of interest to test our membranes for the separation of sugar molecules of different sizes. BNOx is expected to be a promising candidate to separate sugar molecules as the OH and NH groups would be able to interact with the hydroxyls present in the sugars.

For this set of experiments, three different types of sugar molecules were tested: sucrose, a disaccharide; and two polysaccharides: dextran and starch (figure 4.20). As a difference with the testing of dyes, the first sugar to be tested was sucrose, the smallest one, followed by the other two polysaccharides.

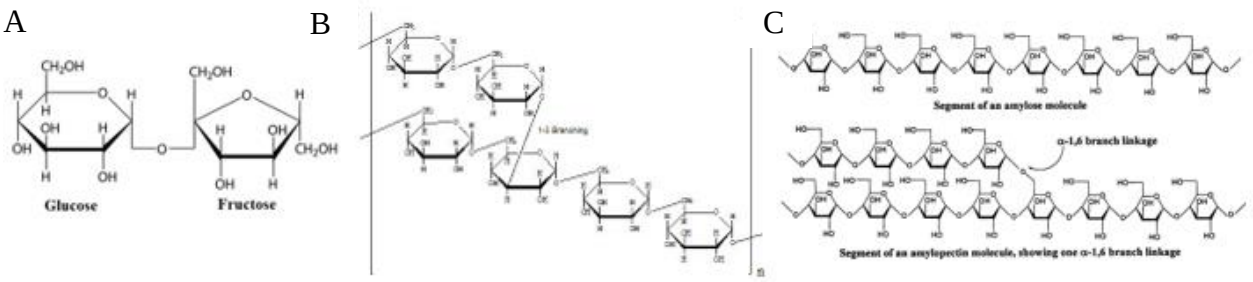

Figure 4.20: Structural representation of the three sugars tested: image A) corresponds to sucrose[30], B) to dextran[31] and C) represents the two structural forms of starch: amylose (linear) and amylopectin (branched) [32].

The solutions obtained after the filtration were evaporated and the weight recorded to calculate the retention, shown in table 4.5. It is important to mention that the values obtained, although presented in a quantitative way, are mostly illustrative, as a better system for this testing wasn't available. This testing method was prone to experimental error; as sugars absorb too much water and it's difficult to get all the hydration off the structure so this will add to the weight.

Table 4.5: Results obtained from testing BNOx membranes with the different sugar molecules, as well as calculations of retention.

Membrane	Sugar	Concentration (mg/mL)	Theoretical weight	Experimental weight	% Retention
BNOx1	Sucrose	342.3	6.8	0.8	15
BNOx2	Sucrose	171.15	3.42	3.4	1
BNOx3	Sucrose	85.58	1.72	1.7	1
BNOx4	Sucrose	17.12	0.34	0.3	12
BNOx5	Sucrose	17.12	0.34	0.29	1
BNOx6	Dextran	10	200	180	10
BNOx7	Dextran	10	200	193	4
BNOx8	Dextran	10	200	60	70
BNOx9	Dextran	10	200	169	16
BNOx10	Dextran	10	200	196	2
BNOx11	Dextran	10	200	193	4
BNOx12	Starch	10	200	0	100
BNOx13	Starch	10	200	9.6	95
BNOx14	Starch	10	200	4.7	98
BNOx15	Starch	10	200	1.7	99
BNOx16	Starch	10	200	0	100
BNOx17	Sucrose	342.3	6.85	6.83	0.2
BNOx18	Sucrose	342.3	6.8	6.75	1
BNOx19	Sucrose	17.12	0.34	0.29	15

The results presented in the table show very relevant information about the membranes and their performance. Different concentrations of sucrose were tested to check whether

saturation was causing the membrane or template to get blocked in some way, which would reduce the retention performance of the membranes. However, even for the lowest concentration (17.12 mg/mL), the retention was significantly lower than the ones obtained with the dyes. The retention obtained didn't go higher than 15%, even with the lower concentrations. Sucrose is the smallest sugar tested, so the lower retention could have been due to the small size, which would allow for most of the sucrose to pass through the membrane.

Then dextran was tested since it is a polysaccharide with side branches, usually containing one or two monosaccharide units[33]. This molecule was much larger than all the molecules tested previously; therefore, if size was the only factor affecting retention, a 100% retention would be expected, or, at least, a close value to those obtained for EB, MO and MB. However, the complete opposite was observed: retention percentages did not go above 15%, except for the one case were 70% retention was obtained, but, since it was an isolated value, it was treated as an accidental error. This debunked our first hypothesis that BNOx membrane selectively filtrated substances based on their size.

Starch was then used to establish whether bigger polysaccharides can be retained by the BNOx based membranes.

After testing the starch, the complete opposite results were obtained. In the table it can observed that the starch retention percentage in all experiments were close to 100%. This leads to believe that the differences between starch and dextran is the key to understanding the properties of molecules that would allow them to pass through or be retained in the BNOx membranes. This indicates that the size of molecules does play an important role but only after a certain size.

A hypothesis regarding the retention of all the dyes, but permeation of dextran, a much larger molecule, was unexpected. All the dyes that were tested contained in their structure benzene rings, which are π-systems, able to form π-π interactions with other structures that contain delocalised π bonding. Layered h-BN has been previously described as an analogue to graphene, with a similar electron arrangement, which makes BN, and thus BNOx, a π system[34,35], able to interact with those of the dyes. All this, makes it not surprising that some interaction between the benzene rings of the dyes and the BN rings is taking place[36,37], and making the permeation harder, since there is some type of

bonding between substrates and membranes. However, dextran does not contain aromatic rings, which could interact via π-π interactions with BN and BNOx.

Consequently, when only looking at size, a large molecule such as dextran is able to pass through, whereas smaller molecules that are able to interact with the BN π-system are retained. If an only-size range was to be established, the one required for an analyte to be retained is much larger than that of any of the tested dyes, it would correspond to something closer to the size of a large polysaccharide such as starch.

This could be the explanation as to why the small dye molecules are retained while large polysaccharides are not, but it is important to understand why sucrose and dextran pass through, whereas starch is effectively retained. Sucrose is a dimer molecule; therefore, it is only intuitive to think that in absence of characteristic interactions, its small size makes it a molecule more likely to pass through the membrane. Now, when looking at the differences between dextran and starch, the commercially available dextran exhibits around 5% branching [33,38] and when purchased from Sigma-Aldrich, its molecular weight ranges from 9000 to 2800 000 Da. Whereas starch from wheat is composed by two differently structured molecules: amylose (unbranched structure contributing 10-30% of overall structure and exhibiting a molecular weight of 300 000 to 2.4 million[39]) and amylopectin (branched, contributing to the remaining 70-90% with a molecular weight ranging from 2 to 15 million[39]). This makes starch a more branched polysaccharide, as well as heavier, and therefore also leading us to believe that in the differences in dextran and starch permeation, size is the crucial factor.

4.2.5 Functionalisation of BNOx using glucose

The retention values obtained with the BNOx membranes for the filtration of sucrose were lower than anticipated. Due to this, it was decided to functionalize the BNOx with glucose, another sugar.

Glucose is a simple sugar and it is the most abundant monosaccharide[40]. Glucose has the molecular formula of $C_6H_{12}O_6$, and it's shown in figure 4.21.

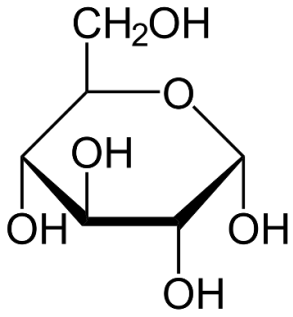

Figure 4.21: Hwaorth projection of α-D-glucose.

Glucose contains several OH- groups, which were thought to be able to interact with the OH and/or NH groups that are present in BNOx. Reactions between boronic acid and carbohydrates had been well documented in the past[19], with different sugars showing different stability constants for the corresponding products. Previously, Chen et al[20] described the dual exfoliation and functionalization of BN using sucrose under ball milling. Based on this, it was decided to use the oxidised BN with the hydroxyl groups already present, to try to exfoliate and functionalize the BNOx under sonication in presence of glucose.

BNOx and glucose were sonicated together in water in 24 hours, so BNOx could be exfoliated and functionalised at the same time. The stability of the solution didn't seemed to change due to the presence of glucose. SEM of the dried solution was taken and it's shown in figure 4.22.

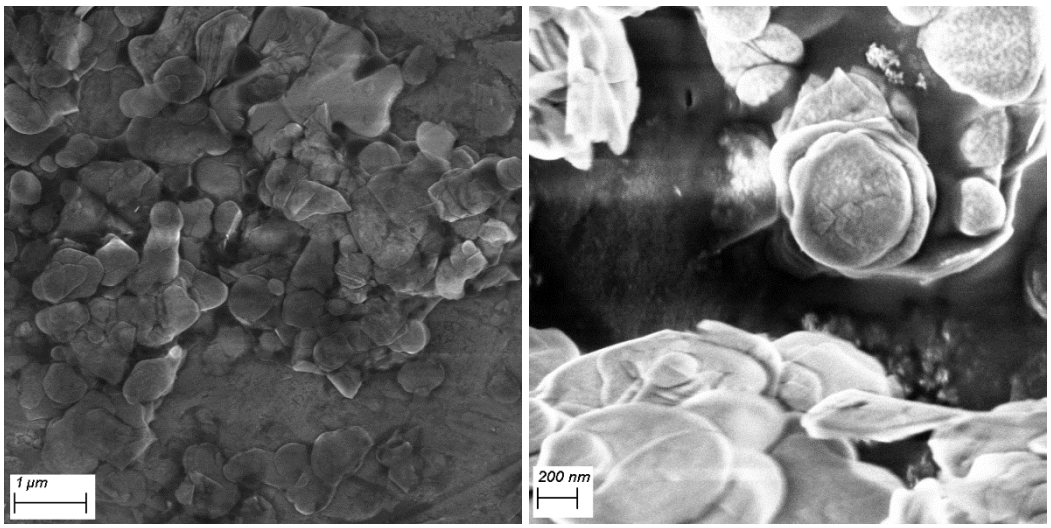

Figure 4.22: SEM of BNOx functionalised with glucose using InLens and EHT: 3.00 kV.

SEM of the BNOx functionalised with glucose after exfoliation doesn't showed any differences with exfoliated regular BN or BNOx, indicating that the functionalisation doesn't changed the nanosheets morphology.

CD spectra of the solution after sonication were recorded in order to confirm the functionalisation and are shown in figure 4.23.

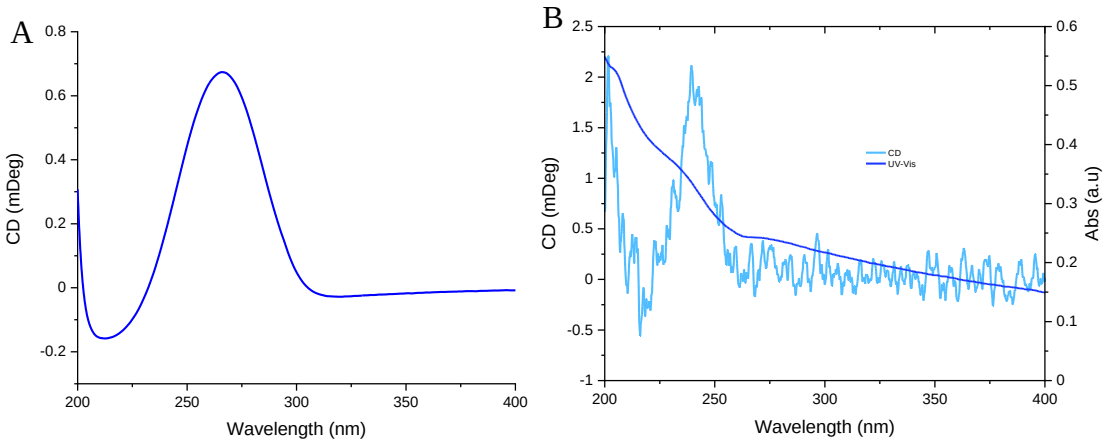

Figure 4.23: A) CD sprectrum of D-glucose and B) UV-Vis and CD spectra of BNOx-glucose.

The CD from the solution shows a CD signal in the region of chiral activity of D-glucose. BN and BNOx are not chiroptically active, so any signal could be assigned to the glucose. When compared to the CD signal of pure D-glucose, there is a slight shift in the spectra, suggesting some interaction between the components. However, the shift is so small that it is not conclusive to determine the functionalisation from this technique.

As glucose can retain quite a lot of water, the samples were very hard to dry from solution, so the membranes were made straight from the solution by filtration. Top-view SEM images of the membrane are shown in figure 4.24.

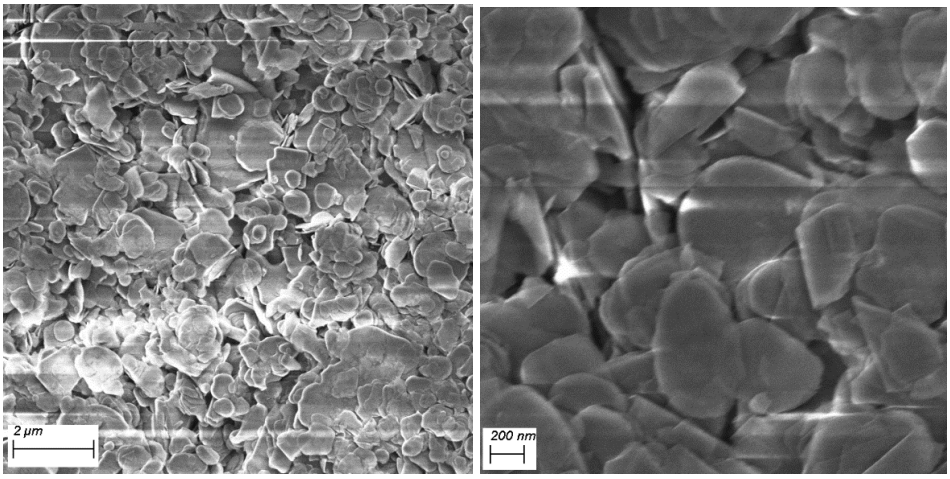

Figure 4.24: Top-view SEM of the BNOx funtionalised with glucose membranes, using InLens and EHT: 3.00 kV

The membranes made using the BNOx functionalised with glucose are very similar to those obtained with regular BN and BNOx. This seems to indicate that the funtionalisation doesn't affect the formation of the membranes.

One of the membranes was washed with MP water (20 mL, simulating filtration) to see how stable the glucose is in the membrane (if the functionalisation was achieved) while another one was not washed to obtain the information on the membrane as it is formed. The solution left after making the first membrane (no washing) and the permeate from the washing of the second membrane were tested using CD, to see if any of the glucose was coming off the membrane or was retained with the BNOx. The CD and UV-Vis spectra of both solutions are presented in figure 4.25.

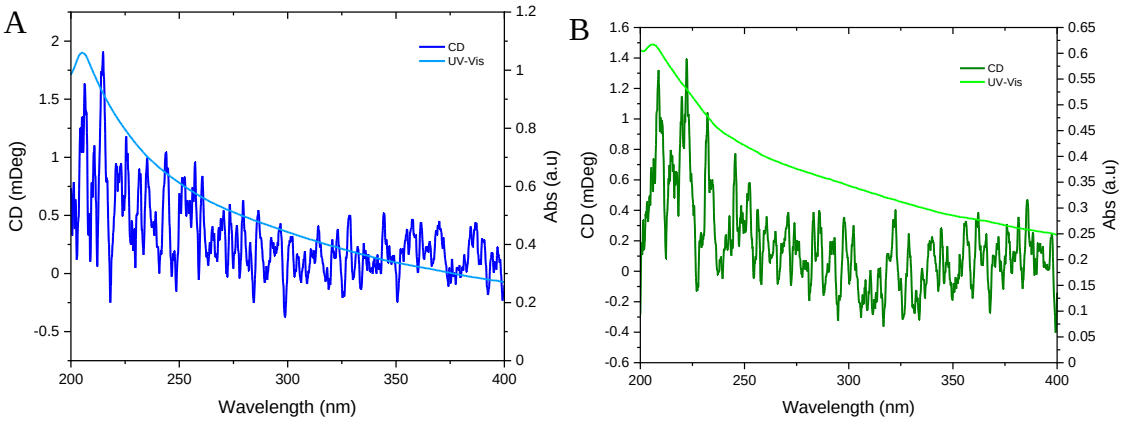

Figure 4.25: UV-Vis and CD spectra of BNOx-glucose membranes A) no washing and B) washed membrane.

The CD signal of both solutions was practically zero, indicating that glucose didn't seem to have come off the membranes. The signals showed no distictic peaks of chiroptical activity in the region where D-glucose is chiroptically active (see figure 4.23 A).

To corroborate these results, the membranes were characterised using FTIR spectroscopy, shown in figure 4.26.

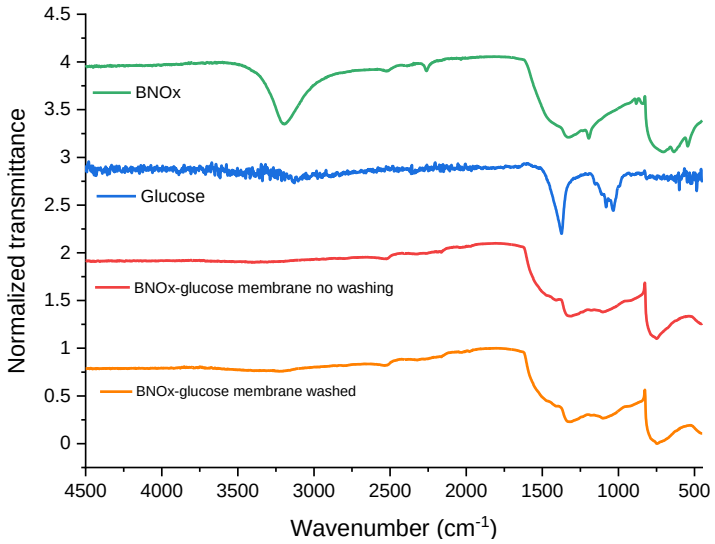

Figure 4.26: FTIR spectra of BNOx (green), glucose (blue), BNOx-glucose membrane not washed (red) and BNOx-glucose membrane (washed).

The FTIR spectra of both membranes look very similar. The first thing that can be noticed is the dissaperance of the 3200 cm^{-1} peak of BNOx, corresponding to the OH- present in the oxydised BN. This could indicate that the glucose was bound to the BNOx through those groups, as expected. Furthermore, the area around 500-600 cm^{-1} also shows differences with the BNOx on its ow. The area around 800-1600 cm^{-1} is also different from both BNOx and glucose on their own, which suggest the presence of glucose components in the membrane.

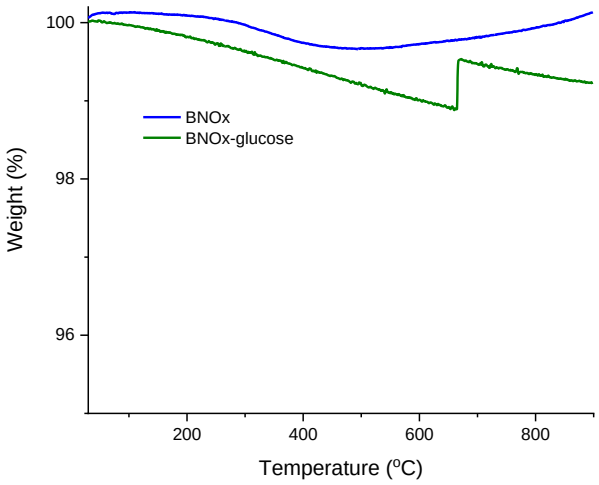

Figure 4.27: TGA curves of BNOX and functionalized BNOx with glucose.

All of these seem to indicate that there was a successful funtionalization of the BNOx in the presence of D-glucose. TGA analysis of the BNOx-glucose membranes after washing (figure 4.27) shows a small loss of weight (around 1%), although it seems to have gained it back at around 700 °C, as TGA was carried out in air and, as a result, the components can be oxidised. The TGA looks similar to previously reported in literature when functionalising the BN in the presence of sucrose[20]. This could be due to different possibilities, like no glucose present in the sample or some of the glucose being eliminated from the heat followed by more OH groups reattaching to the BN structure, as it seemed in the TGA of h-BN that oxidation started happening around that range of temperature. Another possibility is that the BNOx and glucose have bound in a way that a complex was formed, similar to that reported by James et al[19]. The gained in weight after the initial loss could be due to the further oxidation as the heat increases, as it is the same process observed in the furnace. However, more further testing to check this is needed.

4.2.5 Functionalisation of BNOx using glucose and glutaraldehyde

Due to the inconclusive results obtained with the functionalisation of BNOx using only glucose, it was decided to test a new type of functionalisation by introducing a spacer between the two: glutaraldehyde. The reaction between BN nanotubes, sugars and glutaraldehyde had been previously described by Emanet et al[21].

Two concentrations of glucose were tested, 5% w/v and 10% w/v. Following the procedure described by Emanet et al[21], the BNOx was sonicated for 24 hours, followed by the addition of the glutaraldehyde and glucose. The samples were then stirred for 48 hours. UV-Vis spectra of the BNOx, glucose and glutaraldehyde solutions as well as the exfoliated solutions of BNOx with glucose and glutaraldehyde (figure 4.28 A and B).

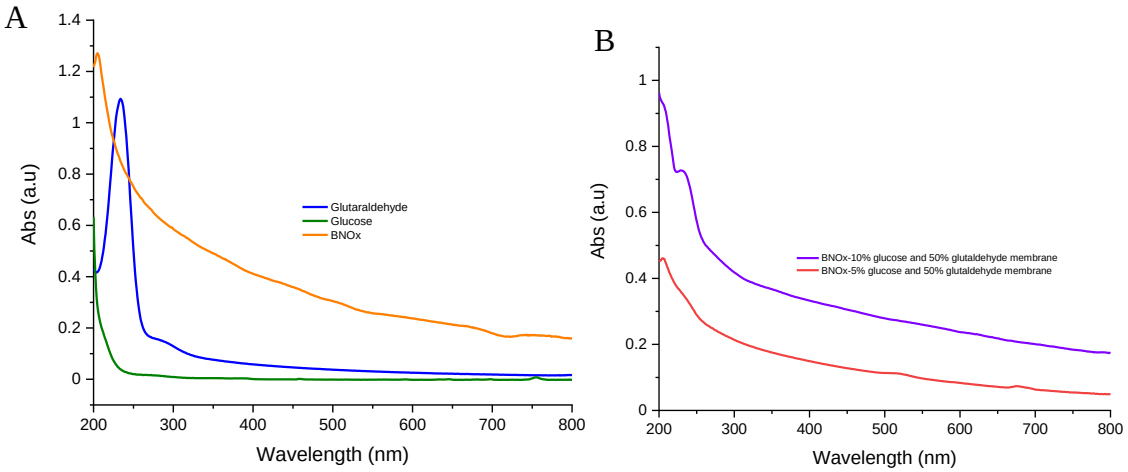

Figure 4.28: UV-Vis spectra of A) glutaraldehyde, glucose and BNOx solutions and B) BNOx-5% glucose (purple) and BNOx-10% glucose (red) and 50% glutaraldehyde.

The UV-Vis of the solutions show their characteristic absorbance spectra, green for glucose, orange for BNOx and blue for glutaraldehyde in figure 4.28 A). When the UV-Vis spectra of the mixed solutions are checked, there are noticeable differences, with the original solutions. Both samples show a similar pattern to the BNOx UV-Vis spectra, indicating that the solution is composed of this material. A shoulder around 230-240 nm can be observed, which is most likely due to the presence of glutaraldehyde in the samples, as its maximum absorbance is at 235 nm[41]. The UV-Vis absorbance overlaps with the BNOx one, so it's more likely hidden by this one, as the concentration of BNOx is higher in the sample.

SEM of the dried solutions were taken and are displayed in figure 4.29 and size distribution are shown in figure 4.30.

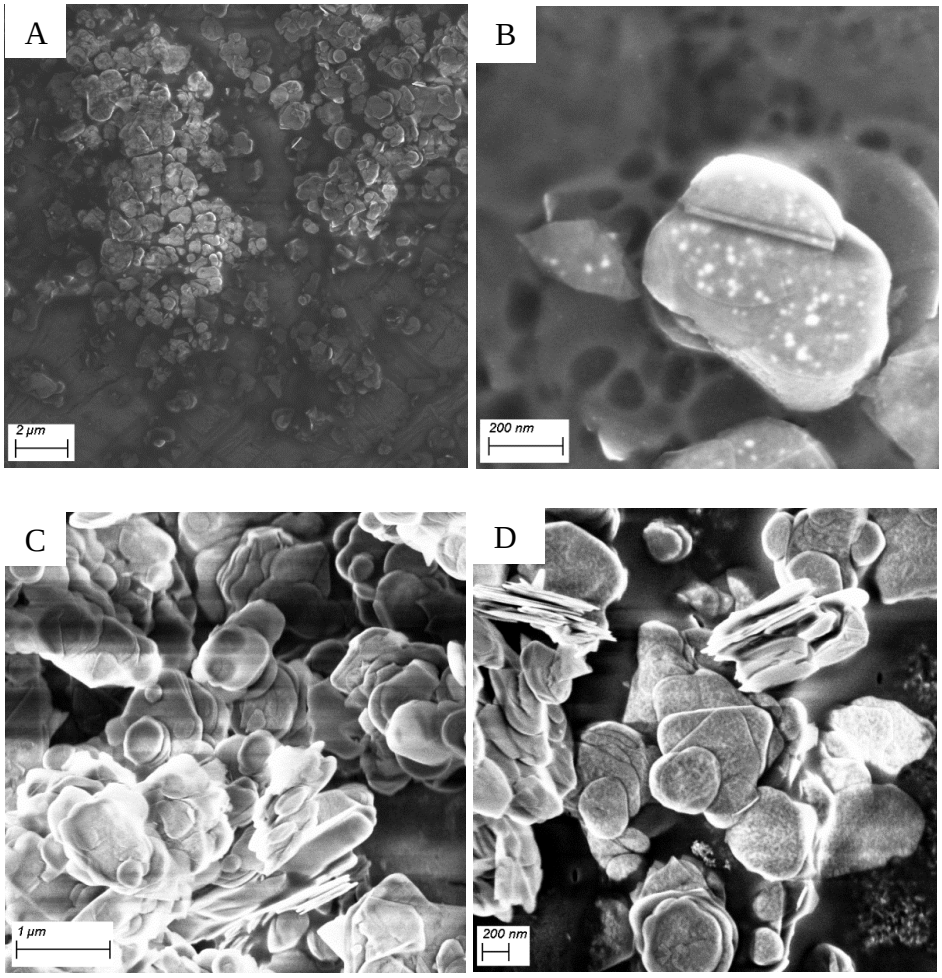

Figure 4.29: SEM images of A) and B) BNOx-5% glucose and glutaraldehyde and C) and D) BNOx-10% glucose and glutaraldehyde mixtures. InLens, EHT: 3.00 kV.

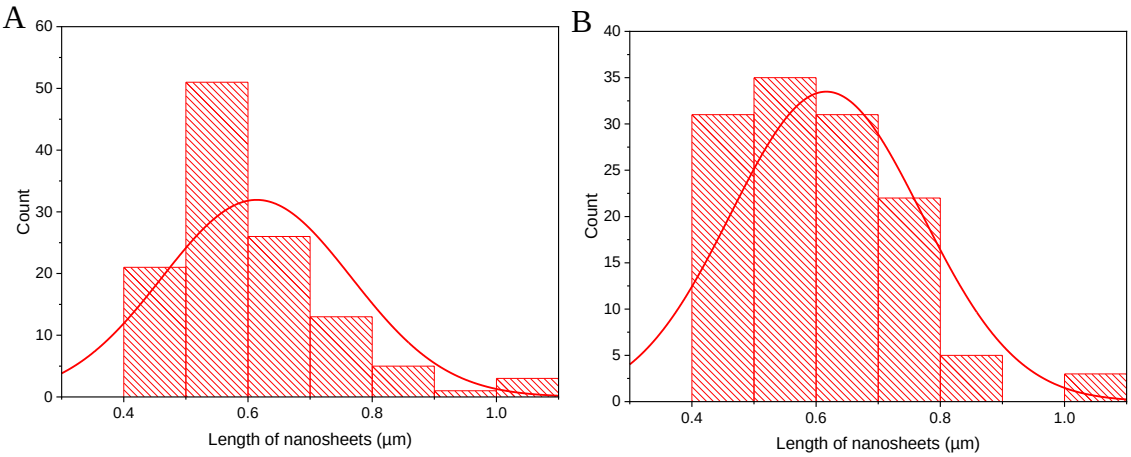

Figure 4.30: Size distribution of A) BNOx-5% glucose and glutaraldehyde and B) BNOx-10% glucose and glutaraldehyde nanosheets after exfoliation.

SEM images don't show major differences between both samples, as the BNOx nanosheets look very similar in both cases. The other two components can't be seen by SEM. These nanoflakes also look very similar to the BN and BNOx nanosheets obtained previously. This indicates that the functionalization using glucose and glutaraldehyde doesn't change the morphology of the material. The size distribution was 0.61 ± 0.15 µm for BNOx-5% glucose and glutaraldehyde and 0.62 ± 0.15 µm for BNOx-10% glucose and glutaraldehyde. The size of the nanosheets is in between the BN (0.5 µm) and BNOx (0.76 µm), which could indicate that the introduction of glucose and glutaraldehyde reduces the size of the nanosheets by 100 nm, more or less.

As the UV-Vis seems to indicate that the interaction between the BNOx, glucose and glutaraldehyde took place, the solution were used to make membranes. SEM images of the top-view membranes were taken and are shown in figure 4.31.

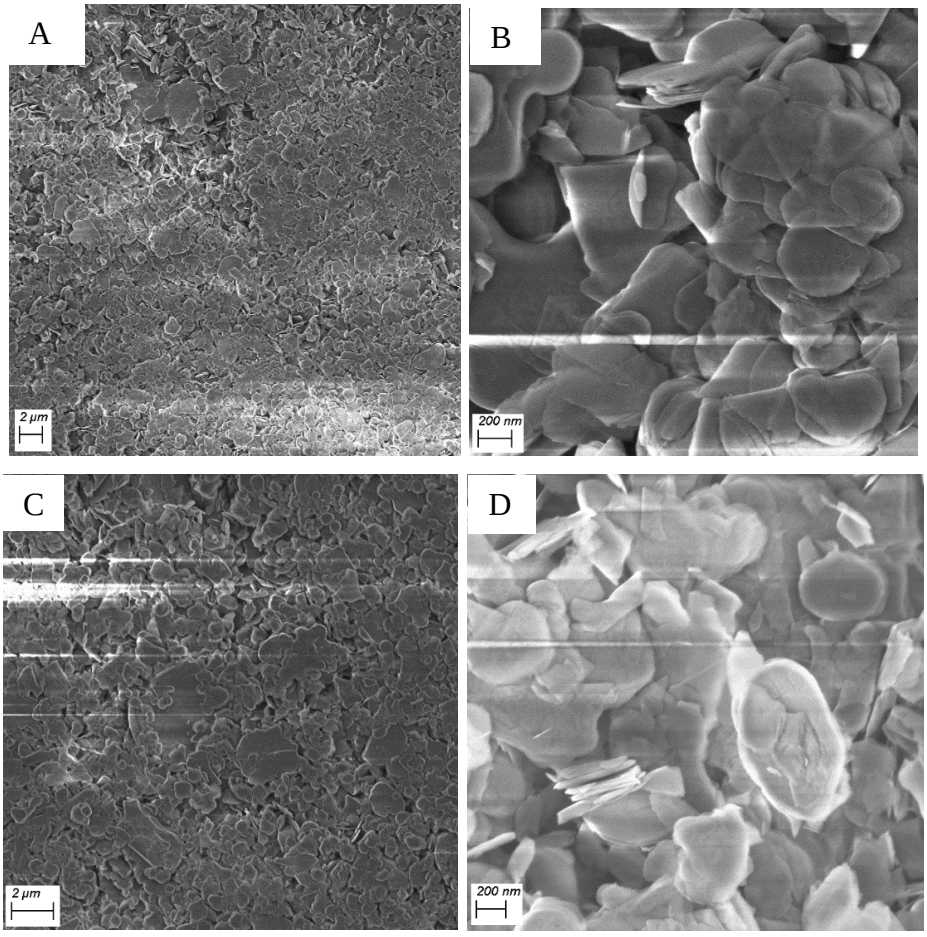

Figure 4.31: Top-view SEM images of A) and B) BNOx-5% glucose and glutaraldehyde membrane and C) and D) BNOx-10% glucose and glutaraldehyde membrane. InLens, EHT: 3.00 kV.

The top-view images of the two membranes, once again, looks very similar between each other, indicating that the different concentrations of glucose don't affect the formation of the membrane. Furthermore, the membranes also look very similar to BN and BNOx membranes previously obtained, which shows that the functionalization of the material doesn't seem to alter the formation of the membrane.

As all the SEM images taken of these two products show to be very similar, cross-section was only carried out using the BNOx-5% glucose and glutaraldehyde membrane, and was taken as a representative of this type of membranes. Cross-section images are shown in figure 4.32.

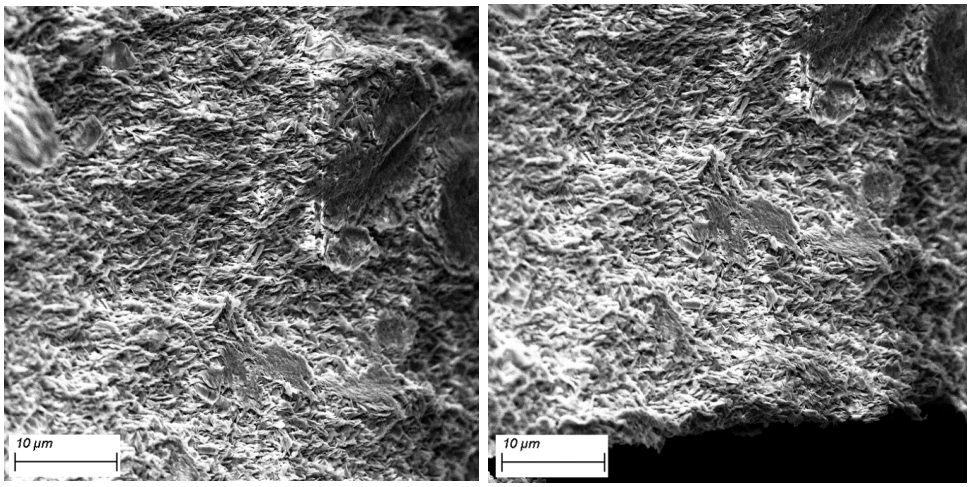

Figure 4.32: SEM images of the cross-section of BNOx-5% glucose and glutaraldehyde membrane. InLens, EHT: 3.00 kV.

Cross-section images showed the nanosheets piled up on top of each other in an orderly way, with no clear gaps in between the layers. The images look very similar to pure BN/BNOx membranes, indicating, once again, that the formation of the membranes is not apparently disturbed by the presence of glucose nor glutaraldehyde.

FTIR spectra of the membrane samples are shown in figure 4.33. As glutaraldehyde is a liquid, a membrane using BNOx and glutaraldehyde was made to compare with the rest.

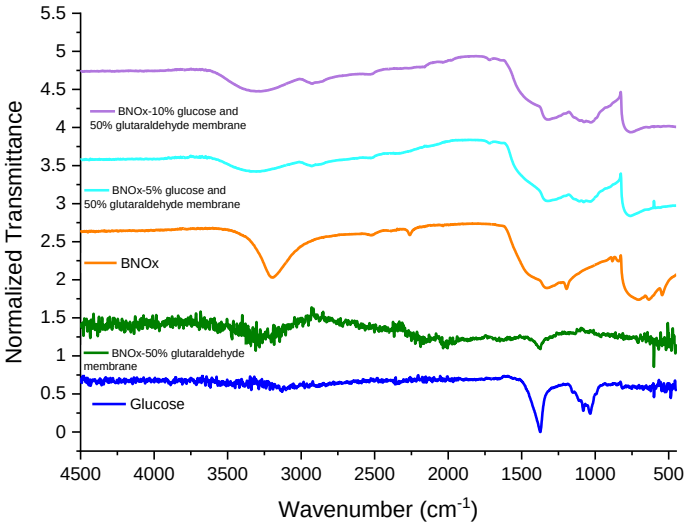

Figure 4.33: FTIR spectra of BNOx (orange), glucose (blue), BNOx-50% glutaraldehyde membrae (green), BNOx-5% glucose and glutaraldehyde membrane (light blue) and BNOx-10% glucose and glutaraldehyde membrane (violet).

The FTIR of both membranes show differences with the FTIR of BNOx, while maintaining the same general shape, indicating that the main material is still BNOx. The FTIR shows a decrease of the peak at 3000-3500 cm^{-1} of the BNOx, most likely due to the interaction with glutaraldehyde, as it can be observed in the spectra of both components. Similar to what was observed when the BNOx was functionalised with glucose (figure 4.26), the area around around 500-600 cm^{-1} also shows differences with the BNOx on its own. This area represents the NH bonds, so there could be some interactions ocurring with the glucose. The area around 800-1600 cm^{-1} is also different from BNOx, glutaraldehyde and glucose on their own, which suggests the presence of these components in the membrane. In particular, there's a peak around 1330 cm^{-1} that appears in the case of BNOx mixed with glutaraldehyde as a distintive peak and seems to be more pronounced in both membranes as it is in the case of BNOx in its own, indicating the presence of glutaraldehyde in the membranes.

TGA of the membranes was also ran. As both membranes don't seem to have big differneces between the two, once again, the BNOx-5% glucose and glutaraldehyde membrane was used as representative of these types of membranes (figure 4.34).

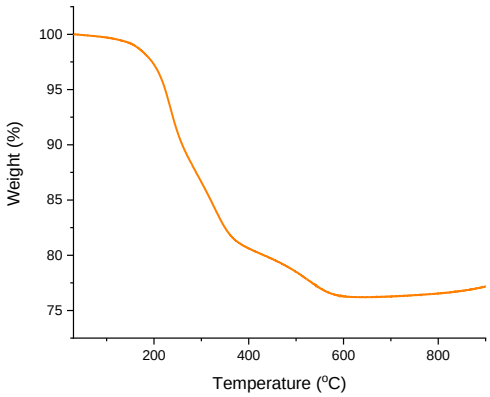

Figure 4.34: TGA of BNOx-5% glucose and glutaraldehyde membrane.

The TGA analysis shows several steps throughout the graph. These different steps at different temperatures show the loss of the different materials present in the membranes. Firstly, there's a loss of around 10% in weight that can be attributed to the loss of the water that remained in the membrane. Followed by a loss of mass off around 10-11%, probably due to the glucose and the final one off 5%, most likely due to glutaraldehyde. This corresponds with the way the two are bound to BNOX (stable at those temperatures), as the glutaraldehyde is the linker between the glucose and the BNOx. This further proves that the functionalisation was successful.

Once the functionalization was shown, the performance of the membranes was tested. Initially, Evans Blue was used for this, as it is the dye most used in this project to characterise membranes. The UV-Vis of the permeates is shown in figure 4.35 and the retention values in table 4.6.

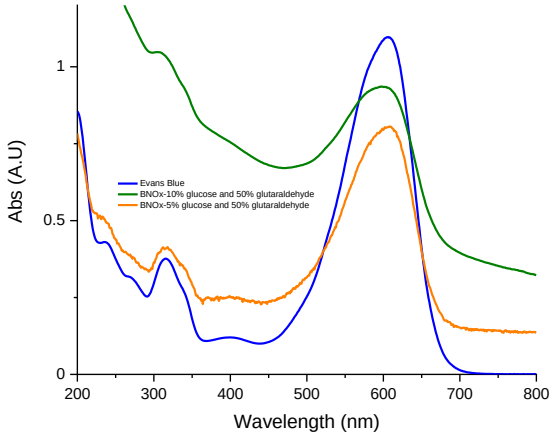

Figure 4.35: UV-Vis spectra of the retention of 20 mL of Evans Blue (15 µM) through BNOx-5% glucose and gluteraldehyde membrane (orange) and BNOx-10% glucose and gluteraldehyde membrane (green).

Table 4.6: Retention values for BNOx-5% glucose and gluteraldehyde membrane and BNOx-5% glucose and gluteraldehyde membrane.

Membrane	% Retention
5% glucose	27
10% glucose	15

The retention values for these membranes were signifincatly lower than any of the BN and BNOx membranes that had been reported in this project so far. This lower retetnion is most likely due to the presence of glucose and glutraldehyde. Although the two don't seem to, visually, affect the formation of the membrane, their incorporation is clearly altering the performance of the membrane, reducing their perforfarce from 99% to 15-27%. However, this could only mean that these membranes are not suitable for this particular application such as dye removal.

With the introduction of glucose, a chiral molecule, into the membrane, the possibility to achieve an enantomieric separation is opened. The goal is to induce the separation of a racemic mixture of two steroisomers, in this case D and L-Phe, due to the presence of D-glucose in the surface of the BNOx throughout the membrane. This would, in turn, produce a solution enriched in one of the two enantiomers, even if this enrichment was only minimal. The UV-Vis and CD of the racemic is shown in figure 4.36.

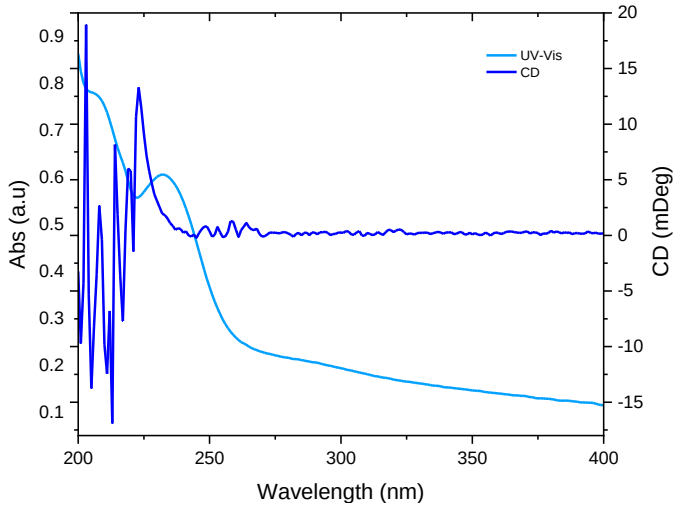

Figure 4.36: UV-Vis and CD spectra of the racemic solution of D- and L-Phe.

Phenylalanine was chosen as it is a chiral molecule presenting a benzyl ring capable of exhibiting π-π interactions with the BNOx, as it has been previously discussed, with the addition of the chirality that, hopefully, will interact with the chiral portion of the membrane (D-glucose) and slow down one of the enantiomers enough to be able to be detected using CD. The CD of the racemic showed a CD signal of basically zero, as the error limit of the instrument will always influence the signal that is close to 0. The UV-Vis absorbance shows two distintive peaks, at 240 nm and 210 nm more or less, which are the region one could expect the molecule to be chiroptically active, as shown by the CD signal.

The BNOx-5% glucose and gluteraldehyde membrane was tested allowing the solution to pass through the membrane using vacuum filtration, as the previous tests and aliquots were taken every 5 min. This was done as the expected is that one of the enantiomer will be slowed down and would elute first, followed by the other. So, if this was the case, some aliquots would be enriched in one of the enantiomer and others in the opposite enantiomer. There were 3 aliquots taken and UV-Vis and CD were carried out for each one (figure 4.37).

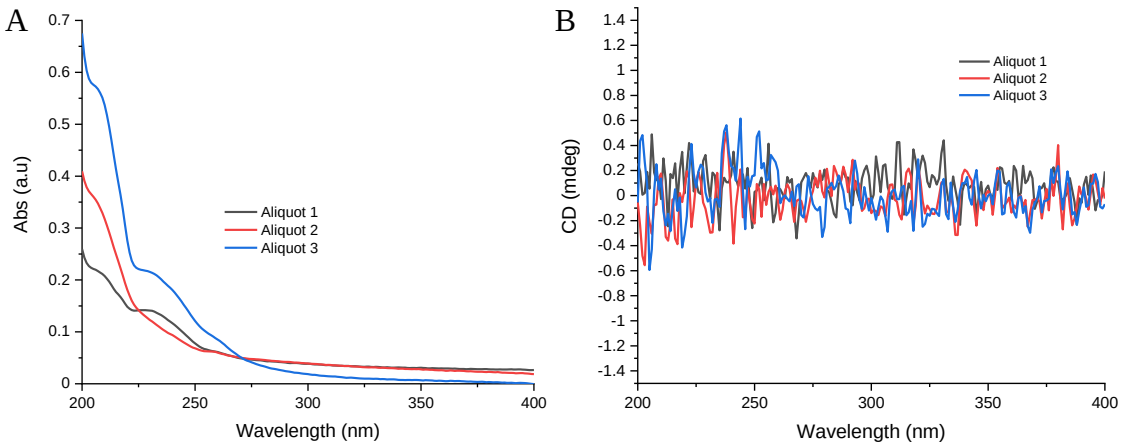

Figure 4.37: A) UV-Vis spectra and B) CD spectra of the three aliquots from the racemic mixture of D and L-Phe through the BNOx-5% glucose and gluteraldehyde membrane.

The shape of the UV-Vis spectra for the three aliquots is very similar to the one observed in figure 4.36, indicating that Phe is passing through the membrane. However, the CD shows no distintive peaks in the 210-240 nm area, which would be the area where the

Phe should show chiral activity. These results indicate that the Phe is not retained in the membrane and that there is no chiral selectivity caused by the membrane.

However, this could also be due to a fast filtration, not allowing the enantiomers to interact enough with the glucose to cause a slow down of one of them. For this, the BNOx-10% glucose and gluteraldehyde membrane was tested, as it has a higher amount of glucose. The solution was passed through the membrane without using vaccuum filtration, to slow down the process and allow the possibility of the Phe and glucose to interact and cause a separation. Aliquots were taken every 5 min and 6 aliquots were taken. The aliquots were then tested using CD and UV-Vis (figure 4.38).

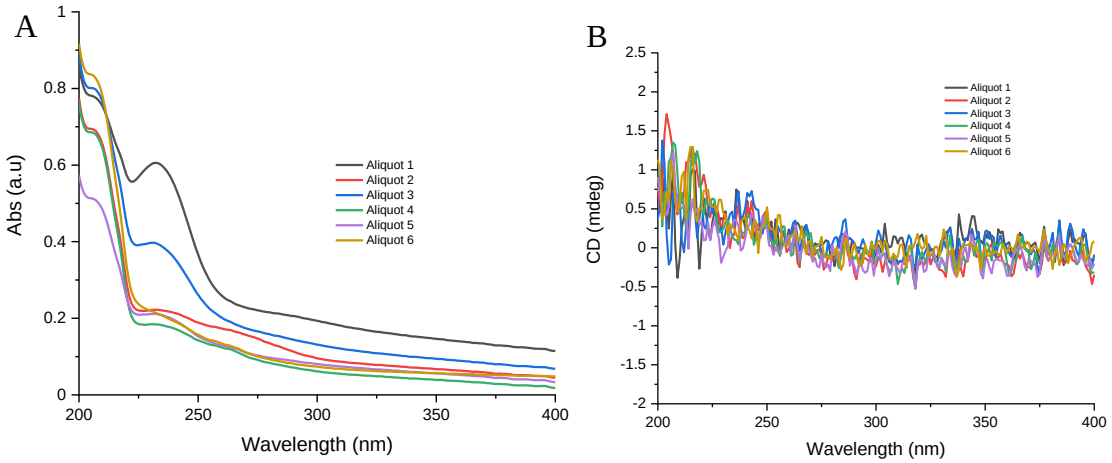

Figure 4.38: A) UV-Vis spectra and B) CD spectra of the three aliquots from the racemic mixture of D and L-Phe through the BNOx-10% glucose and gluteraldehyde membrane.

The shape of the UV-Vis of the aliquots is,once again, very similar to the Phe on its own (figure 4.36), with the stronger peaks appearing in aliquots 1 and 3, indicating a higher concentration of the Phe passing through the membranes at 5 min and 15 min. The rest of the aliquots still show the peaks corresponding to Phe, indicating that Phe passes through the membrane through the filtration. Nevertheless, the CD spectra of the aliquots is still basically zero, showing no chiral separation of D- and L-Phe. This later test indicates that, even though the functionalisation is happening, it is not enough to retain one of the enantiomers and achieving no chiral separation. Furthermore, Phe passes through the membrane throughout the filtration, not being retained by it.

4.3 Conclusions

The oxidation of BN was succesfully achieved by heating the powder in air at 1000 °C, obtaining BNOx. The characterisation of the sample showed the presence of OH groups in FTIR and XRD, with the spectra being very similar to the boric acid one, further proving the oxidation of the BN. The nanosheets and membranes obtained were very similar to the BN ones, indicating that the oxidation doesn't change the morphology of the exfoliated material or formation of the membranes.

The membranes were tested for the same three dyes, exhibiting excellent performances, very similar to the ones obtained with the BN membranes. All of this seems to indicate that the oxidation doesn't affect the performance of the membranes, which opens the possibility to use this oxidation as a route for further fuctionalisation of the material.

BNOx membranes were also tested for sugars separation, with some interestig results. This application will need further testing to optimise the process, including funtionalisation of the membranes.

BNOx was succesfully functionalised using glucose, both in the presence and absence of glutaraldehyde. These membranes were tested for chiral separation, as the glucose was stable in the mebrane and could induce enantiomeric selectivity, which was not successful. This needs further testing and optimisation.

Bibliography

1 Z. Cui, A. J. Oyer, A. J. Glover, H. C. Schniepp and D. H. Adamson, *Small*, 2014, **10**, 2352–2355.

2 F. Xiao, S. Nafi cy, G. Casillas, M. H. Khan, T. Katkus, L. Jiang, H. Liu, H. Li, Z. Huang, F. Xiao, M. H. Khan, T. Katkus, H. Liu, Z. Huang, S. Nafi cy, G. Casillas, L. Jiang and H. Li, *Adv. Mater.*, 2015, **27**, 7196–7203.

3 Y. Andriani, J. Song, P. C. Lim, D. H. L. Seng, D. M. Y. Lai, S. L. Teo, J. Kong, X. Wang, X. Zhang and S. Liu, *Ceram. Int.*, 2019, **45**, 4909–4917.

4 R. Moradian and S. Azadi, *EPL*, , DOI:10.1209/0295-5075/83/17007.

5 J. Wu and W. Zhang, *Solid State Commun.*, 2009, **149**, 486–490.

6 R. S. Singh, *AIP Adv.*, 2015, **5**, 117150.

7 J. W. Feng, Y. J. Liu and J. X. Zhao, *J. Mol. Model.*, 2014, **20**, 1–7.

8 A. Tokarev, E. Kjeang, M. Cannon and D. Bessarabov, *Int. J. Hydrogen Energy*, 2016, **41**, 16984–16991.

9 Q. Weng, D. G. Kvashnin, X. Wang, O. Cretu, Y. Yang, M. Zhou, C. Zhang, D.-M. Tang, P. B. Sorokin, Y. Bando, D. Golberg, Q. Weng, O. Cretu, M. Zhou, C. Zhang, D.-M. Tang, Y. Bando, D. Golberg, D. G. Kvashnin, P. B. Sorokin, X. Wang and Y. Yang, *Adv. Mater.*, 2017, **29**, 1700695.

10 J. Li, P. Jin, W. Dai, C. Wang, R. Li, T. Wu and C. Tang, *Mater. Chem. Phys.*, 2017, **196**, 186–193.

11 J. Xiong, L. Yang, Y. Chao, J. Pang, M. Zhang, W. Zhu and H. Li, *ACS Sustain. Chem. Eng.*, 2016, **4**, 4457–4464.

12 L. H. Li, J. Cervenka, K. Watanabe, T. Taniguchi and Y. Chen, *ACS Nano*, 2014, **8**, 1457–1462.

13 B. Yu, W. Xing, W. Guo, S. Qiu, X. Wang, S. Lo and Y. Hu, *J. Mater. Chem. A*, 2016, **4**, 7330–7340.

14 G. R. Bhimanapati, D. Kozuch and J. A. Robinson, *Nanoscale*, 2014, **6**, 11671–11675.

15 T. Sainsbury, A. Satti, P. May, Z. Wang, I. McGovern, Y. K. Gun'ko and J. Coleman, *J. Am. Chem. Soc.*, 2012, **134**, 18758–18771.

16 B. Zumreoglu-Karan and D. A. Kose, *Pure Appl. Chem.*, 2015, **87**, 155–162.

17 R. Bernardini, A. Oliva, A. Paganelli, E. Menta, M. Grugni, S. De Munari and L. Goldoni, *Chem. Lett.*, 2009, **38**, 750–751.

18 T. E. ACREE, 1973, pp. 208–219.

19 T. D. James, K. R. A. Samankumara Sandanayake and S. Shinkai, *Angew. Chemie-International Ed.*, 1996, **35**, 1910–1922.

20 S. Chen, R. Xu, J. Liu, X. Zou, L. Qiu, F. Kang, B. Liu and H.-M. Cheng, *Adv. Mater.*, 2019, **31**, 1804810.

21 M. Emanet, Ö. Şen, Z. Çobandede and M. Çulha, *Colloids Surfaces B Biointerfaces*, 2015, **134**, 440–446.

22 *Infrared Raman Spectra Inorg. Coord. Compd.*, 2008, 149–354.

23 X. Shen, X. Lin, N. Yousefi, J. Jia and J. K. Kim, *Carbon N. Y.*, 2014, **66**, 84–92.

24 S. Tosoni, K. Doll and P. Ugliengo, *Chem. Mater.*, 2006, **18**, 2135–2143.

25 Y. Lin, T. V Williams, T.-B. Xu, W. Cao, H. E. Elsayed-Ali and J. W. Connell, *J. Phys. Chem. C*, 2011, **115**, 2679–2685.

26 E. S. Tarleton, J. P. Robinson, C. R. Millington, A. Nijmeijer and M. L. Taylor, *J. Memb. Sci.*, 2006, **278**, 318–327.

27 L. H. Li and Y. Chen, *Adv. Funct. Mater.*, 2016, **26**, 2594–2608.

28 R. C. Aran Raffertya, Trevor Woodsb, Alex Conwayc, Yurii Gun'koa, James Kennedyd, Martin Schwentenweine, *Ceram. Mod. Technol.*, 2019, **1**, 145–151.

29 R. Singh, *Membr. Technol. Eng. Water Purif.*, 2015, 179–281.

30 F. Zahra Amchra, S. Chaouqi, A. Khiraoui and A. Benhmimou, *Artic. J. Med. Plants Stud.*, 2018, **6**, 102–108.

31 Sigma Aldrich, Dextran.

32 G. Wiederschain, *Glycoscience. Chemistry and chemical biology*, 2009, vol. 74.

33 J. N. BeMiller, *J. Soc. Dye. Colour.*, 1909, **25**, 220–223.

34 T. Greber, *Handb. Nanophysics Funct. Nanomater.*, 2010, 18-1-18–22.

35 T. Chen, M. Li and J. Liu, *Cryst. Growth Des.*, 2018, **18**, 2765–2783.

36 Y. Xue, P. Dai, X. Jiang, X. Wang, C. Zhang, D. Tang, Q. Weng, X. Wang, A. Pakdel, C. Tang, Y. Bando and D. Golberg, *J. Mater. Chem. A*, 2016, **4**, 1469–1478.

37 M. H. P. B. Vettori, S. M. M. Franchetti and J. Contiero, *Carbohydr. Polym.*, 2012, **88**, 1440–1444.

38 S. S. Maribel Ovando, *J. Nutr. Food Sci.*, , DOI:10.4172/2155-9600.1000263.

39 K. G. G. and U. G. Senay Simsek1*, Maribel Ovando Martinez1, Orhan Daglioglu2, .

40 C. Bastioli, *Handbook of biodegradable polymers*, 2020.

41 A. Abay, G. Simionato, R. Chachanidze, A. Bogdanova, L. Hertz, P. Bianchi, E. Van Den Akker, M. Von Lindern, M. Leonetti, G. Minetti, C. Wagner and L. Kaestner, *Front. Physiol.*, 2019, **10**, 514.

Chapter 5: BN and BNOx based composite membranes

5.1 Introduction

5.1.1 Composite membranes

Inrecent years, the use of 2D nanomaterials for membrane production has attracted a lot of interest, including the development of new composite membranes with improved properties, such as stability, opening up more possibilities for their applications[1]. The use of 2D nanocomposite based membranes could, potentially, be an excellent alternative for the currently widely used polymeric membranes[1].

BN has previously been used as a filler in polymeric membranes, in order to improve the permeation and separation performance of the membranes, without losing mechanical flexibility[1,2], (figure 5.1).

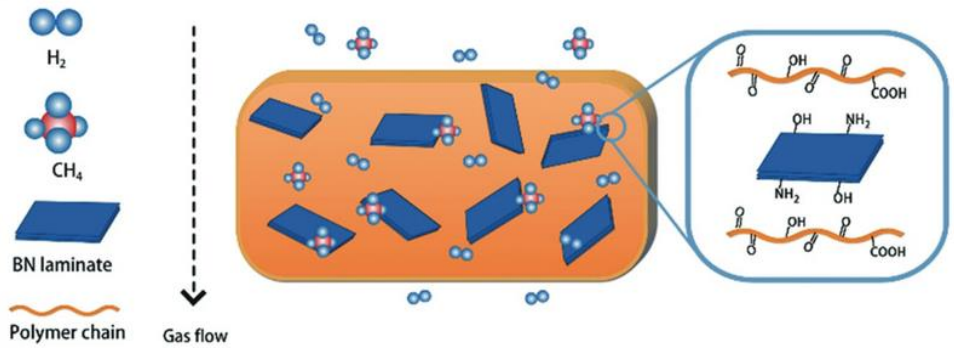

Figure 5.1: Schematic diagram of the polymer-BN composite membrane for selective gas separation. Taken from reference[2].

Hydroxylated BN and sulfonated poly(ether ether ketone) (SPEEEK) have also been used to produce corresponding composite membranes [3]. These membranes have shown high selectivity and high proton conductivity and could also be used to develop fuel cells. BN nanosheets can also be embedded into thermally rearranged polyimide, obtaining a composite membrane that can be employed for separation of H_2[3].

Due to the excellent retention results obtained for BN and BNOx membranes, shown in the previous chapters, it was decided to attempt to improve these membranes by

preparing various composite membranes. The goal was to add new functionalities to the membranes. LDH additives were chosen for their potential capabilities for photodegradation of the dyes[4,5], Fe_3O_4 based fillers - to attempt magnetic separation and CNTs - to control the pore size by introducing different amounts of a 1D nanomaterial.

5.1.2 Photodegradation of dyes by LDH materials

The removal of some organic contaminants can be achieved through photocatalytic degradation, where the contaminants are transformed into carbon dioxide, water and mineral acids[6–8]. A great alternative to avoid the high cost of conventional photocatalyst, which make them unsuitable for treating large amounts of materials, is to use layered double hydroxides (LDHs)[6]. LDH could potentially allow the dual function of adsorbing these contaminants as well as photocatalysing their degradation, being a great option for treating of wastewaters[6].

LDHs, due to their oxidation capabilities, are a promising material for the degradation of organic pollutants[6,9]. LDHs are considered as "doped semiconductors", due to the fact that the ratio between the two or three metals forming the material can be changed. This doping results in defect energy levels between the valence and conduction band, which can act as a jumping-off place for photon generated electrons (e^-)[6]. These electrons can then be activated by photons and promoted to the conduction band under visible light. This means lower photon energy is needed for this process, making the absorption edge be in the visible region of the electromagnetic spectrum[6]. Therefore, the band gap energy of the LDH materials would be tuned, improving their photocatalytic properties[6,10].

There are several examples of the application of LDHs for photocatalytic degradation of dyes such as the degradation of Rhodamine B and 6G by ZnCr-CO_3 LDH[9], Methyl Orange by ZnAl-CO_3 LDH[4], CuAl-CO_3 LDH[11] and Ni-Co LDH[12].

5.1.3 Magnetic filtration

Magnetic materials can be used in water purification, for potential removal of magnetic contaminants present in wastewater and can be adapted for several important applications, such as ore mining and seeding magnetic flocculents[13]. Moreover,

magnetic materials can be combined with other processes, enabling a more efficient purification of water[13]. In terms of magnetic separation, a common type used is a High-gradient magnetic separation (HGMS)[13–17]. HGMS is made of a bed of magnetically sensitive wires which are fixed into an electromagnet (figure 5.2).

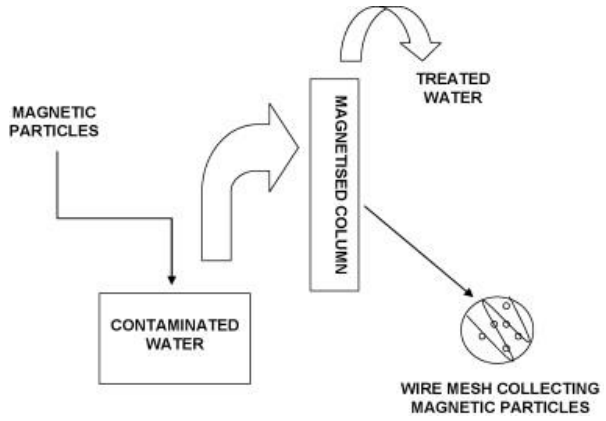

Figure 5.2: HGMS system, adapted from reference[13].

Magnetic separation can be carried out directly as well, where the intrinsic properties of the materials (ions or solids) as a response to a magnetic field can be used for separation[13]. This hinders the salt ions leaking into the pipelines[13]. Removing the salt ions from the pipelines would prevent scaling by the deposition of these ions.

Magnetic nanomaterials present different magnetic behaviour than their bulk counterpart, which alters the filtration process[13]. The regeneration of the filter could be proven difficult if the scaling down produces a hard material. The use of materials with low magnetic remanence and superparamagnetic properties are usually preferable for magnetic separation applications[13]. Magnetic nanoparticles could be separated due to ease of direction of the magnetisation, which varies as a result of the different ordering of the atoms in its structure[13,18].

5.1.4 Carbon nanotubes (CNTs) composite membranes

Carbon nanotubes (CNTs) have been gaining more attention for membrane applications due to their high-specific surface area, high mechanical strength and chemical inertness[19–24].

Polymeric membranes, traditionally used for water purification, have some major drawbacks, such as low selectivity, chemical and thermal resistance and fouling[25]. The combination of polymers and CNTs, due to CNTs inherent properties, could be a solution to some of these issues. CNTs membranes have been shown to be able to discriminate compounds both based on size and functionalization added[25]. CNTs-based membranes have been produced on a wider scalein recent years, especially for water treatment applications[25–30]. Most of these membranes are made by embedding the CNTs into a polymeric matrix, improving the selectivity and permeability of the polymeric matrix[25]. These new membranes, referred as CNTs-MMMs, exhibit good properties, as well as low cost and easy operation. However, their development is still being under study, as there are some issues with aggregation and uneven distribution of the CNTs throughout the membrane[25]. CNTs have also been mixed with reduced graphene oxide (rGO). These membranes were shown to display high removal efficiency of organic compounds, antifouling properties and clean water permeability[31].

5.1.5 Aims of this chapter

The main aim of this piece of our work was to develop novel composite membranes, using BN or BNOx as the main components. The idea is to take advantage of the properties and capabilities of BN/BNOx as a building block for membranes but adding extra functionalities and properties by the addition of other materials.

We plan to introduce LDH component with the goal of degrading the dyes. One of the main problems of membranes is fouling, so being able to remove the material retained is a vital step towards reusability of the membranes. LDHs have been shown to exhibit photocatalytic activity with some of the dyes studied in this work, in particular Methyl Orange. Having the LDH integrated in the membrane opens the possibility for an easy and cost effective way of cleaning the membranes, by exposing them to light in order to degrade the dye present.

Apart from dye removal, the membranes could be used for other filtration applications. Another common contaminant in water is magnetic particles. In order to tackle this issue, we plan to use magnetic nanoplates to produce membranes with magnetic modalities. The goal would be to have magnetic nanoparticles retained in the membrane through the

interaction of those with the magnetic nanoplates present in the membrane. This could offered a simple way to remove magnetic impurities from water.

Another useful option when making membranes would be to be able to tune to pore size and, therefore, selectivity of the membrane. For this purpose, we plan to add CNTs to the BN based membranes. The goal would be to study the effect of different amounts of CNTs into the performance of the membranes. CNTs, most likely, will intercalate in between the nanosheets and layers of the membranes, creating more space which could, in theory, allow for tuning of the retention capabilities of the membrane.

5.2 BNOx and CuAl LDH composites

5.2.1 Investigation of BNOx – LDH mixtures.

Previously LDHs had been used in literature for degradation of dyes like Methylene Blue[5]. Therefore, we decided to mix BN, due to its great retention performance, with LDH to take advantage of their catalysis property and be able to produce composite membranes. The objective is to be able to degrade the dye to overcome the potential fouling of the membranes with the idea of reusing the membranes. LDHs were synthesised and provided by Áine Coogan.

LDH layers have a positive charge, with a zeta potential of +35.4 mV (figure 5.3). Because of this positive charge, the zeta potential of exfoliated BN and BNOx were analysed, with the idea to see if any would have a negative charge so LDH and BN based layers could bind through electrostatic interactions. BN shows a small zeta potential of -5.29 mV (figure 5.3). BNOx was also tested and found to have a negative charge of -44.7 mV (figure 5.3). The zeta potential graph of BNOx displays two peaks, one at -32.8 mV and the other at -52.9 mV. This negative surface charge of the oxidised BN is thought to be due to the OH groups that have been introduced during the oxidation process.

A

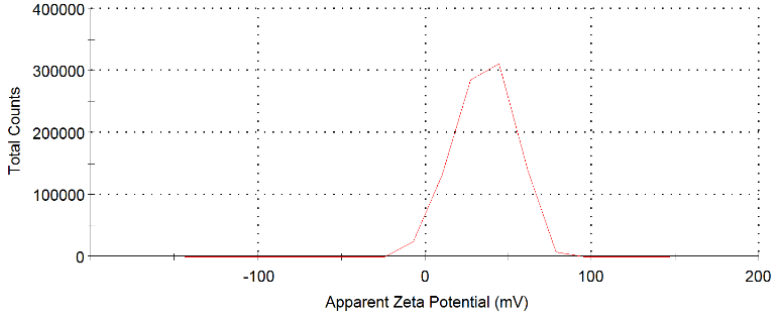

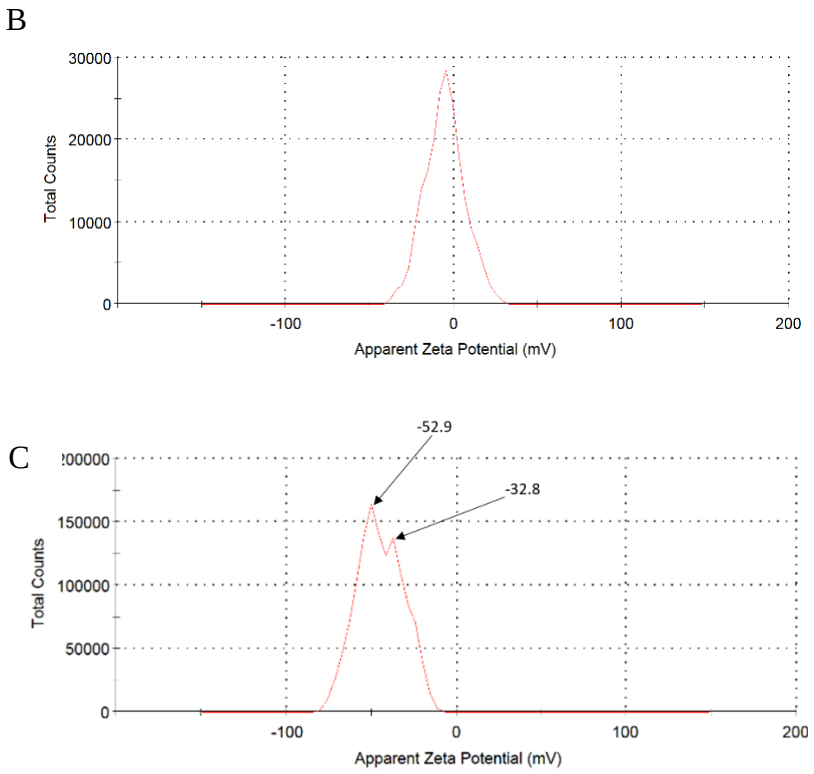

Figure 5.3: Zeta potential measurements of A) CuAl LDH, B) BN and C) BNOx.

Therefore, it was decided to mix the BNOx with the LDH so their different charges would allow the electrostatic interaction and formation of the membrane.

Initially, XRD powder was carried of the individual CuAl LDHs and BNOx to identify the characteristic peaks of each compound (figure 5.4).

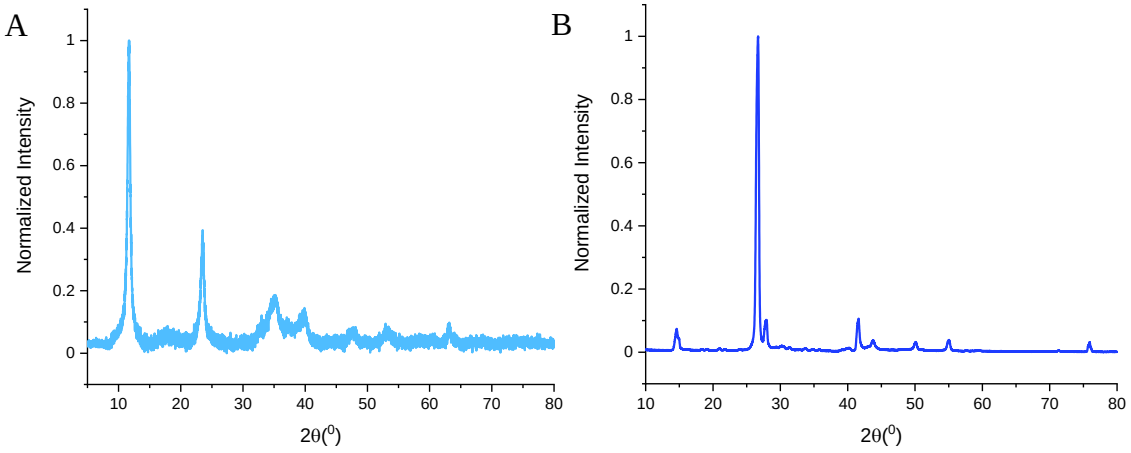

Figure 5.4: Powder XRD patterns of A) CuAl LDH (2θ 5-80°) and B) BNOx (2θ 10-80°).

The powder XRD of the LDH confirms the presence of the CuAl LDH. The powder XRD of the BNOx showed the characteristic peaks corresponding to boron nitride, as well as some peaks corresponding to $B(OH)_3$, confirming the oxidation of BN.

TEM images of the CuAl LDH were taken and are shown in figure 5.5.

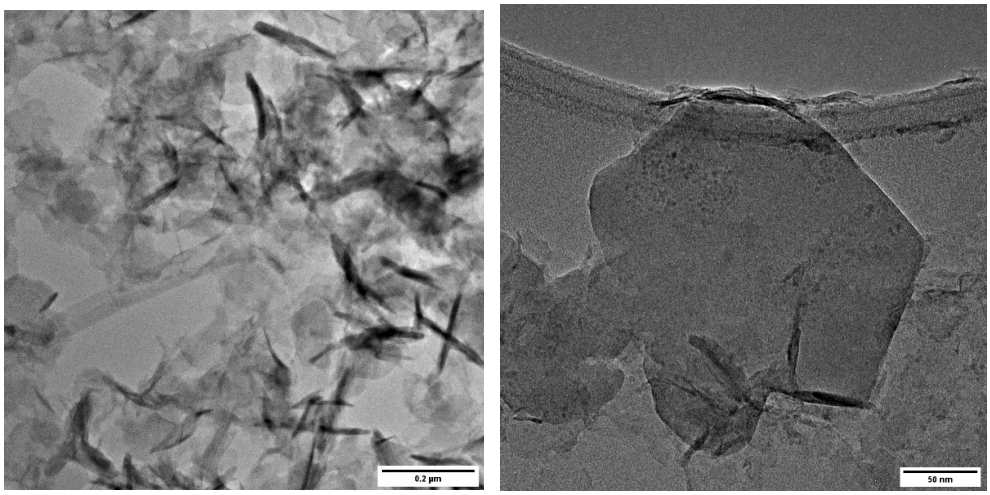

Figure 5.5: TEM images of CuAl LDH.

The mixture of BNOx and LDH were prepared by two ways:

- The two materials were mixed and sonicated together for 24h in Millipore water.
- BNOx was sonicated for 24 hours first and then mixed with the LDH. The mixture was then stirred for 2 hours.

Different percentages in weight of both compounds were used to find the optimal ratio of the BNOx-LDH and to produce the highest quality membranes.

Table 5.1: Percentages weight of LDH and BN-Ox for each solution.

Sample	wt% BN	wt% LDH
A.1	50	50
A.2	50	50
B	80	20
C.1	80	20
C.2	80	20
D	30	70
E	40	60

The initial solution, right after mixing the two, had a light blue colour. However, it was discoveredthat with certain percentages of LDH, particularwt% of LDH (50 wt%), the colour of the solution changed to a light brown colour after the sonication. This was thought to be due to the formation of copper oxide (CuO). The lower percentages in weight of the LDH remained blue after the exfoliation. The 10 % in weight of the LDH wasn't very stable once the sonication was stopped and the suspensions precipitated very quickly (figure. 5.6 F). However, the solution made using 20 % in weight of LDH was stable after the sonication was stopped, while remaining blue in colour.

Powder XRD was carried out of the samples made with 50, 20 and 10 wt % of the LDH.

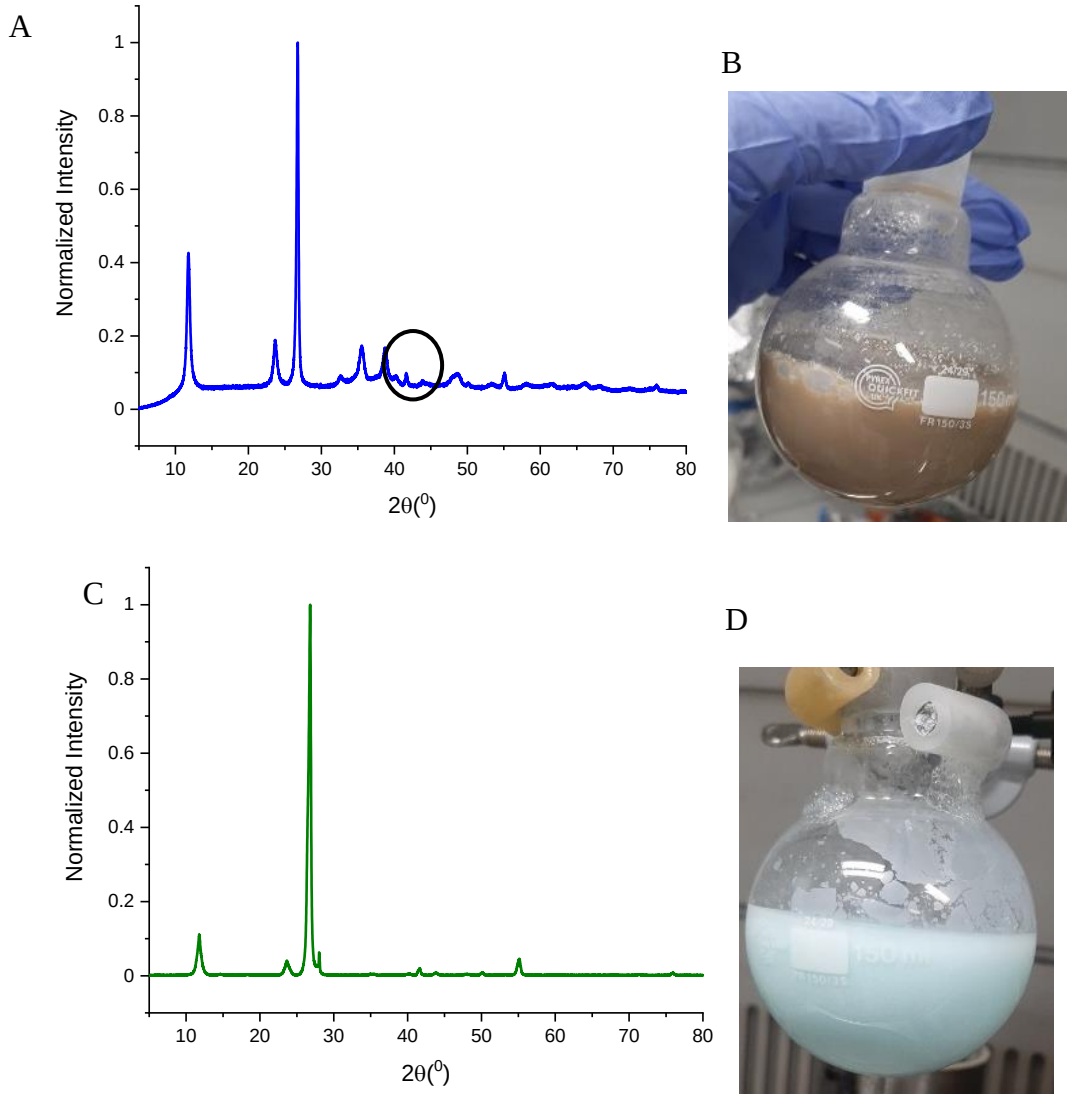

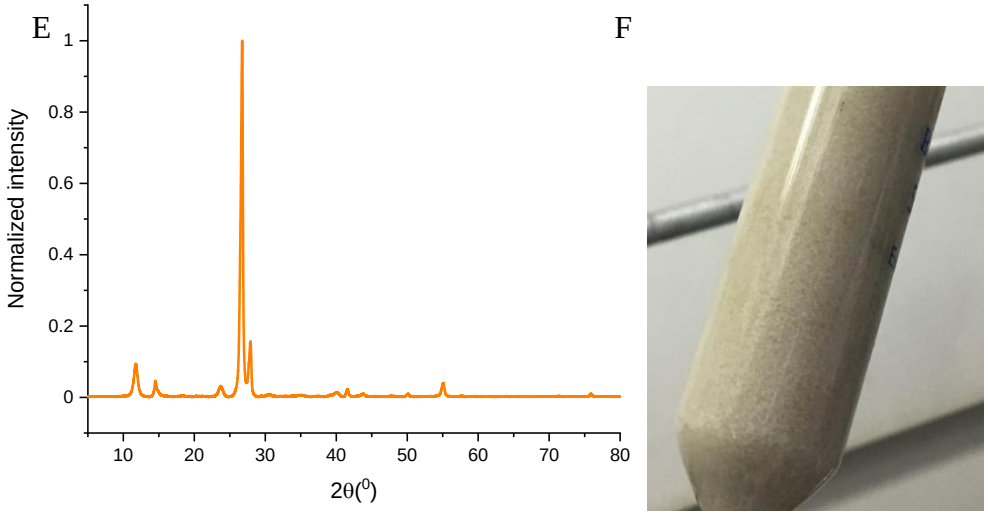

Figure 5.6: Powder XRD patterns of A) 50:50 BNOx:LDH, C) 80:20 BNOx:LDH and E) 90:10 BNOx:LDH and the corresponding images of the solutions, B) 50:50 BNOx:LDH, D) 80:20 BNOx:LDH and F) 90:10 BNOx:LDH.

Powder XRD of the 50:50 BNOx:LDH showed peaks corresponding to copper oxide (CuO), at (002) and (111), marked with the blue circle in figure 5.6 A. This confirms the colour change of the solution from blue to brown is due to the partial transformation of CuAl LDH to CuO. Furthermore, the peaks corresponding to $B(OH)_3$ had disappeared and only the peaks corresponding to BN and CuAl LDH are present, which seems to indicate that the formation of the CuO is facilitated by the presence of the OH groups in the BNOx when the same amount of both compounds are present. The other powder XRD show the characteristic XRD pattern of BN, $B(OH)_3$ and CuAl LDH, and no peaks corresponding to CuO, indicating thatthe LDH didn't transform into the corresponding oxide, which correspond with the blue colour of the solutions.

FTIR spectra of the samples have also been recorded (figure 5.7).

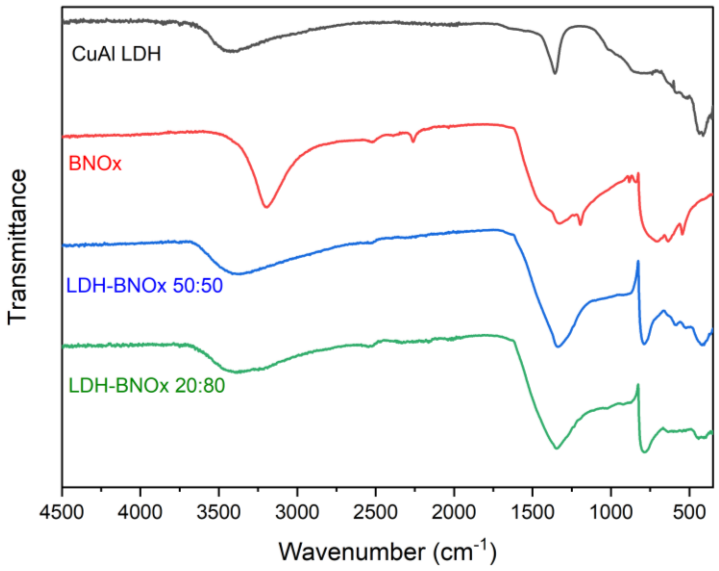

Figure 5.7: FTIR spectra of CuAl LDH (black), BNOx (red), 50:50 LDH:BNOx (blue) and 20:80 LDH:BNOx (green). Spectra ran from 4500-350 cm^{-1}.

The BNOx and both LDH:BNOx show the peaks corresponding to B-N (around 750 cm^{-1}) and B-N-B (1250-1500 cm^{-1}), characteristic of BN. The FTIR of the BNOx also showed a sharp peak around 3000-3200 cm^{-1}, which correspond to the OH stretch and NH corresponding to the partially oxidised BN. The FTIR spectra of LDH shows a broad OH stretch at 3500 cm^{-1}, due to the hydroxide layers. Both the LDH and LDH:BNOx show the characteristic peak at around 400 cm^{-1} due to the metal-oxygen vibrations due to the LDH. LDH:BNOx FTIR show a broader peak around 3000-3500 cm^{-1}, as a result of the interaction of the LDH and BNOx. These FTIR spectra indicate that the two materials have been successfully mixed together, observing peaks characteristic of both materials in the FTIR of BNOx:LDH.

SEM images of the 20:80 LDH:BNOx were taken. The sample was prepared by drop casting the solution on a Cu-mesh lacey carbon TEM grid (figure 5.8).

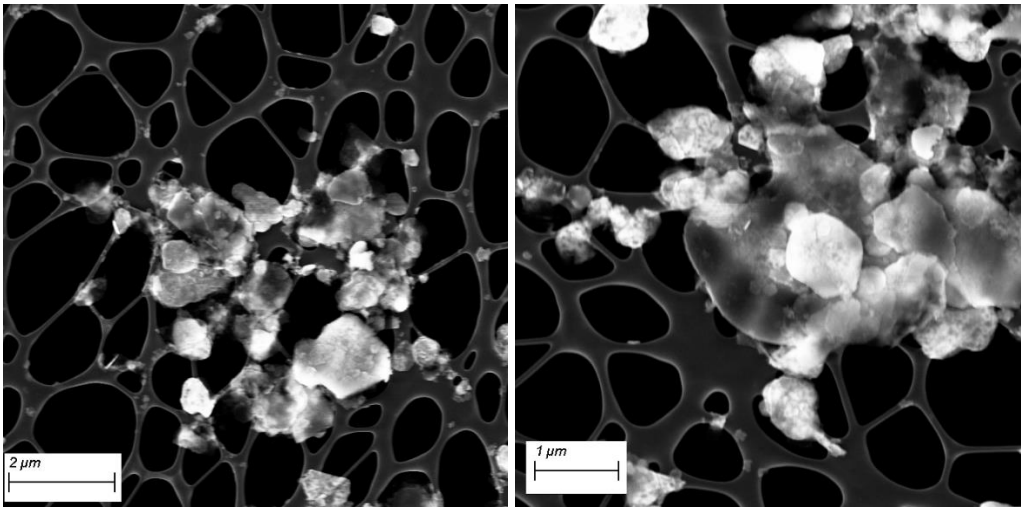

Figure 5.8: SEM images of 20:80 LDH:BNOx taken using InLens, 3.00 kV on TEM carbon grids.

The SEM images showed both the BNOx nanosheets as well as the CuAl LDH. The bigger nanosheets were identified as the BNOx and the smaller ones as LDH. The LDH charge more under the electron beam, so they were easy to identify. The BNOx nanosheets in these SEM images show similar size to the ones obtained when exfoliating the BNOx on its own. The SEM confirmed that the two materials are combined and stay together after the sonication, which indicates that these two materials are compatible and suitable for the formation of membranes.

5.2.2 BNOx-LDH composite membranes

The BNOx-LDH suspensions in water were then used to produce membranes using the same procedures which are described in previous chapters. The membranes were then tested using different dyes. Initially, Evans Blue was the dye chosen for the test. Several membranes were tested to try to figure out the best amount of LDH to keep the high retentions observed with the BN and BNOx. UV-Vis are shown in figure 5.9 and table 5.2.

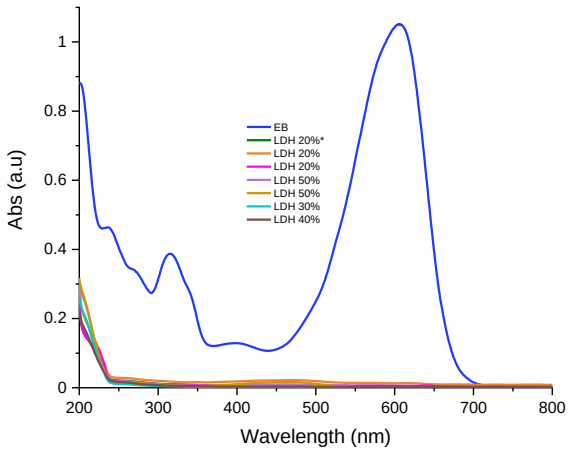

Figure 5.9: UV-Vis spectra of the retention of 20 mL Evans Blue of the BNOx - LDH based membranes (different percentages in weight).

Table 5.2: Retention values of the BN-LDH membranes (different % in weight).

Sample	wt% BN	wt% LDH	% Retention
A.1	50	50	100
A.2	50	50	100
B	80	20	99
C.1	80	20	99
C.2	80	20	99
D	30	70	100
E	40	60	100

The differences in color and stability of the solution, brown in the case of A and blue for the rest and whether the BNOx and LDH would come out of solution, didn't affect the performance of the final membranes, with all of them showing high retention values (99-100%). This indicates that the addition of the LDH doesn't reduce the retention of the membranes, which makes it suitable as a component of the membranes. Even though the retention was pretty much the same for all the different percentages in weight, it was decided that the best combination was 80% BNOx and 20% LDH due to the fact that these membranes exhibited the best mechanical stability.

After the investigation of membranes for the retention of Evans Blue, the membranes were then tested using Methyl orange and Methylene blue dyes (figure 5.10 and table 5.3).

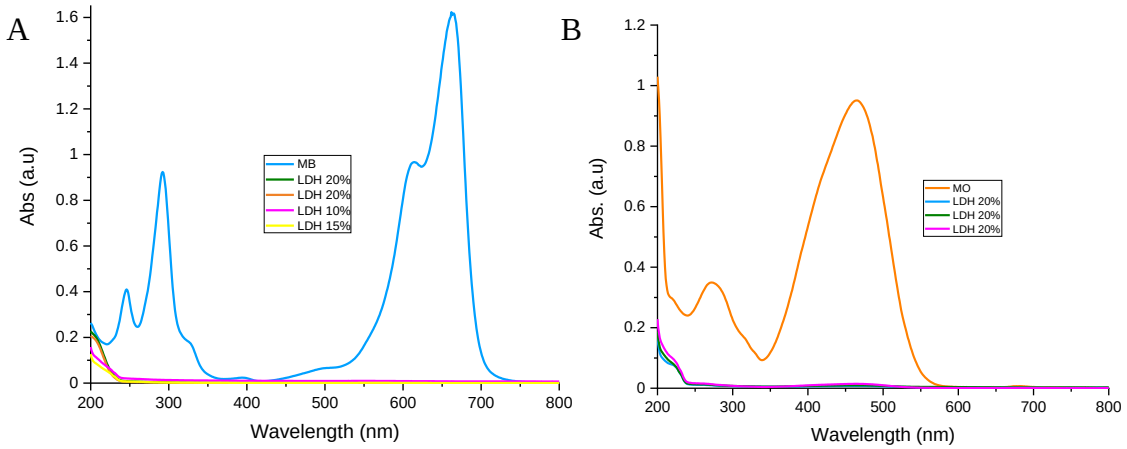

Figure 5.10: UV-Vis spectra of the retention of 20 mL A) Methylene Blue and B) Methyl Orange of the BNOx and LDH membranes.

Table 5.3: Retention values of the BN-LDH membranes.

Membrane	Dye	% Retention
20% LDH	Methylene Blue	100
20% LDH	Methylene Blue	100
10% LDH	Methylene Blue	100
15% LDH	Methylene Blue	100
20% LDH	Methyl Orange	99
20% LDH	Methyl Orange	99
20% LDH	Methyl Orange	99

The retention of the membranes for these other two dyes was also very high (99-100%), which is very similar to the values obtained with the BNOx membranes on their own. All of this indicates that the performance of the membranes is not altered by the introduction of LDH. The membranes with 10 wt% and 15 wt% of the LDH showed lower mechanical stability of the solutions once the sonication was stopped, although the retention wasn't affected. Due to the combination of highest mechanical stability and high retention, it was decided to continue using the 20 wt% LDH membranes for this work.

SEM images were taken of the 20 wt% of the LDH membranes.. Top-view and cross-section images were both taken and are shown in figure 5.11. The thickness of the membrane was recorded to be 65.2 ± 1.8 µm, which is slightly lower than the BNOx on its own (around 20 µm less) and significantly lower than BN membranes (around 75 µm less). This indicates that the membranes with BNOx and LDH are more tightly packed

while still keeping high retention values (99-100%). This tighter packing of the membranes is likely due to the electrostatic interaction between the negatively charged BNOx nanosheets, and the positively charged LDH layers. Another effect could be the lower amount of BNOx present in the membranes. The LDH have a smaller size, so they could be packed more tightly, causing the whole membrane to show a reduction in thickness.

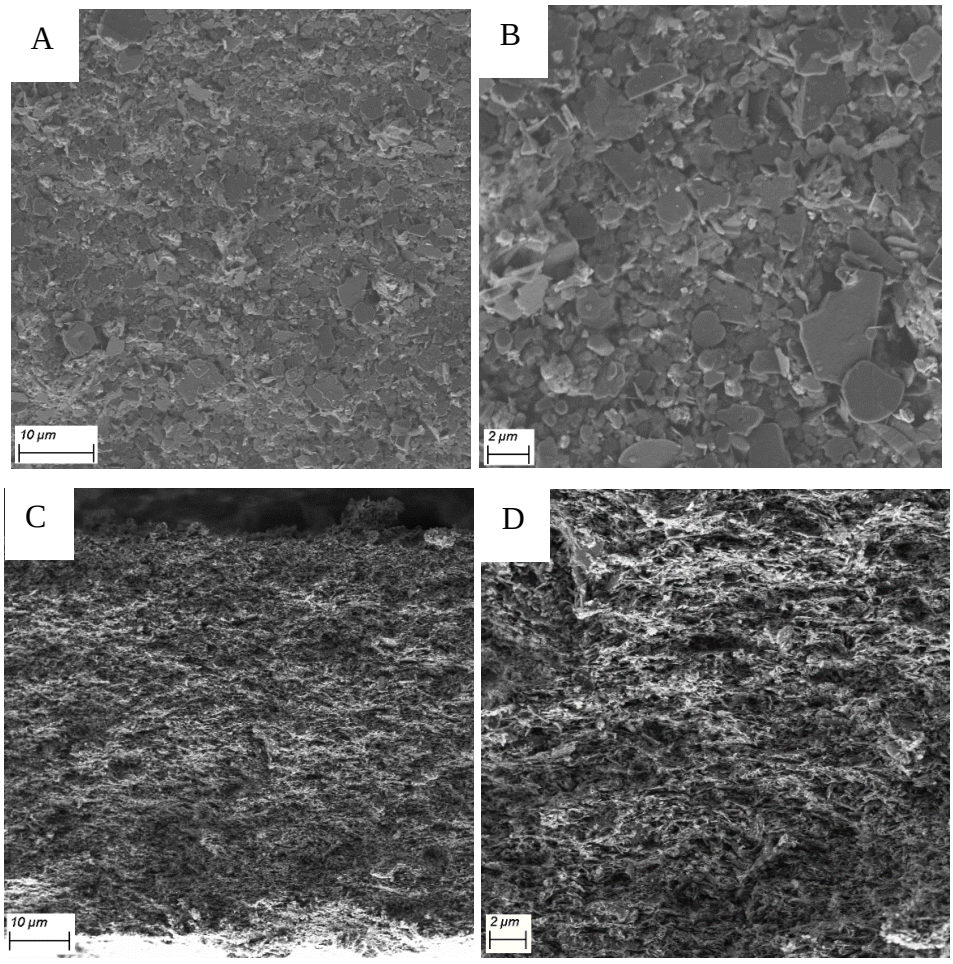

Figure 5.11: SEM images of A) and B) Top view and B) and d) cross-section of the 20% in weight of LDH membranes. Taken with SE2 and EHT: 3.00 kV (top-view) and 2.50 kV (cross-section).

5.2.3 Investigation of photodegradation of dyes

Based on previous work found in the literature, LDHs have been proven to degrade Methylene Blue[5] and Methyl Orange[32], therefore it was decided to try to use these LDHs

for degradation of these dyes. The idea behind this was to be able to reuse the membranes after photodegradation of the retained dye.

The first experiment was to test whether a membrane from pure LDH would be effective. The LDH membrane was produced by filtration and tested, using Methylene Blue. This membrane showed a lower retention (74%) than the BNOx and BNOx-LDH membranes (figure 5.12 A). Furthermore, the membrane was very fragile and, upon drying, it broke completely (figure 5.12 B).

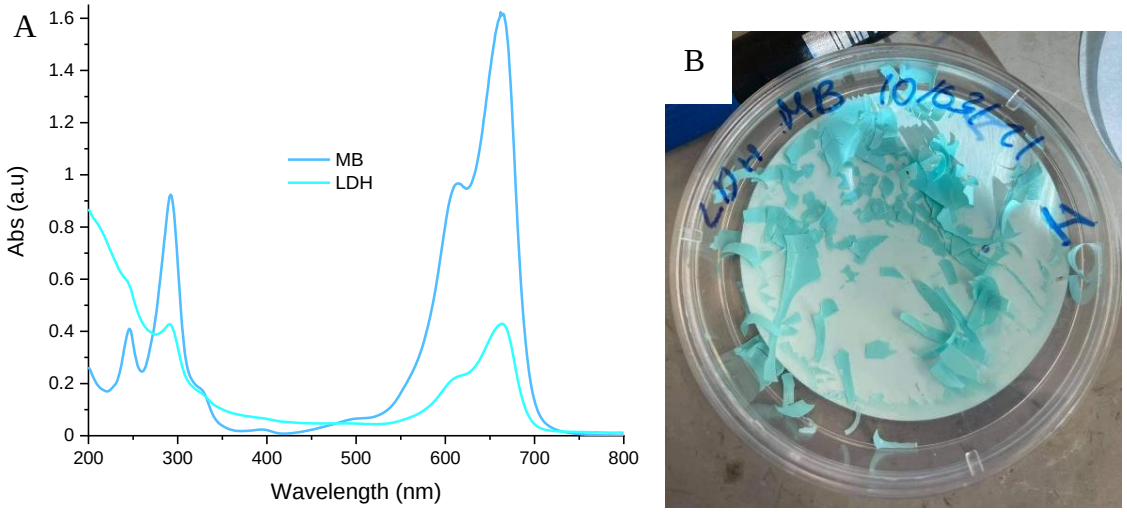

Figure 5.12: A) UV-Vis spectra of the retention of 20 mL Methylene Blue through the LDH membrane and B) picture of the broken LDH membrane after drying.

Therefore, BNOx is necessary component of the membrane to increase its retention and improve the stability. The membranes used for subsequent tests were the ones made with 20 wt% of LDH, as this composition was proven to be the most stable in solution and producing most mechanically stable membrane (see below).

The initial test was done by passing Methylene Blue through a membrane and then illuminating it with UV light (wavelength of 264 nm) overnight. The membrane colour was then compared to BNOx-LDH membranes before and after passing Methylene Blue (figure 5.13).

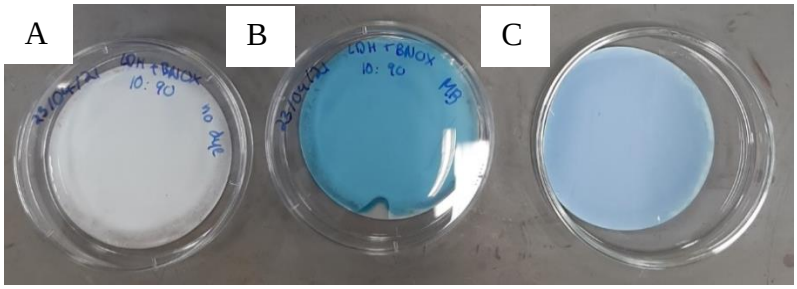

Figure 5.13: Comparison of BNOx-20% LDH membrane A) before, B) after passing Methylene Blue and C) after passing the dye through and illuminating the membrane with UV light.

The comparison of the membranes allows us to see difference in the colour on the surfaces of the three membranes. The membrane with no dye passed through is white with a light tinge of blue due to the LDH. However, the membrane after filtering the dye shows a bright blue color, as a result of the Methylene Blue being retained by the membrane. Moreover, the membrane after illumination with UV light shows a much lighter blue color, which seems to be indicating that the dye is being degraded. This change in colour could also be due to a drying effect. Methyl Orange was also tested for degradation under UV-light.

The tests were carried out by passing Methyl Orange through a membrane with the 20 wt% of LDH and then exposing the membrane to UV light overnight (figure 5.14).

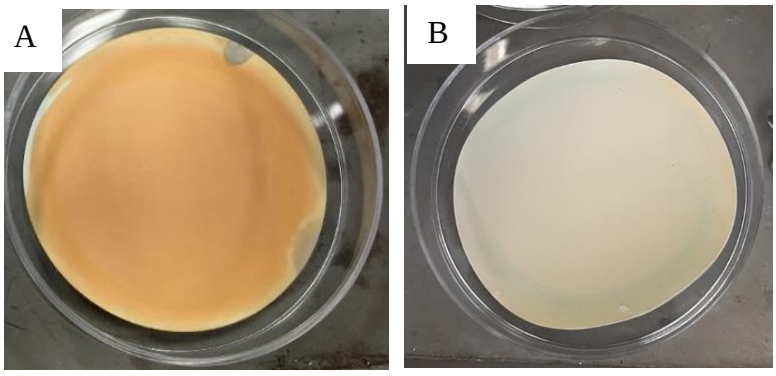

Figure 5.14: Comparison of BNOx-20% LDH membrane A) after passing Methyl Orange and B) after passing the dye through and illuminating the membrane with UV light.

Interestingly, it was noted that Methyl Orange seemed to be degrading under visible light in the lab. Therefore, it was decided to test the effect of illuminating the membranes under visible light to monitor the degradation of Methyl Orange. To compare, two types of membranes were prepared, one with just BNOx and another one with BNOx and 20 wt% of LDH. Both types of membranes were then tested using Methyl Orange and subsequently exposed to ambient light in the lab over a period of 2 weeks, and their change in colour was recorded. In order to test if this degradation was due to the exposure of light, two membranes (one of each type, BNOx and BNOx-LDH) were kept in the dark while the other two were exposed to the light for 24 hours (figure 5.15).

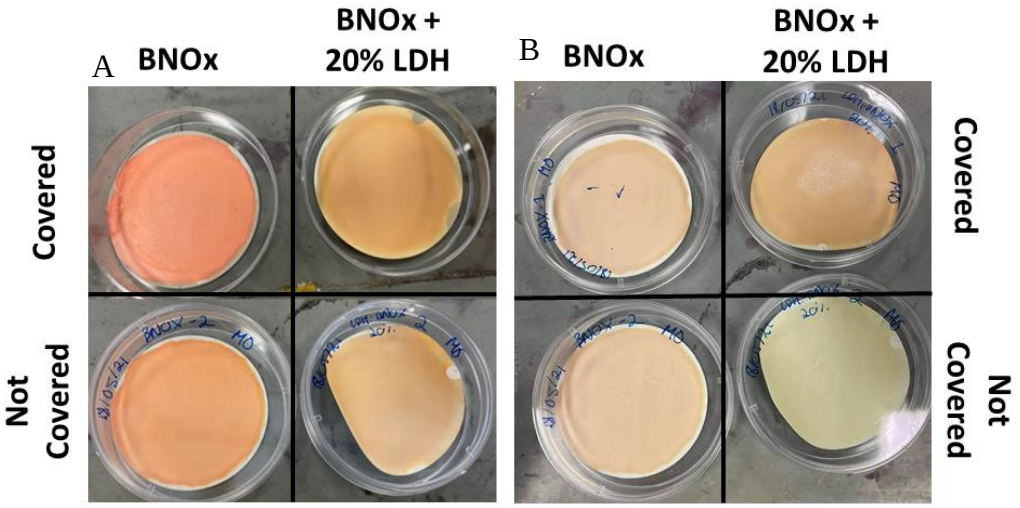

Figure 5.15: Images of BNOX and BNOx-20wt% LDH A) right after passing the Methyl Orange through the membranes and B) after 24 hours under darkness or visible light.

The membranes right after the filtration have a bright orange color, whereas after the 24 hours the color is much lighter. The color of the BNOx + 20 wt% LDH exposed to light shows the lightest color, going from a bright orange to a yellowish-orange, showing what appears to be a higher degree of degradation. The color of the membranes was observed again after 2, 4, 7 and 14 days (figure 5.16).

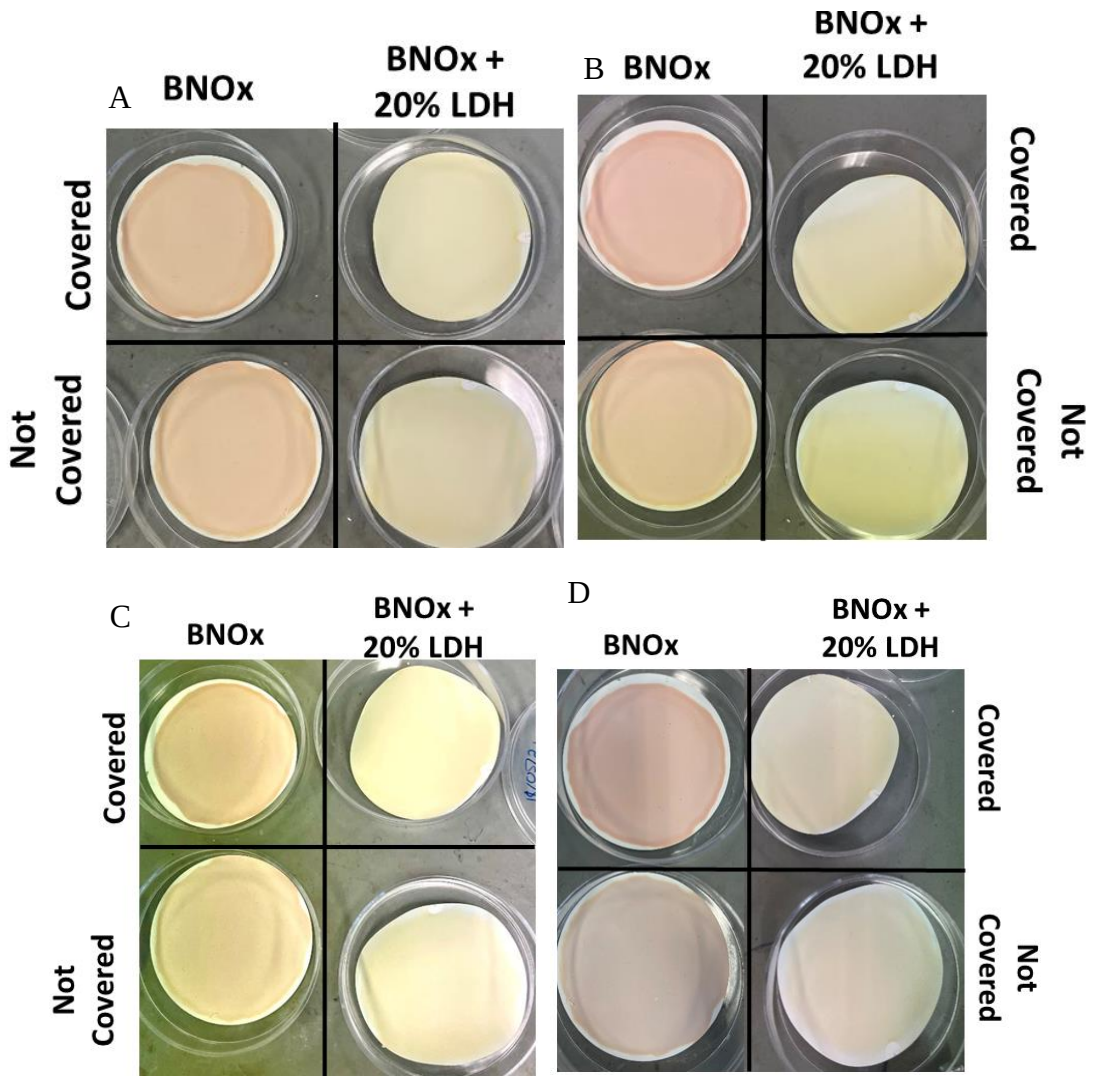

Figure 5.16: Images of BNOX and BNOx-20% LDH A) 2 days, B) 4 days, C) 7 days and D) 14 days after passing the Methyl Orange through the membrane.

The colour of the membranes clearly continue to lighten with the time. Even though decolouring can be observed in both types of membranes, the color change happens faster and is more noticible in the membrane with LDH present, indicating the LDH, potentially, makes the photodegradation process faster. The OH groups present in the BNOx could be also contributing in the degradation process, explaining why decolouring is also observable in the case of the BNOx membranes.However, this could also be due to the a combination of drying effects as well as photodegradation. Nevertheless, the decolouring is more prominent in the case of the BNOx-LDH membrane, where there's a change in colour from orange to pale yellow. However, tests with BNOx membranes would need to be done to prove this. The membranes kept in the dark also showed some

degradation, although not as much as the one observed for the membranes exposed to light. This, however, is likely due to the membranes being exposed to light after passing the dye and then every time a picture was taken, explaining why the color change is happening but to a lesser degree than the ones constantly exposed to light.

As the results seems to indicate that the dye is degraded in the membranes due to the presence of LDH, it was decided to determine the rate of the photodegradation. Initially we tried to disperse the membrane in water and remove the LDH-BN from the suspension by centrifugation. The suspension was centrifuged at 9000 rpm for 10 minutes and the UV-Vis spectrum of the supernantant was recorded (figure 5.17).

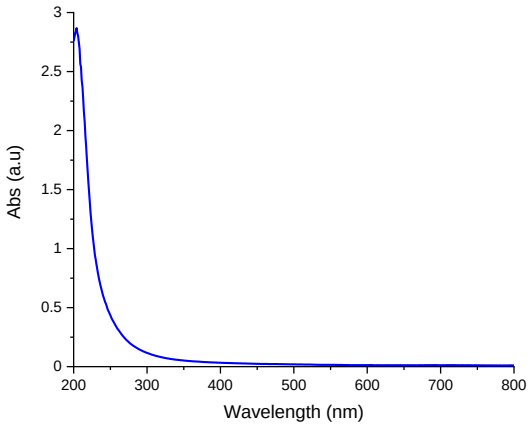

Figure 5.17: UV-Vis spectra of the supernatant of BNOx-LDH after centrifugation at 9000 rpm.

The UV-Vis spectra had no apparent scattering of the sample at the 400-800 nm, indicating that material was mostly removed by the centrifugation. However, a Tyndall effect experiment has shown the presence of some nanomaterial left in the supernatant.

The next step was to check whether decreasing concentrations of Methyl orange would be picked up by the spectophotometer. In order to do so, 4 solutions of different concentrations of the dye were prepared, with the lowering of the concentrations mimicking the degradation of Methyl orange, starting with the concentration used for the retention tests (50 µM). Then, as the dye degrades, the concentration of the dye should decrease. For example, an absorbance of 0.2 from the permeate of one of thesemembranes would correlate to around 80% degradation. To estimate the absorbance, the formula used was:

$$\frac{A_2}{A_1} = \frac{C_2}{C_1}$$

Which comes from the Beer-Lambert Law, A = εcl. The UV-Vis spectra of the different concentrations are shown in fugure 5.18. and the different expected absorbances are shown in table 5.4.

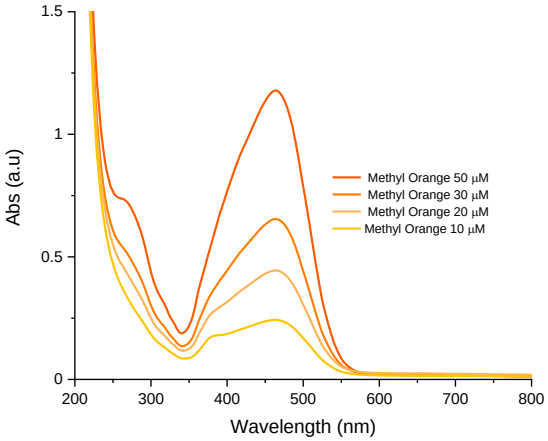

Figure 5.18: UV-Vis spectra of the different concentrations of Methyl Orange.

Table 5.4: Table of the concentrations of the different solutions and their expected absorbances

Sample	Methyl Orange	Expected absorance
1	50 µM	~1
2	30 µM	~0.6
3	20 µM	~0.4
4	10 µM	~0.2

The UV-Vis spectra show that the spectophotometer can pick up the decreasing concentrations of the dye, which indicates that the use of UV-Vis spectroscopy could be used to monitor the degradation of the Methyl Orange.

However, the dye is adsorbed to the membranes, so the dye had to be desorbed from the membrane to be able to monitor its absorbance in solution over time to calculate the amount of dye degraded. In order to do so, the membranes were fully lifted from the template and resuspended in the water. After that the membranes were sonicated in 50 mL of MP water for 20 mins.. The solution was then centrifuged to try to separate the

dye from the BNOx-LDH (9000 rpm for 10 min). However, the supernatant was clear and the pellet, composed of the BNOx-LDH, remained orange. This indicated that the dye was strongly adsorbed in the BNOx-LDH, not coming out in solution. As the dye could not be extracted back in water from the nanomaterials, UV-Vis couldn't be used to monitor the degradation of the dye. This was due to the strong scattering of both nanomaterials in the region where Methyl Orange has the maximum absorbance.

Literature seems to indicate that Methyl Orange can be desorbed from surfaces by using NaOH[33]. Based on this, it was decided to treat the membranes using 0.1 M NaOH to try to desorb the Methyl Orange from the surface of the membrane. The membranes were sonicated for 4 hours in the NaOH solution, with the solution turning yellow, indicating the solution was basic (Methyl Orange turns yellow under basic conditions). The mixture was then centrifuged to get rid of most ofof the BNOx and LDH from suspension. The supernatant had a slight yellow tinge, indicating some of the Methyl Orange is potentially in solution or that the dye and some of the degraded product had been desorbed from the membrane. The supernatant was also concentrated to see if that would help with the detection of the products. The UV-Vis spectra of the supernatant were recorded. Methyl Orange was also put under the same basic conditions to be able to compare the peaks. The peak of normal Methyl Orange and basic Methyl Orange didn't show a major difference in the peak position (figure 5.19 A). However, the spectra obtained by the supernatant was broad and didn't have a distintive band that could be use for quantifying the amount of Methyl Orange or degraded product in the supernantant (figure 5.19 B).

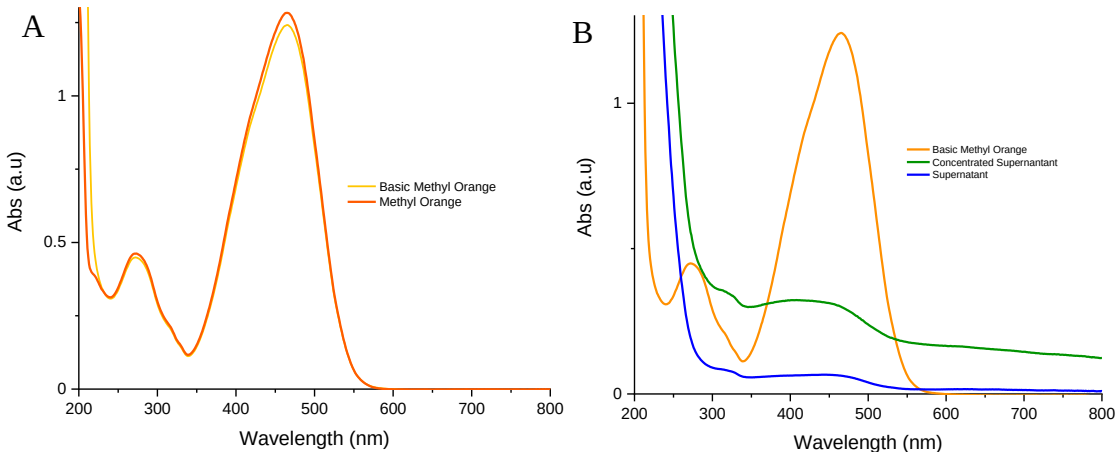

Figure 5.19: UV-Vis of B)Methyl Orange and basic Methyl Orange and B) basic Methyl Orange, supernatant and concentrated supernatant after being mixed with 0.1 M NaOH.

As the tests done to try to quantify the amount of Methyl Orange left after the degradation or the degraded product were inconclusive, it was decided to do a study of the degradation of the dye in solution in the presence of BNOx - LDH mixture..

A higher concentration of Methyl Orange was used (500 µM instead of 50 µM), as once the dye was adsorbed to the BNOx-LDH, the concentration left in solution was too low for measuring. The solution was left in the darkness for 3 hours to allow for the adsorption to happen.

LDHs have been reported as exhibiting photocatalytic degradation of organic dyes in literature, such as rhodamine B and 6G by ZnCr-CO_3 LDH[9], Methyl Orange by ZnAl-CO_3 LDH[4] and CuAl-CO_3[11]. The degradation reported follows a pseudo-first order Langmuir-Hinshelwood reaction. A first order reaction, following the Lagmuir-Hinshelwood model, is characterized by:

$$\ln \frac{C_0}{C} = K_{app} t$$

Where:

- C_0 is the initial concentration of the compound studied, Methyl Orange in this case
- C is the concentration at the moment of measuring
- K_{app} is the apparent reaction rate
- *t* is the time of reaction

After the induction period of 3 hours, to allow for the dye to be adsorbed by the BNOx and LDH, the UV-Vis was recorded and there was a large drop absorbance, of 45%. This indicates that around half of the dye had been adsorbed to the BNOx and LDH during this induction period. The solution was left exposed to ambient light in the lab and aliquots were taken every 30 min for analysis. Each aliquot was centrifuged and the UV-Vis was recorded for each supernatant, to estimate the amount of dye being degraded (figure 5.20 A). The maximum absorbance at each time was used to calculate the ln (C_0/C) and was plotted against the time (figure 5.20 B).

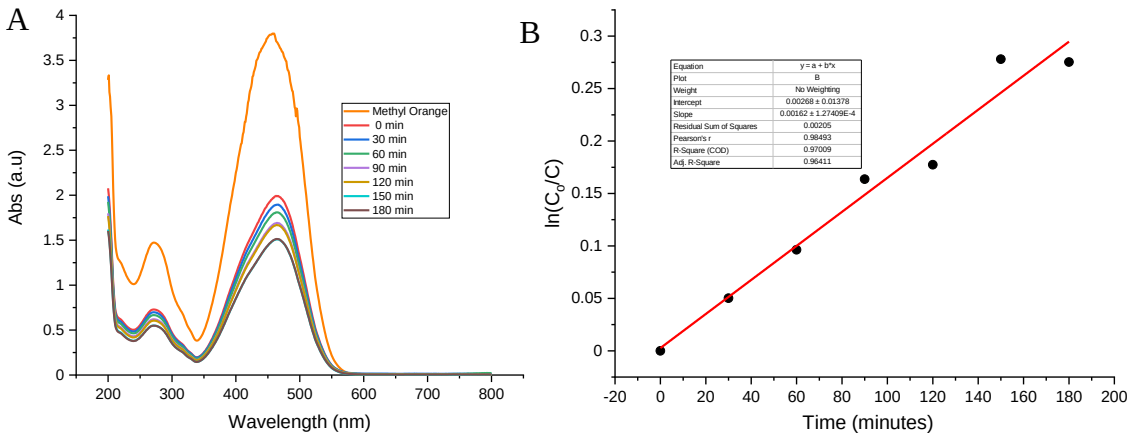

Figure 5.20: A) UV-Vis of Methyl Orange after different times under the presence of BNOx-LDH illuminated with light and B) kinetics of decolourisation of Methyl Orange by BNOx-LDH, adjusted to a pseudo-first order.

The reaction follows a pseudo-first order kinetic model well, following the Lagmuir-Hinshelwood model, with an R^2 value of 0.97. The apparent rate of reaction, $K_{ap}p$, can be calculated using the Langmuir-Hinshelwood model formula, obtaining a value of 0.0016 min^{-1}. This experiment shows that the degradation of Methyl Orange by BNOx-LDH can be observed and the kinetics studied in solution, with a kinetics of pseudo-first order following the Lagmuir-Hinshelwood model. However, this test was done in solution and the kinetics in the membrane (solid) are likely to be different. Therefore, there is the need for a system that would allow the possibility to study this process in the solid state, as it happens in the membranes.

5.3 BN - Fe_3O_4 composites

5.3.1 Fe_3O_4 nanoplates

The Fe_3O_4 nanoplates have been synthesized following a method developed by Dr. Sarah McCarthy. The two iron salts, $FeCl_3$ and $FeCl_2$, were added at the same time, to a solution of ethylene glycol, HMTA and P123K pre-heated to 100 °C. Once the salts are added, the reaction has started and the reaction vessel was kept under Ar for 2 hours. The P123K directed the growth of the nanoparticles to form the nanoplates. After the 2 hours, the nanoplates were cleaned by alternating between KOH in water and MeOH and separating the material with a magnet, to ensure the iron salts that had not reacted and any other

non-magnetic impuritiesstayed in solution. Once the material was cleaned, the sample was dried and characterised by TEM.

Once the nanoplates were prepared, TEM was taken (figure 5.21) to confirm the shape of the material.

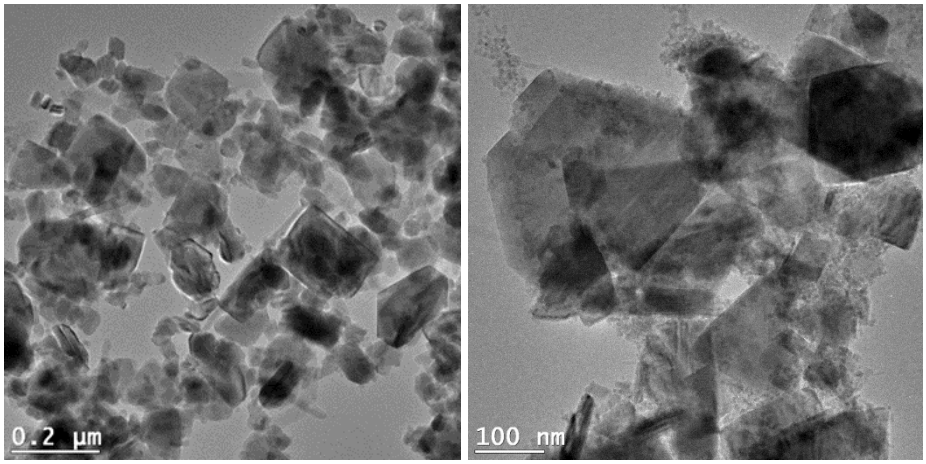

Figure 5.21: TEM images of Fe_3O_4 nanoplates.

The TEM images show nanoplates, with some nanoparticles appearing in the background. The shape of this material is very similar to the BN and BNOx nanosheets, which could make it a good candidate to be mixed with BN/BNOx to produce new composite membranes for several applications, including magnetic separation.

The magnetism of the nanoplates was checked using VSM (figure 5.22).

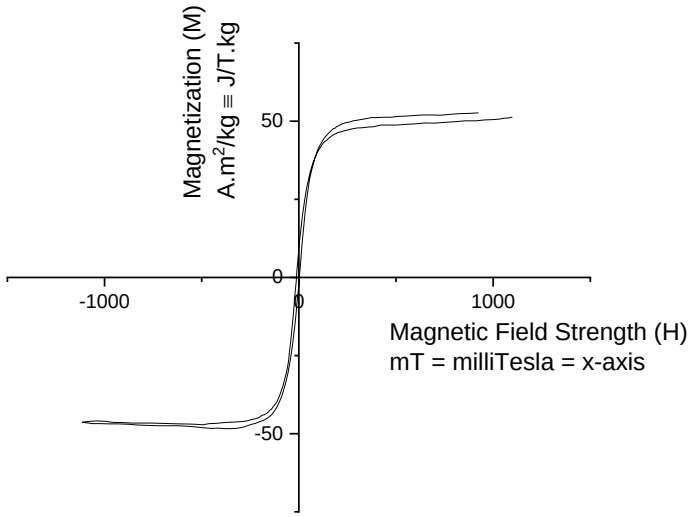

Figure 5.22: VSM curve of Fe_3O_4 nanoplates.

The magnetisation curve of the sample shows a high magnetism and corresponds to a superparamagnetic material. As the nanoplates are superparamagnetic, it confirms that they are ultrathin nanoplates, as the material has to be below a certain critical size in the direction to be considered superparamagnetic.

FTIR spectroscopy was also carried of the Fe_3O_4 sample and compared to the polymer P123K, to confirm that it had been cleaned from the nanoplates' surface (figure 5.23).

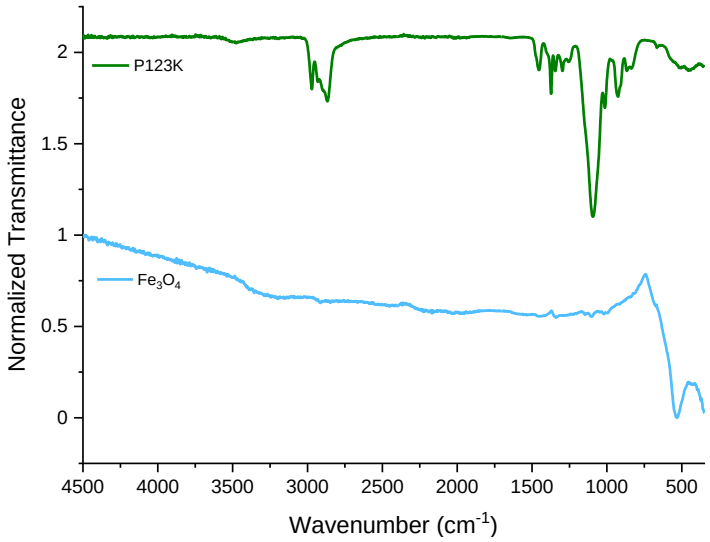

Figure 5.23: FTIR of Fe_3O_4 (blue) and P123K (green).

The FTIR of Fe_3O_4 doesn't show any of the peaks corresponding to the P123K, indicating that it has been cleaned from the surface of the nanoplates. Moreover, the spectra shows the peak around 540 cm^{-1}, corresponding to the vibration of Fe-O[34]. This further proves the formation of this material.

Additionally, powder XRD was also taken of the sample and is shown in figure 5.24.

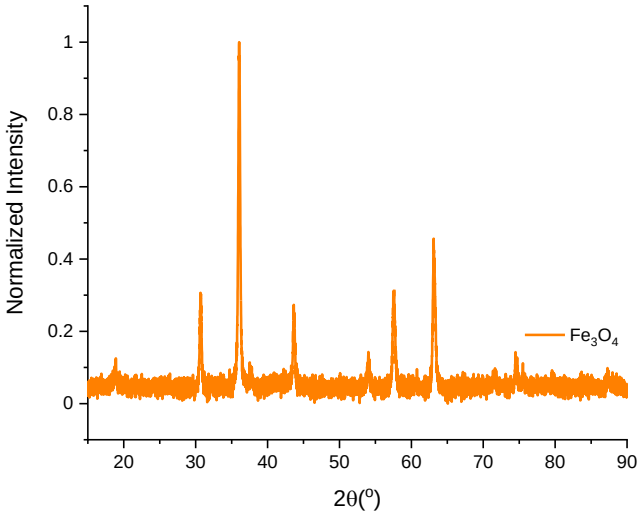

Figure 5.24: Powder XRD pattern of the Fe_3O_4 sample.

The powder XRD shows the peaks corresponding to magnetite. The XRD also shows the typical aspect for magnetite as a nanomaterial[35], which is what it was known by seen the VSM and TEM images.

5.3.2 BN-Fe_3O_4 composite membranes

Different concentrations of magnetite nanoplates were mixed with the BN in water to make membranes by filtration (table 5.5)

Table 5.5: Percentages weight of BN and Fe_3O_4 for each membrane.

Sample	wt% BN	wt% Fe_3O_4
F	95	5
G	90	10
H	85	15
I	80	20
J	50	50
K	40	60

FTIR spectra of one of the evaporated solutions with the 60 wt% of Fe_3O_4, was carried out and compared to BN and Fe_3O_4 on their own (figure 5.25).

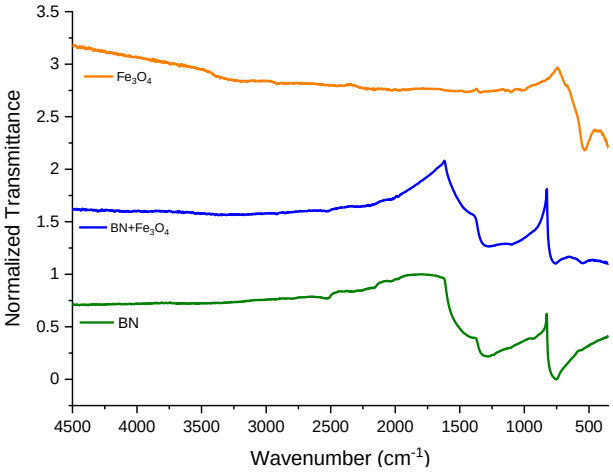

Figure 5.25: FTIR spectra of Fe_3O_4, BN and the mixture of BN-Fe_3O_4.

The shape of the BN-Fe_3O_4 FTIR bands is very similar to the BN FTIR spectra, which indicates that the BN material is present. The area of 500 to 760 cm^{-1} shows two peaks in the case of the BN-Fe_3O_4. The peak corresponding to the vibration of Fe-O is still apparent at 540 cm^{-1} and the B-N bending peak at 760 cm^{-1}, which indicates that the two compounds are present and mixed together in solution.

XRD of the sample of BN-Fe_3O_4 was also carried out to corroborate the presence of both compounds in the membranes (figure 5.26). The XRD pattern of the membrane confirms the presence of both compounds, as it shows peaks corresponding to BN as well as Fe_3O_4.

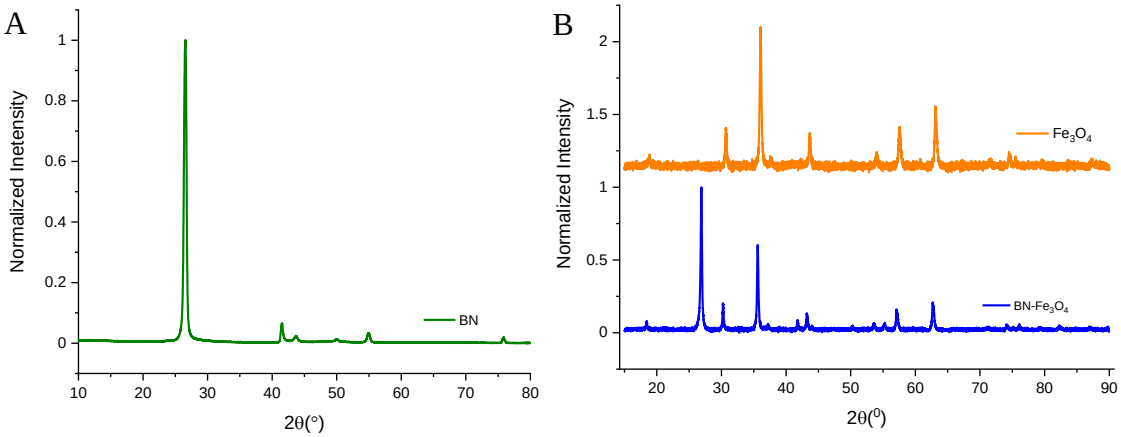

Figure 5.26: XRD patterns of A) BN and B) Fe_3O_4 and mixture of BN-Fe_3O_4.

SEM of the top view and cross-section of the membranes was carried out (figure 5.27).

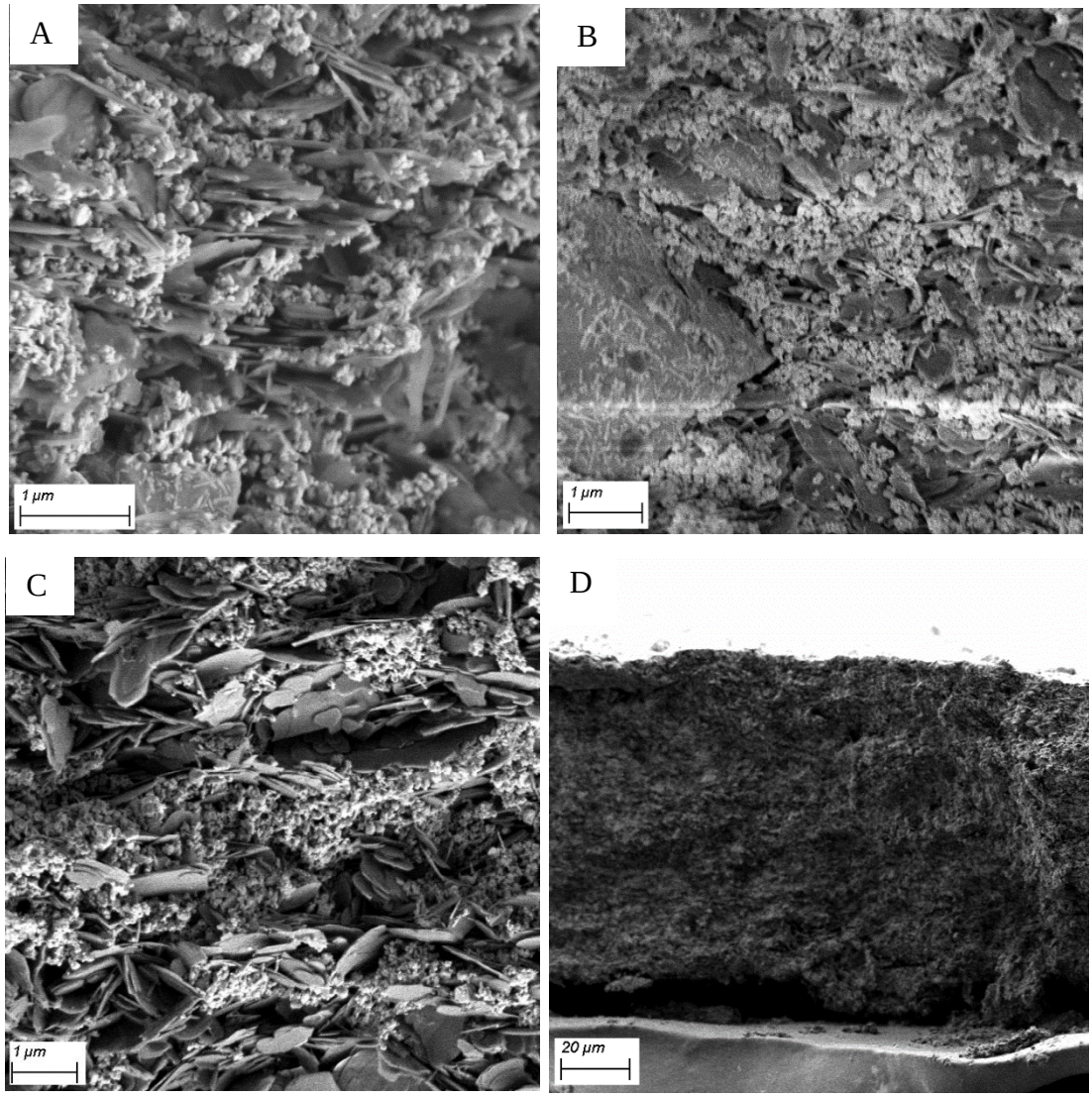

Figure 5.27: SEM images of A) and B) top view and C) and D) cross-section of BN-Fe_3O_4 (40 wt%-60 wt%). Voltage 2.5 kV, SE2.

Magnetite seems to be evenly distributed throughout the membrane and well mixed with the BN. As there was a higher concentration of magnetite than BN, the nanosheets are not as prominent through the sample. The thickness of the membrane was measured to be 98 ± 11 µm. The membranes are thinner than the ones obtained for pure BN (140-170 µm), but a bit thicker than the membranes made with BNOx (80 µm). This indicates that the membranes are more tightly packed than the BN, as well as having less BN in the membrane.

Once the membranes were made, their performance in dye retention was tested using UV-Vis spectroscopy. Evans Blue was used for these tests, as it is the dye with the most

results recorded in this work and can be used as an example of the performance of new membranes by comparing the results with previous ones. The UV-Vis spectra of the permeated are shown in figure 5.28 and the retention values in table 5.6.

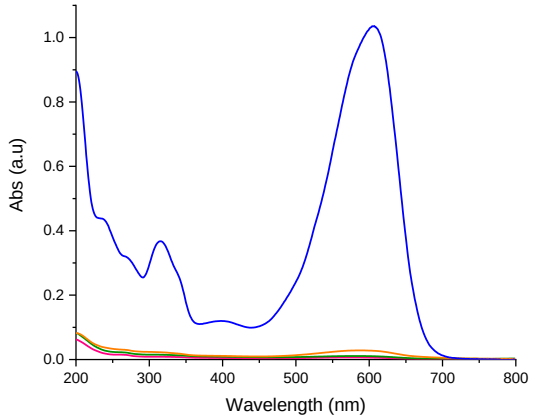

Figure 5.28: UV-Vis spectra of the retention of 20 mL Evans Blue of the BN and Fe_3O_4 membranes (different percentages in weight).

Table 5.6: Retention values for the BN and Fe_3O_4 membranes (different percentages in weight).

Membrane	wt% BN	wt% Fe_3O_4	% Retention
F.1	95	5	100
F.2	95	5	99
G.1	90	10	99
G.2	90	10	100
H.1	85	15	100
H.2	85	15	100
I.1	80	20	100
I.2	80	20	99

The retention values of the membranes with the magnetite added were very high of 99-100% and did not show differences with the values obtained for pure BN membranes. This indicates that the addition of the magnetic nanoplates does not alter the performance of the membranes, which opens the possibility to use the magnetic properties of the magnetite in the membranes.

High amounts of magnetite are required to exploit the potential magnetic properties of these membranes.The membranes made with the 20 wt% of magnetite, the highest amount tested so far, showed the highest values of magnetisation (being pulled towards a magnet), but it was significantly lower than that of the magnetite on its own. Therefore, it was decided to test new membranes, increasing the amount of Fe_3O_4 to 50 and 60 wt% (table5.5). These membranes were also tested for retention of Evans Blue dye. The UV-Vis spectra of the permeate are shown in figure 5.29 and the retention values are given in table 5.7.

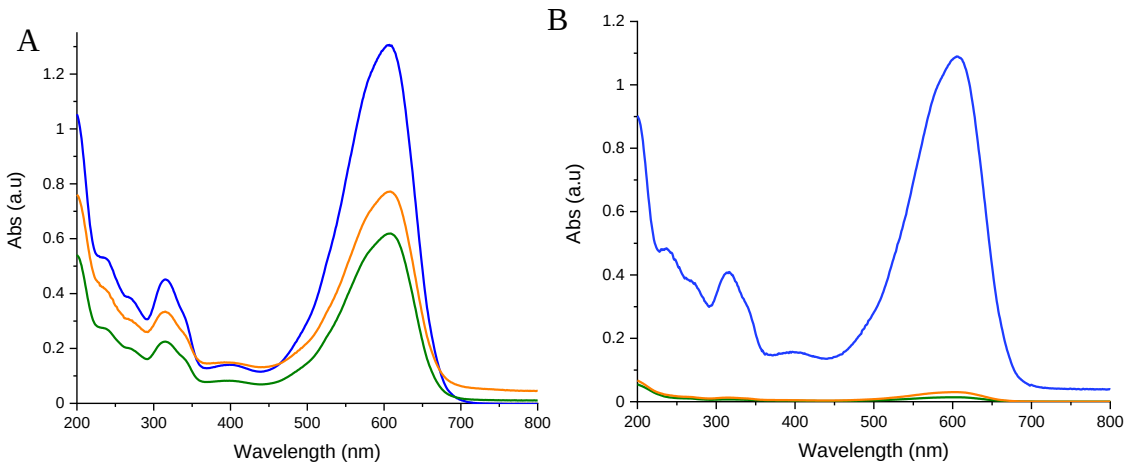

Figure 5.29: UV-Vis spectra of the retention of 20 mL Evans Blue of A) 50 wt% BN and 50 wt% Fe_3O_4 and B) 40% BN and 60% Fe_3O_4 membranes.

Table 5.7: Retention values for the 50 wt% BN and 50 wt% Fe_3O_4 and 40% BN and 60% Fe_3O_4 membranes.

Membrane	wt% BN	wt% Fe_3O_4	% Retention
J.1	50	50	53
J.2	50	50	41
K.1	40	60	99
K.2	40	60	97

The retention of the 50%-50% BN - Fe_3O_4 membranes showed a significant reduction in the performance. However, the 40%-60% membranes showed much higher values, closer to those obtained previously. These new values were slightly lower than those previous

obtained, but the magnetization of the membranes was shown to be higher (more attraction towards the magnet).

In addition, there was a new problem found for the membranes with highest amount of magnetite. The mechanical stability of the membranes was significantly reduced, with the membranes breaking and flaking as soon as they were dried. This presented a significant problem, as once the membranes are dried, they cannot be used again, which is not feasible for applications. Therefore, it was a decided to optimise new membranes to try to improve the membranes stability.

Some additional experiments were done using BNOx mixed with Fe_3O_4 nanoplatelets (see appendix). As well as having lower retentions when compared to the BN-Fe_3O_4 membranes, the Fe_3O_4 would precipitate faster out of solution, causing two clear layers in the membranes. Due to this, the experiments using BNOx and Fe_3O_4 nanomaterials weren't continued.

As the membranes with higher amounts of magnetite show less stability, the BN is necessary to provide the better stability of the membranes. This, however, is relative, as the BN membranes on their own can be very fragile too and will need some modification to make them more mechanically robust. Nevertheless, for these BN-Fe_3O_4 membranes, the lower concentration of magnetite seem to produce more robust membranes, but a compromise has to be reached, where the highest possible amount of magnetite is added for the magnetic properties while keepingthe integrity of the membranes as high as possible. Due to this, a modified approach was adopted. For these new membranes, the amount of BN would be kept the same as a regular BN membrane while adding different quantities of magnetite, in order to find the highest one that could be added before disturbing the membrane (table 5.8).

Table 5.8: Amounts and weight ratio of BN:Fe_3O_4 per solution of 100 mL

Sample	BN (mg)	Fe_3O_4 (mg)	Ratio BN:Fe_3O_4
L	300	150	1:0.5
M	300	200	1:0.6
N	300	250	1:0.8

SEM images of the membrane 1:0.6 BN:Fe_3O_4 were taken, both top view and cross-section (figure 5.30)

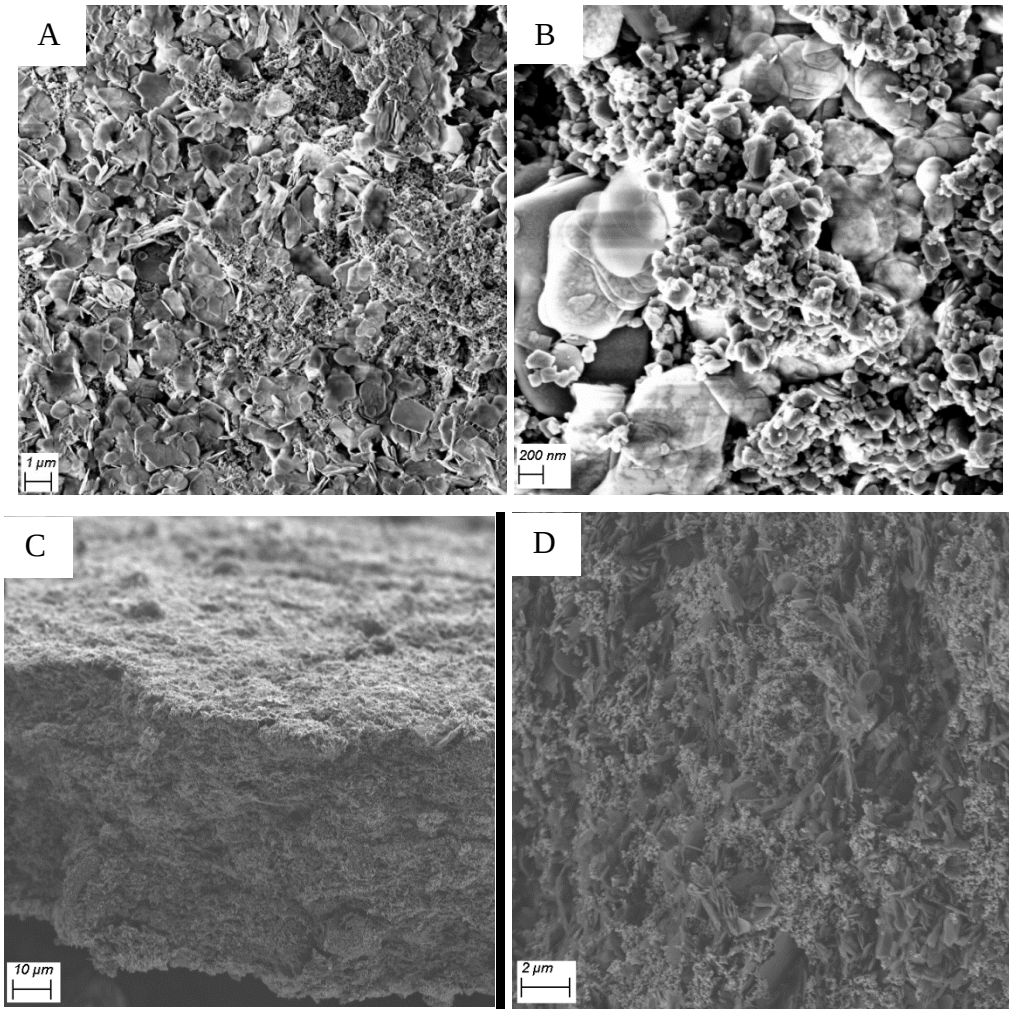

Figure 5.30: SEM images of A) and B) top-view (voltage 3 kV, InLens) an C) and D) cross-section (voltage 3 kV, SE2) of the 1:0.6 BN:Fe_3O_4 membrane.

The magnetite is very well distributed throughout the membrane and quite evenly mixed with the BN. As the amount of BN in these membranes is the same as regular BN-based membranes, the nanosheets could be easily seen through the membrane. The magnetite nanoplates seems to agglomerate slightly, but there are no clear pockets of just one of the materials over the other. This means that, even with the magnetite slightly agglomerating together, the two materials mixed well together to form membranes, with both of them appearing throughout the membrane. The thickness of this membrane was measured to be 64 ± 10 µm. This measurement is thinner than the BN membranes on their own (140-170 µm) but also thinner than the previous BN-Fe_3O_4 (97 µm). A reason for this could

be that the higher amount of both magnetite and BN makes the materials to tightly packed, creating thinner membranes.

The membranes seemed to have sufficiently high magnetism values in all cases, being pulled to the magnet easily. Their performance was tested using the different dyes. Initially, the membranes were tested for retention of Evans Blue, to compare their performance with the previous results. The UV-Vis spectra of the permeates are shown in figure 5.31 and the retention values in table 5.9.

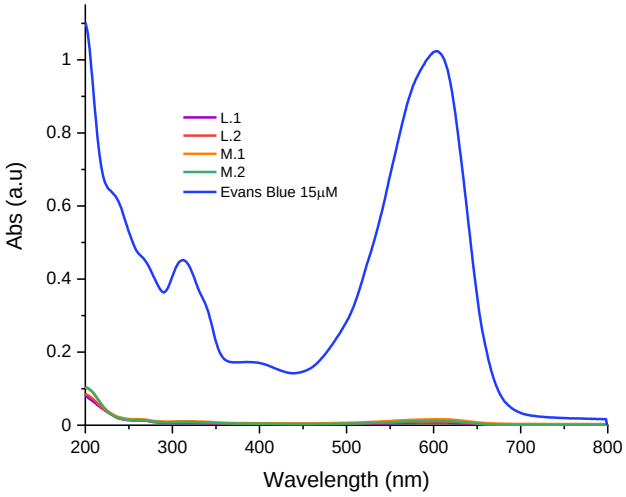

Figure 5.31: UV-Vis spectra of Evans Blue through the BN-Fe_3O_4 membranes, with different ratios, L (1:0.5) and M (1:06).

Table 5.9: Retention values for the BN-Fe_3O_4 membranes, with different ratios, L (1:0.5) and M (1:06).

Membrane	BN (mg)	Fe_3O_4 (mg)	% Retention
L.1	300	150	99
L.2	300	150	98
M.1	300	200	99
M.2	300	200	99

The membranes obtained with 150 mg (75 mg/membrane) and 200 mg (100 mg/membrane) of Fe_3O_4 showed high retention of the dye, with values similar to those obtained with the lower concentrations of magnetite or just BN membranes. Both membranes showed similar stability after drying, with the membranes not flaking as

easily. As the higher the content of magnetite there is in the membrane, the higher the magnetic properties the membrane will have, it was decided to test the 200 mg (100 mg/membrane) of Fe_3O_4 for the separation of other dyes, Methyl Orange and Methylene Blue (figure 5.32 and table 5.10).

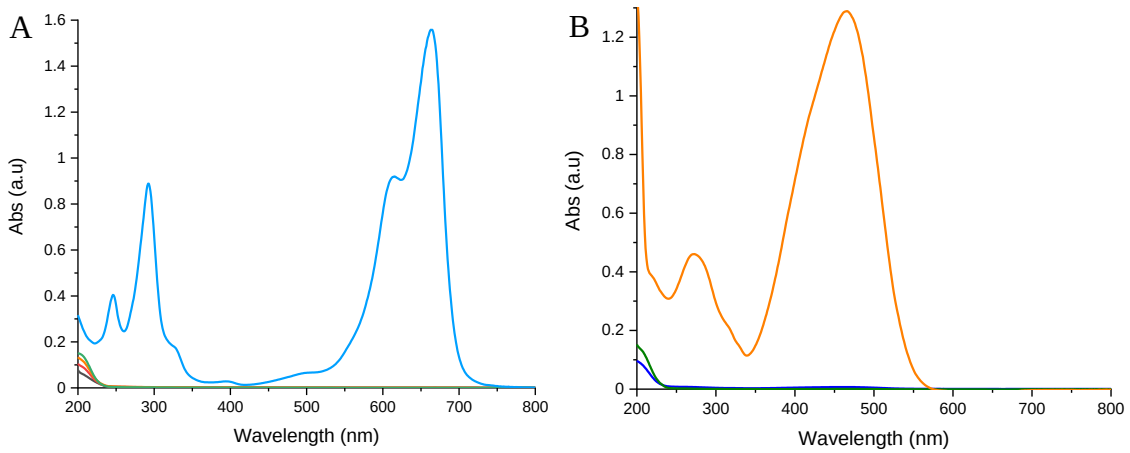

Figure 5.32: UV-Vis spectra of A) Methylene Blue and B) Methyl Orange through the BN-Fe_3O_4 (1:0.6) membranes.

Table 5.10: Retention of Methylene Blue and Methyl Orange for the BN-Fe_3O_4 (1:0.6) membranes.

Membrane	BN (mg)	Fe_3O_4 (mg)	Dye	% Retention
M.3	300	200	Methylene Blue	100
M.4	300	200	Methylene Blue	100
M.5	300	200	Methylene Blue	100
M.6	300	200	Methylene Blue	100
M.7	300	200	Methyl Orange	99
M.8	300	200	Methyl Orange	100

These membranes were capable of retaining all the dyes tested in this work, with 100% retention values in all cases, comparable to those obtained with the regular BN on their own. The membranes seemed to not break after drying, not even when exposed to a magnet, which indicated that the addition of the magnetite to a regular BN membrane seems to best way of introducing the magnetic particles. This way allows for high amount of magnetite to be mixed while keeping the integrity of the membrane.

A VSM of the BN-Fe_3O_4 (1:06) was carried out, to understand the magnetism present in the membrane (figure 5.33).

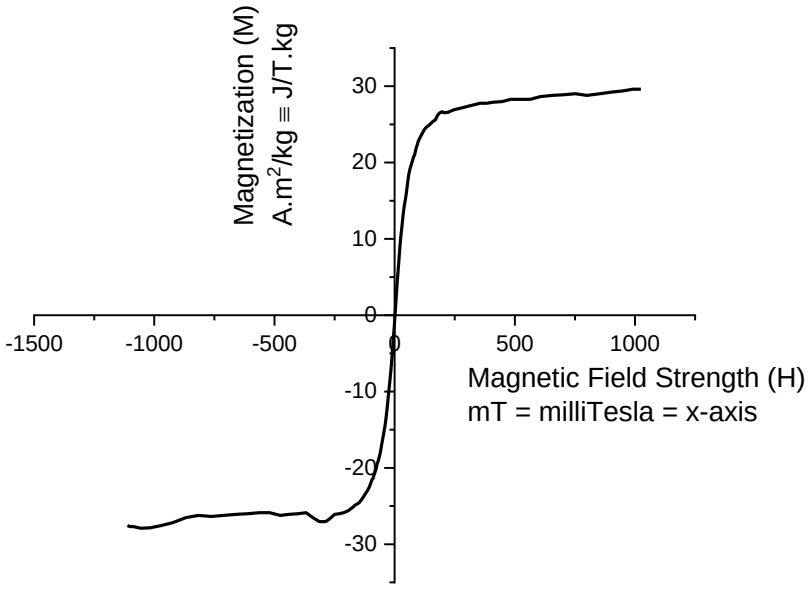

Figure 5.33: VSM curve of the BN-Fe_3O_4 (1:0.6) membrane.

The VSM confirms the presence of magnetism in the membranes, as it was expected due to their interaction with a magnet. The saturation magnetization was reduced from approximately 50 A m^2 kg^{-1} for pure Fe_3O_4 nanoplatelets to approximately 25 A m^2 $kg^{-1}$for BN-Fe_3O_4 composite. The magnetization has decreased due to the presence of non-magnetic BN particles. However, the value was still high enough and showed the superparamagnetic behavior typical for magnetite in the nanoscale.

It was decided to increase the magnetite in a sample membrane to a ratio of 1:0.8 BN:Fe_3O_4 in order to increase the magnetisation. The membranes were tested for retention of the three dyes (see UV-Vis spectra in figure 5.34 and retention values shown in table 5.11).

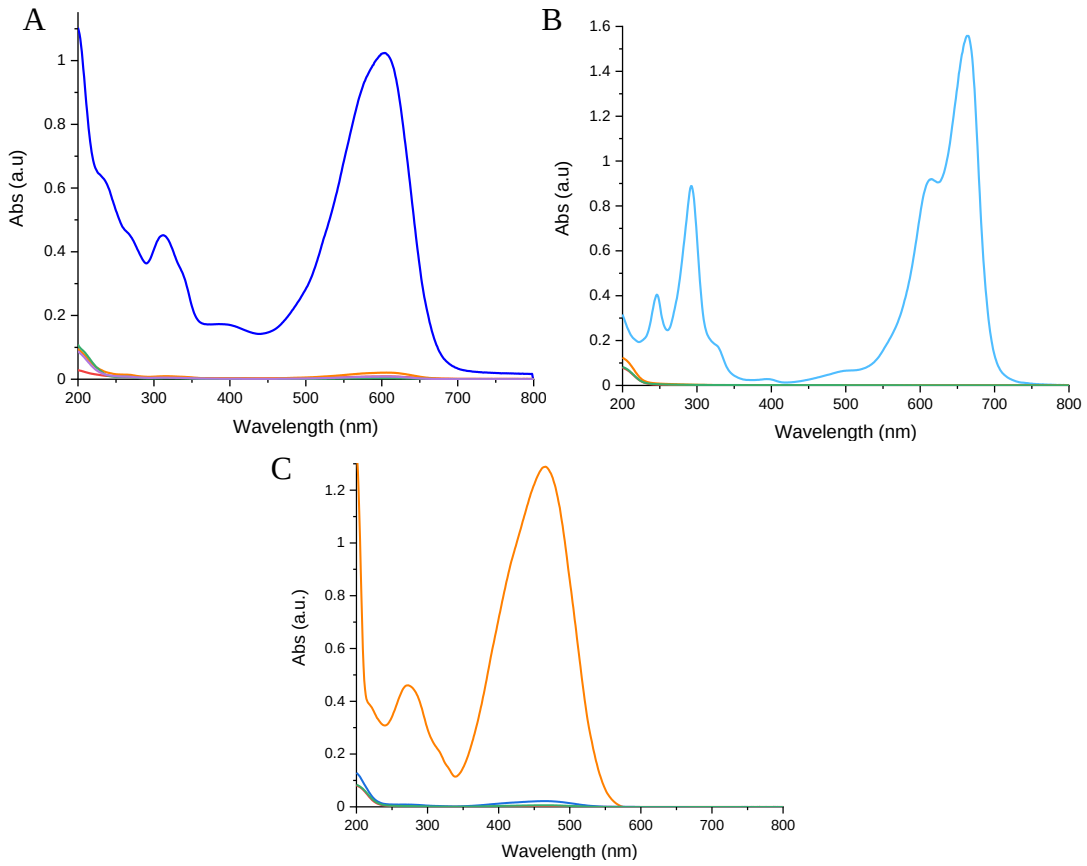

Figure 5.34: UV-Vis spectra of A) Evans Blue, B) Methylene Blue and C) Methyl Orange through the BN-Fe_3O_4 (1:0.8) membranes.

Table 5.11: Retention values of Evans Blue, Methylene Blue and Methyl Orange for the BN-Fe_3O_4 (1:0.8) membranes.

Membrane	BN (mg)	Fe_3O_4 (mg)	Dye	% Retention
N.1	300	250	Evans Blue	94
N.2	300	250	Evans Blue	98
N.3	300	250	Evans Blue	100
N.4	300	250	Evans Blue	100
N.5	300	250	Methylene Blue	100
N.6	300	250	Methylene Blue	100
N.7	300	250	Methylene Blue	100
N.8	300	250	Methyl Orange	100
N.9	300	250	Methyl Orange	98
N.10	300	250	Methyl Orange	100

These membranes with higher amount of magnetite also show excellent retention capabilities for all the dyes tested. Comparing to the previous membranes, made with

different percentages in weight of BN and magnetite, one can see how the reduction of BN content below a certain point negatively affects the retention of the membranes. However, these new BN-Fe_3O_4 membranes do maintain the same retention. Nevertheless, the membranes made with a ratio of 1:0.8 BN:Fe_3O_4 do flake after drying, causing the membrane to break (figure 5.35).

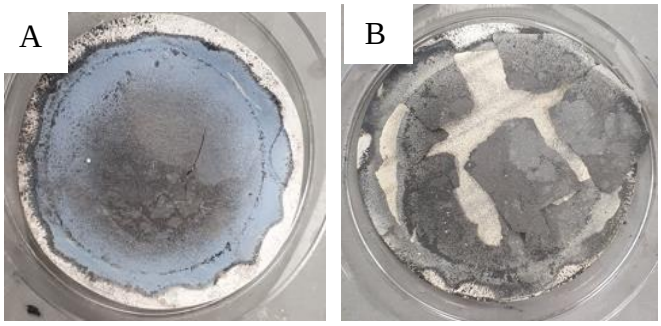

Figure 5.35: Membranes made from A) 1:0.6 BN-Fe_3O_4 and B) 1:0.8 BN:Fe_3O_4 after drying.

Therefore, the membranes with the 1:0.8 BN:Fe_3O_4 were less robust and durable than those obtained using a ratio of 1:0.6 BN:Fe_3O_4. This shows that the best combination of BN-Fe_3O_4 is a ratio of 1:0.6, where the optimal amount of magnetic material present without affecting the performance and stability of the membranes.

5.3.3 Preliminary testing of membranes in separation of magnetic nanomaterials

As the membranes with magnetite showed excellent results for retaining the dyes, it was decided to test them for magnetic separation and removal of magnetic nanomaterials. The aim was to check if the magnetite nanoplatelets present in the membranes would magnetically interact with magnetic nanoparticles in a solution being filtered through the membrane, retaining them in the membrane.

For this test, a batch of bare magnetite nanoparticles was synthesised by Áine Coogan in the group, without the presence of a stabiliser, with the aim of producing a highly polydisperse sample for filtration. The nanoparticles were suspended in Mullipore water to be kept as the stock solution. As the sample wasn't dried before resuspension in solution, the concentration of magnetite was unknown.

20 mL were prepared from the stock solution (5 mL of the magnetite nanoparticles suspension and 15 mL of Millipore water) and passed through the 1:0.6 BN:Fe_3O_4 membranes. The permeate was collected and tested against a magnet. The solution showed no signs of magnetism, indicating that the magnetite nanoparticles were being fully retained in the membrane. As the size for magnetite nanoparticles typically quite small, the nanoparticles sould have passed through the membrane, they seemed to have been retained due to magnetic interactions with the membrane.

Nevertheless, a control experiment was run using a BN membrane with no magnetite. The permeate after passing this membrane also showed no signs of magntetism, indicating that the nanoparticles were retained by the membrane without magnetic components. DLS of the magnetic nanoparticle solution was carried out (figure 5.36).

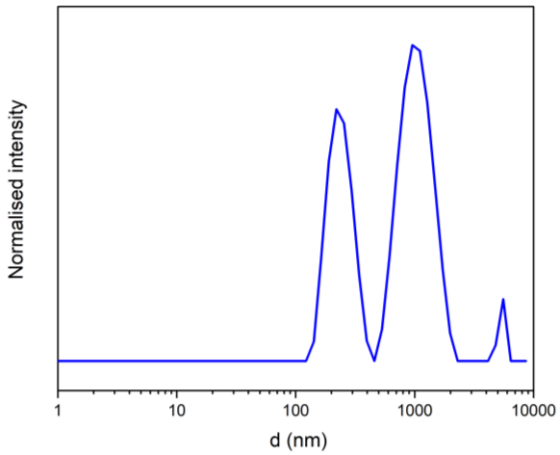

Figure 5.36: DLS of the magnetite solution.

The DLS shows big aggregates, which explains why the BN membranes were capable of retaining the magnetite nanoparticles. Further testing, therefore, is needed to optimise the magnetic separation.

5.4 BN - Carbon nanotubes (CNTs) composite

5.4.1 Exfoliation of BN-CNTs in IPA

It was decided to mix the BN with carbon nanotubes (CNTs) to alter the properties of the membranes. For this, the BN and CNTs were mixed in IPA and sonicated for 24 hours. The sample produced had a grey colour, due to the presence of bothBN (white) and CNTs (black).

Initially, the sample of exfoliated BN and CNTs was characterised by SEM (Figure 5.37 A and B). Once again, the SEM analysis has confirmed a successful BN exfoliation, as nanosheets appeared throughout the image. Moreover, the nanosheets seemed to be similar in size, showing to be a quite homogenous product. Furthermore, the CNTs appeared to be well-mixed with the nanosheets.

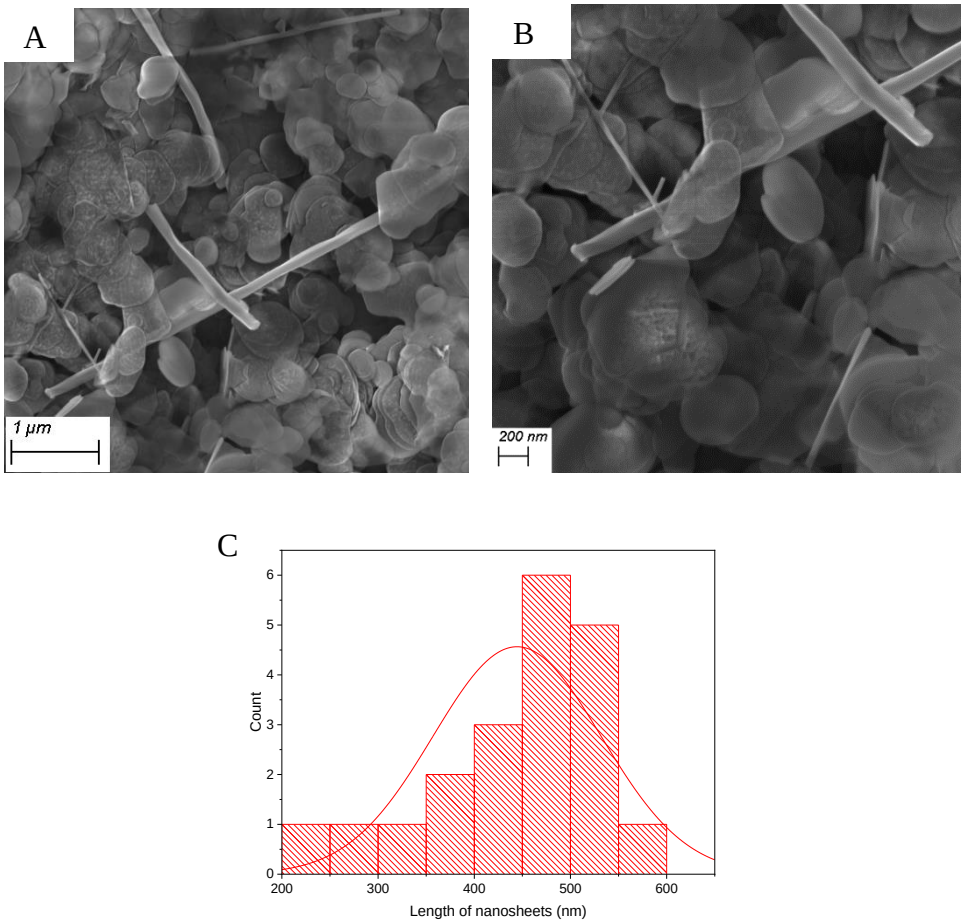

Figure 5.37: (A and B) SEM images of the exfoliated BN and CNTs and (C) size distribution of the length of the nanosheets. Image (B) was taken as a closed up from image (A), which shows the sample from a farther distance. Voltage: 3 kV, InLens.

The size distribution was also recorded, obtaining a mean of length of 444 ± 190 nm, (figure 5.37 C). Although the mean length for both samples is similar, the size of the nanosheets was greater when BN was exfoliated on its own, obtaining lateral sizes of around 500 nm, whereas the maximum for the BN nanosheets exfoliated in the presence of CNTs was around 400 nm. This could be due to the interactions of CNTs with BN while the exfoliation is taking place.

5.4.2 BN-CNTs based membranes from exfoliation in IPA

The exfoliated BN and CNTs mixtures were used to produce membranes, using vacuum filtration as described previously. The membranes were grey in colour, which indicated the successful mixture of both BN and CNTs (figure 5.38).

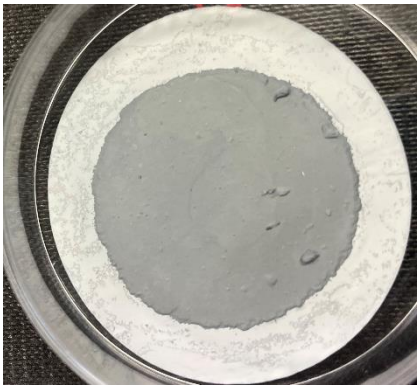

Figure 5.38: Photograph of BN-CNTs membrane, showing the grey colour indicating the mixture of the two materials.

SEM images of the resulting membranes were taken, both top-view and cross-section (figure 5.39)

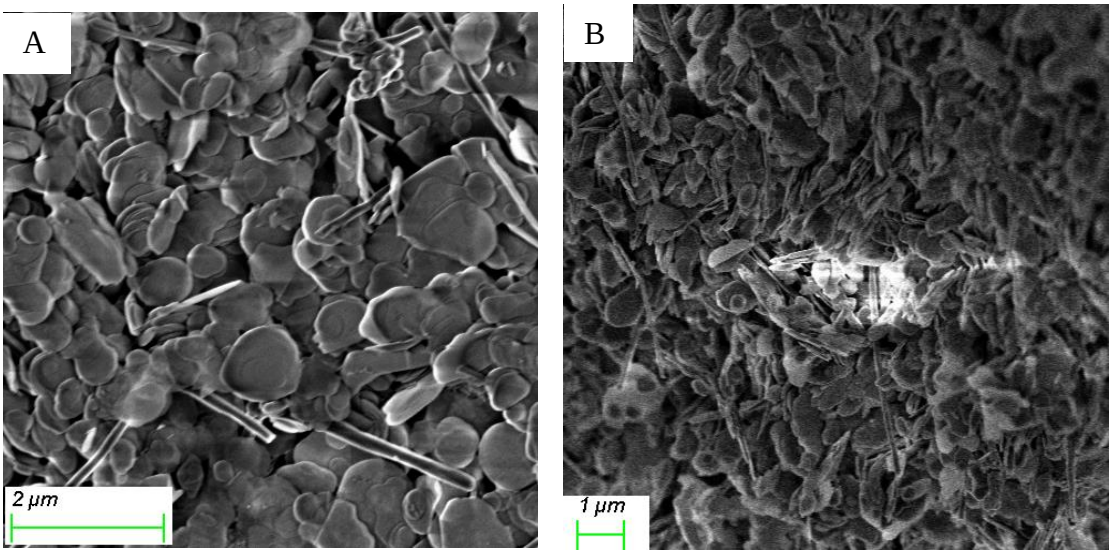

Figure 5.39: SEM images of A) top and B) cross-section of the BN and CNTs membrane. Voltage: 1.5 kV, SE2.

The SEM images of the top view of the BN and CNTs membrane (figure 5.39 A) shows both the nanosheets and nanotubes. The nanotubes appear to be intercalating between the nanosheets. The cross-section of the BN and CNTs membrane (figure 5.39 B) shows the nanosheets partly pile up on top of each other. Furthermore, the nanotubes appear across of the entire cross-section of the membrane, meaning the nanotubes intercalated in between the nanosheets through all the layers. The images obtained from the cross-section didn't allow for the measurement of the thickness of the membrane, as the membranes were too brittle and wouldn't stick properly to the stub.

The membranes were tested for retention of Evans Blue, as it is the dye used to do the first tests for all the membranes. The UV-Vis spectra of the dye after retention by the membranes is shown in figure 5.40 and the retention values are displayed in table 5.12.

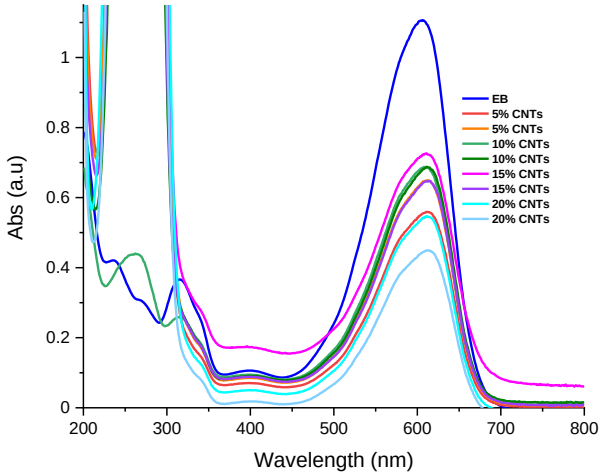

Figure 5.40: UV-Vis spectra of the retention of 20 mL Evans Blue (15 µM) by the BN-CNTs membranes.

Table 5.12: Retention values of the BN-CNTs membranes.

Membrane	% Retention
5% CNTs	50
5% CNTs	41
10% CNTs	41
10% CNTs	41
15% CNTs	38
15% CNTs	45
20% CNTs	53
20% CNTs	62

The retention of the membranes was significantly lower than those obtained with regular BN. These results indicate that the addition of CNTs does not improve the retention of the membranes; in fact, it reduces the retention values of these membranes.

The retention of the membranes with different percentages in weight of CNTs was very similar for 5% to 15% and improved slightly for the 20 wt% in CNTs, but only achieving maximum retention range of 53-62%. However, it has to be noted that these membranes were obtained by exfoliating both the BN and CNTs in IPA, so the results should be compared to the results obtained with the BN exfoliated in the same solvents. When comparing the results from the BN exfoliated in IPA and the BN-CNTs composites, we can see a different picture. The mean retention for these BN membranes was 55% with a standard deviation of 12%, which would place the results obtained with the CNTs in the same range as the BN membranes. This indicates that, even though the retention was not

improved, the addition of the CNTs doesn't seem to be affecting the performance of the membranes. However, the retention wasn't improved or controlled by adding the CNTs.

Nevertheless, as the results obtained with the BN and CNTs exfoliated IPA seemed to be reflecting the results obtained when exfoliating the BN in IPA, it was decided to test the exfoliation in NMP. This was done for two reasons: the first one is that CNTs are usually exfoliated in NMP; and secondly because the results obtained with the BN exfoliated in NMP were better than those obtained with IPA. The idea was to check whether the retention would improve and maybe introduce a size control aspect by varying the amount of CNTs.

5.4.3 Exfoliation of BN-CNTs in NMP

Different amounts of CNTs were also used when mixing BN and were exfoliated in NMP, 5%, 10%, 15% and 20%. All the samples had a grey colour, as it was the mixture of the BN (white) and CNTs (black).

SEM images of the exfoliated BN nanosheets with 20% CNTs are shown in figure 5.41, as a representation of the samples.

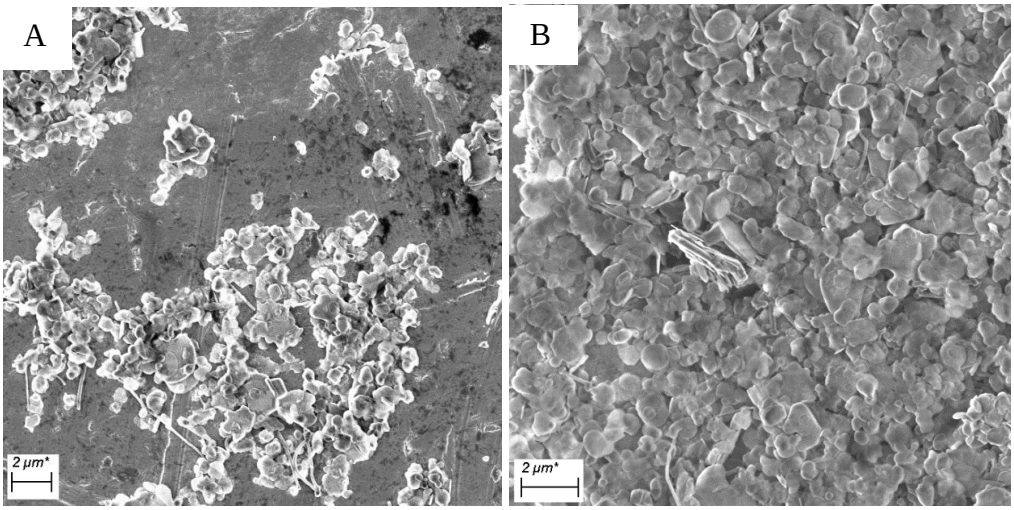

Figure 5.41: SEM images of exfoliated BN and 20% CNTs in NMP. Voltage: 3 kV, InLens.

The SEM images show no major differences when compared to the BN and CNTs exfoliated in IPA. The CNTs are mixed in between the nanosheets, showing a good interaction between the two components.

5.4.4 BN-CNTs based membranes from exfoliation in NMP

The exfoliated BN and CNTs in NMP mixtures were used to form membranes, using vacuum filtration as described previously. Visually, the membranes appeared grey in colour, which indicates the mixture of both, as was seen with the BN-CNTs exfoliated in IPA (figure 5.38).

SEM images of the resulting membranes were taken, both top-view and cross-section (figure 5.42).

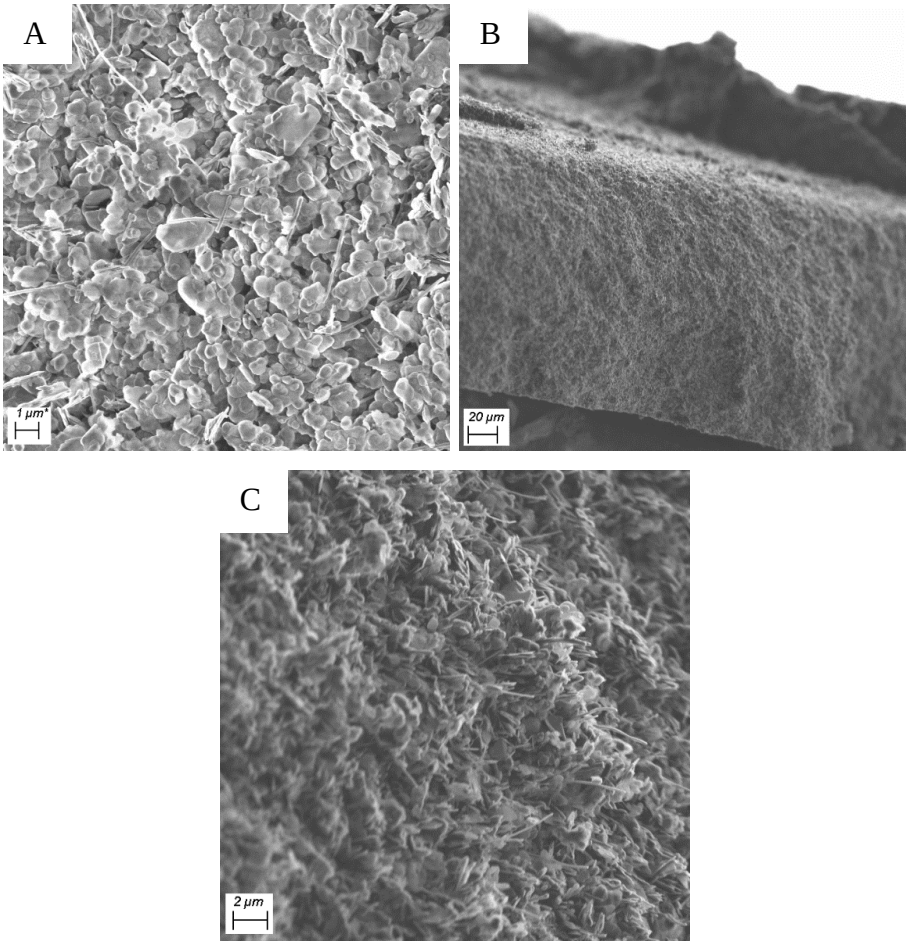

Figure 5.42: SEM images of A) top (voltage: 3 kV, InLens) and B) and C) cross-section (voltage: 3 kV, SE2) of the BN - CNTs membrane.

The SEM images of the membranes show an even distribution of the CNTs throughout the membrane, with no clear spots of just one of the materials. This means that the two compounds mix really well together and the membranes are formed by the two materials evenly. The nanotubes intercalate in between the nanosheets, which pile up on top of each other as it has previously been seen. The thickness of the membrane was measured to be 162± 7 µm, which is thicker than the one obtained when making the BN exfoliated in NMP membrane. This indicates that the addition of CNTs creates a more loosely packed membrane, increasing the thickness. The CNTs are most likely intercalating in between the nanosheets, which, in turns, creates more space between the layers of the membrane and increasing its thickness.

The membranes were then tested for retention of Evans Blue. The UV-Vis spectra of the dye after the retention by membranes is shown in figure 5.43 and the retention values are displayed on table 5.13.

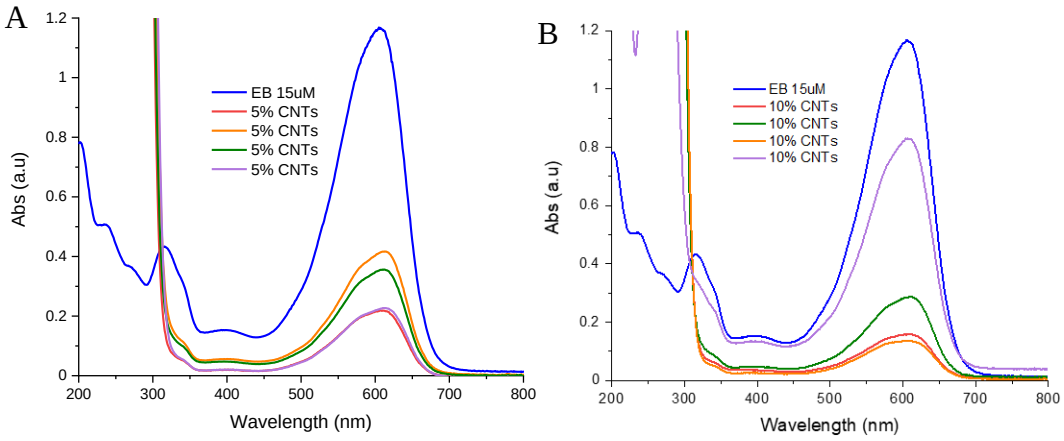

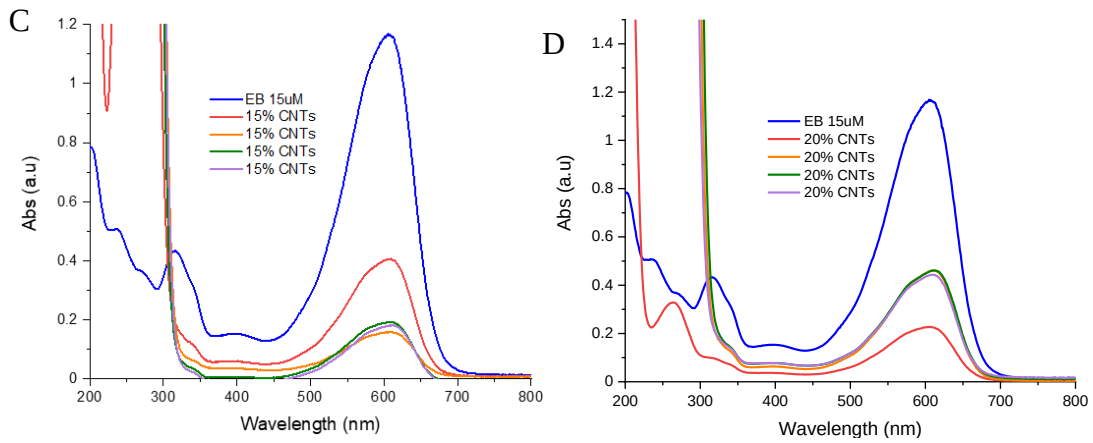

Figure 5.43: UV-Vis spectra of the retention of 20 mL Evans Blue of the BN and A) 5% CNTs, B) 10% CNTs, C) 15% CNTs and D) 20% CNTs exfoliated in NMP membrane.

Table 5.13: Retention values of the BN and 5% CNTs, 10% CNTs, 15% CNTs and 20% CNTs exfoliated in NMP membranes.

Membrane	%Retention	Membrane	%Retention
5% CNTs	81	15% CNTs	46
5% CNTs	64	15% CNTs	82
5% CNTs	70	15% CNTs	83
5% CNTs	81	15% CNTs	83
10% CNTs	86	20% CNTs	80
10% CNTs	74	20% CNTs	59
10% CNTs	88	20% CNTs	59
10% CNTs	25	20% CNTs	60

The retention reflected by these membranes show an interesting trend. The membranes initially showed a retention similar to the ones obtained with the membranes made with BN exfoliated in NMP (around 80%). There are some retention values that deviate from the trend, but as they are the minority, they can be excluded. However, these retention values decreases when the amount of the CNTs is increased to 20% CNTs. This indicates that the amount CNTs might be affecting the performance of the membranes. These results show that the addition of the CNTs, up to 15%, doesn't change the retention observed with membranes based on just the exfoliated BN, as it was noted in the case of IPA. Although, the addition of 20% CNTs does decrease the retention of the membranes to values closer to those obtained with the BN and BN-CNTs exfoliated in IPA.

After analysing these results, it was decided to also test membranes with larger amounts of CNTs. This was done to test whether higher amount of CNTs would increase or change the retention observed up to this point. For this purpose, membranes with 50% and 75% of CNTs were chosen. The membranes looked a darker grey than the previously observed, as it was expected as there is a larger amount of CNTs, which are black. The membranes were then tested for retention of Evans Blue dye.

The retention of the membranes with 50% and 75% CNTs is presented in figure 5.44 and the values are shown in table 5.14.

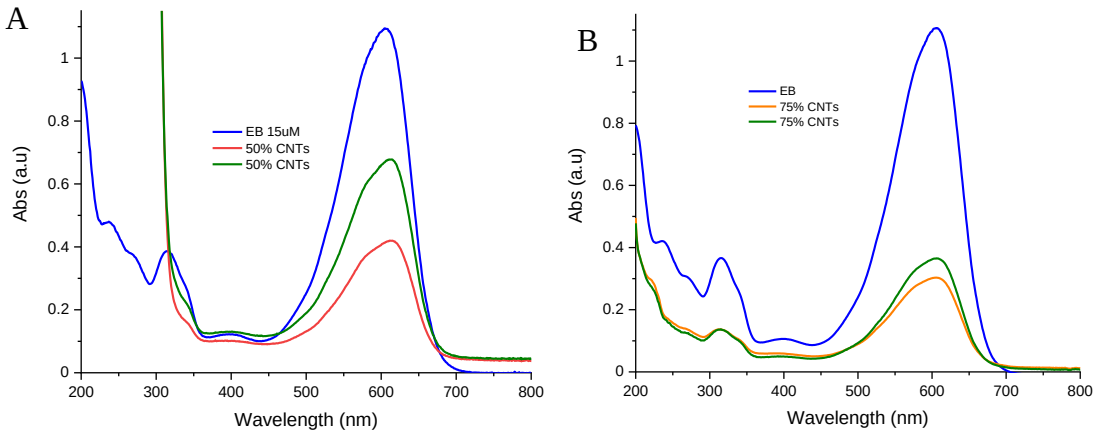

Figure 5.44: UV-Vis spectra of the retention of 20 mL Evans Blue through A) BN and 50% CNTs and B) BN and 75% CNTS exfoliated in NMP membrane.

Table 5.14: Retention values of the BN-50% and 75% CNTs exfoliated in NMP membranes.

Membrane	% Retention
50% CNTs	62
50% CNTs	38
75% CNTs	70
75% CNTs	64

The retention obtained with these membranes showed lower values than those observed with the membranes with lower amounts of CNTs, which indicates that higher amounts of CNTs decrease the retention performance of the membranes. However, the retention

is quite similar to the ones obtained with 20% CNTs as well as the IPA membranes. This demonstrates that the retention is only affected up to a certain amount of CNTs present.

5.4.5 Exfoliation of BN-CNTs in water

After analysing the results obtained with the NMP and IPA, it was decided to try to exfoliate the BN and CNTs in water. The goal was to check whether the trend observed so far, where the retentions are very similar to the BN membranes, would still occur when using water as the solvent for exfoliation. For this test, only 20 wt% of CNTs were used.

SEM images were taken of the exfoliated evaporated solutions and are shown in figure 5.45

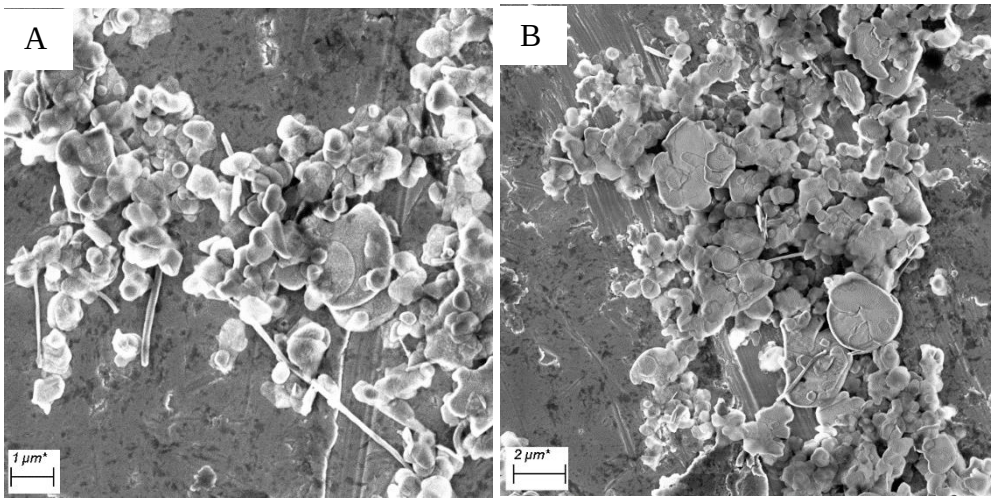

Figure 5.45: SEM images of exfoliated BN and 20% CNTs in water. Voltage: 3 kV, InLens

The SEM images don't show any major differences with the BN and CNTs exfoliated in the previously usedsolvents, showing the CNTs and BN well dispersed together in the sample

5.4.6 BN-CNTs based membranes from exfoliation in water

The membranes were prepared as previously described, and were similar to the ones obtained with NMP and IPA, showing a grey colour, which indicates a successful mixing of the BN and CNTs throughout the sample (figure 5.38).

SEM images of the membranes were also taken, both top-view and cross-section (figure 5.46).

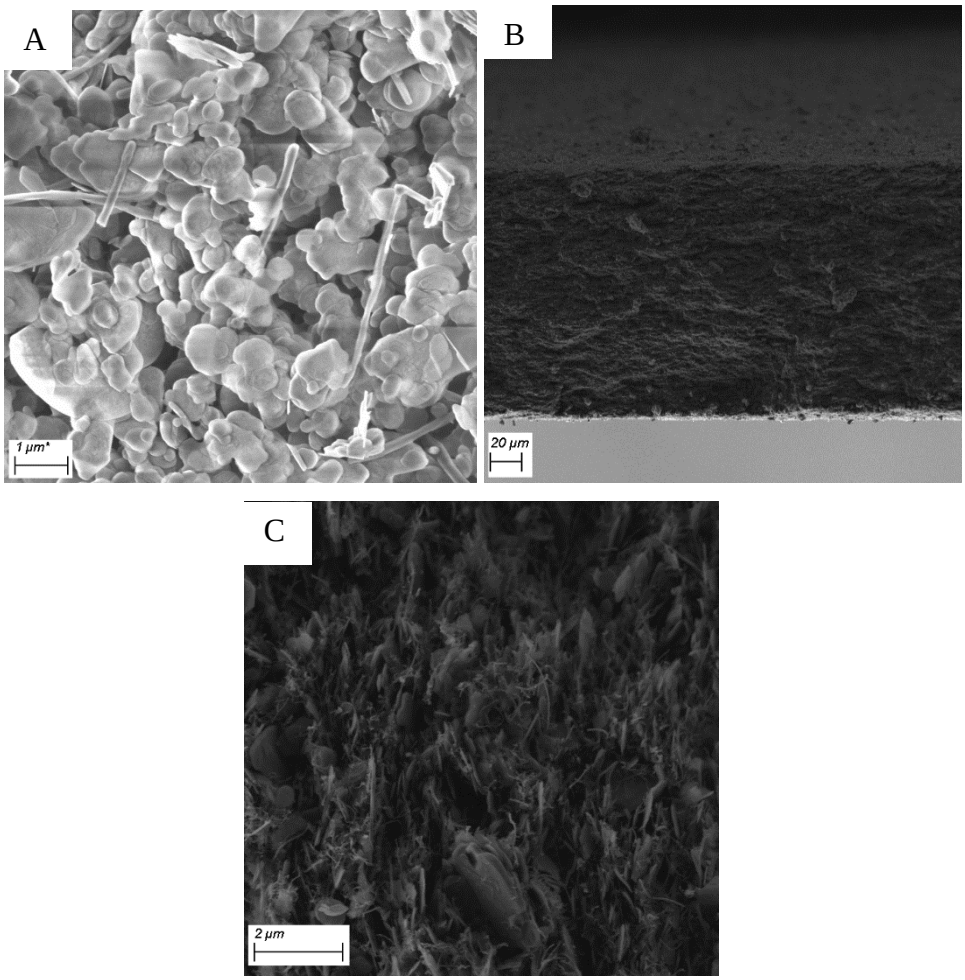

Figure 5.46: SEM images of A) top-view (voltage 3 kV, InLens) and B) and C) cross-section (voltage 3 kV, SE2) of the BN and CNTs membrane.

The SEM images of the membranes show an even distribution of the CNTs throughout the membrane, with no clear spots of just one of the materials. This means that the two compounds mix really well together and the membranes are formed by the two materials evenly. The nanotubes intercalated in between the nanosheets, which stack on top of each other ashas previously been seen. The thickness of the membrane was measured to be 165± 6 µm, which is thicker than the BN exfoliated in water membrane (142 µm). This seems to indicate that introducing CNTs into the membrane makes the BN nanosheets pack more loosely, increasing the thickness. This is most likely an effect of the CNTs intercalating in between the BN nanosheets. The thickness of this membrane was very

similar to that of the BN-CNTs exfoliated in NMP, which also keeps with the values obtained with the membranes of BN exfoliated in water and NMP. This indicates that the CNTs have the same effect on the packing of the membranes, regardless of the solvent used.

The membranes were then tested for retention of Evans Blue dye, the retention of the membranes is shown in figure 5.47 and the retention values are displayed on table 5.15.

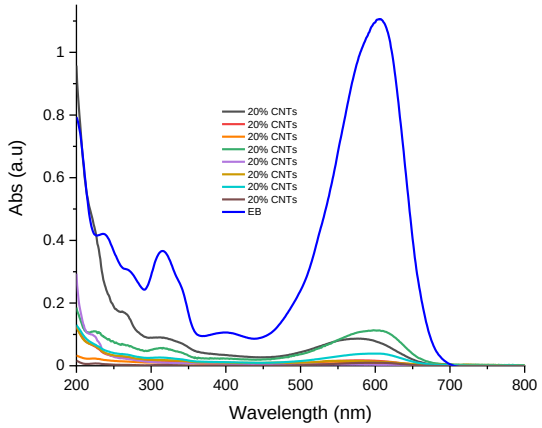

Figure 5.47: UV-Vis spectra of the retention of 20 mL Evans Blue of the BN and 20% CNTs exfoliated in water membrane.

Table 5.15: Retention values of the BN-20% CNTs exfoliated in water membranes.

Membrane	% Retention
20% CNTs	93
20% CNTs	99
20% CNTs	99
20% CNTs	91
20% CNTs	100
20% CNTs	99
20% CNTs	97
20% CNTs	99

The retention obtained with the membranes made with BN and 20% CNTs in water showed the highest values observed for these membranes, with the lowest retention at 93%. These results are in line with the trend that IPA and NMP were showing. The retentions are very similar to the ones obtained with the BN-water membranes. This seems to indicate that the addition of the CNTs doesn't affect the retention of these

membranes too much. An interesting feature with the water membranes is that 20% results in values comparable of BN alone, whereas in the case of the NMP resulted in lower retention values, closer to those obtained with IPA. This could indicate that membranes of BN exfoliated in water are more efficient for retention of this dye, not being affected by increased percentage of CNTs.

However, as in the case of NMP, even higher amounts of CNTs resulted in lower retention, it was decided to check if this would affect the membranes made from exfoliating in water too. For these tests, 50% in weight of CNTs were used. The membranes looked darker, as expected due to the higher number of CNTs (black). The retention of the membranes was tested using Evans Blue (figure 5.48) and the percentages are shown in table 5.16.

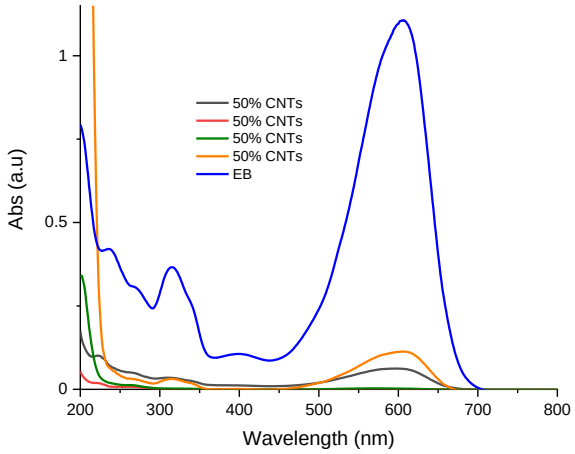

Figure 5.48: UV-Vis spectra of the retention of 20 mL Evans Blue of the BN and 50% CNTs exfoliated in water membrane.

Table 5.16: Retention values of the BN-50% CNTs exfoliated in water membranes.

Membrane	% Retention
50% CNTs	95
50% CNTs	100
50% CNTs	100
50% CNTs	91

The membranes produced using50% in weight of CNTs show high retentions, similar to those obtained with lower amount of CNTs. This seems to indicate that the membranes made with BN exfoliated in water are more resilient and capable of tolerating higher

amounts of extra materials without having their retention affected. However, this could indicate that the addition of CNTs is not going to be enough to tune the size-dependent retention of the membranes by altering the size of the pores.

75% in weight of CNTs was also tested, to see the extent of the membranes when tolerating additional material. The retention was tested using Evans Blue (figure 5.49) and values are shown in table 5.17.

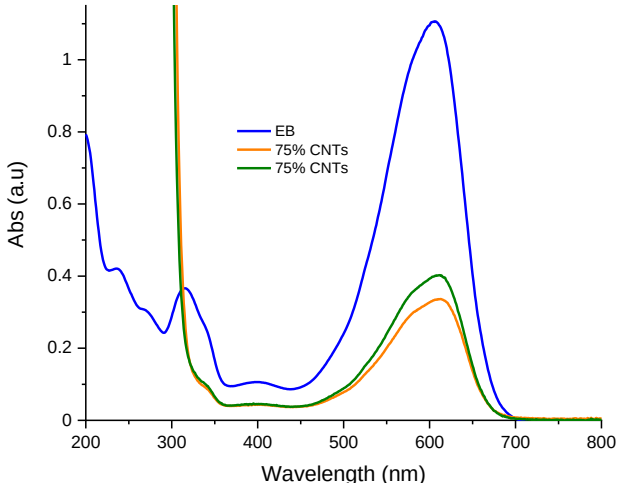

Figure 5.49: UV-Vis spectra of the retention of 20 mL Evans Blue of the BN and 75% CNTs exfoliated in water membrane.

Table 5.17: Retention values of the BN-75% CNTs exfoliated in water membranes.

Membrane	% Retention
75% CNTs	73
75% CNTs	67

Retention of the membranes went down to 70% when increasing the amount of CNTs, indicating that BN is needed in the same or higher amounts to exhibit the high retention performance. Additionally, this indicates that BN plays a crucial role in the retention and any reduction in the amount of BN present will cause the retention to drop.

5.5 Conclusions

BNOx and LDH composite membranes were successfully prepared and optimised to determine the ideal ratio of both components present. The composite membranes showed

high retention for the three dyes tested (98-100%), indicating that these membranes can be used for water treatment. Furthermore, the addition of the LDH to the BNOx increases the rate at which the colour of the dye disappears. This effect can be due to a drying effect, but it's also correlated to the photodegradation of the dye. Preliminary studies to understand and quantify the process had been carried out and the kinetics of the decolourisation in solution was established as a pseudo firstorder. These degradation studies open the possibility to develop new reusable membranes, but further studies are necessary to understand all processes involved.

Magnetic nanoplates were also successfully mixed with BN, forming magnetic composite membranes. These membranes were optimised using several concentrations of Fe_3O_4 and BN, showing excellent capabilities for the retention of the dyes (99-100%). The membranes showed reasonably good magnetic characteristics, being attracted strongly to a magnet. The membranes were capable of highly retaining the dyes, even at high amounts of the magnetite, but their integrity at higher concentrations of Fe_3O_4 was low. This indicates that the optimal amount of both components was needed to maintain high retention, magnetic behaviour and integrity of the composite membranes. These membranes were also preliminary tested for the retention of magnetic nanoparticles, but more testing is needed to make clear conclusions.

Finally, BN was mixed with a 1D nanomaterial, CNTs. The carbon nanotubes were added in different concentrations to study the effect they would have on the composite membranes. Moreover, the solutions were exfoliated using NMP, IPA or water, to optimise the exfoliation and formation of the membranes. These results pointed out at a strong effect of the solvent and the retention of the dyes being performed by the BN mostly, as the results for each solvent were mirror images of the results obtained with regular BN membranes. BN-CNTs exfoliated in water showed the best results in retention of the dyes (followed by NMP and then IPA) up to a certain point, where the amount of BN was too low, affecting the previously seen high retention values.

Bibliography

1 S. Kim, H. Wang and Y. M. Lee, *Angew. Chemie Int. Ed.*, 2019, **58**, 17512–17527.

2 Y. Wang, Z.-X. Low, S. Kim, H. Zhang, X. Chen, J. Hou, J. G. Seong, Y. M. Lee, G. P. Simon, C. H. J. Davies and H. Wang, *Angew. Chemie Int. Ed.*, 2018, **57**, 16056–16061.

3 J. Ren, L. Stagi and P. Innocenzi, *J. Mater. Sci.*, 2021, 56, 4053–4079.

4 S. Dutta, P. K. Gan and K. Chatterjee, *AIP Conf. Proc.*, 2020, **2265**, 030120.

5 Y. Mutharasi, N. J. Kaleekkal, T. Arumugham, F. Banat and M. S. Kapavarapu, *Chem. Eng. Process. - Process Intensif.*, 2020, **158**, 108191.

6 Z. Yang, F. Wang, C. Zhang, G. Zeng, X. Tan, Z. Yu, Y. Zhong, H. Wang and F. Cui, *RSC Adv.*, 2016, **6**, 79415–79436.

7 V. K. Gupta, R. Jain, A. Mittal, M. Mathur and S. Sikarwar, *J. Colloid Interface Sci.*, 2007, **309**, 464–469.

8 S. Yuan, Y. Li, Q. Zhang and H. Wang, *Colloids Surfaces A Physicochem. Eng. Asp.*, 2009, **348**, 76–81.

9 L. Mohapatra and K. M. Parida, *Sep. Purif. Technol.*, 2012, **91**, 73–80.

10 S. J. Xia, F. X. Liu, Z. M. Ni, W. Shi, J. L. Xue and P. P. Qian, *Appl. Catal. B Environ.*, 2014, **144**, 570–579.

11 N. Baliarsingh, K. M. Parida and G. C. Pradhan, *Ind. Eng. Chem. Res.*, 2014, **53**, 3834–3841.

12 W. Y. Lim and G. W. Ho, *Procedia Eng.*, 2017, **215**, 163–170.

13 R. D. Ambashta and M. Sillanpää, *J. Hazard. Mater.*, 2010, **180**, 38–49.

14 C. W. Notebaart and F. P. van der Meer, *Miner. Eng.*, 1992, **5**, 767–778.

15 A. Shalom and C. R. Price, *IEEE Trans. Magn.*, 1981, **17**, 3305–3307.

16 J. Reffle, V. Krautwurm, H. Schewe and H. Hoffmann, *J. Magn. Magn. Mater.*, 1979, **13**, 11–12.

17 C. de Latour, *J. Am. Water Works Assoc.*, 1976, **68**, 498–500.

18 J. Sun, R. Xu, Y. Zhang, M. Ma and N. Gu, *J. Magn. Magn. Mater.*, 2007, **312**, 354–358.

19 L. Ma, X. Dong, M. Chen, L. Zhu, C. Wang, F. Yang and Y. Dong, *Membr. 2017, Vol. 7, Page 16*, 2017, **7**, 16.

20 M. F. L. De Volder, S. H. Tawfick, R. H. Baughman and A. J. Hart, *Science (80-.).*, 2013, **339**, 535–539.

21 J. Kim and B. Van Der Bruggen, *Environ. Pollut.*, 2010, **158**, 2335–2349.

22 R. Das, M. E. Ali, S. B. A. Hamid, S. Ramakrishna and Z. Z. Chowdhury, *Desalination*, 2014, **336**, 97–109.

23 K. Goh, H. E. Karahan, L. Wei, T. H. Bae, A. G. Fane, R. Wang and Y. Chen, *Carbon N. Y.*, 2016, **109**, 694–710.

24 K. J. Lee and H. D. Park, *New pub Balaban*, 2016, **57**, 26706–26717.

25 A. V. Herrera-Herrera, M. ángel González-Curbelo, J. Hernández-Borges and M. ángel Rodríguez-Delgado, *Anal. Chim. Acta*, 2012, **734**, 1–30.

26 E. Celik, L. Liu and H. Choi, *Water Res.*, 2011, **45**, 5287–5294.

27 H. A. Shawky, S. R. Chae, S. Lin and M. R. Wiesner, *Desalination*, 2011, **272**, 46–50.

28 V. Vatanpour, S. S. Madaeni, R. Moradian, S. Zinadini and B. Astinchap, *J. Memb. Sci.*, 2011, **375**, 284–294.

29 Y. Shirazi, M. A. Tofighy and T. Mohammadi, *J. Memb. Sci.*, 2011, **378**, 551–561.

30 E. Celik, H. Park, H. Choi and H. Choi, *Water Res.*, 2011, **45**, 274–282.

31 Y. Wang, Y. Liu, Y. Yu and H. Huang, *J. Memb. Sci.*, 2018, **551**, 326–332.

32 J. Li, S. Zhang, Y. Chen, T. Liu, C. Liu, X. Zhang, M. Yi, Z. Chu and X. Han, , DOI:10.1039/c7ra03848h.

33 L. Zhai, Z. Bai, Y. Zhu, B. Wang and W. Luo, *Chinese J. Chem. Eng.*, 2018, **26**,

657–666.

34 N. R. Jannah and D. Onggo, *J. Phys. Conf. Ser.*, 2019, **1245**, 12040.

35 M. E. Compeán-Jasso, F. Ruiz, J. R. Martínez and A. Herrera-Gómez, *Mater. Lett.*, 2008, **62**, 4248–4250.

1 S. Kim, H. Wang and Y. M. Lee, *Angew. Chemie Int. Ed.*, 2019, **58**, 17512–17527.

2 Y. Wang, Z.-X. Low, S. Kim, H. Zhang, X. Chen, J. Hou, J. G. Seong, Y. M. Lee, G. P. Simon, C. H. J. Davies and H. Wang, *Angew. Chemie Int. Ed.*, 2018, **57**, 16056–16061.

3 J. Ren, L. Stagi and P. Innocenzi, *J. Mater. Sci.*, 2021, 56, 4053–4079.

4 S. Dutta, P. K. Gan and K. Chatterjee, *AIP Conf. Proc.*, 2020, **2265**, 030120.

5 Y. Mutharasi, N. J. Kaleekkal, T. Arumugham, F. Banat and M. S. Kapavarapu, *Chem. Eng. Process. - Process Intensif.*, 2020, **158**, 108191.

6 Z. Yang, F. Wang, C. Zhang, G. Zeng, X. Tan, Z. Yu, Y. Zhong, H. Wang and F. Cui, *RSC Adv.*, 2016, **6**, 79415–79436.

7 V. K. Gupta, R. Jain, A. Mittal, M. Mathur and S. Sikarwar, *J. Colloid Interface Sci.*, 2007, **309**, 464–469.

8 S. Yuan, Y. Li, Q. Zhang and H. Wang, *Colloids Surfaces A Physicochem. Eng. Asp.*, 2009, **348**, 76–81.

9 L. Mohapatra and K. M. Parida, *Sep. Purif. Technol.*, 2012, **91**, 73–80.

10 S. J. Xia, F. X. Liu, Z. M. Ni, W. Shi, J. L. Xue and P. P. Qian, *Appl. Catal. B Environ.*, 2014, **144**, 570–579.

11 N. Baliarsingh, K. M. Parida and G. C. Pradhan, *Ind. Eng. Chem. Res.*, 2014, **53**, 3834–3841.

12 W. Y. Lim and G. W. Ho, *Procedia Eng.*, 2017, **215**, 163–170.

13 R. D. Ambashta and M. Sillanpää, *J. Hazard. Mater.*, 2010, **180**, 38–49.

14 C. W. Notebaart and F. P. van der Meer, *Miner. Eng.*, 1992, **5**, 767–778.

15 A. Shalom and C. R. Price, *IEEE Trans. Magn.*, 1981, **17**, 3305–3307.

16 J. Reffle, V. Krautwurm, H. Schewe and H. Hoffmann, *J. Magn. Magn. Mater.*, 1979, **13**, 11–12.

17 C. de Latour, *J. Am. Water Works Assoc.*, 1976, **68**, 498–500.

18 J. Sun, R. Xu, Y. Zhang, M. Ma and N. Gu, *J. Magn. Magn. Mater.*, 2007, **312**, 354–358.

19 L. Ma, X. Dong, M. Chen, L. Zhu, C. Wang, F. Yang and Y. Dong, *Membr. 2017, Vol. 7, Page 16*, 2017, **7**, 16.

20 M. F. L. De Volder, S. H. Tawfick, R. H. Baughman and A. J. Hart, *Science (80-.).*, 2013, **339**, 535–539.

21 J. Kim and B. Van Der Bruggen, *Environ. Pollut.*, 2010, **158**, 2335–2349.

22 R. Das, M. E. Ali, S. B. A. Hamid, S. Ramakrishna and Z. Z. Chowdhury, *Desalination*, 2014, **336**, 97–109.

23 K. Goh, H. E. Karahan, L. Wei, T. H. Bae, A. G. Fane, R. Wang and Y. Chen, *Carbon N. Y.*, 2016, **109**, 694–710.

24 K. J. Lee and H. D. Park, *New pub Balaban*, 2016, **57**, 26706–26717.

25 A. V. Herrera-Herrera, M. ángel González-Curbelo, J. Hernández-Borges and M. ángel Rodríguez-Delgado, *Anal. Chim. Acta*, 2012, **734**, 1–30.

26 E. Celik, L. Liu and H. Choi, *Water Res.*, 2011, **45**, 5287–5294.

27 H. A. Shawky, S. R. Chae, S. Lin and M. R. Wiesner, *Desalination*, 2011, **272**, 46–50.

28 V. Vatanpour, S. S. Madaeni, R. Moradian, S. Zinadini and B. Astinchap, *J. Memb. Sci.*, 2011, **375**, 284–294.

29 Y. Shirazi, M. A. Tofighy and T. Mohammadi, *J. Memb. Sci.*, 2011, **378**, 551–561.

30 E. Celik, H. Park, H. Choi and H. Choi, *Water Res.*, 2011, **45**, 274–282.

31 Y. Wang, Y. Liu, Y. Yu and H. Huang, *J. Memb. Sci.*, 2018, **551**, 326–332.

32 J. Li, S. Zhang, Y. Chen, T. Liu, C. Liu, X. Zhang, M. Yi, Z. Chu and X. Han, , DOI:10.1039/c7ra03848h.

33 L. Zhai, Z. Bai, Y. Zhu, B. Wang and W. Luo, *Chinese J. Chem. Eng.*, 2018, **26**, 657–666.

34 N. R. Jannah and D. Onggo, *J. Phys. Conf. Ser.*, 2019, **1245**, 12040.

35 M. E. Compeán-Jasso, F. Ruiz, J. R. Martínez and A. Herrera-Gómez, *Mater. Lett.*, 2008, **62**, 4248–4250.

Chapter 6. MoS_2 based membranes

6.1. Introduction

The recent interest in TMDs has been driven by their exceptional properties (e.g. semiconductor state, conductivity, flexibility, transparency, large surface area, light emission, etc.) and potential applications such as materials for photonics, sensing, catalysis, solid lubrication, energy storage, high performance electronics and optoelectronics. For example TMDs can be synthesised in metallic or semiconducting forms depending of the structure they present[1,2], they have a tuneable bandgap dependant of the number of monolayers[3]and some of them demonstrate photoluminescence in the visible region which could potentially be used for sensing and optoelectronics[4,5].

A particularly interesting and most studied TMD is molybdenum disulfide (MoS_2). This material has very interesting electrical[6–8], biological[9], mechanical[8] and physicochemical[10] properties, which makes it to be a very promising for several applications, including electronics[6,7], catalysis[8,10], filtration[11–13], biomedical[9,14] and energy-related[15,16]. Another field where MoS_2 is expected to be used is catalytic and environmental applications. MoS_2, in its bulk form, can be found in nature as the mineral molybdenite, which is quite abundant, and has been considered before as a catalyst[8,17] as well as an adsorbent[18]. MoS_2 is also used in a range of applications including as a solid state lubricant and as a catalyst for a range of reactions including the hydrodeoxygenation of phenols[19]. MoS_2, in its bulk form, has an energy gap of ~1.2 eV, and is an indirect band gap semiconductor[20]. The band gap increases with a decreasing number of layers and is calculated to become 1.8 eV for a monolayer[21]. This makes this nanomaterial useful for potential in electronics and photonic applications. Finally, MoS_2 can also be used for preparation of membranes which have shown higher water permeance than previously described graphene membranes, with similar thickness and reject ratio [11–13] due to the higher level of interaction between the MoS_2 sheets. In addition, it has been reported that the nanochannels present in the MoS_2 membranes do not get deformed under pressure as high as 1.0 MPa, as it has been proved by the linear relationship between pressure and water permeance.

6.1.1 Structure of MoS_2

Bulk MoS_2 exists as a black powder and particles. The bulk MoS_2 is assembled by monolayers, which demonstrate strong covalent Mo-S bonds within each monolayer but weak Van-der-Waals forces in between the layers, which allows the possibility of separation in few to monolayers[22]. The MoS_2 layers are composed by two S atom layers sandwiching a Mo atom layer with a interlayer spacing of 0.62 nm and free spacing of 0.30 nm[22,23] (as shown in figure 6.1 a). Bulk MoS_2 is chemically stabilized due to the saturated sulphur atoms on the basal plane, with the exception of those on the edge, as well as the monolayers.

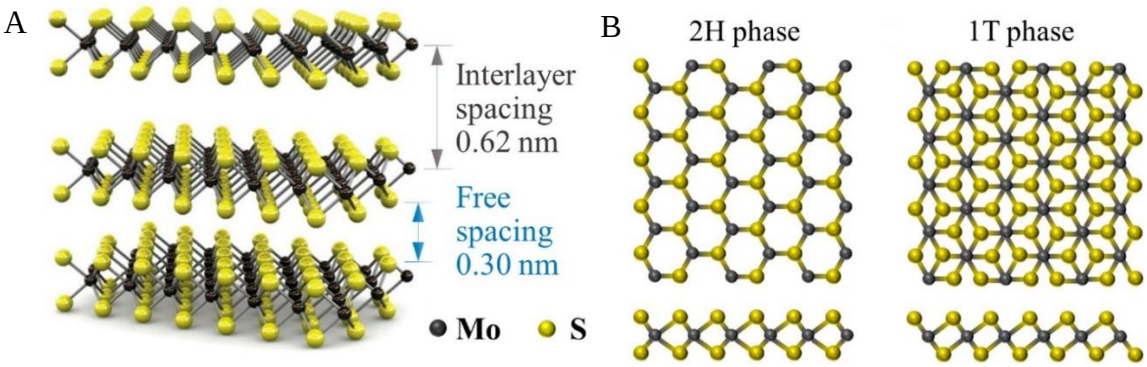

Figure 6.1: MoS_2 strcuture A) 3D ilustration and B) atomic positions 2H (trigonal prismatic coordination) and 1T(octahedral coordination) phases[22].

The MoS_2 can be found in two crystal structures, trigonal prismatic 2H phase and octahedral 1T phase (figure 6.1 B), which depends on the stacking configurations of the atoms in the structure[22,24]. Naturally occurring molybdenite (bulk MoS_2) appears more commonly as the semiconducting and thermodynamically stable 2H phase, whereas the polymorph 1T (metallic and metastable) doesn't appear naturally[22,25]. The monolayers can be produced by exfoliation due to the weak forces between the layers (see next section). Depending on the exfoliation method chosen, the nanosheets can form in either 2H or 1T phases but also transformed from one to the other via Li intercalation, because of interlayer atomic sliding (phase 2H to 1T)[26] or through annealing (1T to 2H)[20].

6.1.2 Synthesis methods

The preparation of few to monolayer MoS_2 nanosheets can be done by several methods, tailored for different applications. These approaches are divided into two types: top-down methods that consist of exfoliating the bulk materials by breaking the weak Van-der-Waals forces in between the layers, and the bottom-up methods where MoS_2 nanosheets are synthesised from appropriate molecular precursors[22]. For membrane applications, the top-down methods are usually preferred.

For exfoliation of 2D nanomaterials, several methods can be used. The main ones are liquid-based and chemical exfoliation. Liquid-phase exfoliation is carried out by sonicating bulk MoS_2 in the presence of an organic solvent (like NMP[27]) or in aqueous phase with a surfactant (like sodium cholate) to stabilize the suspension[28]. Liquid exfoliation present several advantages, such easy scalability, use for a wide range of environmental applications (when using water as the solvent), as well as keeping the semiconducting 2H phase. However, the main disadvantages is the product stays in multilayer form[27,29] and the need, sometimes, to remove the surfactant or solvents [30,31]. Chemical exfoliation can be achieved by intercalation of lithium ions through incubation of bulk MoS_2 in a organolithium containing organic solvent followed by the reaction of Li_xMoS_2 intermediate with water under sonication, creating a stable dispersion[20]. Partial loss of the 2H phase happens as a result of structural deformation caused by the intercalation of the lithium, but can be recovered through mild annealing[20,32], laser irradiation[33] or microwave treatment[34].

6.1.3 Membrane-based separation

Much like other 2D nanomaterials such as graphene, MoS_2 can be used for membrane-based separation applications[11,35–37]. MoS_2 is thought to be a great candidate to use as a building block for membranes with great separation capabilities and, potentially, enabling to facilitate antifouling and multifunctional properties. This is due to MoS_2 high mechanical stability[22,35], easy and scalable synthetic procedure and attractive properties, including photocatalysis and antibacterial properties[22]. One of the general types of

membranes that can be produced with MoS_2 nanosheets is layer-stacked membranes (figure.6.2)

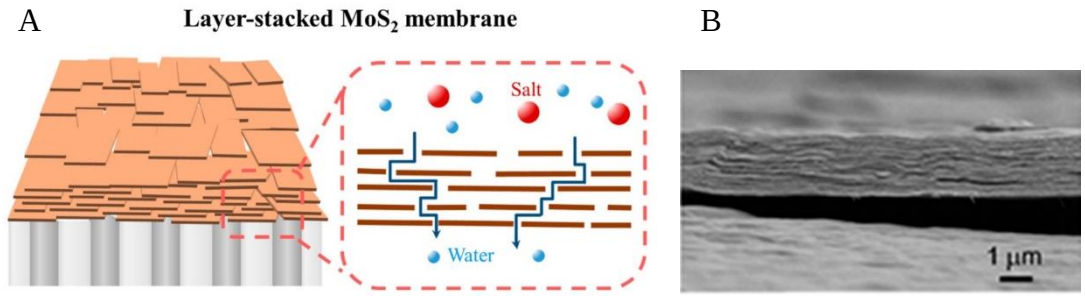

Figure 6.2: A) Schematic illustration of a layer-stacked MoS_2 membrane and separation mechanism[22] and B) SEM image of a layer-stacked MoS_2 membrane prepared by vacuum filtration[11].

One way of making MoS_2-based membranes is through restacking the exfoliated MoS_2 monolayers using vacuum-filtration on top of a template[11]. The chemically exfoliated MoS_2 is present more as monolayers with large lateral dimensions, whereas the liquid exfoliated MoS_2 commonly appears in smaller sheets and coated with surfactants. Therefore, chemically exfoliated MoS_2 is preferred as the building blocks for membranes, although liquid-exfoliated nanosheets can be used too. Some studies have shown that using MoS_2 with a 1.7 um thickness exhibited a water flux of 245 L h^{-1} m^{-2} bar^{-1}, which is higher than that obtained with a similar thickness GO membrane (45 L $h^{-1}m^{-2}bar^{-1}$), while maintaining the retention of small molecules (Evans blue and cytochrome *c*) at around 90%[11]. High water flux is attributed to low hydraulic resistance of the smooth channel surface due to MoS_2 layers not having functional groups. On the contrary, GO has quite a few oxygenated groups that stick out of the carbon plane, which creates hydraulic resistance to the water flow[22]. While GO membranes are impermeable to light organic vapors due to the pathways being blocked by the oxygenated groups, the MoS_2 smooth channels allow the continuous flow of these molecules[38]. Additionally, the water permeance of the MoS_2 membrane can be further improved by adding ultrathin nanowires between the layers, which has already been shown for another TMD, WS_2[36]. Another advantageous property of the layer-stacked MoS_2 membranes is its great stability in water, even without any stabilization treatment, like cross-linking[22]. MoS_2 membranes have also displayed exceptional integrity in aqueous solutions of various

pHs[38]. This is most likely due to the absence of hydrophilic groups on the surface, as well as the Van-der-Waals forces in between the nanosheets holding the layers together and preventing the redispersion in solution[38]. This presents an advantage in relation to GO membranes, as they are hydrophilic and, therefore, unstable in water[39] and need some stabilization strategy, like cross-linking[40].

Layer-stacked MoS_2 membranes also display linear correlation between permeance of water and applied pressure, which differs from the saturation of water flux under high pressure that GO membranes show. This flux behavior as well as the stability of MoS_2 layers seems to indicate that MoS_2 could be used as a building block of novel membranes, with the possibility of adapting the membrane separation capability[22].

Moreover, sinceMoS_2 is lipophobic, the scaling and organic fouling could be avoided. This is a problem that is present in graphene-based membranes as a result of cation-π and π-π interactions. However, research into the performance and mechanisms of layer-stacked MoS_2 membranes it's still on its early stages[22].

6.1.4 Aims of this chapter

The aims of this work were to use MoS_2 as a building block for membranes. To do this, we needed firstly to optimize the exfoliation of the material, in order to obtain the best material for the membranes. Secondly, we aimed to functionalize the MoS_2 to add additional properties to the membrane. These properties would allow the use of these membranes for different applications, like separation of chiral materials, such as D- and L-lactic acid due to the increased demand for the enantiomerically pure lactic acid, not only in the food industry, but also in the chemical and agricultural sectors[41]. Another potential interesting application for these membranes is the separation of mono- from di- and polysaccharides. Finally, we were also aiming to test these membranes to optimize the formation and performance of the MoS_2 membranes to obtain the best results.

6.2. Results and discussion

6.2.1 Exfoliation of MoS_2

MoS_2 was exfoliated using a liquid-phase mechanical approach. The colour of the solution after exfoliation changed from black to light green, as was expected. This colour change demonstrated successful exfoliation, as MoS_2 has been reported to acquire a green colour in its exfoliated form. However, the colour obtained was light and there were a lot of precipitate after centrifugation, which indicates that only a small fraction of the MoS_2 was successfully exfoliated. Due to this, it was decided to add a surfactant to facilitate the exfoliation. For this purpose, sodium cholate was chosen.

Sodium cholate was added to the MoS_2 after the cleaning step and before the sonication (according to the materials and methods section). The addition of the surfactant was immediately noticable, as the solution produced had a much darker green colour and less precipitate appeared after centrifugation, all indications that most of the MoS_2 had been successfully exfoliated.

The characterisation of the exfoliated MoS_2 was carried out using UV-Vis, powder XRD and SEM.

The UV-Vis spectra were recorded for the mechanically exfoliated, as well as a solution of the bulk MoS_2. The UV-Vis spectra were clearly different between the exfoliated and bulk MoS_2 (Figure 6.3)

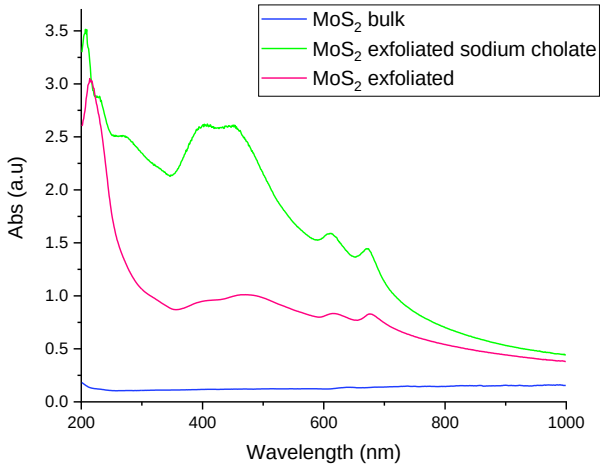

Figure 6.3: UV-Vis spectra of bulk MoS_2 and mechanically exfoliated MoS_2 in the absence and presence of sodium cholate showing the characteristic bands of mechanically exfoliated MoS_2. λ: 200-1000 nm

UV-Vis spectra alone can determine whether the exfoliation was successfully achieved, as the spectrum of bulk MoS_2 is distinctly different from that of exfoliated MoS_2, regardless of the presence of sodium cholate. In comparison, the spectrum of bulk MoS_2 shows no characteristic bands at any wavelength and uniform absorbance at all wavelengths; on the other hand, exfoliated MoS_2 spectrum shows distinctive bands appearing at certain wavelengths. In the spectra of the sample exfoliated in the presence of sodium cholate, these bands appear more clearly, being clearly distinguishable from one another. However, in the case of the sample exfoliated without sodium cholate, these bands are less distinct, indicating less stability of the exfoliated material. Furthermore, the spectrum corresponding to the exfoliated MoS_2 in the presence of sodium cholate shows more defined bands for those wavelengths (400-450 nm, 600 nm and 700 nm) , as well as higher concentration than the MoS_2 exfoliated on in the absence of sodium cholate. This correlates with the more intense green colour presence when using this surfactant, indicating that the use of this type of chemical improves the rate of exfoliation, as well as the stability of the nanosheets.

Powder XRD was carried out only for the MoS_2 exfoliated in the presence of sodium cholate, as that showed the best results for exfoliation, as well as the bulk MoS_2 to use as comparison (Figure 6.4). In the pattern, it is possible to see the diffraction peaks that coincide with that of MoS_2, as compared with the bulk sample. Moreover, there were other peaks that could be related to other molecules that are consistent with those used during the exfoliation. Firstly, the peaks corresponding to sodium cholate were identified in the low angle area, corresponding to organic compounds. This is consistent with the method of exfoliation, as that was the surfactant used to stabilise the MoS_2 once exfoliated. Moreover, even after cleaning steps, the sodium cholate was still present in the sample, so further cleaning steps might be needed to get rid of the sodium cholate after the exfoliation. This surfactant is most likely not totally removed, still being present in the solution and appearing in the XRD pattern. Interestingly, there were still some unidentified peaks that were found to be due to the presence of sodium molybdenum sulphide. This seems to indicate that the sodium from the surfactant interacts with the MoS_2, forming sodium molybdenum sulphide and this could be the reason for the increased stability of the exfoliated material. This, however, requires further testing.

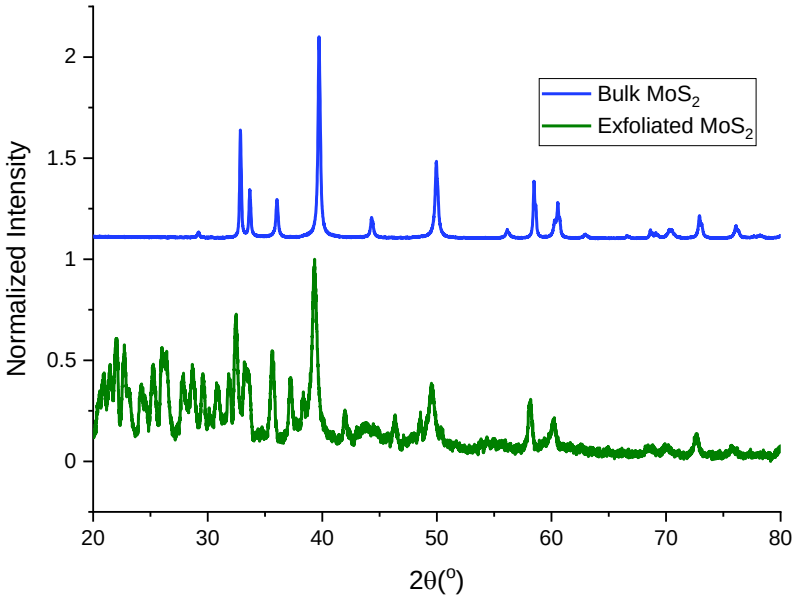

Figure 6.4: Powder XRD pattern of bulk MoS_2 and exfoliated MoS_2 in the presence of sodium cholate. 2θ: 20-80, fluorescence correction applied.

FTIR of MoS_2 was carried out, both bulk and exfoliated in the presence of sodium cholate. Peaks at around 469-500 cm^{-1} are attributed to the Mo-S stretching vibration[42–45]. From around 700 to 1150 cm^{-1} can be assigned to the sulfate group. The peak around 1080-1090 cm^{-1}, corresponding to SO_3^{2-} can be found in the exfoliated MoS_2[46–48], which happens due to the dissociation of H_2SO_3 caused by the adsorbed water as a result of the exfoliation in presence of water. Peaks corresponding to O-H can also be observed.(3400-3500 cm^{-1})[43,49,50]. Peaks corresponding to sodium cholate (2850-2933 cm^{-1} and 2047-2158 cm^{-1}) also appear in the exfoliated MoS_2 in the presence of sodium cholate, which points to the interaction between the sodium cholate and MoS_2. This interaction, even after the centrifugation step is also apparent in the powder XRD pattern. Most peaks are less defined in the bulk sample, whereas the peaks are more defined in the exfoliated MoS_2. This seems to suggest that the functional groups are formed during the exfoliation[46].

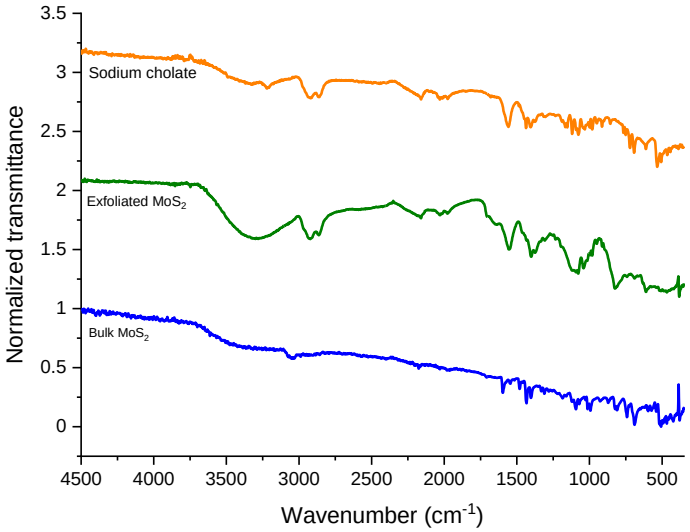

Figure 6.5: FTIR spectra of bulk MoS_2, exfoliated MoS_2 in the presences of sodium cholate and sodium cholate.

In order to confirm the presence of nanosheets, SEM imaging was performed on the exfoliated MoS_2 (figure 6.6). When examining the images produced from the SEM, the appearance of nanosheets could be noticed. The sizes of the nanosheets seemed to be fairly similar, pointing to a homogenous distribution. In addition, the images obtained from the sample showed nanosheets appearing throughout the sample. In comparison to the BN nanosheets, MoS_2 nanosheets were less smooth, showing uneven edges. In some cases, rectangular shapes appeared in the sample, which didn't correspond to the morphology of MoS_2 bulk or exfoliated forms. These shapes could correspond to crystals of sodium cholate, which was still present in the sample as it could be seen in the XRD pattern. The lateral size of the nanosheets was recorded, obtaining a mean length of 0.24 ± 0.06 µm (figure 6.7).

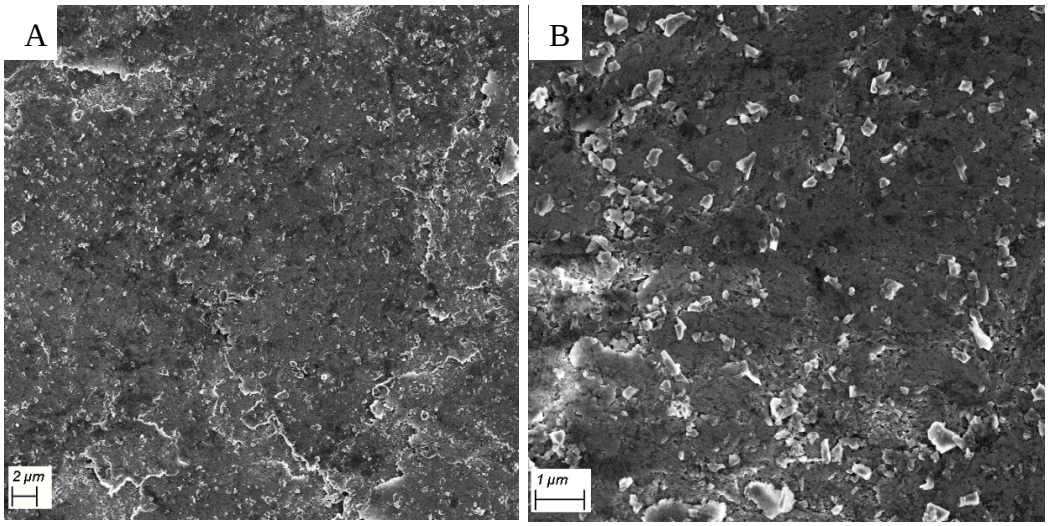

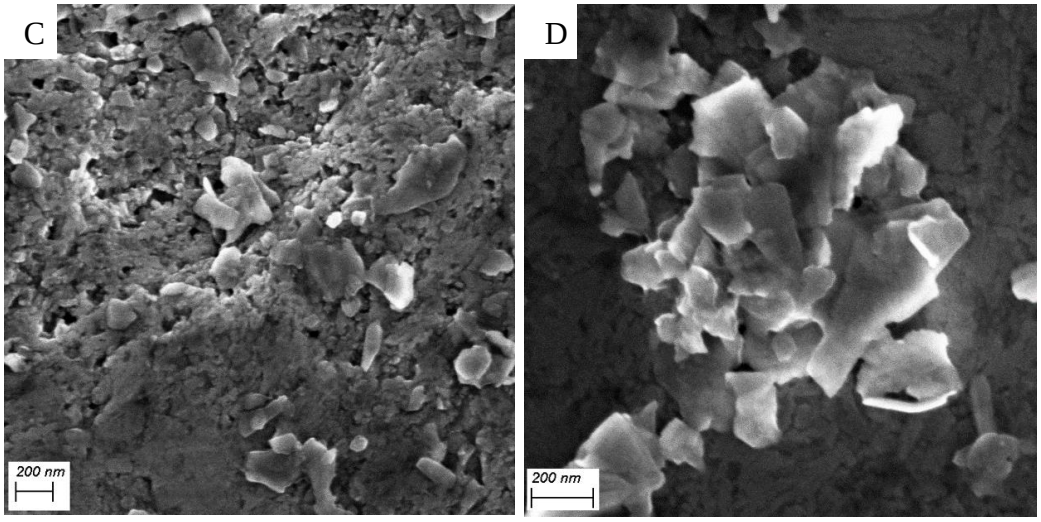

Figure 6.6: SEM images of MoS_2 nanosheets after mechanical exfoliation. Image A and B show the sample from a further distance and image C and D were taken as a closed up. Voltage: 3 kV, InLens.

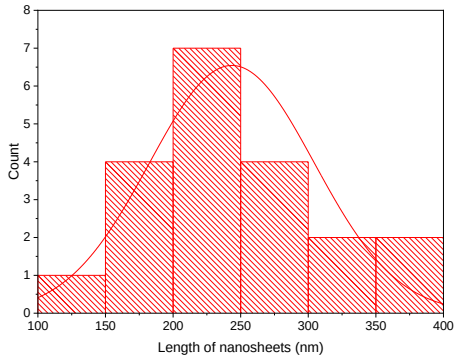

Figure 6.7: Distribution of the length of the MoS_2 nanosheets obtained from the SEM images, presented in Figure 6.6.

6.2.2 MoS_2 based membranes

6.2.2.1 Preparation and characterisation of MoS_2 based membranes

Once the exfoliated MoS_2 dispersionswere obtained, the membranes were prepared by vacuum filtration through a template, specifically a polycarbonate membrane of 47 mm in diameter and with a 20 nm pore size. The membranes were grey in colour and the membrane was imaged by SEM, both the top layer and the cross-section (Figures 6.8 and 6.9).

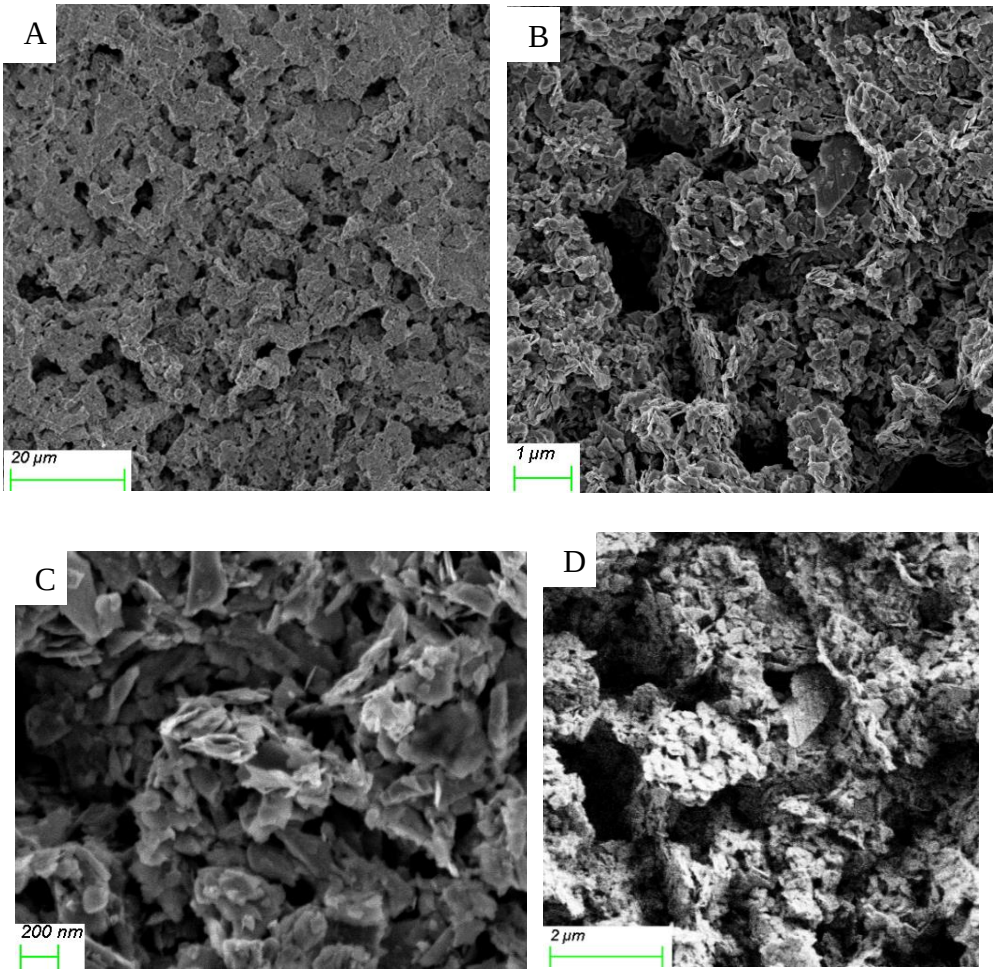

Figure 6.8: SEM images of the surfaces of MoS_2 membranes, taken with InLens (A, B and C) and SE2 D). Images B and C were taken as a closed up from image A, which shows the sample from a farther distance. Voltage: 3 kV, InLens and 5 kV, SE2

According to the SEM images (Figure 6.9) of membranes, they consist of random aggregated nanosheets. The surface is relatively uniform, but rough. The pores of the membrane are visible in the surface. When using SE2, the pores are more easily to see.

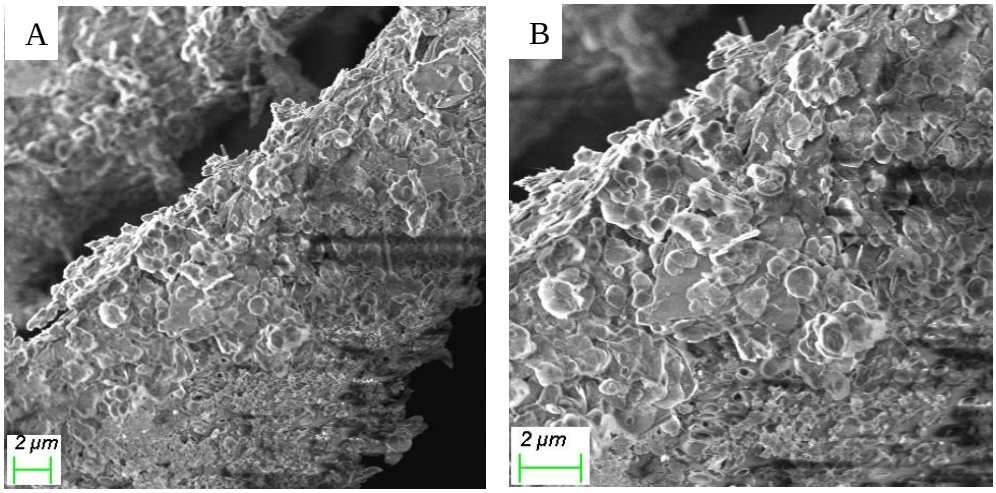

Figure 6.9: SEM images of the cross-section of MoS_2 membranes. Image B was taken as a closed up from image A, which shows the sample from a farther distance. Voltage: 3 kV, InLens.

The cross-section of the membranes (figure 6.9) showed the uniform distribution of the nanosheets throughout the membrane. This indicated an even formation of the membrane, with no apparent disturbances present throughout the membrane.

6.2.2.2 Testing the membranes

The membranes were then tested by checking their retention of an organic dye, Evans Blue. In order to be able to quantify the retention, UV-Vis spectroscopy was used. The spectrum of the Evans Blue solution (15 μM) was recorded before and after passing through the membrane, as shown in Figure 6.10. The retention of by the membranes was compared with the stock solution of Evans Blue to get the retention values (shown in figure 6.10) and calculated by comparing the absorbances.

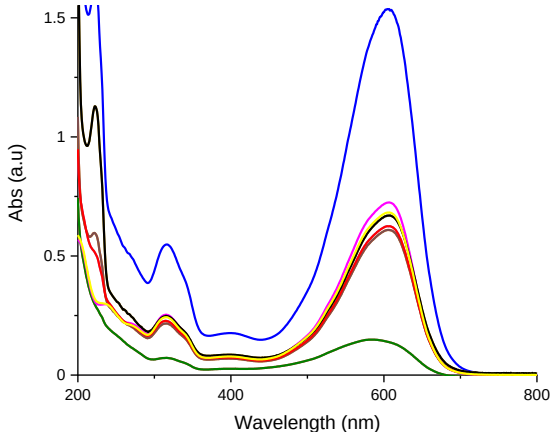

Figure 6.10: UV-Vis spectra of the 15 µM Evans Blue solution before (dark blue) and after filtration through the MoS_2 membrane (rest of the colours). λ:200-800 nm.

The retention values are shown in table 6.1 and the mean values and statistics are shown in table 6.2.

Table 6.1: Absorbance and retention of the MoS_2 membranes tested with Evans Blue 15 µM

Sample	Abs	% retention
EB	1.54	0
MoS_2 membrane	0.72	53
MoS_2 membrane	0.15	90
MoS_2 membrane	0.15	90
MoS_2 membrane	0.61	60
MoS_2 membrane	0.63	59
MoS_2 membrane	0.67	56
MoS_2 membrane	0.61	60
MoS_2 membrane	0.63	59
MoS_2 membrane	0.67	56
MoS_2 membrane	0.68	56

Table 6.2: Statistics from the retention of the MoS_2 membranes. Row one was calculated using all the values from the membranes, whereas row two was calculated discarding the two highest values. The values where calculated using Origin 2018

	N total	Mean	Standard Deviation	Sum	Minimum	Median	Maximum
MoS_2 membrane	10	64	14	641	53	59	90
MoS_2 membrane	8	58	3	461	53	58	60

The MoS_2 membranes showed variability in retention, with some membranes showing higher retention, around 90%, whereas other membranes showed significantly lower retentions around 50-55%. The reported retention for this dye is around 80% for MoS_2 membranes [11,22], so the values obtained are lower than those found in literature. These results seem to indicate that the membranes obtained are less efficient at retaining Evans Blue than those reported [11,22], therefore, further development of these membranes is needed to optimise the process.

Due to this lower retention, we decided to produce the membranes using other templates to test their performance. As the BN membranes worked best when using PVDF templates, we decided to use PVDF templates, testing both 0.45 and 0.22 µm pore size. The membranes were prepared in the same way as previously explained, using 50 mL per membrane. We observed that a significant amount of the exfoliated MoS_2 passed through the template, resulting in less material in each membrane. Once the membranes were produced, they were tested using Evans Blue (20 mL, 15 µM) and quantified using UV-Vis. The retention of these membranes are shown in figure 6.11 and the values are displayed in table 3.

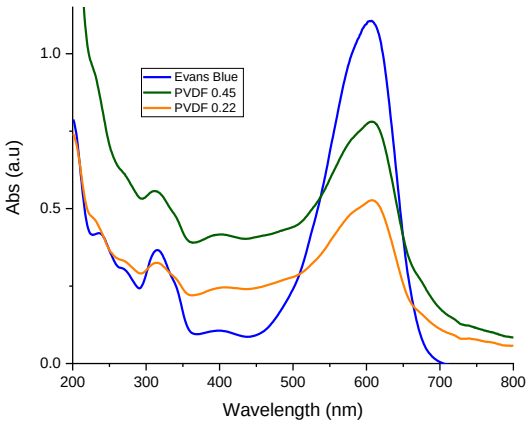

Figure 6.11: UV-Vis spectra of the 15 µM Evans Blue solution before (dark blue) and after filtration through the MoS_2 membrane formed using PVDF 0.45 µm (green) and PVDF 0.22 µm (orange). λ:200-800 nm.

Table 6.3: Absorbance and retention of the MoS_2 membranes made with PVDF as template tested with Evans Blue 15 µM

Sample	% Retention
EB	0
PVDF 0.45 µm	29
PVDF 0.22 µm	52

The retention of the membranes when using the PVDF templates didn't show any major improvements than when using polycarbonate as the template. In fact, the retention was significantly lower when using bigger pores (29%) and around the same as when using polycarbonate templates with the smaller pores (52%). This indicates that the PVDF templates are not the right choice for making MoS_2 membranes, as it doesn't interact correctly with the material, leading to some of it passing through the template freely when making the membrane and achieving lower retentions than when using a polycarbonate template. These values are still very distant from the 80% that has been reported in literature [11,22]. Therefore, more testing of the MoS_2 membranes is needed to optimise the formation and retention of these membranes.

6.2.3 Functionalization of MoS_2

One of the aims of this project is to develop membranes for the chiral separation of D- and L-lactic acid (amongst other enantiomeric molecules). Therefore, one of the approaches that can be taken to achieve this is the chiral functionalisation of the 2D material from which the membrane is going to be made. Initially, the functionalisation of the mechanically exfoliated MoS_2 was carried out. For this, two chiral ligands, cysteine and pencillamine, were chosen and both enantiomers, D and L, were used. These ligands were chosen because of their thiol group, which can bind to the Mo atom of MoS_2. The functionalisation was carried out by adding the ligands to the already exfoliated MoS_2 and the sample was further sonicated for 90 min. After washing out the excess ligand, the samples were characterised using CD (figure 6.12).

Initially, the functionalisation was carried out only with the cheaper enantiomer, L-cysteine, to test the feasibility of whether this would work.

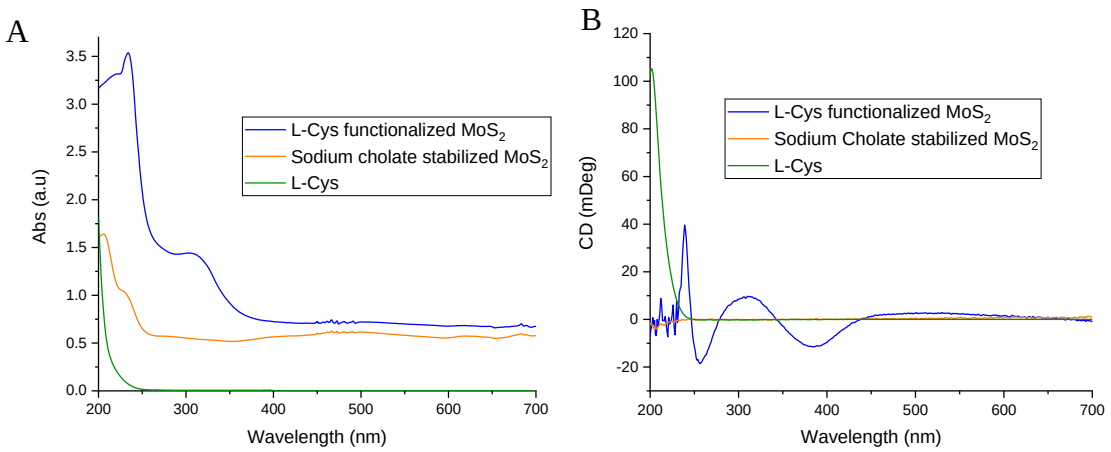

Figure 6.12: A) UV-Vis spectra and B) CD spectra of L-Cys ligand, and exfoliated MoS_2 with sodium cholate, and L-Cys. λ:200-700 nm.

The sample of functionalised exfoliated MoS_2 was compared to that of the non-functionalised exfoliated MoS_2. The UV-Vis spectra show no major variations in the shape, which demonstrates that no change in the state of the MoS_2 occurred, with it still being exfoliated. Furthermore, the sample with the L-Cys has a stronger signal, meaning that it's more concentrated. Since that sample comes from the one with sodium cholate, and the same volumes were taken from both solutions to run both the UV-Vis and CD (1mL of sample in 2mL of water), it seems that the extra 90 min under sonication needed to exchange the ligand must have exfoliated further the MoS_2 present, obtaining a higher concentration as result.

CD was measured for both samples. The exfoliated MoS_2 pre-functionalisation (exfoliated using sodium cholate) showed no CD signal at all, meaning that the sample didn't present any chirality. However, the L-cysteine functionalised MoS_2 showed quite an intense CD signal (Figure 6.12). The CD signal, moreover, shows peaks in the region where the UV-Vis bands for exfoliated MoS_2 would appear, proving that the ligand had interacted with the exfoliated material and that the chiral signal is a product of the interaction between L-cysteine and MoS_2. In addition, the CD signal of the exfoliated MoS_2 functionalized with L-cysteine is different of that of L-cysteine on its own, showing that the CD signal of the functionalized MoS_2 is due to an interaction between the 2D material and the chiral ligand and not because of the ligand itself.

Once the functionalisation was successfully proven, other chiral ligands were tested for MoS_2 functionalisation. Firstly, D-cysteine was tested and checked against the L-cysteine spectrum, to see whether the mirror image, typical from enantiomers, would appear.

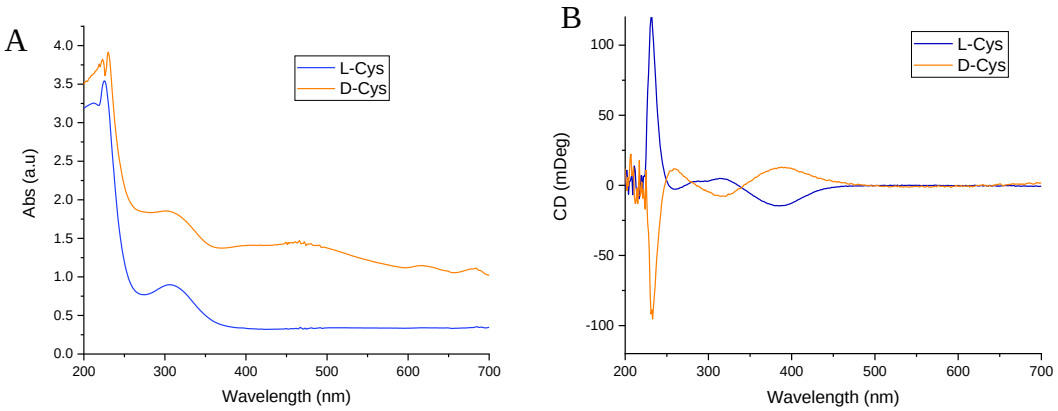

Figure 6.13: A) UV-Vis spectra and B) CD spectra of exfoliated MoS_2 with L and D-cysteine, showing the characteristic mirror images of enantiomers. λ:200-700 nm

The UV-Vis spectra were the same for both samples, which was the expected result upon seeing the result for the other enantiomer. When comparing the CD spectra of both L- and D-cysteine functionalised samples, it can be seen that both enantiomers are mirrored, which would be the expected result (Figure 6.13). This means that the interaction of each molecule produces a chiral signal, opposite to each other. This proves that MoS_2 can be successfully functionalized using cysteine.

After the successful experiments with D- and L-cysteine, we have performed the functionalisation using penicillamine, another chiral ligand with a thiol group. The functionalisation was carried out in the same manner as was used for the functionalisation with cysteine.

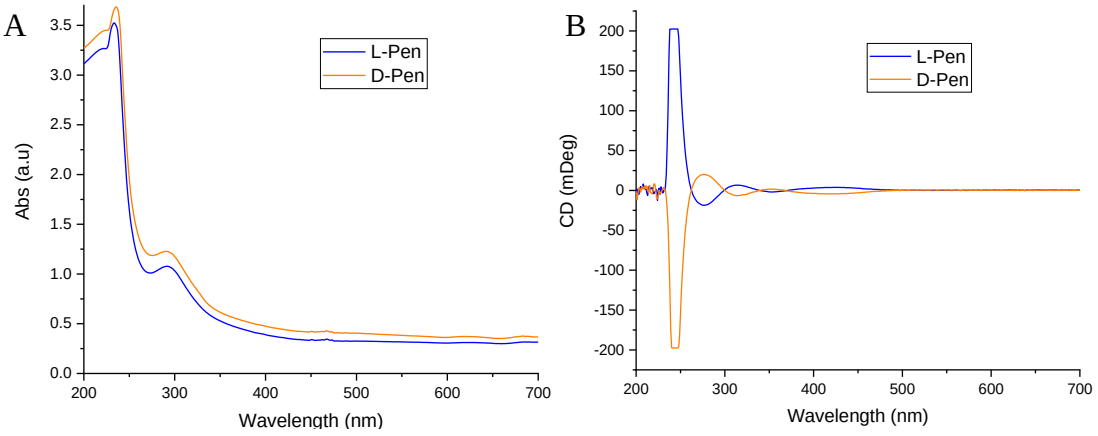

Figure 6.14: A) UV-Vis spectra and B) CD spectra of exfoliated MoS_2 with L and D-penicillamine, showing the characteristic mirror image of enantiomers. λ:200-700 nm.

Once again, UV-Vis and CD of both samples were recorded (figure 6.14). As above, UV-Vis shows no difference between both samples or with the UV-Vis spectra of the exfoliated MoS_2. Furthermore, the CD spectra show the successful functionalisation of the MoS_2. The spectra from each enantiomer again are present as mirror images of the other and are a result of the interaction between the exfoliated MoS_2 and the ligands.

SEM images were taken of the MoS_2 functionalized with L-Cys (figure 6.15).

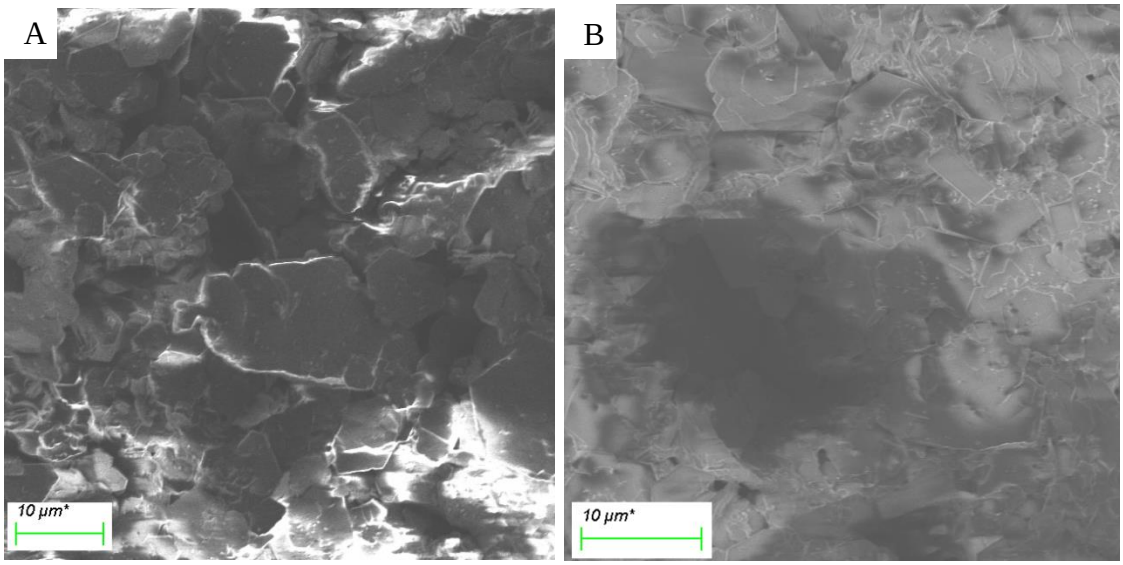

Figure 6.15: SEM images of exfoliated MoS_2 functionalized wit L-Cys. Image A was taken using SE2 and image B was taken using InLens. Voltage 2.3 kV

Nanosheets were present in these samples as well, showing no morphological differences with those obtained prior to the functionalisation. This means that the functionalization of exfoliated MoS_2 doesn't change the shape or size of the nanosheets. However, the sample where the ligand exchange took place showed the appearance of, what it seemed, some hexagonal plates. This is probably due to the conversion of an excess of cysteine into cystine and the crystallisation of the latter, since the sample had a white layer, was less soluble (attributed to the cystine) and the MoS_2 seemed to have lost its exfoliated state in solution, as the sample was black in colour instead of green. This seems to be supported by the SEM images, as cystine produces crystal with a hexagonal shape[51,52]. These samples were stable for 24 hours before the conversion of cysteine to cystine took

place, so they were suitable for making membranes as long as the membranes were prepared within 24 hours of the functionalization.

6.2.3.1 Membranes from L-Cys functionalised MoS_2

Once the functionalization of the MoS_2 with chiral ligands was successfully achieved, it was decided to prepare membranes from this material. Since the L-Cys functionalised sample was available in larger amounts and more rigorously tested, it was determined to use this sample for the preparation of the membranes.

Membranes were prepared in the same way as non-functionalized MoS_2 membranes were produced, making sure this didn't exceed the 24 hours where the sample was stable, before the conversion of cysteine to cystine. The aim was to use these membranes to attempt chiral separation.

The membranes looked very similar to those obtained with non-functionalized MoS_2 (figure 6.8). This was expected as the nanosheets produced were very similar. However, crystalline structures could be observed of what was assumed to be sodium cholate. This was an interesting result as these structures didn't appear in the case of the non-functionalized MoS_2, which could indicate that the addition of the L-Cys stabilised the sodium cholate in the sample, which causes crystals to appear once the membranes are formed. Some nanosheets could also be observed, showing that this structure is not lost after forming the membranes. However, cystine crystals couldn't be observed once the membranes were prepared, which may indicate that once the membrane is formed, the cysteine is stabilised and doesn't convert to cystine.

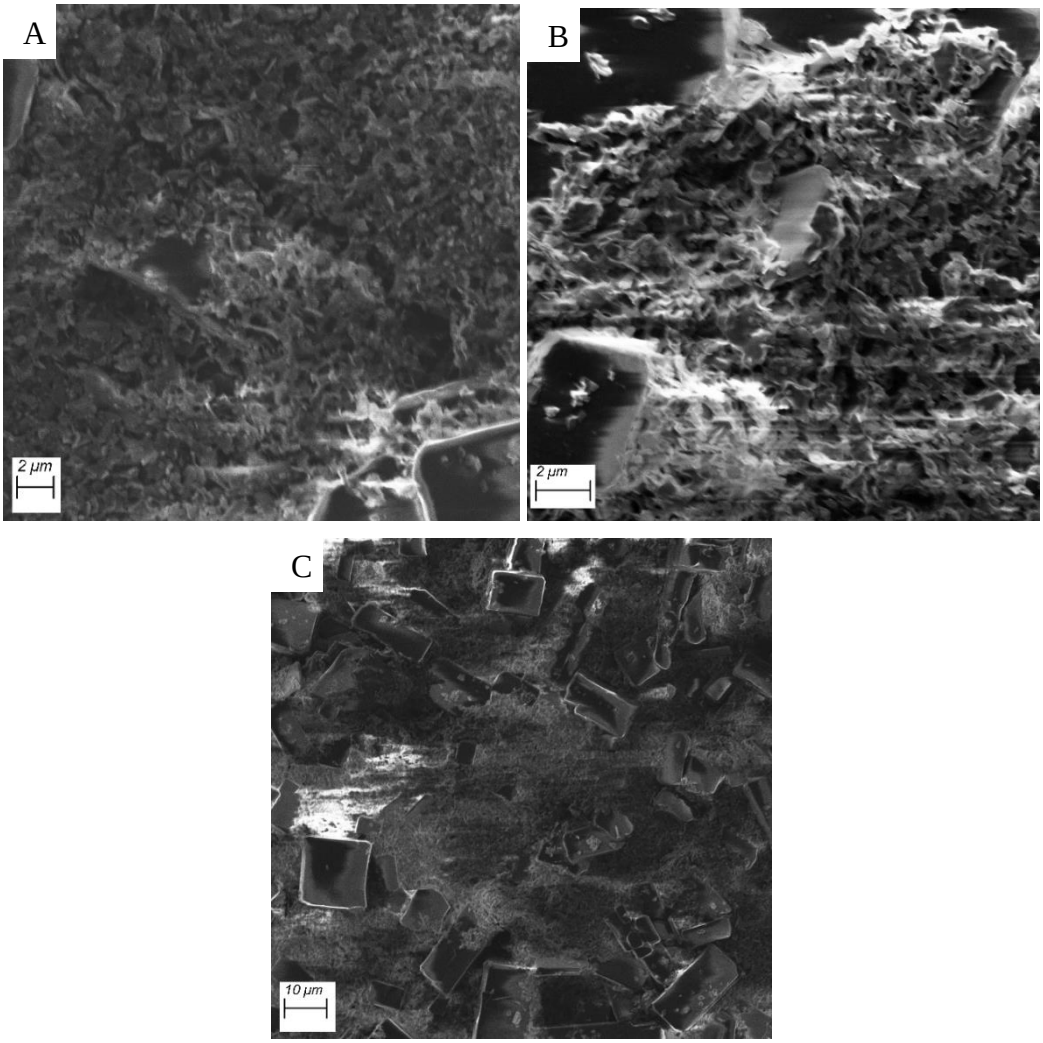

Figure 6.16: SEM images of L-Cys functionalized MoS_2 membranes. Image A was taken using a voltage 5.0 kV, image B was taken using a voltage 3.0 kV and C was taken using a voltage of 5.0 kV. Images A and B were taken closer to the sample whereas image C was taken further away. Images taken using SE2 signal.

6.2.3.2 Testing the chiral membranes

Once the membranes were prepared and their morphology was analysed by SEM, it was decided to test their retention capabilities.

In order to do this, a racemic solution of cysteine was prepared. For this, equal amounts of the same concentration of L- and D-Cys were mixed and their CD signal was analysed (Figure 6.17). This solution was then passed through the membrane and the permeate CD signal was recorded (Figure 6.17).

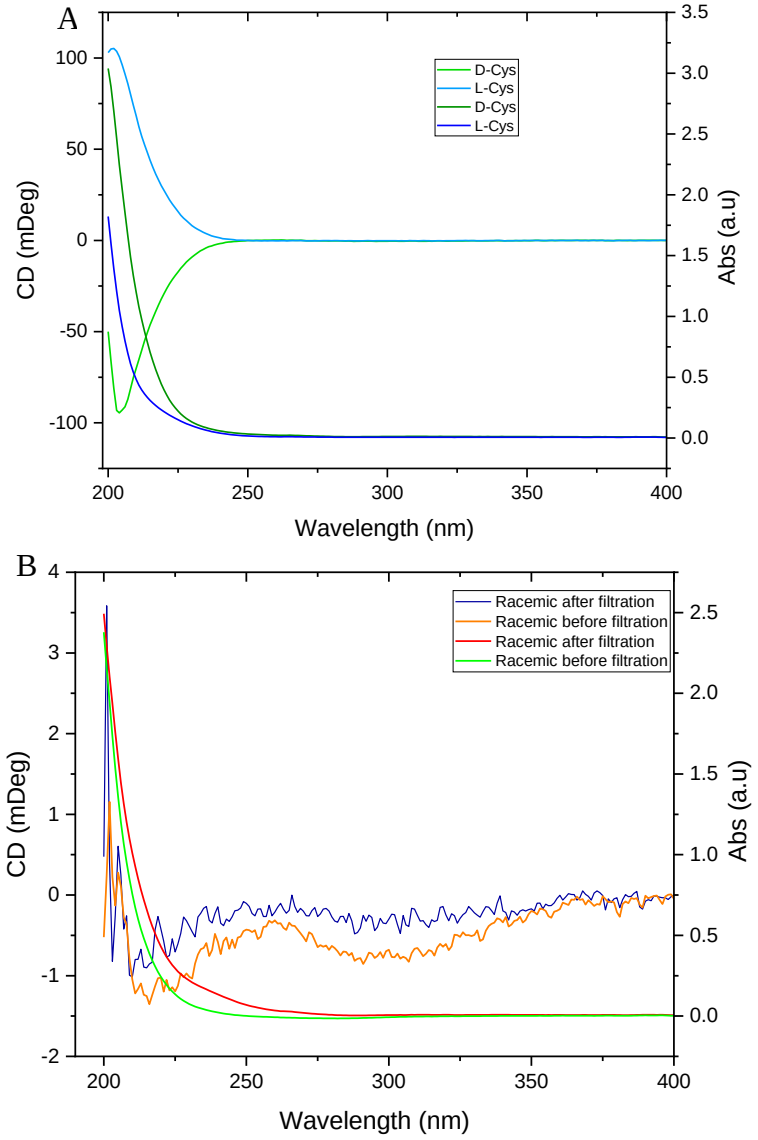

Figure 6.17: A) CD and UV-Vis spectra of the L- and D-Cys solutions and B) CD and UV-Vis spectra of racemic mixture of L- and D-Cys before and after filtration. λ:200-400 nm.

There were no differences between the racemic solution CD signal before and after filtration, indicating that no chiral separation occurs, which indicates that the membranes are not effective at separating the two enantiomers. This could be due to the membrane not being able to discriminate between L- and D-cysteine. However, it is possible there's no separation because the L-cysteine in the membrane is not stable enough and can be eluted with the solution. In order to test this, water was passed through an L-cysteine functionalized MoS_2 membrane and CD was recorded between 400 to 200 nm, as it is

there where the characteristic bands for free cysteine appear, until there was no signal (figure 6.18).

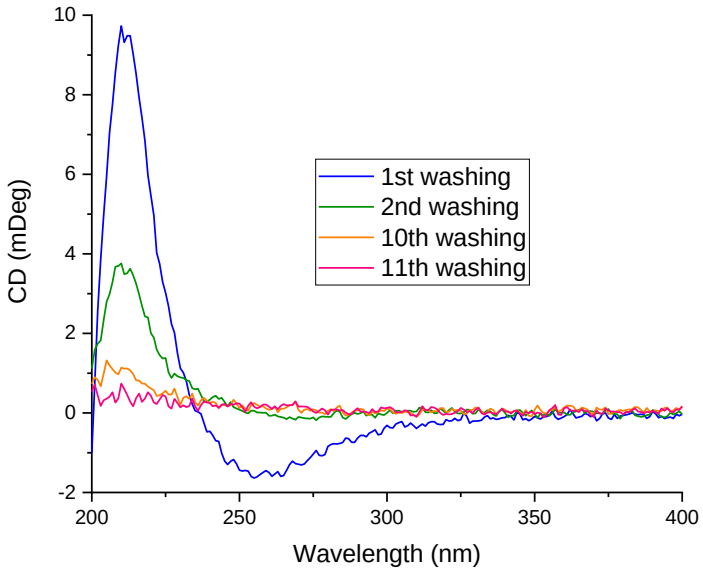

Figure 6.18: CD spectra of the washing through the L-Cysteine functionalise MoS_2 membrane. λ:200-400 nm.

As the CD spectra shows, just by washing the membrane once, a strong signal corresponding to the L-cysteine can be observed, meaning that quite a lot of the ligand is being washed out of the membrane. As the washing continues, the intensity of the bands decreases, meaning that most of the ligand has already been washed out. By the time the 11^{th} washing occurs, the signal is practically zero, which means that all the ligand has been washed out. However, during the chiral filtration of a racemic mixture, the CD signal for the L-cysteine is not visible, as would be expected as there would be an increment of L-cysteine added to the racemic mixture from the L-cysteine present in the membrane. This could indicate that the L-cysteine from the racemic is substituting the L-cysteine in the membrane, which would indicate that some stays bound to the MoS_2. This is not useful, though, as the cysteine bound to the membrane still is eluted from the membrane and no chiral filtration is achieved. This seems to suggest that, although the functionalisation with this ligand is possible, the interaction between the MoS_2 and Cysteine is not strong enough, as the chiral ligand gets washed out.

6.2.4 MoS_2 and BN composites

Due to the lower performance of the MoS_2 membranes on their own, it was decided to prepare MoS_2-BN composite membranes. The aim was to improve the performance of the membranes due to the presence of BN, but to still be able to benefit from the properties of the MoS_2 membranes. It was decided to use the partially oxidised BNOx, as the OH- groups present in it were more likely to interact with the MoS_2 and potentially improve the stability of the membrane formed.

The first step was to produce the exfoliated materials. Due to the sensitivity of MoS_2 when being exfoliated to avoid the formation of the metallic form, the two materials were exfoliated separately. Once the BNOx and MoS_2 were exfoliated, the membranes were formed by filtration. Initially, the membranes were prepared by putting a layer of BNOx directly on top of the template followed by the filtration of 50 mL of MoS_2 that were used to form the membranes. The idea behind this method was to create a stable layer, provided by the BNOx, which would allow the MoS_2 layer to deposit on top of it without any loss of material through the template. Since MoS_2 was present in higher amounts in the membrane than BNOx, it was expected that the performance of the membrane would be defined by this material, but with improved stability and performance due to the presence of BNOx layer.

As the first layer of the membrane was made using BNOx, the templates used were PVDF, 0.45 µm pore size, due to previously optimised performance of the BNOx membrane when using these templates. Once this layer was prepared, 50 mL of exfoliated MoS_2 was added to form the rest of the membrane. Different volumes were tested for the BNOx layer, starting at 20 mL and then decreasing it by half until 5 mL, as the purpose was to find the lowest amount of BNOx possible that would stabilise the membrane. When using this method, no leaks of MoS_2 through the BNOx layer or template were observed, which was already an improvement on some of the previous methods. The membranes were tested using Evans Blue (20 mL, 15 µM) and the retention was quantified using their absorbance.

SEM images of the membranes made with the BNOx layers (5, 10 and 20 mL), both top view and cross-section, were obtained (figure 6.19-6.21).

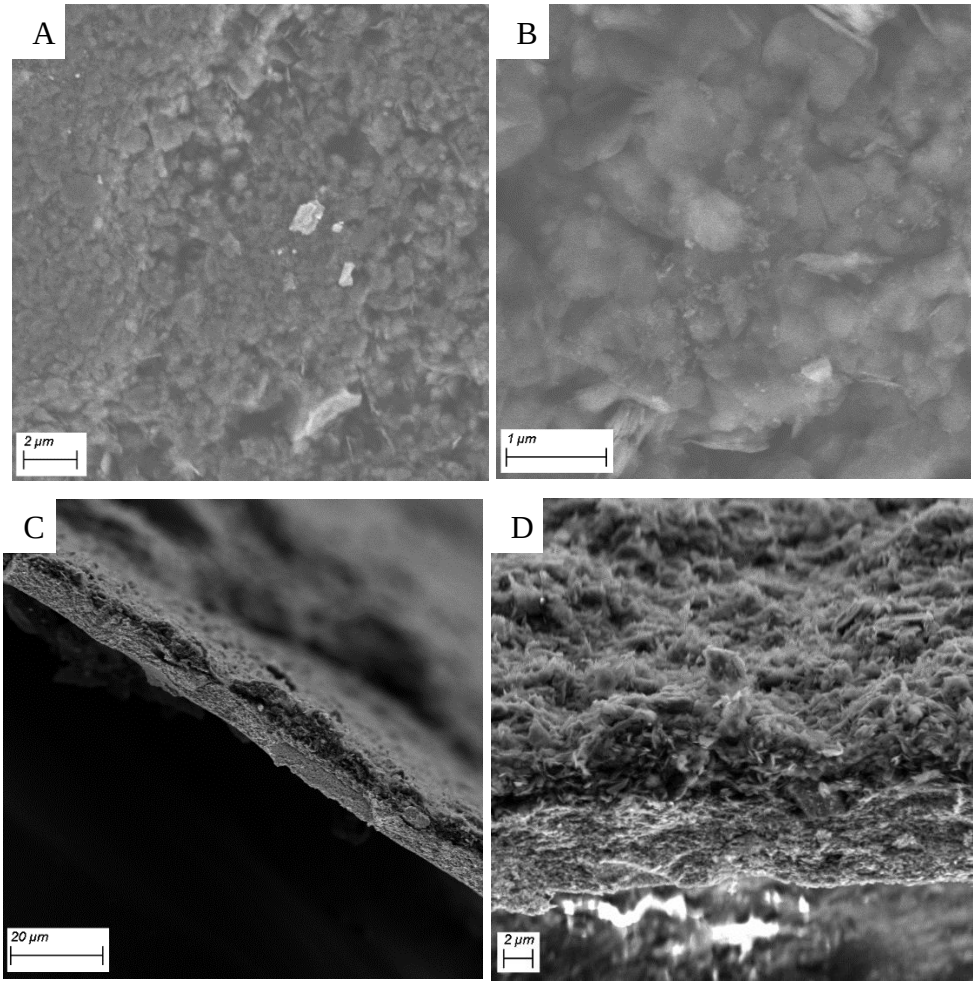

Figure 6.19: SEM images of MoS_2 membrane over 5mL layer of BNOx taken from the bottom-view (BNOx layer, A and B) and cross-section (C and D). Voltage 5.00 kV

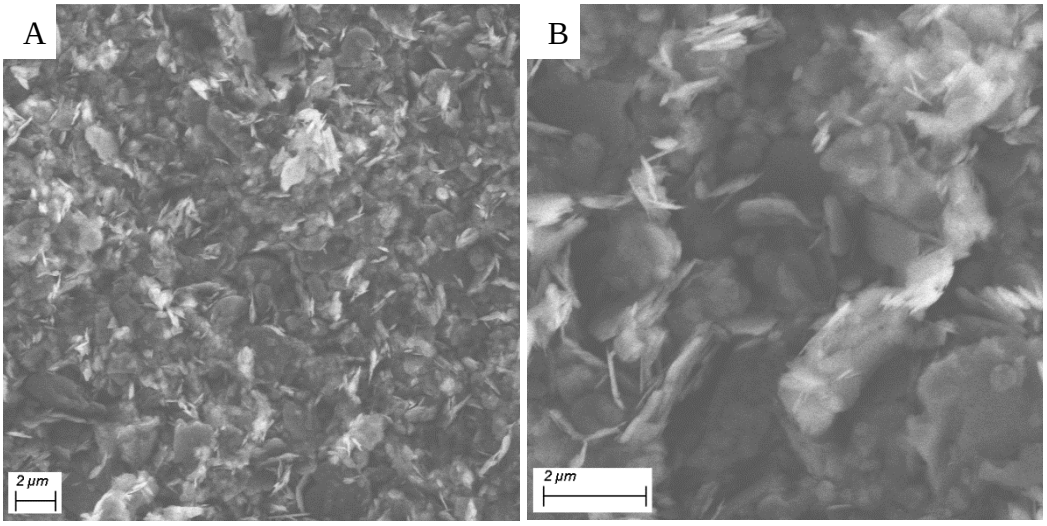

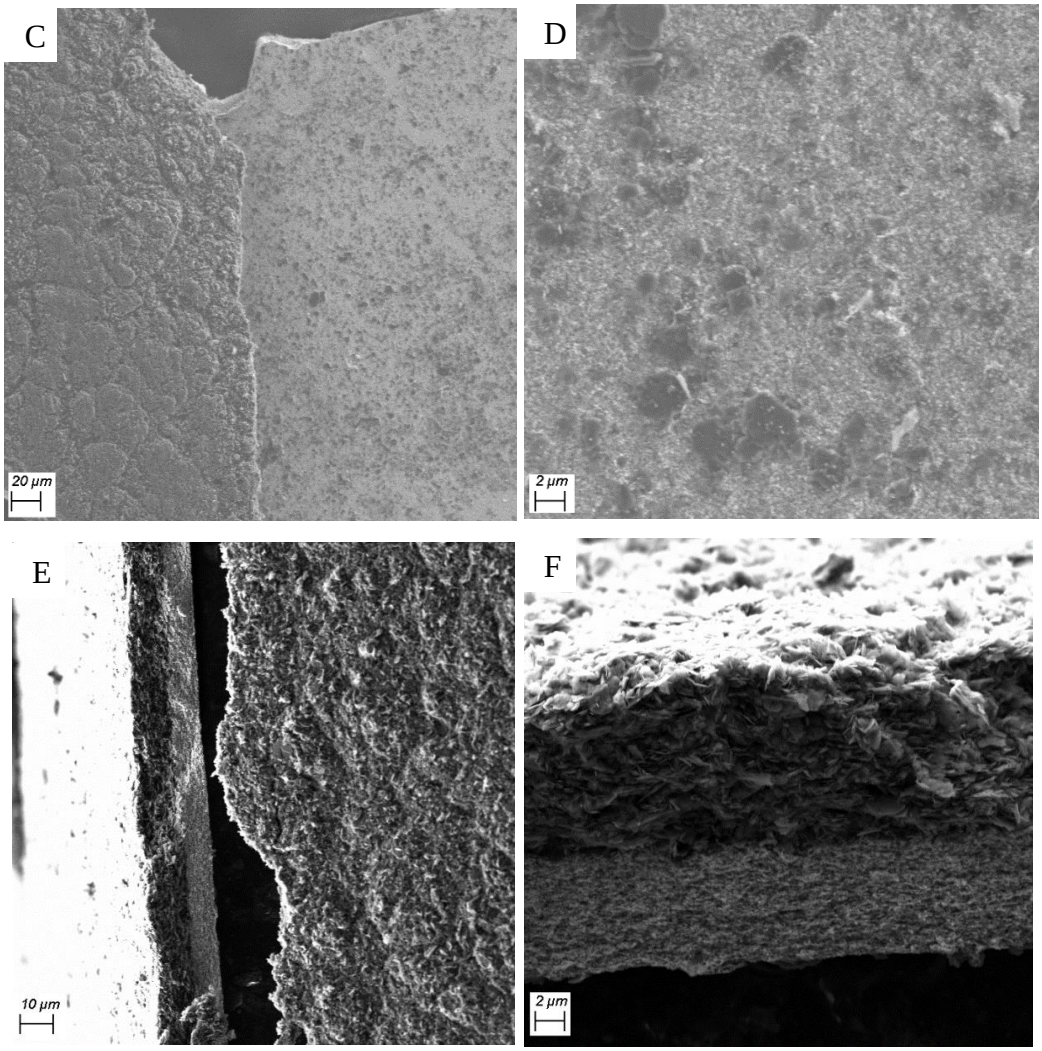

Figure 6.20: SEM images of MoS_2 membrane over 10mL layer of BNOx taken from the bottom-view (BNOx layer, A and B), top-view (MoS_2 layer, C and D) and cross-section (E and F). Voltage 5.00 kV

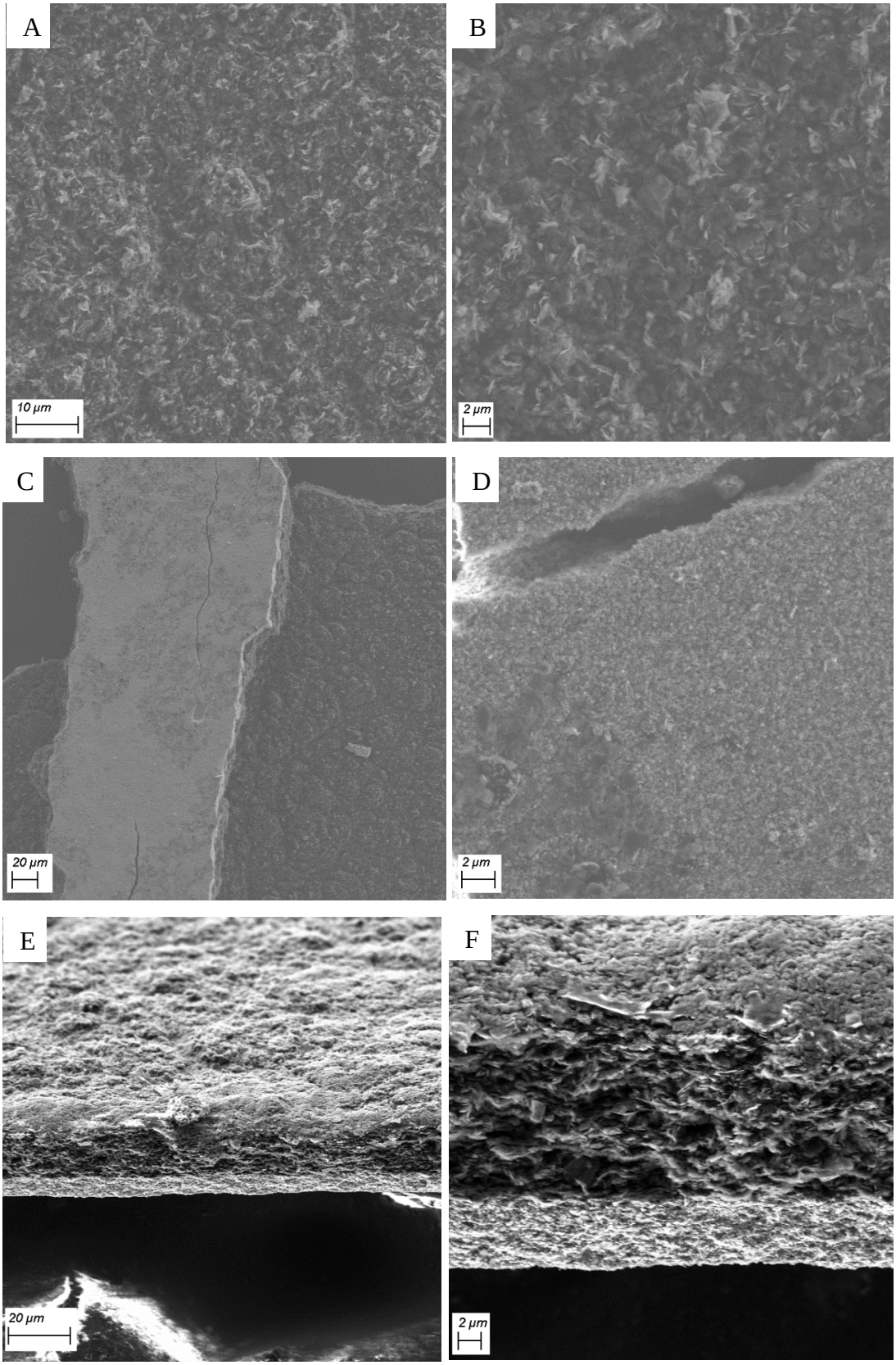

Figure 6.21: SEM images of MoS_2 membrane over 10mL layer of BNOx taken from the bottom-view (BNOx layer, A and B), top-view (MoS_2 layer, C and D) and cross-section (E and F). Voltage 5.00 kV

Top-view images were taken from both sides of the membranes, as each side of the membrane was composed of different materials (BNOx layer on the bottom and MoS_2 layer at the top). In the case of the 5 mL solution used for preparation of MoS_2 layer, it was not possible to obtain an image of the MoS_2 layer. The BNOx layer looked very similar in all cases, with the nanosheets stacked on top of each other. This layerlooked very similar to the BNOx and BN membranes that were made previously. The MoS_2 layer was easy to differentiate from the BNOx layer, as can be seen in figure 6.20 C and 6.21 C, where the MoS_2 can be identified as the lighter layer and the BNOx layer as the darker one, which corresponds with the layers in the cross-sections images. MoS_2 layer also shows the nanosheets stacked on top of each other. This layer also looked very similar to the MoS_2 membranes prepared previously, which shows that the membrane forms as normal on top of the BNOx layer.

The cross-section of the membranes showed that two clear layers were formed. The MoS_2 layer can be identified as the lighter grey one, as the MoS_2 nanosheets charge more than BNOx under illumination from the electron beam. A very interesting observation is the difference in thickness of both layers. Firstly, the BNOx layers increase in thickness as the volume of material is increased in each membrane, which was expected. However, the thickness of the BNOx layer appears to be thicker than the MoS_2 membrane, even though the volumes and, therefore, amounts of MoS_2 were greater. The 5 mL layer of BNOx (5.3±0.9 µm) is the same thickness, more or less, r than the MoS_2 layer (5.9±0.6 µm) with the whole membrane having a thickness of 10.03 ±1.2 µm), but the 10 mL layer seems to be thicker (11.3±0.7 µm) than the 50 mL MoS_2 (8.02±0.6 µm), with the membrane showing a thickness of 19.32 ±0.9 µm. The 20 mL layer BNOx appears to be double (15.37±1.7 µm) the thickness of the MoS_2 (6.23±0.7 µm), even though it's less than half the volume of the MoS_2 layer. This last composite membrane had a thickness of 21.94±2.1 µm. This seems to be due to the difference in size of the nanosheets (BNOx being more than double the size of the MoS_2) as well as the way the nanosheets were packed. The MoS_2 layer seems to be more compact and, therefore, thinner than the BNOx layer.

The membranes were then tested using Evans Blue (15 µM, 20 mL) and the UV-Vis absorbances are shown in figure 6.22.

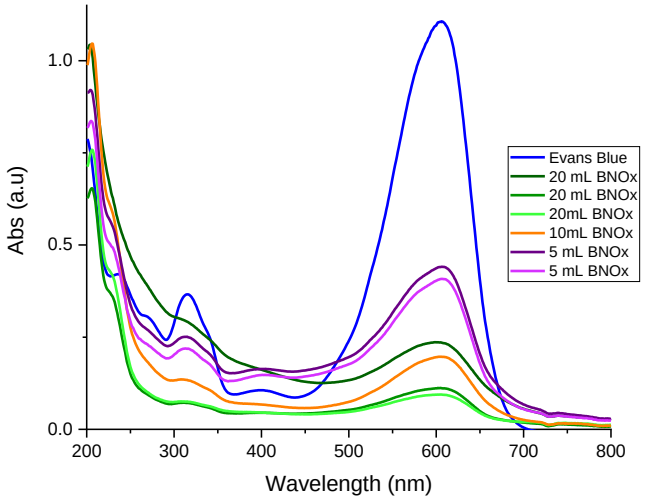

Figure 6.22: UV-Vis absorbance of Evans Blue before and after passing through the MoS_2 membranes with BNOx layer.

Table 6.4: Absorbance and retention of the MoS_2 membranes with a BNOx layer tested with Evans Blue 15 µM

Sample	% Retention
EB	0
20 mL BNOx	77
20 mL BNOx	89
20 mL BNOx	91
10 mL BNOx	81
5 mL BNOx	57
5 mL BNOx	61

The membranes made with 20 mL of BNOx showed two set of results. The first one demonstrates a lower retention that the other ones, but still showing a higher retention (table 6.4) than the MoS_2 membranes on their own (77% vs. 64%). The other membranes showed higher retention (around 90%), which much higher than the MoS_2 membranes on their own, but still lower than the BN/BNOx membranes. However, when the amount and thickness of BNOx layer is decreased, the retention is also lowered. For the 10 mL of BNOx the retention lowers by 10%, and upon using 5 mL of BNOx, the retention values are the same as not using a BNOx layer at all. Nonetheless, this retention is higher than the MoS_2 on PVDF filters. The BNOx layer seems to stabilise the membrane and help with the dye retention. The highest retentions are obtained when using 20 mL of

BNOx, which produces results more similar to those found in literature[53]. And, therefore, higher amounts of BNOx could results in higher retentions.

The next step in preparing the MoS_2-BNOx composite membranes was mixing equal parts of both compounds for each membrane. In order to do so, once both materials were exfoliated, 50 mL of MoS_2 were added to 50 mL of BNOx and sonicated together for 10 minutes. After this, 50 mL of the mixture were used to form each membrane. As BNOx was being used, it was decided to use the PVDF templates, as the previous experiments indicated that this would give the best results. The aim of these experiments was to examine if the mixture of both compounds would result in more stabilised, high-performance membranes. This would present several advantages; for example, the use of MoS_2 would allow for exploitation of thematerial's properties (e.g. catalytic properties, photoluminescence for sensing), while still taking advantage of the mechanical and chemical stability of BNOx as a membrane building block. This would enable to produce multipurpose membranes that could be tuned for the required application.

However, when the membranes were made, some leaking of the mixture through the template was observed, which could point towards to a poorly formed, non-robust membrane. SEM images of top view and cross-section of the 0.45 μm were taken (figures. 6.23 and 6.24).

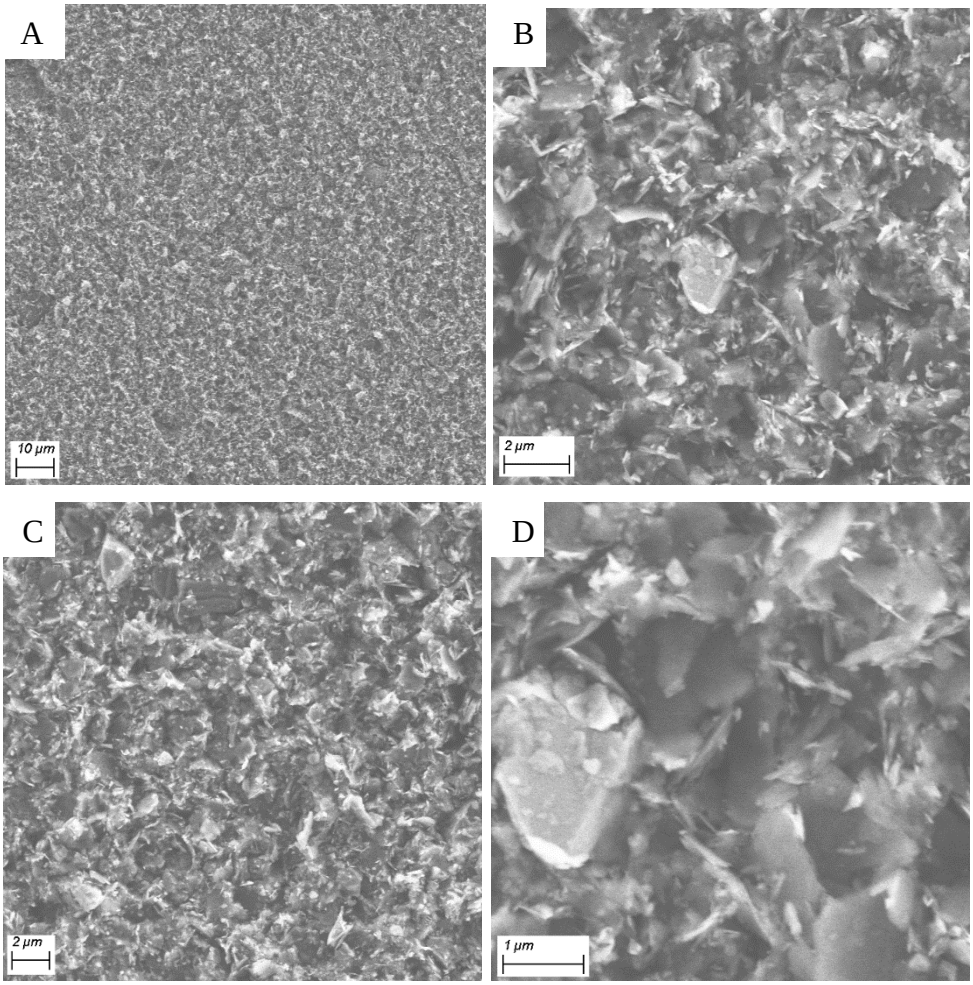

Figure 6.23: Top-view of membranes made with equal volumes of exfoliated BNOx and MoS_2, taken using SE2. Voltage 5.00 kV.

The top view of the membranes made with equal amounts of BNOx and MoS_2 show good mixture between the two materials. Bigger nanosheets can be seen throughout the surface of the membrane. These bigger nanoflakes are identified as the BNOx, as they have over double the size of the MoS_2 nanoflakes. Smaller nanosheets, identified as MoS_2, can be seen mixing with the bigger BNOx nanosheets. This mixture looked very even on the surface, with no pockets of just one of the materials, indicating that these materials are excellent candidates for the production of composite membranes, which could be used for several potential applications.

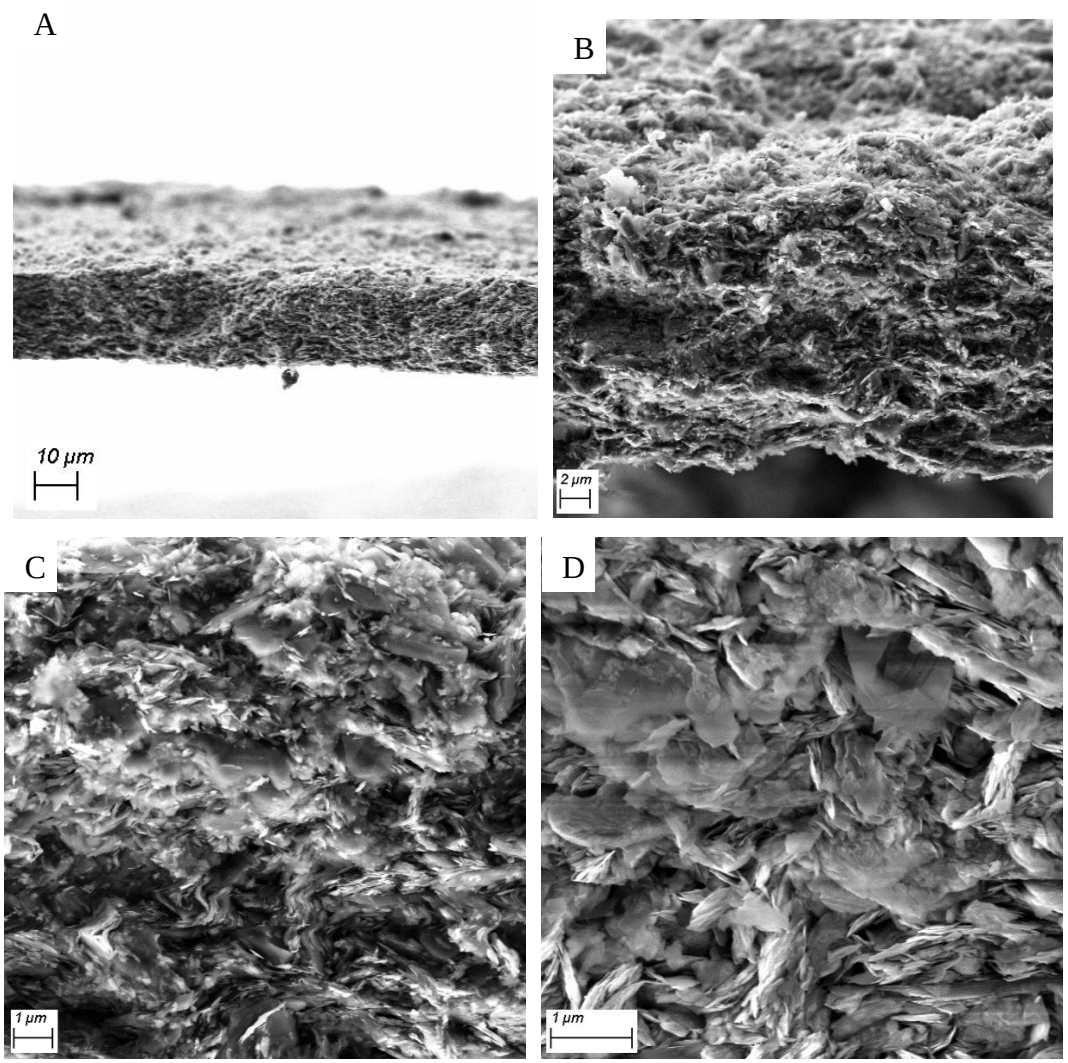

Figure 6.24: Cross-section of membranes made with equal volumes of exfoliated BNOx and MoS_2, taken (A-C) using SE2 and (D) taken with InLens. Voltage 5.00 kV.

The cross-section of the membrane shows a great mixture of both materials throughout the membrane. MoS_2 and BNOx are mixed evenly in the membrane, not showing any separation of the two materials. Under the InLens beam, it is not easy to differentiate between the two. However, when using SE2 the two are easier to tell apart from the difference in charging. Smaller nanosheets appear to be deposited on some bigger nanosheets. As the BNOx are more than double the size of the MoS_2, it is thought that the smaller MoS_2 are partially deposited on the BNOx, along with the full mixture of both materials. The membrane had a thickness of 19.7±1.3 µm.

Once the membranes were formed, they were tested using Evans Blue dye and (20 mL, 15 µM) and the retention was quantified using their absorbance (figure 6.25 and table 6.5).

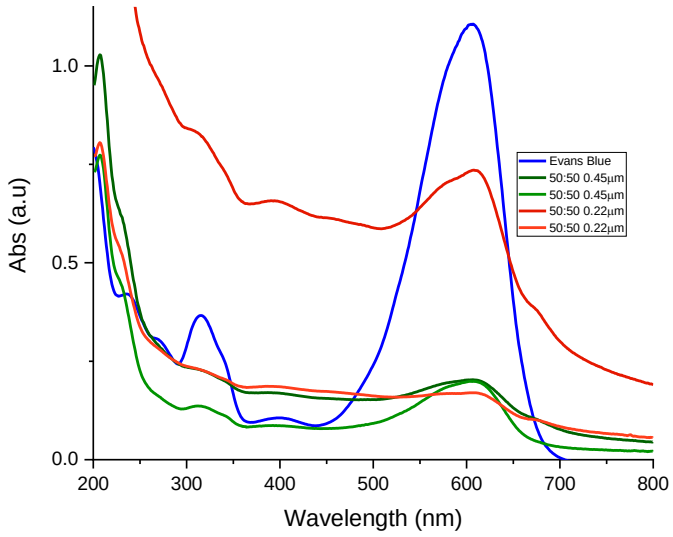

Figure 6.25: UV-Vis absorbance of Evans Blue before and after passing through the MoS_2: BNOx membranes with PVDF 0.45 µm (green) and 0.22 µm (orange) templates.

Table 6.5: Absorbance and retention of the MoS_2: BNOx membranes with PVDF 0.45 µm and 0.22 µm templates tested with Evans Blue 15 µM

Sample	% retention
EB	0
50:50 0.45 µm	81
50:50 0.45 µm	82
50:50 0.22 µm	33
50:50 0.22 µm	84

PVDF templates with two different pore sizes (0.45 and 0.22 µm) were used, to test if this would have any effect on the performance of the membranes. For the membranes formed using PVDF 0.45 µm, the retention value was higher than the MoS_2 membranes on their own, yet lower than both BNOx membranes on their own and the MoS_2 membranes with a BNOx layer. In the case of the membranes made with PVDF 0.22 µm, the results demonstrated more variability, with one of the membranes showing very low

retention (33%) and the other higher retention (85%). This higher retention is also higher than those obtained with the 0.45 μm template, therefore, higher than the MoS_2 membranes on their own, but still lower than the BNOx, and MoS_2-BNOx layered membranes. This could indicate that the layer of BNOx creates a stable film onto which the MoS_2 layers more efficiently than directly onto the template. This could be due to the small size of the MoS_2 nanoflakes (0.243 ± 0.564 μm), as it can be observed that smaller pore sizes increase the retention of the membrane, a case that is even more dramatic when the BNOx is not added (table 6.3). This could imply that the BNOx layer has smaller pore sizes than the templates, therefore, allowing the MoS_2 to deposit more efficiently on top of it. This could also explain why the MoS_2 membranes had lower retention than these membranes where the BNOx was introduced. It could be interesting, therefore, to use a BNOx layer with the polycarbonate template, as that was the template where higher retentions were observed for MoS_2 membranes.

Nevertheless, there is another possibility for these results to be taken into consideration. The increase in retention observed could be due to the introduction of BNOx, as this material has shown far better retention capability with this dye. Therefore, the MoS_2 would only retain a small percentage of this dye, with the BNOx capturing it more efficiently. However, if this was the case, this combination seems to lower the retention capabilities of the BNOx, probably due to the interaction with the MoS_2. This result, nonetheless, doesn't eliminate the usefulness of these membranes, as the combination of both materials could still allow the tuning of the membrane depending on the potential application. This, though, requires further optimisation and testing in order to produce more efficient membranes. It is important to notice that these membranes could also be used for other applications such as catalysis or sensing. Further investigation will be needed to develop membranes for these applications.

6.3 Conclusions

MoS_2 was successfully exfoliated in water and it was optimised with the addition of sodium cholate, which stabilises the exfoliated MoS_2 nanoflakes. It was found that this surfactant stays in the exfoliated solution even after cleaning, as shown by XRD and FTIR analysis. This indicates that further cleaning steps might need to be taken to remove it. Interestingly, the XRD also shows the presence of sodium molybdenum sulphide,

which could point out to a closer interaction between the sodium cholate and MoS_2, and in turn would explain why the solution is more stable, and the surfactant is unable to be removed through cleaning steps.

These MoS_2 exfoliated suspensions were used to produce new membranes. These membranes were used to test the retention of Evans Blue dye. However, the results obtained were lower than those reported in literature[53], so further testing and optimisation is needed.

MoS_2 was also functionalised with chiral molecules, cysteine and penicillamine. The functionalisation in solution was a success for both molecules and a chiral signal was recorded. However, the chiral molecules weren't retained in the membrane and were easily washed out with water. Therefore, further work on the incorporation of the chiral ligand onto the MoS_2 membranes is needed.

Finally, MoS_2 was mixed with BNOx to form composite membranes. This was done in two ways; firstlyby introducing a layer of BNOx where the MoS_2 was deposited, and secondly by mixing the two in the same amounts. The retention of the MoS_2 membranes with the BNOx layer was increased in when compared with the pristine MoS_2 membranes with highest results (77-91%) being obtained using the thickest BNOx layer. Nevertheless, these results were lower than the BN/BNOx membranes. In the case of the 50:50 MoS_2:BNOx membranes, although the retention was improved with respect to the MoS_2 membranes (80-85% vs 53-60%), the retention values were lower than when using the layered approach.

Bibliography

1 C. Ataca, H. Şahin and S. Ciraci, *J. Phys. Chem. C*, 2012, **116**, 8983–8999.

2 K. F. Mak, C. Lee, J. Hone, J. Shan and T. F. Heinz, *Phys. Rev. Lett.*, 2010, **105**, 136805.

3 K. F. Mak, C. Lee, J. Hone, J. Shan and T. F. Heinz, *Phys. Rev. Lett.*, 2010, **105**, 136805.

4 H. Tian, J. Tice, R. Fei, V. Tran, X. Yan, L. Yang and H. Wang, *Nano Today*, 2016, **11**, 763–777.

5 A. Soni, C. M. Pandey, M. K. Pandey and G. Sumana, *Anal. Chim. Acta*, 2019, **1055**, 26–35.

6 D. Lembke, S. Bertolazzi and A. Kis, *Acc. Chem. Res.*, 2015, **48**, 100–110.

7 B. Radisavljevic, A. Radenovic, J. Brivio, V. Giacometti and A. Kis, *Nat. Nanotechnol.*, 2011, **6**, 147–150.

8 P. Raybaud, J. Hafner, G. Kresse, S. Kasztelan and H. Toulhoat, *J. Catal.*, 2000, **190**, 128–143.

9 W. Yin, J. Yu, F. Lv, L. Yan, L. R. Zheng, Z. Gu and Y. Zhao, *ACS Nano*, 2016, **10**, 11000–11011.

10 M. A. Lukowski, A. S. Daniel, F. Meng, A. Forticaux, L. Li and S. Jin, *J. Am. Chem. Soc.*, 2013, **135**, 10274–10277.

11 L. Sun, H. Huang and X. Peng, *Chem. Commun.*, 2013, **49**, 10718.

12 H. Huang, Y. Mao, Y. Ying, Y. Liu, L. Sun and X. Peng, *Chem. Commun.*, 2013, **49**, 5963–5965.

13 L. Qiu, X. Zhang, W. Yang, Y. Wang, G. P. Simon and D. Li, *Chem. Commun.*, 2011, **47**, 5810–5812.

14 T. Liu, C. Wang, X. Gu, H. Gong, L. Cheng, X. Shi, L. Feng, B. Sun and Z. Liu, *Adv. Mater.*, 2014, **26**, 3433–3440.

15 X. Xie, Z. Ao, D. Su, J. Zhang and G. Wang, *Adv. Funct. Mater.*, 2015, **25**, 1393–1403.

16 Z.-T. Shi, W. Kang, J. Xu, Y.-W. Sun, M. Jiang, T.-W. Ng, H.-T. Xue, D. Y. W. Yu, W. Zhang and C.-S. Lee, *Nano Energy*, 2016, **22**, 27–37.

17 L. S. Byskov, J. K. Nørskov, B. S. Clausen and H. Topsøe, *J. Catal.*, 1999, **187**, 109–122.

18 M. Takaoka, N. Takeda, Y. Shimaoka and T. Fujiwara, *Toxicol. Environ. Chem.*, 1999, **73**, 1–16.

19 Y. Q. Yang, C. T. Tye and K. J. Smith, *Catal. Commun.*, 2008, **9**, 1364–1368.

20 G. Eda, H. Yamaguchi, D. Voiry, T. Fujita, M. Chen and M. Chhowalla, *Nano Lett.*, 2011, **11**, 5111–5116.

21 T. Li and G. Galli, *J. Phys. Chem. C*, 2007, **111**, 16192–16196.

22 Z. Wang and B. Mi, *Environ. Sci. Technol.*, 2017, **51**, 8229–8244.

23 K. Ai, C. Ruan, M. Shen and L. Lu, *Adv. Funct. Mater.*, 2016, **26**, 5542–5549.

24 M. Chhowalla, H. S. Shin, G. Eda, L.-J. Li, K. P. Loh and H. Zhang, *Nat. Chem.*, 2013, **5**, 263–275.

25 A. N. Enyashin, L. Yadgarov, L. Houben, I. Popov, M. Weidenbach, R. Tenne, M. Bar-Sadan and G. Seifert, *J. Phys. Chem. C*, 2011, **115**, 24586–24591.

26 F. Wypych and R. Schöllhorn, *J. Chem. Soc. Chem. Commun.*, 1992, 1386–1388.

27 J. N. Coleman, M. Lotya, A. O'Neill, S. D. Bergin, P. J. King, U. Khan, K. Young, A. Gaucher, S. De, R. J. Smith, I. V. Shvets, S. K. Arora, G. Stanton, H. Y. Kim, K. Lee, G. T. Kim, G. S. Duesberg, T. Hallam, J. J. Boland, J. J. Wang, J. F. Donegan, J. C. Grunlan, G. Moriarty, A. Shmeliov, R. J. Nicholls, J. M. Perkins, E. M. Grieveson, K. Theuwissen, D. W. McComb, P. D. Nellist and V. Nicolosi, *Science (80-.).*, 2011, **331**, 568–571.

28 R. J. Smith, P. J. King, M. Lotya, C. Wirtz, U. Khan, S. De, A. O'Neill, G. S. Duesberg, J. C. Grunlan, G. Moriarty, J. Chen, J. Wang, A. I. Minett, V. Nicolosi and J. N. Coleman, *Adv. Mater.*, 2011, **23**, 3944–3948.

29 K. Lee, H.-Y. Kim, M. Lotya, J. N. Coleman, G.-T. Kim and G. S. Duesberg, *Adv. Mater.*, 2011, **23**, 4178–4182.

30 B. Akesson and K. Paulsson, *Occup. Environ. Med.*, 1997, **54**, 236 LP – 240.

31 U. Halim, C. R. Zheng, Y. Chen, Z. Lin, S. Jiang, R. Cheng, Y. Huang and X. Duan, *Nat. Commun.*, 2013, **4**, 2213.

32 S. S. Chou, Y.-K. Huang, J. Kim, B. Kaehr, B. M. Foley, P. Lu, C. Dykstra, P. E. Hopkins, C. J. Brinker, J. Huang and V. P. Dravid, *J. Am. Chem. Soc.*, 2015, **137**, 1742–1745.

33 X. Fan, P. Xu, D. Zhou, Y. Sun, Y. C. Li, M. A. T. Nguyen, M. Terrones and T. E. Mallouk, *Nano Lett.*, 2015, **15**, 5956–5960.

34 D. Xu, Y. Zhu, J. Liu, Y. Li, W. Peng, G. Zhang, F. Zhang and X. Fan, *Nanotechnology*, 2016, **27**, 385604.

35 D. Wang, Z. Wang, L. Wang, L. Hu and J. Jin, *Nanoscale*, 2015, **7**, 17649–17652.

36 L. Sun, Y. Ying, H. Huang, Z. Song, Y. Mao, Z. Xu and X. Peng, *ACS Nano*, 2014, **8**, 6304–6311.

37 J. Kou, J. Yao, L. Wu, X. Zhou, H. Lu, F. Wu and J. Fan, *Phys. Chem. Chem. Phys.*, 2016, **18**, 22210–22216.

38 M. Deng, K. Kwac, M. Li, Y. Jung and H. G. Park, *Nano Lett.*, 2017, **17**, 2342–2348.

39 S. Zheng, Q. Tu, J. J. Urban, S. Li and B. Mi, *ACS Nano*, 2017, **11**, 6440–6450.

40 M. Hu and B. Mi, *Environ. Sci. Technol.*, 2013, **47**, 3715–3723.

41 J. Sikder, C. Pereira, S. Palchoudhury, K. Vohra, D. Basumatary and P. Pal, *Desalination*, 2009, **249**, 802–808.

42 G. A. M. Ali, M. R. Thalji, W. C. Soh, H. Algarni and K. F. Chong, *J. Solid State Electrochem.*, 2020, **24**, 25–34.

43 E. G. da Silveira Firmiano, A. C. Rabelo, C. J. Dalmaschio, A. N. Pinheiro, E. C. Pereira, W. H. Schreiner and E. R. Leite, *Adv. Energy Mater.*, 2014, **4**, 1301380.

44 S. Liu, X. Zhang, H. Shao, J. Xu, F. Chen and Y. Feng, *Mater. Lett.*, 2012, **73**, 223–225.

45 J. Zhao, Z. Zhang, S. Yang, H. Zheng and Y. Li, *J. Alloys Compd.*, 2013, **559**, 87–91.

46 H. Ma, Z. Shen and S. Ben, *J. Colloid Interface Sci.*, 2018, **517**, 204–212.

47 S. Zhong, X. Cui, H. Cai, T. Fu, C. Zhao and H. Na, *J. Power Sources*, 2007, **164**, 65–72.

48 L. Grosmaire, S. Castagnoni, P. Huguet, P. Sistat, M. Boucher, P. Bouchard, P. Bébin and S. Deabate, *Phys. Chem. Chem. Phys.*, 2008, **10**, 1577–1583.

49 E. Y. L. Teo, G. A. M. Ali, H. Algarni, W. Cheewasedtham, T. Rujiralai and K. F. Chong, *Mater. Chem. Phys.*, 2019, **231**, 286–291.

50 K. Zhou, S. Jiang, C. Bao, L. Song, B. Wang, G. Tang, Y. Hu and Z. Gui, *RSC Adv.*, 2012, **2**, 11695–11703.

51 E. Ramachandran and S. Natarajan, *Cryst. Res. Technol.*, 2004, **39**, 308–312.

52 M. S. Al-Marhoon, *Hereditary kidney stones*, 2015.

53 L. Sun, H. Huang and X. Peng, *Chem. Commun.*, 2013, **49**, 10718–10720.

Chapter 7. Conclusions and future work.

7.1 Conclusions

This work has resulted in the development of numerous membranes based on 2D nanomaterials, ranging from BN, BNOx, BN/BNOx composite membranes and MoS_2. All membranes have been characterized by various instrumental techniques and tested for several filtration and separation applications.

In respect to BN exfoliation, three test solvents (IPA, NMP and water) were effective in exfoliating BN and for producing corresponding BN-based membranes. It was found that the solvent choice played a key role in exfoliation of BN based materials and in the corresponding membrane performance. The use of water resulted in high levels of exfoliation and membranes with the best performance. The Raman peaks of water-exfoliated BN showed the largest shift, compared to those of the bulk BN. TEM and STEM images demonstrated the prevalence of monolayers to be highest in water-exfoliated BN samples. NMP demonstrated very effective exfoliation too, with AFM showing clear steps in the deposited sheets indicative of a highly exfoliated material in solution, with results showing no distinction between water and NMP in this case. In contrast, in all the tests carried out, IPA showed the lowest degree of exfoliation.

The membranes from IPA and NMP showed similarities in terms of the packing of the nanosheets. The BN-exfoliated in water packed differently, in a much more efficient way. The best retention-testing values (up to 100%) were obtained for the water-exfoliated membrane. Pore size and surface area were also shown to play an important role, with smaller pores and high surface areas giving the best retention values. The water-exfoliated membranes displayed excellent performance retaining several different dyes.

BNOx was proven to be an easy and fast way to introduce functionalisation (OH groups) in BN. This functionalisation could be used for further modifications for several potential applications, including cross-linking and enantiomeric separation. BN can be oxidised in the furnace, starting to gain OH groups at 700°C, but it has been shown that the additional oxidation can be achieved by sonicating the BNOx in water. This sonication results in both the exfoliation of the BN material as well introducing more OH into the BN structure, producing B-OH groups at the edges. It has been shown that further

functionalisation of BNOx could be achieved by its interaction with glucose by simply sonicating the BNOx in the presence of glucose. This functionalisation, although successful, has been proved to be insufficient for chiral separation. Furthermore, the addition of glutaraldehyde as a spacer between the BNOx and glucose opened the possibility for cross-linking of the membranes, which could improve their strength.

BNOx nanoflakes, due to their negative charge, were also successfully mixed with positively charged LDH layers. The addition of the LDH opened up a new approach for cleaning and recycling of the membranes by the photodegradation of the dyes which was demonstrated in our work. Our preliminary studies in liquid phase have shown that photodegradation reaction of methyl orange by BNOx-LDH corresponds to a pseudo-first order kinetic. However, more studies are necessary to fully establish the kinetics of this process inside BNOx – LDH membranes as well as the detailed analysis of the degraded materials.

BN-Fe_3O_4 composite membranes were also developed. The addition of magnetic nanomaterials opened up the possibility to perform magnetic separation and removing magnetic nanomaterials from wastewaters. Furthermore, the magnetic modality potentially enables to clean the membranes by burning the dye using magnetic induction heating. The membranes were optimised in terms of amount of BN vs amount of magnetite, with excellent retention values (up to 100%) for the dyes obtained, which shows that the performance of the membranes hasn't been altered by the addition of the Fe_3O_4 magnetic nanoplates.

BN and CNTs were successfully exfoliated together in water and used to produce new hybrid membranes with very high retention values of organic dyes. The addition of the CNTs doesn't alter the performance of the BN membranes, but the combination of BN and CNTs could allow the possibility to control the retention of different compounds, by altering the sizes of the pores of the membranes.

The exfoliation and functionalisation of MoS_2 was also developed. It was found that MoS_2 is better exfoliated in the presence of sodium cholate, as it stabilises the MoS_2 flakes in solution. XRD shows the presence of sodium molybdenum sulphide, indicating that the sodium ions from the surfactant interacts with the MoS_2, stabilising its exfoliated form. However, the exact mechanism by which this occurs is not known yet and further studies will be necessary to determine it. Testing of the MoS_2 based membranes, gave

results slightly lower than previously reported in literature. MoS_2 was successfully functionalised in solution with chiral ligands, cysteine and penicillamine. However, the ligands weren't stable enough in the membrane, and were easily washed out by passing water through it.

MoS_2 was successfully mixed with BNOx to produce composite membranes. There were two methods used for this purpose. The first one involved making a BNOx layer onto which the MoS_2 was deposited, with different amounts of BNOx tested. The higher the amount of BNOx used for the layer, the higher the retention obtained by the membranes. These retention values were higher than the ones obtained when using only MoS_2, but lower than in the case of BN or BNOx on their own. The second method was based on the mixing of the MoS_2 and BNOx, after exfoliation, in a 50:50 ratio. These membranes showed higher retention values than the MoS_2 membranes, but slightly lower than those produced by the first method using the BNOx layer approach.

Overall, we believe that our project has contributed to further development of functionalised 2D BN and MoS_2 based nanomaterials, corresponding membranes and their applications in separation and nanofiltration technologies.

7.2 Future work

Future work on the development and optimisation of BN membranes is still necessary. Currently, the main problem is that our membranes are for one use only and cannot be recycled. The retained dyes stay in the membrane and their removal has proven to be quite difficult. Further studies are necessary in order to develop an efficient removal of these dyes, allowing to reuse the membranes for multiple filtrations. The addition of LDH to the membranes seems to have an effect on the photodegradation of the dyes on the membranes' surface. However, this degradation needs to be fully studied and understood. It is necessary to determine an approach to quantify the amount of dye left in the membrane and clearly identify the photodegraded product. Several methods could be studied here, including NMR, solid state NMR and solid-state UV-Vis spectroscopy. The use of these techniques could help elucidate the kinetics and mechanisms taking place when the dye is being photodegraded inside the membrane. As the degradation of the dyes by LDH is a result of an oxidation, some oxidising agents (e.g. H_2O_2) could also be

tested with the dye degradation and removal. The effect of oxidises on the BNOx should also be tested, as it could result in potential BN oxidation and also affect the properties of membranes. The regenerated membranes will be tested and optimised for multiple filtration and dye removal applications.

A different option to reuse the membranes would be to burn off the retained dyes in the membrane as BN can sustain very high temperatures up to 900 ºC and still maintain its properties. This can be done by the addition of magnetic nanoplates (Fe_3O_4), which did not alter the retention properties of the BN membranes, as we have shown in our work. The magnetic nanoplates could be used to induce magnetic induction heating in the membrane, which, potentially, would raise the temperature of the membrane to a high enough temperature to burn off the dyes out of the membrane while still maintaining the integrity of the membrane. The advantage of using this type of heating versus external is that the heating will be distributed more evenly throughout the membrane, as the nanoplates are present across the entire membrane. The heating of the membrane would allow to burn the dye off consistently in the membrane, achieving higher removal. However, magnetic induction heating tests are necessary to determine that these membranes are suitable and can sustain the induction heating. Additionally, we need to find if the heating produced is sufficient to burn off the dye out of the membrane and the rate that this happens at. The addition of magnetic membranes could also be used for magnetic separation and magnetic impurities removal. This would potentially allow for a fast and cheap way of eliminating magnetic contaminants from wastewaters. Therefore, it will be necessary to check if whether these magnetic nanoparticles would be retained by membranes based on pure BN and magnetic membranes. We plan to test our membranes for filtration of mixtures of various magnetic nanoparticles with different stabilisers. The solution containing these nanoparticles would be filtered through a BN and BN-Fe_3O_4 membrane, and the retention would be noted. If the nanoparticles would be retained by the BN-Fe_3O_4 membranes, the retention of other magnetic contaminants could be tested.

Another aspect that should be studied is the possibility of alterations introduced to the membrane. As it has been shown before, oxidation in BN starts around 700 °C, which could potentially alter the function of the membrane. Therefore, studies into the effect of lower heating temperatures in BN would be needed. Furthermore, the sonication after exfoliation increases the degree of oxidation in BN samples. Therefore, studies to

determine the effect of different sonication times on the oxidation of BN needs to be carried out. The BN, after being treated in the furnace at lower temperatures, is to be sonicated in water at different times and the amount of oxidation would be monitored using XRD and FTIR spectroscopy, where the intensity and the B-OH peaks would be more prominent. The combination of different temperatures and sonication could be applied to control oxidation rates in the BN, which could be used for further functionalisation of BN based membranes.

Another problem with our BN based membranes is the low mechanical stability of the membranes. BN membranes were shown to be quite fragile on their own, flaking when separating from the template. The way this issue was addressed was to change the template from PTFE to PVDF, which had better interaction with BN, preventing flaking. However, this new template is bound so well to BN that the membrane couldn't be removed from the template. This poses additional problems, as the template now plays an important role in the membrane and would intervene in the cleaning process. Further research is needed to produce more mechanically robust membranes. An approach to address this issue is to introduce cross-linking of the BN flakes throughout the membrane structure. Therefore, on the development of more complex functionalisation of the BN to produce the cross-linking. One possible option is to use the oxidised BN, with the OH groups and further functionalise item with saccharide and polysaccharide molecules. This would allow for different layers of the membrane to cross-link together. The cross-linking of the membrane could make the membranes more robust, preventing them from breaking apart. In addition, these sugar functionalised membranes can potentially be used for mono-, di and poly-saccharide separation. The functionalisation of membranes with saccharides could, potentially, result in new membranes for separation. In our work, the retention of several sugars of different sizes was tested, with not very successful results, except in the case of retaining starch. Membranes functionalised with glucose and glutaraldehyde and glucose were produced in this project and their use could allow for the potential separation of smaller sugar molecules, like sucrose or dextran, due to the interactions of these saccharides and the glucose present in the membrane.

Even though the retention of the MoS_2 membranes was improved by the addition of BNOx to the membrane, the retention values obtained are still not as good as those achieved with other membranes. This could mean that these membranes are still not optimal for retention of dyes and use for water treatment. However, these membranes

could be used for other applications, where the properties of both components are used, like separation due to BNOx and catalysis of the substrates using the MoS_2.

The further functionalisation of MoS_2 was also achieved by sonicating the exfoliated MoS_2 in the presence of chiral ligands containing a thiol group. This functionalisation was proven by CD spectroscopy. However, the membrane obtained from this functionalised material couldn't be used for chiral separation, as the ligand was easily removed by washing the membrane. So, further optimisation of this process is necessary. A possible solution is using a chiral ligand that binds via covalent bonding to the MoS_2, so it won't be washed out. Initially, in order to functionalise MoS_2 covalently, MoS_2 was exfoliated with n-butyllithium (BuLi) using previously reported procedure.[1] Once the excess of BuLi was removed, the MoS_2 was further exfoliated in water. The UV-Vis spectrum of the chemically exfoliated MoS_2 was recorded and is shown in Figure 7.1. The spectrum obtained looked different to that one of the mechanically exfoliated MoS_2, as the bands at 400-450, 600 and around 700 nm disappeared, with new bands appearing at, 205, 250 and 350 nm. Still, the spectrum was also different from the one of the bulk MoS_2 confirming that the exfoliation was successful. The difference of the bands from the mechanically exfoliated MoS_2 is due to the difference of the MoS_2 state, as BuLi reduces it, allowing for the intercalation of the Li^+ ions between the Mo^- layers.

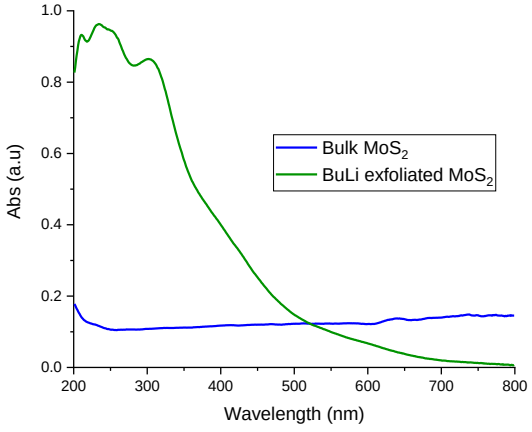

Fig 7.1: MoS_2 exfoliated with n-butyllithium, showing the characteristic bands of chemically exfoliated MoS_2. λ: 200-800 nm.

After that, the chemically exfoliated MoS_2 was functionalised with (S)-(+)-citronellyl bromide. This is a chiral molecule, which could bind covalently to the lithiated MoS_2, with an elimination of LiBr. This should induce chirality to the MoS_2 and allow the

production of MoS_2 based chiral membranes. However, further research is needed in order to establish whether the functionalisation with (S)-(+)-citronellyl bromide was achieved. For example, the samples should be characterised by CD spectroscopy, which should show a chiral signal due to the ligand and by FTIR spectroscopy, where peaks corresponding to the bond between the MoS_2 and the (S)-(+)-citronellyl bromide would be observed. The plan is to characterise all exfoliated MoS_2 samples by TEM in the near future. Once the functionalization was proven, this material could be used to produce membranes, where the chiral property would need to be tested. We expect that these new chiral membranes can be used to separate different enantiomeric molecules.

This approach is more likely to result in better membranes with better retention values, closer to those reported in the literature[2,3]. Furthermore, as the chiral ligand will be covalently bound to the MoS_2, therefore, the membranes could be used to induce chiral separation, as the chiral moiety of the membrane won't be removed by passing water through the membrane.

Bibliography

1 D. Voiry, A. Goswami, R. Kappera, C. de C. C. e Silva, D. Kaplan, T. Fujita, M. Chen, T. Asefa and M. Chhowalla, *Nat. Chem.*, 2014, **7**, 45.

2 L. Sun, H. Huang and X. Peng, *Chem. Commun.*, 2013, **49**, 10718.

3 Z. Wang and B. Mi, *Environ. Sci. Technol.*, 2017, **51**, 8229–8244.

Appendix

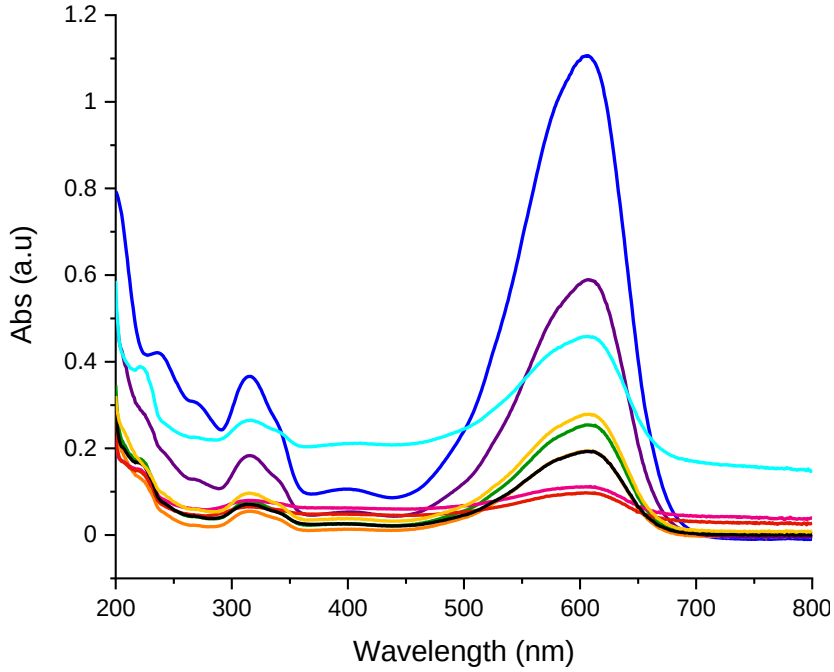

Figure A.1. UV-Vis spectra of the retention of 20 mL Evans Blue of the BNOx and Fe_3O_4 membranes (different percentages in weight)

Table A.1: Retention values for the BN and Fe_3O_4 membranes (different percentages in weight).

Membrane	% Retention
BN-Ox + 60% Fe_3O_4	77
BN-Ox + 60% Fe_3O_4	82
BN-Ox + 60% Fe_3O_4	46
BN-Ox + 60% Fe_3O_4	58
BN-Ox + 60% Fe_3O_4	90
BN-Ox + 60% Fe_3O_4	91
BN-Ox + 50% Fe_3O_4	82
BN-Ox + 50%Fe_3O_4	75
BN-Ox + 60% Fe_3O_4	65
BN-Ox + 60% Fe_3O_4	87
BN-Ox + 40% Fe_3O_4	100
BN-Ox + 40% Fe_3O_4	86

Table A.2: Statistics from the retention of the membranes obtained with BNOx and Fe_3O_4. The values were calculated using Origin 2018.

	N total	Mean	Standard Deviation	Minimum	Median	Maximum
BN-Ox + 60% Fe_3O_4	12	78	15	46	82	100

List of Publications

Papers:

- **Natalia García Doménech**, Finn Purcell-Milton, Yurii K. Gun'ko, "Recent progress and future prospects in development of advanced materials for nanofiltration", Materials Today Communications, Volume 23, 2020, 100888, ISSN 2352-4928, https://doi.org/10.1016/j.mtcomm.2019.100888.
- **García Doménech, N.**; Purcell-Milton, F.; Sanz Arjona, A.; Casasín García, M.-L.; Ward, M.; Cabré, M.B.; Rafferty, A.; McKel-vey, K.; Dunne, P.; Gun'ko, Y.K. High Performance Boron Nitride Based Membranes for Water Purification. *Nanomaterials* **2022**, *12*(3), 473; https://doi.org/10.3390/nano12030473

Conferences:

2020:

- "Development of New Nanofiltration Membranes Using 2D Nanomaterials" (poster) at the MRS fall Conference, Boston (Online).

2021:

- "Development of New Nanofiltration Membranes Using 2D Nanomaterials" (talk) at the 75th Irish Chemistry conference, Limerick (online).
- "How to write a lab report: a hands-on approach to improve chemistry undergraduate writing skills" (talk) at the Eurovariety conference, Slovenia (online).